

**IMMOBILIZED METALLODITHIOLATE LIGAND SUPPORTS FOR
CONSTRUCTION OF BIOINORGANIC MODEL COMPLEXES**

A Dissertation

by

KAYLA NANCE GREEN

Submitted to the Office of Graduate Studies of
Texas A&M University
in partial fulfillment of the requirements for the degree of

DOCTOR OF PHILOSOPHY

December 2007

Major Subject: Chemistry

**IMMOBILIZED METALLODITHIOLATE LIGAND SUPPORTS FOR
CONSTRUCTION OF BIOINORGANIC MODEL COMPLEXES**

A Dissertation

by

KAYLA NANCE GREEN

Submitted to the Office of Graduate Studies of
Texas A&M University
in partial fulfillment of the requirements for the degree of

DOCTOR OF PHILOSOPHY

Approved by:

Chair of Committee,	Marcetta Y. Darensbourg
Committee Members,	Kevin Burgess
	David H. Russell
	J. Martin Scholtz
Head of Department,	David H. Russell

December 2007

Major Subject: Chemistry

ABSTRACT

Immobilized Metallodithiolate Ligand Supports for Construction
of Bioinorganic Model Complexes. (December 2007)

Kayla Nance Green, B.S., Tarleton State University

Chair of Advisory Committee: Dr. Marcetta Y. Darensbourg

The A-cluster active site in acetyl coA synthase exploits a Ni(CGC)²⁻ metallopeptide as a bidentate ligand to chelate the catalytically active square-planar nickel center used to produce acetyl coA. As Nature utilizes polypeptides to isolate and stabilize the active sites, we have set out to immobilize biomimetic complexes to polyethylene-glycol (PEG) rich polystyrene polymer beads (TentaGel). The PEG rich resin-beads serve to imitate the peptidic superstructure of enzyme active sites as well as to protect the resin-bound models from O₂ decomposition. As a model of the NiN₂S₂ ligand observed in the A-cluster of acetyl coA synthase, the CGC tripeptide was constructed on resins using Merrifield solid phase peptide synthesis and then metallated with Ni^{II} to produce bright orange beads. Derivatization with M(CO)_x (M = Rh, W) provided qualitative identification of O-Ni(CGC)M(CO)_xⁿ⁻ via ATR-FTIR. Additionally, Neutron Activation Analysis (NAA) and UV-vis studies have determined the concentration of Ni and CGC, and qualitatively identify O-Ni(CGC)²⁻. Furthermore, infrared studies and NAA experiments have been used to identify and quantify O-Ni(CGC)Rh(CO)₂¹⁻.

The S-based reactivity of Ni(ema)²⁻, a good model of Ni(CGC)²⁻, toward oxygenation and alkylation has been pursued and compared to neutral NiN₂S₂ complexes. The spectroscopic, electrochemical and structural effects of these modifications will be discussed and supported using DFT computations and electrostatic potential maps of the resulting Ni(ema)•O₂²⁻ and Ni(ema)•(CH₂)₃ complexes.

Having firmly established the synthesis, characterization and reactivity of NiN₂S₂²⁻ systems in solution and resin-bound, Cu^{II}N₂S₂ analogues were explored. The synthesis and identification of solution complexes, Cu(ema)²⁻, Cu(emi)²⁻, and Cu(CGC)²⁻ via UV-Vis, EPR, and ⁻ESI-MS will be discussed in addition to their S-based reactivity with Rh(CO)₂⁺. Furthermore, the resin-bound Cu(CGC)²⁻ complex has been produced and characterized by EPR and its Rh(CO)₂ adduct identified by ATR-FTIR and compared to the analogous NiN₂S₂²⁻ systems.

As the active site of [FeFe] Hydrogenase utilizes a unique peptide-bound propane dithiolate bridge to support the FeFe organometallic unit, [FeFe]Hydrogenase models have been covalently anchored to the resin-beads via similar carboxylic acid functionalities. The characterization (ATR-FTIR, EPR, Neutron Activation Analysis), stability and reactivity of the immobilized models complexes are discussed as well as work toward establishing the microenvironment of resin-bound complexes.

DEDICATION

To my family – past, present and future.

This dissertation is dedicated to those who I have lost during my time here in College Station: Richard “PaPa” Green, Aunt Lovie Sides, JoAnne Keith, Iva Dunning and my beloved friend Duke. Richard you were a pillar of strength and will always be my example for someone who truly serves God. My dog Duke, as silly as it may seem, was a safe place in a world of turmoil. I will miss you all but treasure the times I had with each of you.

“Everyday I remind myself that my inner and outer life are based on the labors of other men, living and dead, and that I must exert myself in order to give in the same measure as I have received and am still receiving.” –Albert Einstein

ACKNOWLEDGEMENTS

During my graduate studies at Texas A&M University, I have been blessed with so many opportunities. Many of these have been directly instigated by my advisor. Marcetta, I will always build on the the scientific foundation that you have laid for me. What you have taught me about inorganic chemistry and life in academia will always be appreciated. Your imagination, attention to detail, and dedication to science and upholding its ideals has made my learning experience so much more than I had ever hoped for. Thank you for taking the time to make me a better scientist.

I would like to thank my advisory committee members, Drs. Kevin Burgess, David H. Russell, and J. Martin Scholtz for their advice and willingness for me to drop by with questions. Dr. Joseph H. Reibenspies deserves my sincere thanks for hours of discussions over x-ray crystallography. Your patience and willingness to help, even at the last minute, will always be appreciated. Dr. Don J. Darensbourg deserves special thanks as I concomitantly bombarded him with questions and annoyances. I have always appreciated your smile and words of encouragement.

It is with much gratitude that I acknowledge the help from collaborators, visiting professors and students that I have had the good fortune of knowing during my time here: Dr. Dennis James, Dr. David Rockcliffe, Dr. Craig Grapperhaus, Dr. Rolf Thauer, Dr. Patrick Toy, Dr. Pat Desrochers, Eric Schwerdtfeger, Ben Vastine, Paulo Botarelli, and Olaf Rudiger. I would like to acknowledge funding from the NIH Chemistry-Biology

Interface Program and to Dr. Kevin Burgess and Paul Lindahl for all their hard work in organizing the program.

Thanks also go to past MYD and DJD group members Drs. Melissa L. Golden, Joey Chiang, Wonsook Choi, Stephen Jeffery, Rosario Mejia-Rodriquez, Marilyn Rampersad and Jesse Tye. Each of you took the time to help me get a good start in graduate school. I would like to express special gratitude to Steve as you taught me a lot of chemistry and got me through the tough days. Thanks to current MYD and DJD group members Elky Almaraz, Jeremy Andreatta, Scott Brothers, Shawn Fitch, Eric Frantz, Roxanne Jenkins, Jen Hess, Tianbiao Liu (Leo), Adrianna Moncada, Osit Karroonnirun, Ross Poland, Michael Singleton and Dr. Christine Thomas. Your friendships and help will always be remembered and appreciated. Eric, I could always depend on you for a talk, a smile, and the ever important laugh. Thanks Jen for being yourself. What you lack in stature you more than make up in heart. Thank you, Scott, for all of the hugs and your uncanny way of knowing my every thought. Jeremy thank you for being a leader, one day it will pay off! Thank you Roxanne for always helping me to keep my priorities straight and to Elky for keeping me in line. I would also like to thank Sue for always being willing to help and giving me encouragement. I hope I have taught ya'll that if you believe in your project-eventually something good will happen! So stick with it. These are things that I have learned, maybe they will help you: Patience is a virtue. *Graduate School is an opportunity.* And no matter where you go there is always going to be someone who knows more than you and there will always be someone who knows less. So be thankful for both as you can learn from each.

Most importantly, thanks to my family. Daric you have been so patient and understanding through this process. You believed in me and pushed me to keep going even when I didn't think I could finish. Thank you Mom and Dad for making me the person I am. The strong moral character that you have instilled in me has allowed me to stay true to my beliefs while accomplishing this goal. I have achieved this because you took the time to teach me to do the right thing, help others, and believe in myself. Kellen, Kody, Tera, Charles and Vicki have always been a phone call away on the lonely walk home or a surprise visit to brighten my weekend. You have been there for me in some of the most devastating times but we have shared the brightest memories as well. Thanks to my blessed family by marriage. I can't say how lucky I am to have another set of parents, Aaron and Elaine, who have faithfully and tirelessly supported me with patience and understanding. And for all of your love, thank you Morgan, Jeanetta, Jimmy, Jan, and the rest of the Greens, Williams, Nances and Swaims.

Finally, I would like to thank the teachers at Tolar Schools and Tarleton State University, especially Mrs. Bell and Coach Lowry, Dr. Walter, Dr. Schultz, Rex Gamble, Dr. Low, Dr. Rathburn, and Dr. Konvicka. A Big thanks goes to everyone in the Department of Chemistry that make our jobs as researchers a little easier: employees of the graduate office, NMR, X-Ray, and Mass Spectrometry facilities, physical plant, maintenance, custodial, glass and machine shops. And finally, thank you to everyone who works to make our country a great place where a small town girl can grow up get her Ph.D. and live her dreams. Thank you.

TABLE OF CONTENTS

		Page
ABSTRACT		iii
DEDICATION		v
ACKNOWLEDGEMENTS		vi
TABLE OF CONTENTS		ix
LIST OF FIGURES		xii
LIST OF TABLES		xvi
CHAPTER		
I	INTRODUCTION.....	1
	The Roots of Immobilization	2
	Applications of Immobilization	9
	Metalloenzymes as Inspiration for Immobilized Ligands.....	12
II	EXPERIMENTAL SECTION FOR CHAPTERS	17
	Abbreviations	17
	General Procedures and Physical Methods	18
	Experimental Details for Chapter III.....	19
	Experimental Details for Chapter IV	25
	Experimental Details for Chapter V.....	27
	Experimental Details for Chapter VI	30
	Experimental Details for Chapter VII	33
III	A NICKEL TRIPEPTIDE AS A METALLODITHIOLATE LIGAND ANCHOR FOR RESIN-BOUND ORGANOMETALLICS.....	39
	Synthesis and Characterization of $[\text{Ni}(\text{CGC})][\text{W}(\text{CO})_4]^{2-}$ and $[\text{Ni}(\text{CGC})][\text{W}(\text{CO})_5]^{2-}$	41
	Preparation of Resin-Bound $\text{O-Ni}(\text{CGC})\text{W}(\text{CO})_5^{2-}$	44
	Preparation of Resin-Bound $\text{O-Ni}(\text{CGC})\text{Rh}(\text{CO})_2^{1-}$	48

CHAPTER	Page
Synthesis of Solution Analogues, [(Ni-1)Rh(CO) ₂][PF ₆] and “[NEt ₄][Ni(ema)Rh(CO) ₂]”	49
Conclusions for Chapter III	52
IV THE ACETYL CoA SYNTHASE PARADIGM FOR HYBRID BIO-ORGANOMETALLICS: QUANTITATIVE MEASURES FOR RESIN-BOUND Ni-Rh COMPLEXES	55
Loading of Ni on O-Ni(CGC) ²⁻	56
Loading of Rh on O-Ni(CGC)Rh(CO) ₂ ¹⁻	60
Stability of O-Ni(CGC)Rh(CO) ₂ ¹⁻	62
Conclusion for Chapter IV	63
V AN EXPERIMENTAL AND COMPUTATIONAL STUDY OF SULFUR-MODIFIED NUCLEOPHILICITY IN A DIANIONIC NiN₂S₂ Complex	64
Synthesis and Molecular Structures (Ni(ema)•(CH ₂) ₃) and ([Et ₄ N] ₂ [Ni(ema)•O ₂])	67
Solution Characterizations of Ni(ema)•(CH ₂) ₃ and [Et ₄ N] ₂ [Ni(ema)•O ₂]	68
Computational Details of Ni(ema) ²⁻ , [Ni(ema)•O ₂] ²⁻ , Ni(ema)•(CH ₂) ₃ and Ni(ema)•(Me) ₂	75
Conclusions	82
VI SYNTHESIS AND CHARACTERIZATION OF A SERIES OF CuN₂S₂²⁻ COMPLEXES AND STABILIZATION THROUGH A RESIN-BOUND Cu^{II} ANALOGUE	85
Synthesis and Characterization of [Et ₄ N] ₂ [Cu(ema)] and [Et ₄ N] ₂ [Cu(emi)]	93
Thiolate Reactivity of Cu(ema) ²⁻ and Cu(ema) with Rh(CO) ₂ ⁺	100
Synthesis and Characterization of [K] ₂ [Cu(CGC)]	103
Synthesis and Characterization of O-Cu(CGC) ²⁻	105
Thiolate Reactivity of Cu(CGC) ²⁻ and O-Cu(CGC) ²⁻ with Rh(CO) ₂ ⁺	109
Conclusions	111

CHAPTER	Page
VII RESIN-BOUND MODELS OF THE [FeFe] HYDROGENASE ENZYME ACTIVE SITE AND REACTIVITY	114
Immobilization of [FeFe]H ₂ ase Models	118
Synthesis of Monosubstituted Derivatives via Ligand Substitution on Immobilized FeFe Carbonyls.....	125
Disubstituted Derivatives and Their Reactivity	127
Interactions of TentaGel S-RAM [®] Beads with O-am-[A]	134
Comments and Conclusions	138
VIII CONCLUSIONS	140
REFERENCES	148
APPENDIX A	163
APPENDIX B	179
VITA	202

LIST OF FIGURES

FIGURE	Page
I-1 Representation of the A-Cluster of acetyl coA synthase.....	1
I-2 Examples of linkers used for reaction initiation sites in solid phase synthesis.	5
I-3 Representation of TentaGel Beads with a Rink Amide Linker, TentaGel S-RAM®	6
I-4 Representation of TentaGel resins showing the PEG chains forming microdomains.	8
I-5 (a) A Rh-diphosphine-cyclooctadiene complex is anchored via biotin (green) to (strept)avidin (b) Manganese salen complex attached to apo sperm whale myoglobin to form a synthetic enzyme active site mimic	11
I-6 Representation of the active sites from (a) nitrile hydratase and (b) Ni(SOD).	13
I-7 Examples for thiolate reactivity of NiN ₂ S ₂ complexes.	14
II-1 Synthesis of O-CGC and CGC using solid-phase peptide synthesis	19
II-2 A suspension of O-am-[A] in CDCl ₃ for NMR spectroscopy.....	34
III-1 Representation of the A-cluster active site of acetyl coA synthase.	39
III-2 Rank of electron donor ability as evidenced by (NiN ₂ S ₂)W(CO) ₄ derivatives and their respective ν(CO) IR bands and force constants.....	43
III-3 (a) The O-CGC; (b) The bright orange beads consisting of O-Ni(CGC) ²⁻ suspended in CH ₂ Cl ₂ ; (c) The O-[Ni(CGC)]W(CO) ₅ ²⁻ and its ATR-FTIR spectrum	46
III-4 Two views of [(Ni-1)Rh(CO) ₂] ⁺ , D, represented by a thermal ellipsoid plot as well as a ball and stick drawing; PF ₆ ⁻ anion excluded.....	50
III-5 Two views of [(Ni-ema)Rh(CO) ₂] ₂ ²⁻ , E, represented by a thermal ellipsoid plot and a ball and stick drawing, with Et ₄ N ⁺ cations excluded..	51

FIGURE	Page
IV-1 (a) Representation of the A-Cluster active site of acetyl coA synthase and (b) presumed structure of ACS-inspired complex immobilized on TentaGel Resin.....	56
IV-2 Loading of Mmt-protected O-CGC; O-Ni(CGC) ²⁻ ; and O-Ni(CGC)Rh(CO) ₂ ⁻	59
IV-3 Synthetic route to O-Ni(CGC)Rh(CO) ₂ and its infrared spectrum obtained on vacuum dried polystyrene beads via ATR-FTIR.....	61
V-1. Structures of (a) Ni(ema) ²⁻ , (b) [Et ₄ N] ₂ [Ni(ema)•O ₂], (c) Ni(ema)•(Me) ₂ and (d) Ni(ema)•(CH ₂) ₃ with selected bond distances (Å) and angles (°).....	69
V-2. Cyclic Voltammogram of a 0.037 mM DMF solution of Ni(ema)•(CH ₂) ₃ at a scan rate of 200 mV/s using an Ag/AgNO ₃ reference electrode, 0.1 M [ⁿ Bu ₄ N][BF ₄] electrolyte, a glassy carbon electrode and standardized to Fc/Fc ⁺ and reported vs. NHE.	72
V-3 X-band EPR spectra obtained from an oxidized solution of Ni(ema)•(CH ₂) ₃ in DMF at 10 K.	73
V-4 Frontier molecular orbitals of (a) Ni(ema) ²⁻ , (b) [Ni(ema)•O ₂] ²⁻ , (c) Ni(ema)•(CH ₃) ₂ , and (d) Ni(ema)•(CH ₂) ₃	77
V-5 The principal resonance structures of Ni(ema) ²⁻ and Ni(ema)•(CH ₃) ₂ as identified by natural bond orbital (NBO) analysis.	79
V-6 In order of descent: Electrostatic potentials of Ni(ema) ²⁻ , [Ni(ema)•O ₂] ²⁻ , Ni(ema)•(CH ₂) ₃ and Ni(ema)•(Me) ₂	81
VI-1 Salen-peptide complex by Burrows <i>et al</i>	85
VI-2 Active site of plastocyanin.....	86
VI-3 Representation of Cu ₅ S ₄ adamantane.	87
VI-4 A comparison of tetragonal distortion in plastocyanin (Pc), cucumber blue protein (CBP) and nitrite reductase (NiR) showing positions of the S _{Cys} and S _{Met} compared to the N-Cu-N plane.....	88

FIGURE	Page
VI-5 Representative drawing of (a) the active site of acetyl coA synthase and (b-d) a few examples of small molecule models for the Ni ₄ site acetyl coA synthase	89
VI-6 Examples of biomimetic CuN ₂ S ₂ ^{x-} complexes.....	92
VI-7 Thermal ellipsoid plots of [Et ₄ N] ₂ [Cu(emi)] showing 50% probability and the atom labeling scheme	94
VI-8 ⁻ ESI-MS spectra and theoretical isotopic bundles of (a) Cu(ema) ²⁻ and (b) Cu(emi) ²⁻	96
VI-9 CV overlay of the Ni ^{III/II} couple of [Et ₄ N] ₂ [Ni(ema)] (3.7 mM) in grey and the Cu ^{III/II} couple of [Et ₄ N] ₂ [Cu(emi)] (2.3 mM) in black using DMF solvent at a scan rate of 100 mV/s using a Ag/AgNO ₃ reference electrode, 0.1 M [ⁿ Bu ₄ N][BF ₄] electrolyte, and a glassy-carbon electrode	98
VI-10 Experimental and simulated X-Band EPR spectra of (a) [Et ₄ N] ₂ [Cu(ema)] and (b) [Et ₄ N] ₂ [Cu(emi)] (2mM in DMF at 9 K, 9.75 GHz).....	100
VI-11 Molecular structure of [Et ₄ N] ₂ [Ni(ema)Rh(CO) ₂] ₂ with cations omitted .	102
VI-12 FTIR spectra (DMF) of (a)[Et ₄ N][Cu(ema)Rh(CO) ₂] and (b)[Et ₄ N][Cu(emi) Rh(CO) ₂].....	103
VI-13 Experimental and simulated X-Band EPR spectra of (a) Cu(CGC) ²⁻ and (b) O-Cu(CGC) ²⁻	104
VI-14 The resulting EPR spectra obtained from (a) TentaGel beads incubated with Cu(OAc) ₂ •4H ₂ O and (b) 20 equivalents of Cu(OAc) ₂ •4H ₂ O mixed with O-CysGlyCys.....	108
VI-15 FTIR spectra of (a) O-Cu(CGC)Rh(CO) ₂ ¹⁻ (ATR-FTIR) and (b) Cu(CGC)Rh(CO) ₂ ¹⁻	111
VII-1 Representation of the dinuclear iron active site of [FeFe]H ₂ ase.....	115

FIGURE	Page
VII-2 Comparison of infrared spectra for O-am-[A] (ATR-FTIR) (top) and [A] (THF) (Bottom)	119
VII-3 The ATR-FTIR and ³¹ P spectra of O-am-[B]	124
VII-4 Targets for reactivity studies of resin-bound [FeFe]H ₂ ase models	128
VII-5 (Top) Assignment of vibrational modes for the (μ-pdt)[Fe(CO) ₃] ₂ molecule and (Bottom) deconvoluted IR spectrum of O-am-[A] with the resulting fitted spectrum (- - -) and the experimental ATR-FTIR spectrum (—) overlaid	136
VII-6 Overlay of Infrared Spectra of O-am-[A] and (μ-pdt)[Fe(CO) ₃] ₂ dissolved in polar to non-polar solvents.....	137
VIII-1 Representation of O-M(CGC) ²⁻ where M = Ni or Cu (left) and O-[A] (Right)	144
VIII-2 The stepwise understanding of resin-bound complexes reported in this dissertation using O-am-[A] as an example	146

LIST OF TABLES

TABLE		Page
III-1	CO stretching frequencies ($\text{NiN}_2\text{S}_2\text{W}(\text{CO})_4$ in dimethylformamide, DMF, and $\text{NiN}_2\text{S}_2\text{W}(\text{CO})_5$ in Tetrahydrofuran, THF, solvent) and calculated force constants (FC) for the $\text{W}(\text{CO})_x$ ($x = 4,5$) derivatives of the tripeptide $\text{Ni}(\text{CGC})^{2-}$ and the $\text{Ni}(\text{ema})^{2-}$ complex ions.....	42
IV-1	Average loading of $\text{O-Ni}(\text{CGC})^{2-}$ (mmol Ni/g resin bead) determined via Neutron Activation Analysis on separately prepared samples.....	58
IV-2	Ni and Rh loadings for $\text{O-Ni}(\text{CGC})\text{Rh}(\text{CO})_2^{1-}$ resulting from induced stress conditions	62
V-1	Summary of electronic absorption spectra for $\text{Ni}(\text{ema})^{2-}(\text{EtOH})$, $\text{Ni}(\text{ema})\cdot(\text{Me})_2$ (CH_3CN), $\text{Ni}(\text{ema})\cdot(\text{CH}_2)_3$ (MeOH), $\text{Ni}(\text{ema})\cdot\text{O}_2^{2-}$ (MeOH)	70
VI-1	Selected bond distances and angles for $[\text{Et}_4\text{N}]_2[\text{Cu}(\text{emi})]$ compared to $[\text{Et}_4\text{N}]_2[\text{Cu}(\text{phmi})]$ and $[\text{Et}_4\text{N}]_2[\text{Ni}(\text{ema})]$	95
VI-2	Summary of Electronic Absorption Spectra for $\text{Cu}(\text{ema})^{2-}$, $\text{Cu}(\text{emi})^{2-}$, $\text{Cu}(\text{CGC})^{2-}$ in CH_3CN solvent.....	97
VI-3	Comparison of g_{\parallel} , g_{\perp} and A_{\parallel} values for $\text{CuN}_2\text{S}_2^{2-}$ complexes.....	105
VI-4	Comparison of $\text{MN}_2\text{S}_2\text{Rh}(\text{CO})_2^{1-}$ complexes ($\text{M}=\text{Cu}, \text{Ni}$).....	110
VII-1	Comparison of Resin-Bound $[\text{FeFe}]\text{H}_2\text{ase}$ model complexes with solution analogues.....	121

CHAPTER I

INTRODUCTION

With the discovery of the dinickel site in the acetyl coA synthase (ACS) metalloenzyme (Figure I-1), a new paradigm for di- and poly-metallic enzyme active site construction has been recognized.^{1,2} In this case, one nickel is incorporated into a Cys-Gly-Cys tripeptide motif, bound by two carboxyamido nitrogens of a cysteine and the glycine, along with the sulfurs of both cysteines, in a secure, square-planar N_2S_2 coordination site.^{1,2} The cysteinyl sulfur atoms in turn capture a second nickel ion whose coordination environment is well-suited for the organometallic reactions required of the ACS enzymatic cycle which include oxidative addition of CH_3^+ , methyl-CO migratory insertion, and reductive elimination of $RSC(=O)R'$.³ It has been suggested, and corroborated by computational chemistry, that the NiN_2S_2 portion of the active site may be considered as a supporting ligand, capable of stabilizing the second nickel in a low-

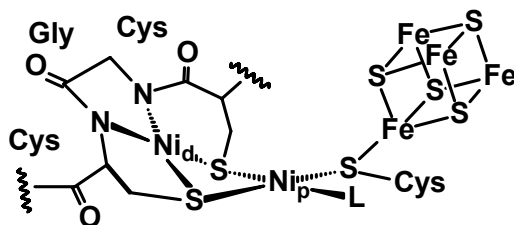


Figure I-1. Representation of the A-Cluster of acetyl coA synthase.¹

This dissertation follows the style of *Journal of the American Chemical Society*.

valent redox level required for the oxidative addition of Me^+ .³ Another possible advantage of the NiN_2S_2 metalloligand in the ACS active site is its hemi-labile, ring-opening property which generates an open site on the catalytic metal.⁴

Interestingly there is a passage between ACS and its partner, carbon monoxide dehydrogenase (CODH), in the form of a hydrophobic channel through which CO is directed from its site of production in CODH to its site of utilization in ACS.^{1,2} While the evolutionary design in proteins produce channels through protein folding, synthetic chemists may crudely mimic such isolated catalyst sites by imbedding active site mimics in solid-supports.⁵ Semi-porous resin-beads with solvent channels or microdomains formed by lengthy polyethylene glycol chains permit attached catalyst site isolation with possibilities for substrate size recognition.^{5,6,7} The goal of the work described below is to lay the foundation for the use of natural metallopeptides as resin-bound ligands for potentially catalytically active metals. In this Introduction I will review solid supports and their use to tether reagents or catalysts.

The Roots of Immobilization

The separation of reagents and purification of products by anchoring one to a solid phase has found many applications throughout chemical history. The use of heterogeneous media to carry out a desired chemical process finds its roots at least a decade before R.B. Merrifield applied it to the synthesis of peptides, *vide infra*. Ion-exchange resins for catalysis were arguably the first application that utilized polymers to

support chemical reactions.⁸ Since the initial work over half a century ago, investigations directed toward the heterogenizing of known solution chemistry via solid-supports have found use in an ever-expanding number of fields. The Novabiochem Catalog carries insoluble organic polymeric supports, commonly called resin-beads, that are used for solid-phase peptide synthesis, solid-phase organic synthesis, chromatography, nucleophilic and electrophilic scavengers, and oxidizing or reducing agents.⁹

Solid-phase supports include silica, nanoparticles, dendrimers, ionic liquids, sol-gels, and insoluble organic polymers. Insoluble organic polymers will be the focus of this work. Similar underlying principles are utilized in each application using these solid supports. That is, the use of a solid support permits easy separation of reagents from products, an increased stability of product or catalyst, and, in most cases, an easy recovery of the immobilized species.⁶ These properties serve as the major motivation for the enormous number of studies examining the use of various metal complexes for catalysis in the past 50+ years.^{6,7,10}

The ground-breaking application of reagent-product separation using an organic polymer solid-support began with Merrifield's solid-phase peptide synthesis which was recognized by the Nobel prize in 1984 twenty-one years following the initial reports.^{11, 12} It began in 1963 when the *Annual Reports on the Progress of Chemistry* had a brief section dedicated to highly significant advances in pure chemistry.¹³ This article highlighted Merrifield's synthesis of a tetra peptide via consecutive attachment of amino acids to an insoluble and microporous solid support.¹⁴ As a number of byproducts were also reported, several criticized the work as prevailing wisdom assumed complete

reactions and purification of polymer supported species would be more difficult than solution chemistry.¹³ However, later that year in the Journal of the American Chemical Society, Merrifield reported the total synthesis of the vasodilator bradykinin (9 amino-acids in length, Arg-Pro-Pro-Gly-Phe-Ser-Pro-Phe-Arg).¹⁵ This initial discovery could not have come at a better time as medicinal chemists were realizing the importance of peptides as hormones, antibiotics, and other biologically active species.¹² During the short period of time ~50 years, the synthesis and purification of peptides, up to 200 amino acid units, has been greatly optimized resulting in higher yields.¹⁶ The field has grown to include oligonucleotide and pseudopeptide synthesis. Currently, the automated synthesis of peptides based on Merrifield's approach is considered common-place.

Merrifield's contributions were two-fold: 1) through the use of protecting groups, peptide purity increases and racemization decreases. 2) The use of a solid-support facilitates the separation of reagents from products.¹² These initial contributions have since been expanded upon.

It should be pointed out that there are two regimes to consider when working with solid-supports. The first is the synthetic chemistry used to produce the resin-bound species, while the second are the properties of by the solid-support itself. Focusing on the latter, choosing the correct resin-bead is the foundation for designing a successful synthesis. For example, the ability for solvent molecules to interact with the resin-beads reflects a property known as swelling. This property permits access of reagents to sites embedded *within* the polymer and is typically considered a desirable attribute. Lower cross-linking, i.e. the extent to which polymer chains are linked to one another, results in

greater mobility of the polymer chain and hence greater swelling in the presence of solvents. Cross-linking is necessary for these supports, however, as it engenders structural robustness. As an example, for polystyrene crosslinked with divinylbenzene, an optimal cross-linking of ~1% has been found to give good swelling while avoiding a fragile polymer.¹¹

The development of new linkers for catalyst or substrate attachment to resin-beads has advanced the field of solid phase synthesis. A few examples are shown in Figure I-2. The linker (1) aids in protection of the C-terminal α -carboxyl group during the peptide synthesis, and the linker (2) serves as a chemically reversible linkage between the peptide product and the solid-support. Linkers are usually attached to the terminus of a polystyrene backbone. If a PEG chain is present (discussed below) the linker will be attached to the terminus of this moiety. The number of linkers, or available reactive sites is termed the “loading” of the resin and is measured in mmol of reactive sites per gram of resin-beads (mmol/g).

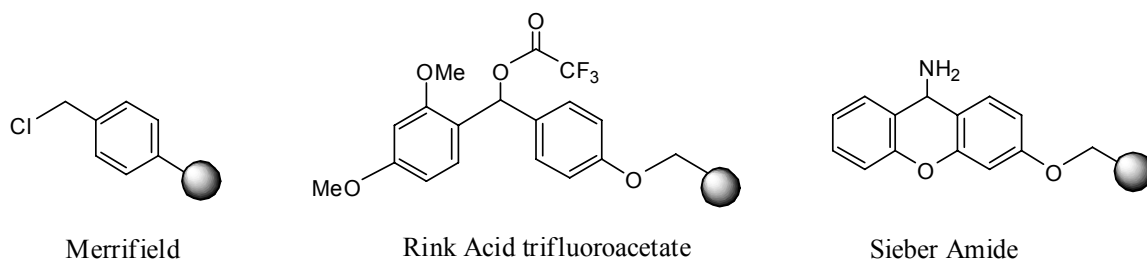


Figure I-2. Examples of linkers used for reaction initiation sites in solid phase synthesis.¹⁷

Many of the physical properties of the beads, discussed above, can be manipulated to fit the particular needs of an application. In particular, it is important to consider the loading of an immobilized compound. For example, if the product of a solid-phase peptide synthesis is composed of 20+ amino acids, resins with low loading >0.3 mmol/g provide the highest yields and purity.¹⁸ An additional consideration is that the linker generally determines the C-terminal functional group in the final product.⁹ For example, the Rink Amide linker, shown in Figure I-3, uses a primary amine as the platform for peptide construction. Following cleavage, or removal of the peptide from the bead, the resulting resin-free peptide has an amidated C-terminus. Finally, the ultimate mode of product cleavage is a factor to consider when choosing an appropriate linker. Linkers may be acid or base labile; they may be cleaved by nucleophiles or even light.¹⁷ Thus the reaction conditions for cleavage must be quite different from those used to produce the immobilized compound.

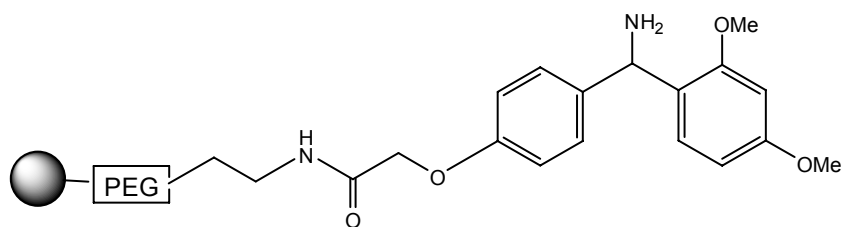


Figure I-3. Representation of TentaGel Beads with a Rink Amide Linker, TentaGel S-RAM[®]. PEG = polyethylene glycol, $-\text{CH}_2\text{-O-CH}_2\text{-CH}_2\text{-[O-CH}_2\text{-CH}_2\text{-]}_n\text{-O-CH}_2$.

In Merrifield's original studies a chloromethylated polystyrene-divinylbenzene polymer was utilized.¹⁴ Such hydrophobic polystyrene is acceptable for short peptides,

but it does not provide the appropriate environment for longer or hydrophilic peptides. Therefore, taking account of the factors above, new polymeric solid supports have been developed for peptide synthesis as well as other applications. For example, the grafting of polyethylene glycol (PEG) onto the hydrophobic polystyrene backbone, endows polymers with hydrophilic character. The grafting technique produces polymers with PEG chains of ~3000 M.W. when optimized.¹⁶ Such solid-supports are therefore roughly 70% PEG and 30% polystyrene matrix.^{16, 19} Thus, the properties of the polymers that lead to microenvironments about the reactive sites are largely imparted by the PEG portion of the support.¹⁶ Additionally, these PEG functionalities increase the range of solvents compatible with the support. The greater degree of swelling imparted by the PEG unit is a key component in optimizing the immobilization of reagents on these polymers. The greater the swelling, the more access reagents have to interior sites through resulting solvent channels, as shown in Figure I-4. For these reasons PEG is a common graft or spacer used in designing resins.

Resin-beads are not limited to polystyrene-divinylbenene polymer backbones. A number of monomer combinations have been used to produce resin-beads. NovaSyn TG[®] resins are composed of low cross-linked hydroxyethylpolystyrene and grafted with PEG between 3000 and 4000 M.W. The beads are about 90-130 μm in diameter making them suitable for producing resin-bound chemical libraries as well as for use in continuous flow solid-phase peptide synthesis.²⁰

Other resin compositions, such as polyacrylamides, are available as well. Their hydrophilic character is more conducive to the synthesis of long-chain peptides and

serves as an alternative to low loading polystyrene based resins.¹⁶ However, these beads degrade over time, particularly in the presence of light, and are prone to uneven distribution of reaction sites.²¹ The grafting of PEG chains, 800 M.W., onto the acrylamide backbone provides increased stability to the polymer, making these new resins viable for synthesis.²² These PEG-acrylamide (PEGA[®]) composite resins are generally utilized for continuous flow peptide synthesis and are gaining usage in solid-phase organic synthesis. The beads are permeable to macromolecules up to 35 kDa, making them ideal for peptide libraries or on resin-enzyme assays, similar to those discussed below.²³

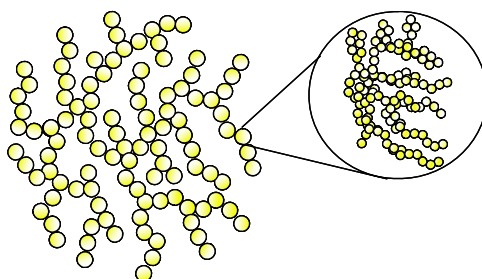


Figure I-4. Representation of TentaGel[®] resins showing the PEG chains forming microdomains.¹⁹

A resin-bead commonly used for peptide synthesis and the focus of the studies herein is TentaGel S-RAM beads, Figure I-3. These beads are composed of a polystyrene backbone with 1% crosslinking, grafted with PEG, and the PEG termini are easily functionalized with a Rink Amide Linker (RAM). They are purchased from Advanced ChemTech or Novabiochem, but are available from many companies in nearly

identical form. The mobility of the PEG chains is reminiscent of tentacles which accounts for the name TentaGel beads. The the primary amine linker which is covalently linked to the carboxy functionality of the amino acid provides the site of reactivity. These resins are largely PEG based, and the bulk of the bead mass is found in the length of the PEG chains.¹⁸ Therefore the number of amine functionalized groups is limited. The number of sites available for reactivity, or loading, generally ranges between 0.20 - 0.40 mmol/g.²⁴ Cleavage of the resulting peptide is affected with 95% trifluoroacetic acid resulting in an amidated C-terminus.²⁵ This resin-bead will serve as the basis of the studies herein.

Applications of Immobilization

The properties imparted by solid-phase peptide synthesis have inspired researchers to investigate a range of organic-transformation reactions using polymer supported substrates, reagents or catalysts. The field of heterogeneous catalysis embraces the same basic principles as solid phase peptide synthesis; it has also contributed to understanding the resin-environment of immobilized species. A number of excellent reviews have detailed the use of polymer supports for catalysis.^{6,10,26,27} One of the earliest contributions in this field utilized Wilkinson's catalyst anchored via a phosphine linkage to Merrifield resins (polystyrene crosslinked with chloromethylated divinylbenzene) for the hydrogenation of alkenes.⁵ By relating the size of the olefin to the rate of hydrogenation, Grubbs and co-workers concluded that the majority of the catalytic activity occurred on the *inside* of the polymer bead.⁵ This type of bead has since been used to produce

supported catalysts for olefin metathesis and asymmetric catalysis.^{28, 27,28,29} Other types of insoluble polymer supports have been used to immobilize catalysts as well. Examples of these supports include, but are not limited to: polyvinylpyridine³⁰, PEGA-NH₂³¹, butyldiethylsilyl polystyrene (PS-DES)³², and more recently, PEG based polymers.³³

The above studies have all shown that when designing a supported catalytic system the choice of resin is a paramount factor to consider as different resins result in significantly different catalytic performances. The selection of a resin to support a catalyst is guided by many factors which include whether interaction of catalyst sites with one another is needed, as in salen type complexes used for asymmetric catalysis.²⁸ A resin-bead with high loading and poor swelling is used when catalyst-catalyst interaction is desired; the polystyrene beads utilized by Jacobsen for the enantioselective addition of phenols to terminal epoxides are an example.³⁴ On the other hand, catalyst isolation has been enhanced through the use of long, flexible spacers, such as PEG, which produce a highly swellable polymer support providing separation and more degrees of freedom. The latter property allows these catalysts to perform more like a homogeneous catalyst while retaining the advantages incurred by the solid support.^{27,28}

Despite numerous scientific advances in this field, the number of heterogeneous catalysts used in industry is actually quite small as they are plagued by catalyst leaching.³⁵ Thus the need for a robust linkage between the catalytic complex and the solid support is critical to the development of such a system.²⁷ As such, advances in developing what Gladysz terms “an ideal catalyst” has been the focus of many reports which have culminated in a number of reviews.³⁶

Nature is the ultimate designer of catalysts, metalloenzymes in particular, and in the process use proteins or amino acid polymers to provide stable supports for catalytic activity which originate in the active site. As evolution-optimized natural catalysts, metalloenzymes utilize peptides as ligands to the catalytic metal and as superstructures housing the catalytic site creating a system superior to any man-made analogues. It is not surprising, therefore, that approaches to catalyst design have drawn inspiration from nature. For example, recent work by Ward and coworkers has shown that a rhodium-diphosphine complex inserted directly into the enzymatic cavity of (strept)avidin will support enantioselective hydrogenation chemistry.³⁷ Ward's research takes advantage of weak contacts between the catalytic metal site and the protein environment, termed the secondary coordination sphere, to optimize the enantioselectivity of the reaction, Figure I-5. Similarly, Lu and co-workers have covalently linked a manganese salen (salen = salicylaldehyde ethylene diamine) complex to apo sperm whale myoglobin resulting in a synthetic enzyme active site mimic capable of sulfoxidation activity.³⁸

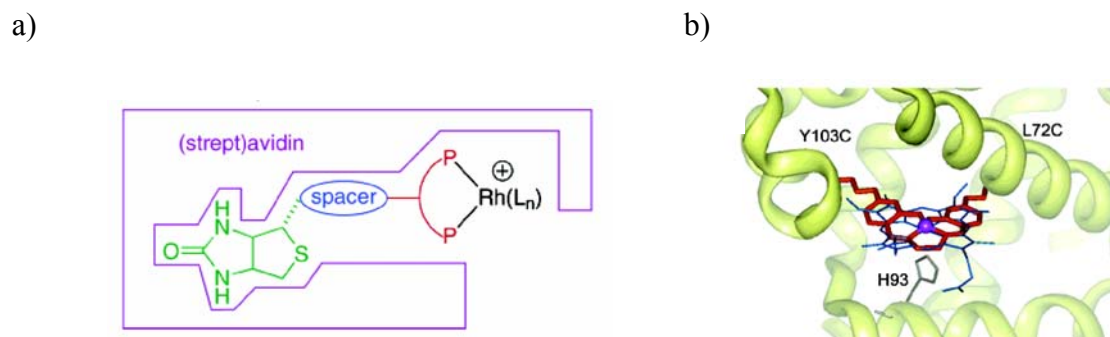


Figure I-5. (a) A Rh-diphosphine-cyclooctadiene complex is anchored via biotin (green) to (strept)avidin³⁷ (b) Manganese salen complex attached to apo sperm whale myoglobin to form a synthetic enzyme active site mimic.³⁸

Monitoring the ability of enzymes to enter into swollen resin-beads with immobilized substrates, cleave the substrate, and exit has recently garnered interest from those studying bio-catalyzed transformations.³⁹ Lebl *et al.* and Bradley *et al.* have shown that enzymes (M.W. = 22-90 KDa) can access and react with substrates (organic or peptide) bound to simple polystyrene based resin-beads through solvent channels provided by swelling in an aqueous medium.⁴⁰ The fruit of these labors has revealed that each resin-support is unique in its ability to allow access to sites embedded within and for biocatalysis to occur inside .

Metalloenzymes as Inspiration for Immobilized Ligands

Nature has utilized peptide polymers to provide an environment that is substrate selective through solvent channels and to stabilize metallopeptide catalytic intermediates. Nature's constructs also permit separation of the resulting product from the peptide attached catalyst. Although these enzymes are clearly not insoluble polymers, the properties imparted by the enzyme superstructure are nevertheless similar to properties of resin-beads used for solid-phase peptide synthesis. Inspired by such properties, the attachment of biologically relevant molecules derived from thiolate rich metalloenzymes through strong covalent linkages has been explored.

Metalloenzymes utilize N, S, and O donors from amino acids to strongly chelate metal ions, forming stable coordination sites. The side chains of the amino acid residues may be solely responsible for holding a metal center, as exemplified in most metalloproteins, or in a growing number of examples the metal may be bound by the

deprotonated carboxyamido nitrogens of the peptide bonds, between residues. A combination of these would surround the metal by the carboxyamido nitrogens as well as residue side chains. A prime example of this hybrid motif is found in the A-cluster active site of acetyl coA synthase/carbon monoxide dehydrogenase.¹ The A-Cluster utilizes a Cys-Gly-Cys (CGC) motif to enforce a square planar geometry on the Ni^{II} center furthest from the 4Fe4S cluster, Ni_d, through the backbone amido nitrogens of one cysteine and the glycine. The side chains of the two cysteine sulfurs complete the 4-donor set arrangement. Interestingly, this biological NiN₂S₂ complex serves as a dithiolate-metalloligand to a second Ni, Ni_p, which is responsible for the C-C coupling reaction necessary for the production of acetyl coA, Figure I-1.^{1,2}

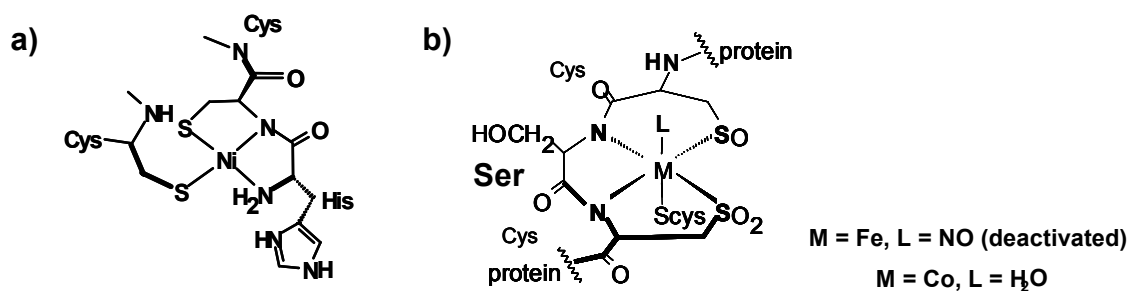


Figure I-6. Representation of the active sites from (a) nitrile hydratase⁴¹ and (b) Ni(SOD).^{42, 43}

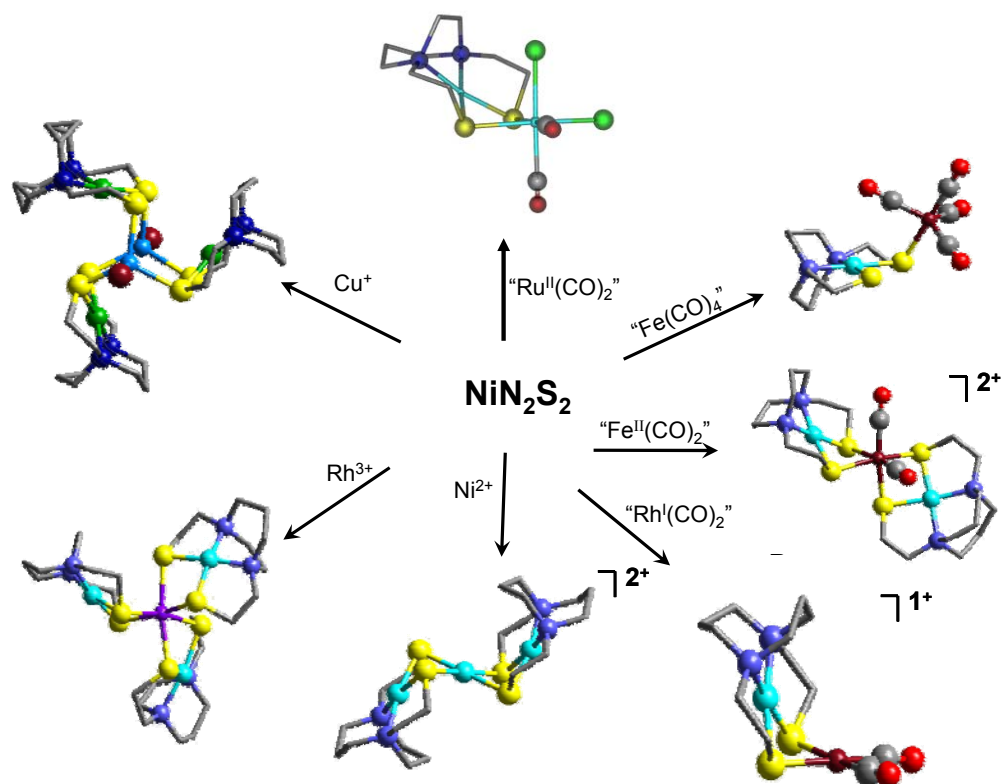


Figure I-7. Examples for thiolate reactivity of NiN_2S_2 complexes.⁴⁴

The N_2S_2 binding motif is not unique to acetyl coA synthase. Other enzymes such as nitrile hydratase and Ni superoxide dismutase (NiSOD), Figure I-6, construct an N_2S_2 donor set using cysteine thiolates and backbone or terminal amines.^{41,42,43} As such, a collection of MN_2S_2 complexes have been constructed as small molecule models to study the reactivity of these N_2S_2 complexes, with reactivity of added exogenous metals an obvious target for NiN_2S_2 models of the Ni_d site in ACS. Shown in Figure I-7, clusters and aggregates dominate the products of metal reactivity with the NiN_2S_2 thiolates.⁴⁴ Such aggregation has proven difficult to prevent in the designed synthesis of “simple”

bimetallic complexes, such as that observed in acetyl coA synthase. This will be discussed further in Chapter III. Therefore, an approach similar to that of the enzyme appears to be needed for selective assembly of analogues of the biological active site.

As Nature utilizes peptide chains to isolate and stabilize active sites, we have set out to use polyethylene glycol rich resin-beads as mimics of the enzyme superstructure. via covalent amide bonds which serve as the anchor for the resin-bound, immobilized biomimetic complexes. Thus far, examples of resin-bound catalytic sites has included (1) organometallic catalysts anchored to solid-supports (2) organometallic catalysts housed in holo-enzymes and (3) biotransformations of immobilized substrates by enzymes entering into resins-beads. The advantages to separation of reagents and purification of products by anchoring one or the other to a solid phase have resulted in a merging of classic heterogeneous organometallic complexes and biological chemistry. Nature's ability to assemble stable metalloptides embedded within the protein superstructure provides inspiration for utilizing these peptide linkages to affix ligands within resin-beads.

This dissertation will focus on the work inspired by the enzymatic NiN_2S_2 complex, $\text{Ni}(\text{CGC})^{2-}$, and the recent advances in immobilization of organometallic catalysts and metalloptide synthesis. The immobilized metalloptide, $\text{O-Ni}(\text{CGC})^{2-}$, obtained by the metallation of the CGC tripeptide immobilized on TentaGel S-RAM[®] beads provides the foundation for this work. Qualitative and quantitative studies were used to identify this bio-inspired resin-bound complex. These studies spurred on the synthesis of resin-bound CuN_2S_2 systems and [FeFe]-Hydrogenase model complexes in order to discover properties that the TentaGel S-RAM[®] polymer support imparts to resin-

bound complexes and to expand the characterization techniques used to identify resin-bound species.

CHAPTER II

EXPERIMENTAL SECTION FOR CHAPTERS III-VII

Abbreviations

DIC = 1,3-diisopropylcarbodiimide

DIPEA = N,N-diisopropylethylamine

Fmoc = 9-fluorenylmethoxycarbonyl

HOBt = 1-hydroxy-7-azabenzotriazole

IMes = 1,3-bis(2,4,6-trimethylphenyl)imidazol-2-ylidene

Mmt = 4-methoxytrityl

Ni(bmedaco) = Ni-1 = (N-N'-bis-2-mercaptoethyl-N-N'-diazocyclooctane) nickel(II)

Ni(bme*daco) = bis-(N, N'-2-mercapto-2-methylpropyl)-1,5-diazocyclooctane

Ni(ema)•(CH₂)₃ = Ni(II) N,N'-ethylenebis(2-propylmercapto-acetamide)

Rink linker = Trialkoxybenzhydrylamine

[Et₄N]₂[Ni(ema)] = (Tetraethylammonium)(N,N'-ethylenebis-2-mercaptoacetamide)
nickel(II)

[Et₄N]₂[Ni(ema)•O₂] = [Tetraethylammonium][Ni(II) N,N'-ethylene(N-
mercaptoacetamide)(N'-sulfinatoacetamide)]

General Procedures and Physical Methods

Air sensitive reagents and complexes were handled under an inert atmosphere using standard Schlenk techniques or a glove box containing an Argon atmosphere. Solvents were purified according to standard procedures and were freshly distilled under N₂ prior to use or purified and degassed via a Bruker solvent system.⁴⁵ Reagents were purchased from commercial sources and used as received unless noted.

Solution infrared spectra were recorded on a Bruker Tensor 27 FTIR spectrometer using 0.1 mm NaCl sealed cells. The Pike MIRacle™ attachment from Pike Technologies was used for Attenuated Total Reflectance Infrared Spectra for solid state samples. UV-Vis spectra were recorded on a Hewlett Packard HP8452A diode array spectrometer using quartz cells (1.00 cm path length). Mass spectrometry experiments (ESI-MS) were performed by the Laboratory for Biological Mass Spectrometry at Texas A&M University. Elemental analyses were performed by the Canadian Microanalytical Services, Ltd., Delta, British Columbia, Canada.

Cyclic Voltammograms were obtained under an Ar atmosphere at 22°C using a BAS100W potentiostat equipped with a 3.0 mm glassy carbon working electrode, a platinum wire auxiliary electrode, and Ag/AgNO₃ reference electrode. Measurements were performed in a DMF solution with 0.1 M [Bu₄N][BF₄] as supporting electrolyte. Ferrocene was used as an internal standard and values reported are relative to NHE (Fc/Fc⁺ = +692 mV in DMF vs. NHE).⁴⁶

EPR spectra were obtained with a Bruker ESP 300 spectrometer equipped with an Oxford ER910 cryostat operating at 10 K. Samples were 1-2 mM in analyte in DMF

solution and were frozen in liquid N₂ prior to recording the EPR spectra at low temperature (9-12 K). The g values reported were simulated using the WinEPR Simfonia program.⁴⁷

Experimental Details for Chapter III

Materials. The Fmoc protected peptides and TentaGel S-RAM[®] beads were obtained from Advanced Chem Tech. The preparation of O-CGC and CGC is shown in Figure II-I and followed standard solid-phase peptide techniques. The *cis*-(pip)₂W(CO)₄ (pip = piperidine), was prepared as described by Darensbourg et al.⁴⁸ The synthesis of K₂[Ni(CGC)] and [Et₄N]₂[Ni(ema)] largely followed literature procedures with small deviations and is described in detail below.^{49,50} The preparation of K₂[Ni(CGC)W(CO)₄] and K₂[Ni(CGC)W(CO)₅] followed literature procedures.^{4,51}

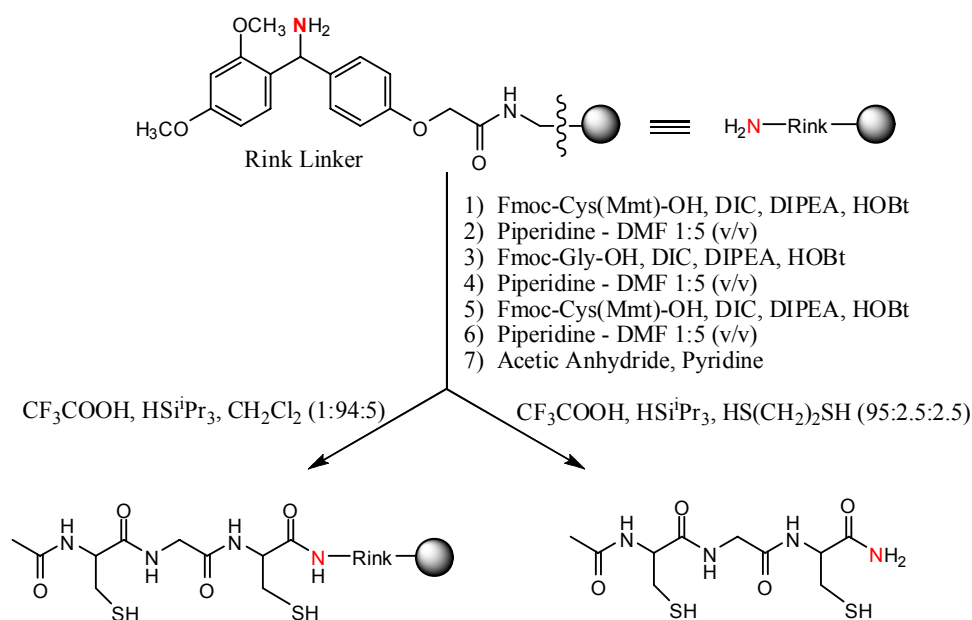


Figure II-I. Synthesis of O-CGC and CGC using solid-phase peptide synthesis.

Synthesis of $K_2[Ni(CGC)]$. The Ac-CGC-CONH₂ tripeptide (H₄CGC) (120 mg, 0.38 mmol) and 80 mg (1.44 mmol) of KOH were dissolved in DMF (~20 mL) under an argon blanket and allowed to stir for 30 min. A degassed DMF solution of Ni(acac)₂ (94 mg, 0.36 mmol) was added drop wise to the solution of the tripeptide. The solution developed into a red color over the course of 1 h and was allowed to stir overnight. The red solution was then filtered through a pad of Celite and Et₂O was added to precipitate a light pink solid. The residual DMF was removed via canula. The product was washed copiously with Et₂O and CH₃CN and then dried under vacuum. The pink solid is soluble solely in DMF. Yield, 152 mg (89.6%). ¹H NMR (d₆-dmsO): δ 7.44 (d, NH, 1H), 7.36 (br, NH₂, 1H), 6.75 (br, NH₂, 1H), 3.57 (br, CH(NHCOCH₃), 1H), 3.53 (m, CH(CONH₂), 1H), 3.45-3.18 (m, NCOCH₂N, 2H), 2.28 (dd, CH₂CH(CONH₂), 1H), 1.81 (m, SCH₂CH(NHCOCH₃), 1H), 1.77 (s, CH₃, 3H), 1.66 (m, SCH₂CH(CONH₂), 1H), 1.51 (m, SCH₂CH(NHCOCH₃), 1H). UV-Vis [EtOH, λ_{max} (ε, L/mol⁻¹cm⁻¹): 550 (62), 445 (127), 275 (12,600)]. ESI-MS, m/z: 415.1 {K[Ni(CGC)]}⁻ and 377.1 {H[Ni(CGC)]}⁻. *The Et₄N⁺ salt was also prepared using two equivalents of Et₄NCl and was found to be soluble in DMF and CH₃CN.

Synthesis of Resin-Bound [Ni(CGC)]²⁻. The N-acylated CysGlyCys peptide was constructed on the TentaGel resin-beads using standard Fmoc techniques as shown in Figure II-I. Deprotection of the Mmt protected cysteine with minimal cleavage of the tripeptide from the resin was accomplished via a 1:94:5 mixture of trifluoroacetic acid:dichloromethane:triisopropylsilane. The solution was deployed in 5 mL aliquots at 5 min intervals until the deprotection mixture removed from the peptide-bound resins was

no longer yellow, indicating removal of the cysteinyl Mmt thiol-protecting group. Following washes (3 x 5 mL each) with pure CH₂Cl₂ and MeOH solvents, a basic solution of green nickel acetylacetonate (25 mg, 0.1 mmol + 22 mg, 0.4 mmol KOH) in 5 mL of dichloromethane was introduced to the resin bed. The light-yellow color of the beads changed to a bright orange within 30 seconds. After 10 minutes, the solution containing the nickel source was removed and the beads were again washed with CH₂Cl₂ solvent until the residual washes were completely colorless. The beads were dried *in vacuo* and stored in a vacuum desiccator. They were frequently handled in air with no apparent deleterious effects.

Synthesis of Resin-Bound Ni(CGC)M(CO)_xⁿ⁻, O-Ni(CGC)W(CO)₅²⁻ and O-Ni(CGC)Rh(CO)₂¹⁻. A portion of O-Ni(CGC)²⁻ (~20 mg) was placed in a syringe and CH₂Cl₂ was used to swell the resin beads. A yellow solution of (pip)₂W(CO)₄ (added in excess, ca. 2 mg) in CH₂Cl₂ was drawn up into the syringe and the mixture was agitated for 10 minutes on an automated shaker. The color of the beads slowly changed from bright orange to burnt yellow. The beads were washed (6 x 10 mL CH₂Cl₂) and dried under vacuum. ATR-FTIR on dried beads: $\nu(\text{CO})$: 1967w, 1917s, 1850w cm⁻¹. An alternative route a product with identical $\nu(\text{CO})$ IR spectrum utilized (THF)W(CO)₅.

In the same way a red solution of (Rh(CO)₂Cl)₂ in MeOH/CH₂Cl₂ was exposed to the resin-bound nickel tripeptide. The resulting dark red beads after washing and drying had $\nu(\text{CO})$ at 2067s and 1990s cm⁻¹.

Synthesis of [Et₄N]₂[Ni(ema)]. **(1) Preparation of N,N'-ethylenebis(2-(acetylthio)acetamide).** (Part a) Chloroacetylchloride (24.0 mL, 301 mmol) was added to a 500 mL three-neck round bottom flask containing 300 mL chloroform and a large stir bar. A large addition funnel was fitted on top of the three neck flask and filled with 10 mL of ethylenediamine (150 mmol) and 40 mL chloroform. The system was then degassed with nitrogen and cooled using an ice bath. The ethylenediamine solution was added drop wise over the course of 2-3 h and allowed to stir an addition 30 min. Then the addition funnel was filled with pyridine (24.0 mL, 297 mmol) which was added drop wise. The reaction mixture was then allowed to warm to room temperature and stirred for 12-14 h. Solvent was removed *in vacuo* to yield a white solid which was treated with water and filtered. The resulting yellow/white solid was with copious amounts of water and a small amount of ether. (Yield: ~13 g, 40%) ¹H NMR (DMSO-d₆): δ 3.16 (dd, 4), 4.03 (s, 4), 8.26 (br, 2). (Part b) A slurry of 13.6 g (64 mmol) of the above ligand in 200 mL EtOH was combined with a solution composed of 8.60 g (153 mmol) of KOH and 12.0 mL (168 mmol) of thiolacetic acid in 100 mL of methanol. This solution was refluxed for 3 h and then stirred at room temperature for 12 h. During this time, a white precipitate formed which was collected via filtration and washed with copious amounts of water. Yellow/white crystalline product was obtained by recrystallizing the product from hot EtOH. (Yield: ~16 g, 95%) ¹H NMR (CDCl₃): δ 2.43 (s, 6), 3.37 (dd,4), 3.54 (s, 4), 6.67 (br, 2). **(2) Preparation of the Ni complex.** In a large Schlenk flask, 1.61 g (5.51 mmol) of the ligand from Part b above, 1.54 g (27.4 mmol) of KOH and 1.65 g (10.0 mmol) of Et₄NCl were combined and degassed. They were then dissolved in 75 mL of

MeOH and allowed to stir for 30 min. A methanol (~50 mL) solution of Ni(OAc)₂•4H₂O (1.24 g, 4.98 mmol) was added drop wise. The resulting red solution was dried *in vacuo* and redissolved in a minimal amount of CH₃CN (~50 mL). This solution was filtered through a pad of Celite, reduced to 20 mL and filtered again. This concentrated deep red solution was then canulated into a Schlenk tube and layered with Et₂O, as always under a blanket of argon. Large deep red crystalline blocks were obtained after ~3 days at room temperature. ¹H NMR (CD₃CN): δ 2.65(s, 4), 2.80 (s, 4).

Synthesis of [Et₄N]_x[Ni(ema)Rh(CO)₂]_x (x = 1,2), Complex E. Under an Ar atmosphere, red solids (Rh(CO)₂Cl)₂, ν_{CO} (MeCN) 2097, 2026 cm⁻¹, (30 mg, 0.077 mmol) and (Et₄N)₂Ni(ema) (80 mg, 0.154 mmol) were dissolved in 25 mL of CH₃CN and stirred for 1 h and filtered through a Celite pad. A red/brown solid was obtained after precipitation with ether and removal of supernatant fluid via cannula. The crude product yield was 0.0434 g (51%). Further purification involved redissolving the solid in CH₃OH, precipitation with ether and removal of the supernatant fluid followed by further washing with Et₂O. Due to air sensitivity, CO lability, and solvation proclivity, efforts to obtain analytically pure compound were not entirely successful. Crystals of crystallographic quality were obtained by layering the CH₃CN solution with ether. ESI-MS (MeCN): {[Ni(ema)Rh(CO)₂]}⁻ 420 (100%). ν(CO) (CH₃CN): 2061s, 1996s cm⁻¹. Anal. Calcd (found) for [NEt₄]₂[Ni(ema)₂(Rh(CO)₂)₂]•CH₃OH or C₃₃H₆₀N₆Ni₂O₉Rh₂S₄: C, 34.88 (35.85); H, 5.32 (6.91); N, 7.40 (6.98).

Preparation of [(Ni-1)Rh(CO)₂][PF₆], Complex D. Under Ar a sample of [Rh(CO)₂Cl]₂ (0.0281 g, 0.072 mmol) was dissolved in 5 mL CH₃CN resulting in a pale

yellow solution. In a separate flask, **Ni-1** (0.042 g, 0.144 mmol) and TlPF₆ (0.0503 g, 0.144 mmol) solids were mixed and dissolved in 10 mL CH₃CN. Cannula transfer of the purple **Ni-1** solution to the Rh source resulted in immediate formation of an orange solution with a yellow precipitate of TlCl. Following 2 h of stirring the solution was filtered through Celite, $\nu(\text{CO}) (\text{CH}_3\text{CN}): 2077\text{s}, 2017\text{s cm}^{-1}$. The solvent was removed *in vacuo* leaving behind a red brown solid, crude yield of 0.013 g, 15.1 % yield. ESI-MS (CH₃CN): $\{[(\text{Ni-1})\text{Rh}(\text{CO})_2]\}^+$ 420 (100%). Diffraction quality red needles were obtained by layering a concentrated CH₃CN solution with Et₂O. Anal. Calcd (found): C, 24.2 (24.5); H, 3.39 (3.49); N, 4.71 (4.83).

X-ray Diffraction Analysis: Experimental conditions for data collection and the crystal data for the NiRh bimetallic complexes are shown in Appendix B. Complete reports for structures **D** and **E** are deposited in the Cambridge Database (**D**, **E**: CCDC # 291355, 291353). Low temperature (110K) x-ray diffraction data were collected on a Bruker SMART CCD-based diffractometer (Mo-K α radiation, $\lambda = 0.71073 \text{ \AA}$) and covered a hemisphere of space upon combining three sets of exposures. Structures were solved by direct methods. Programs used for data collection and cell refinement, Bruker XSCANS; data reduction, SHELXTL; absorption correction, SADABS; structure solution, SHELXS-97 (Sheldrick); structure refinement, SHELX-97 (Sheldrick), and molecular graphics and preparation of material for publication, SHELXTL-Plus, version 5.1 or later (Bruker).

Experimental Details for Chapter IV

Preparation of Samples for Neutron Activation Analysis. In a typical experiment a large batch of $\text{O-Ni(CGC)Rh(CO)}_2^{-1}$ was synthesized using standard procedures described previously and identified via its signature $\nu(\text{CO})$ bands. The batch was divided into four separate samples for the analysis as shown in the Table on page 97. Sample 1 was stored in a vacuum dessicator and not exposed to any further physical stress. Sample 2 was suspended in benzene and shaken vigorously using a lab-shaker for two days before being washed with ether and dried *in vacuo*. As the $\text{O-Ni(CGC)Rh(CO)}_2^{-1}$ shows a marked air stability not observed for its solution analogue, $\text{Ni(ema)Rh(CO)}_2^{-1}$, the air stability of the resin-bound material was further explored. Thus, Sample 3 was loaded into a round bottom flask, filled with benzene, and bubbled with atmospheric air continuously for 2 days. Finally, the beads were tested for their ability to retain the $\text{Ni(CGC)Rh(CO)}_2^{-1}$ moiety through the physical stress of repeated swelling (in CH_2Cl_2). In this experiment, the beads were placed in a fritted syringe with benzene, shaken for 2 hrs, washed with Et_2O and dried repeatedly for 2 days.

Neutron Activation Analysis Method for the Determination of Rh and Ni in Organics. The neutron activation analysis was performed by Dr. Dennis James and staff at the Center for Chemical Characterization at Texas A&M University. Rhodium was determined by irradiation of samples and standards for 15 seconds, followed by a 10 minute delay and 300 second count. The reaction used was $^{103}\text{Rh} (n,(\gamma) ^{104}\text{Rh})$ which produces a metastable state with half life of 4.4 seconds and a ground state with half life of 42 seconds. The metastable state decays by isomeric transition to the ground state.

The cross sections are 11 and 135 barns, respectively. ^{104}Rh decays by beta emission associated with the characteristic gamma line at 555 keV, which was used for quantification in this work. Standards were typically small portions of high purity metal weighing 2 to 4 mg. Peak areas for the 555 peak for standard irradiations typically exceeded 100,000 counts. Typically, three standards were processed during each day's experiment, with standard constants being computed and averaged for comparison to unknown samples for elemental determinations. Relative standard deviations for the distribution of standard results were typically less than 1%. Portions of the sample matrices weighing 9 to 13 mg were processed in a similar fashion. Peak areas for unknown samples were from a few thousand to several tens of thousand counts. Computed detection limits for rhodium using this procedure were about 500 ppm by weight.

Nickel was measured following a 4 minute irradiation and 500 second count. Delay times, up to 3 hours, varied, depending on the concentration levels encountered, to maintain an acceptable input count rate and detector dead time. The $^{64}\text{Ni}(n,\gamma)^{65}\text{Ni}$ reaction and the characteristic reaction product gamma line at 1482 keV were used. The reaction cross section was 1.49 barns. The half-life of ^{65}Ni is 2.52 hours. Standards consisted of a 1% solution of Ni prepared commercially by dissolution of metal salts in dilute nitric acid. The solution was deposited gravimetrically into the irradiation vial and dried prior to analysis. Again, typical standard peak areas were on the order of 100,000 counts. Unknown samples of mass about 10 mg resulted in peak areas of a few thousand to a few tens of thousands of counts and a detection limit of about 700 ppm. A prepared

secondary standard, Ni(bmedach), was analyzed as a quality control material. QC results were always acceptable, within a few percent (relative) of the expected results.

Experimental Details for Chapter V

Materials. Cerium ammonium nitrate (CAN) was used as obtained from Strem Chemicals. The $[\text{Et}_4\text{N}^+]_2[\text{Ni}(\text{ema})^{2-}]$ and $\text{Ni}(\text{ema})\cdot(\text{Me})_2$ complexes were prepared following published procedures and used in CV analysis to be consistent with conditions used for the new complexes reported herein.^{50, 52}

Synthesis of $\text{Ni}(\text{ema})\cdot(\text{CH}_2)_3$. To a dark red solution of $[\text{Et}_4\text{N}]_2[\text{Ni}(\text{ema})]$ (120 mg, 0.230 mmol in 30 mL CH_3CN), dibromopropane (23 μL , 0.230 mmol) was added via micro syringe. The solution developed a bright red hue within 30 sec. The solution was stirred for an additional 20 min and stored at -20°C for 3 days. Red, X-ray quality blocks, stable to air, slowly grew during this time and were collected by filtration and washed with ether and *small* amounts of CH_3CN , 41.6 mg (59% yield). Anal. Calcd (found) for $\text{C}_9\text{H}_{14}\text{N}_2\text{NiO}_2\text{S}_2$: C 35.44(34.83), N 4.63(4.68), H 9.02(9.18). Absorption spectrum (MeOH): λ_{max} (ϵ , $\text{M}^{-1} \text{cm}^{-1}$) 204(20,200), 242(1,547), 396(79), 476(29) nm. ⁺ESI-MS: m/z 326.98 $[\text{M}+\text{Na}]^+$, 304.5 $[\text{M}+\text{H}]^+$. Decomposition Point: 233°C .

Synthesis of $[\text{Et}_4\text{N}]_2[\text{Ni}(\text{ema})\cdot\text{O}_2]$. (Route A) A 100 mL Schlenk flask containing a dark red solution of $[\text{Et}_4\text{N}]_2[\text{Ni}(\text{ema})]$ (50 mg, 0.96 mmol in 20 mL CH_3CN) was backfilled with $\text{O}_2(\text{g})$ and stirred for 30 min. The solution was filtered through Celite and layered with ether to yield bright red X-ray quality block crystals after 2 weeks. Yield: 16 mg (29%). (Route B) A CH_3CN solution of $[\text{Et}_4\text{N}]_2[\text{Ni}(\text{ema})]$ (100 mg, 0.19 mmol in

20 mL CH₃CN) was layered with ether to obtain dark red crystals of [Et₄N]₂[Ni(ema)] after 1 week.⁸ The supernatant was removed and replaced with ether, covering all crystalline material. The flask was then exposed to small quantities of air and the resulting bright red X-ray quality crystals of [Et₄N]₂[Ni(ema)·O₂] were collected after one day. Yield: 83 mg (78%). Anal. Calcd (found) for C₂₂H₄₈N₄NiO₄S₂: C 47.57 (47.64), N 10.09 (10.66), H 8.71 (9.43). Absorption spectrum (MeOH): λ_{max} (ε, M⁻¹ cm⁻¹) 250(13,841), 297(469), 413(35) nm. ESI-MS: (m/z) 293.9 [M]⁻, 261.93 [M -O₂]⁻, 229.97 [M -SO₂]⁻. Melting Point: 157.5-159°C. IR (CH₃CN) ν(S=O) 1151, 1030 cm⁻¹.

Oxidation of Ni(ema)•(CH₂)₃. To a 1 mg (4x10⁻⁶ mol) sample of Ni(ema)•(CH₂)₃ dissolved in 4 mL of DMF was added 2 mg (1 equiv) of solid CAN at 22°C. The red solution turned to a clear brown color within 10 seconds; over the course of minutes the solution turned yellow with subsequent complete bleaching. An EPR sample of the brown product was obtained by placing 200 μL of the reaction mixture into a 5-mm tube and immediately freezing in liquid N₂. With NOBF₄ as oxidant, no reaction was observed.

Structure Solution and Refinement. A BRUKER SMART 1000 X-ray three-circle diffractometer was employed for crystal screening, unit cell determination and data collection. The goniometer was controlled using the SMART software suite, version 5.625. The X-ray radiation employed was generated from a Mo sealed X-ray tube (K_α = 0.70173 Å with a potential of 50 kV and a current of 40 mA) and filtered with a graphite monochromator in the parallel mode (175mmcollimator with 0.5 mm pinholes). Integrated intensity information for each reflection was obtained by reduction of the data

frames with the program SAINT V6.63.⁵³ The integration method employed a three-dimensional profiling algorithm and all data were corrected for Lorentz and polarization factors, as well as for crystal decay effects. Finally the data was merged and scaled to produce a suitable data set. The absorption correction program SADABS was employed to correct the data for absorption effects.⁵⁴ X-Seed was employed for the final data presentation and structure plots.⁵⁵ The tetraethyl ammonium cation of $[\text{Et}_4\text{N}]_2[\text{Ni}(\text{ema})\cdot\text{O}_2]$ in MeCN was found to be disordered between two positions. The anions were modeled by employing local bond distance restraints and included in the final refinement. CCDC reference numbers: 637429 and 637428.

Computations. All computations were set-up and analyzed by group member Scott Brothers. Density functional theory (DFT) calculations, including geometry optimization and natural bond orbital (NBO) analysis, were performed using a hybrid functional (the three-parameter exchange functional of Becke (B3)⁵⁶ and the correlation functional of Lee, Yang, and Parr (LYP)⁵⁷) (B3LYP) as implemented in GAUSSIAN 03.⁵⁸ For each calculation, all atoms were optimized via use of the 6-311g(d,p) basis set. Additional NBO calculations were performed with a mixed basis set using Dunning's correlated consistent polarized valence double- ζ (cc-pVDZ) for nitrogen and sulfur atoms,⁵⁹ D95 for hydrogen atoms,⁶⁰ and double- ζ + polarization (DZP) for carbon and oxygen atoms.⁶¹ The nickel center was calculated using a contracted cc-pVTZ basis set, whereby the last shell of each type of function was removed to form a cc-pVDZ for Ni. Cartesian coordinates for the starting input geometries were extracted from the crystallographic structures. A frequency calculation was performed alongside each

geometry optimization to ensure the stability of the ground state as ascertained by the absence of imaginary frequencies. Graphical visualizations of the electron density of the individual molecular orbitals and the electrostatic potentials were first generated as cube files from GAUSSIAN, and these images were implemented into and viewed by the Cerius² software package.⁶² Optimized geometries of each of the complexes were imported into and visualized with JIMP2.⁶³ Geometric parameters were extracted from the optimized structures by use of the GaussView program.⁶⁴ For each complex in this text, the energies have been converted from values in Hartrees to eV.

Experimental Details for Chapter VI

Synthesis of [Et₄N]₂[Cu(ema)]. In a degassed Schlenk flask N, N'-ethylenebis(2-mercaptoacetamide) (2.09 g, 4.61 mmol), KOH (1.5 g, 27.8 mmol) and tetraethyl ammonium chloride (1.65 g, 10.0 mmol) were combined with 100 mL of MeOH and magnetically stirred for 30 min. The solution was cooled to -78°C and a bright blue methanol (100 mL) solution of Cu(OAc)₂•4H₂O (0.8 g, 4.3 mmol) was added drop wise over the course of 5 minutes. The reaction was stirred for 15 min during which time the light yellow solution changed to maroon and then purple. The solution was *quickly* filtered through Celite and a purple solid (1.74 g, 83% yield) was obtained from the filtrate by addition of 250 mL of Et₂O. Absorption spectrum (CH₃CN): λ_{max} (ϵ , M⁻¹ cm⁻¹) 233(24,880), 293 (28,700), 320sh (22,100), 407 (1740) nm. ⁻ ESI-MS: m/z 266.9275 [M]⁻.

Synthesis of $[\text{Et}_4\text{N}]_2[\text{Cu}(\text{emi})]$. The solids N,N'-ethylenebis(2-benzylthio)isobutyramide) (1.61 g, 4.62 mmol), KOH (1.5 g, 27.8 mmol) and tetraethyl ammonium chloride (1.65 g, 10.0 mmol) were dissolved in 200 mL methanol and stirred for 30 min under a blanket of argon. The slow addition of $\text{Cu}(\text{OAc})_2 \cdot 4\text{H}_2\text{O}$ (0.8 g, 4.3 mmol) to this solution followed by stirring at room temperature for 30 min produced a red solution. The solution was allowed to stir for an additional 30 min and filtered through a Celite pad; addition of Et_2O resulted in a microcrystalline mauve solid (1.36 g, 74% yield). Crystals suitable for x-ray diffraction were obtained at -10° by layering a concentrated CH_3CN solution with hexane and then ether. Absorption spectrum (CH_3CN): λ_{max} (ϵ , $\text{M}^{-1} \text{cm}^{-1}$) 231 (23,799), 294 (25,250), 319sh (21,300), and 413 (2120) nm. $^1\text{ESI-MS}$: m/z 323.0042 $[\text{M}]^+$.

Synthesis of $[\text{Et}_4\text{N}][\text{Cu}(\text{ema})\text{Rh}(\text{CO})_2]$. Under an argon blanket, the purple solid, $[\text{Et}_4\text{N}]_2[\text{Cu}(\text{ema})]$ (20 mg, 0.037 mmol), was suspended in 20 mL DMF. After 30 minutes stirring the solid was completely dissolved to give a yellow-red solution. A yellow solution of $[\text{Rh}(\text{CO})_2\text{Cl}]_2$ (7.373 mg, 0.0189 mmol) was then added drop wise. After stirring for 2 h the resulting red-brown solution showed $\nu(\text{CO}) = 2061, 1982 \text{ cm}^{-1}$. A brown solid was obtained following precipitation with Et_2O . Absorption spectrum (DMF): λ_{max} (ϵ , $\text{M}^{-1} \text{cm}^{-1}$) 270(27,610) and 330(18, 610) nm.

Synthesis of $[\text{Et}_4\text{N}][\text{Cu}(\text{emi})\text{Rh}(\text{CO})_2]$. To a red solution of $[\text{Et}_4\text{N}]_2[\text{Cu}(\text{emi})]$ (20 mg, 0.034 mmol) in 20 mL DMF, a yellow solution of $[\text{Rh}(\text{CO})_2\text{Cl}]_2$ (7.373 mg, 0.0189 mmol) was added drop wise. The resulting brown-red solution provided $\nu(\text{CO}) =$

2062, 1984 cm^{-1} . A brown solid was obtained following precipitation with Et_2O . Absorption spectrum (DMF): λ_{max} (ϵ , $\text{M}^{-1} \text{cm}^{-1}$) 289(25,260) and 390(18,540) nm.

Synthesis of $[\text{K}]_2[\text{Cu}(\text{CGC})]$. The H_4CGC (20 mg, 0.062 mmol) ligand and KOH (13.92 mg, 0.0248 mmol) were combined in 20 mL of DMF and allowed to stir for 20 minutes. To this a blue solution of $\text{Cu}(\text{OAc})_2 \cdot 4(\text{H}_2\text{O})$ (15.6 mg, 0.0610 mmol) was added drop wise. The reaction mixture developed into a mauve purple after 15 minutes and was allowed to stir for 1h. A light purple solid was obtained after precipitation with Et_4O . Yield 16.3 mg (70.0% yield). Absorption spectrum (CH_3CN): λ_{max} (ϵ , $\text{M}^{-1} \text{cm}^{-1}$) 232 (26,185), 294 (18,962), 322sh (13,450) and 367(930) nm. ESI-MS: m/z 326.98 $[\text{M}+\text{Na}]^+$, 304.5 $[\text{M}+\text{H}]^+$.

Synthesis of $\text{O-Cu}(\text{CGC})^{2-}$. Synthesis of $\text{O-Cu}(\text{CGC})^{2-}$ in a fritted syringe paralleled the procedure used for $\text{O-Ni}(\text{CGC})^{2-}$ described above for Chapter III. Deprotection of the TentaGel-bound, N-acylated, Mmt Cys-S-protected CysGlyCys tripeptide was accomplished via a 1:94:5 mixture of trifluoroacetic acid:dichloromethane:triisopropyl silane as described for the synthesis of $\text{O-Ni}(\text{CGC})^{2-}$. Following washes (3 x 5 mL each) with pure CH_2Cl_2 and MeOH solvent, a basic solution of $\text{Cu}(\text{OAc})_2 \cdot 4\text{H}_2\text{O}$ in 5 mL of 50:50 methanol: CH_2Cl_2 was introduced to the resin bed. The light-yellow TentaGel beads changed to a deep purple after 2 minutes. After 30 min, the Cu^{II} supernatant solution was expelled and the beads were again washed with MeOH, CH_2Cl_2 , and Et_2O solvent until the residual washes were completely colorless. The beads were dried *in vacuo* and stored in a vacuum desiccator.

Synthesis of O-Cu(CGC)Rh(CO)₂¹⁻. In an analogous manner to the preparation of O-Ni(CGC)Rh(CO)₂¹⁻, a sample of O-Cu(CGC)²⁻ was placed in a fritted syringe and swelled in DMF. A yellow CH₂Cl₂ solution of [Rh(CO)₂Cl]₂ was added resulting in dark red beads after 10 min. The beads were washed thoroughly with CH₂Cl₂, MeOH, and Et₂O (3 x each) and then dried *in vacuo*. ATR-FTIR $\nu(\text{CO}) = 2061, 1983 \text{ cm}^{-1}$.

Experimental Details for Chapter VII

Materials. Complexes [A], (μ -pdt-COOH)(Fe(CO)₃)₂, and [B], (μ -pdt)[Fe(CO)₃][Fe(CO)₂P(C₂H₄COOH)₃], were made according to published procedures by group members Dr. Christine Thomas and Tianbiao Liu.⁶⁵ The IMes carbene was obtained as its chloride salt from Acros Chemicals.

Methods. All substitution reactions of O-am-[A] and O-am-[B] were carried out using 20 mg of [FeFe-COOH]H₂ase model complexes placed in a 10 mL sample vial. The vial was fit with a rubber septa, degassed, covered with foil and then 20 mL of degassed THF was added. The IMes ligand was deprotonated using literature methods but is described in detail below.⁶⁶

Infrared spectra of the [FeFe-COOH]H₂ase model complex loaded beads were obtained using the MIRacle attachment for solid phase samples (ATR-FTIR). The NMR samples were prepared by placing ~30 mg of the [FeFe-COOH]H₂ase model loaded beads into a regular NMR tube and then adding CDCl₃ to obtain a suspension of the beads. To ensure the best homogeneity and signal the height of the beads was compared to the location of the magnetic field for the instrument, as depicted in Figure II-2. All ³¹P NMR

spectra were referenced to phosphoric acid. In a typical experiment, a sample of Ni(dppe)Cl₂ in CDCl₃ was used to obtain a lock signal and to shim. The phosphoric acid reference was then loaded, scanned, and referenced. Then, the Ni(dppe)Cl₂ sample was loaded as a double check. Finally, the resin-bead sample was loaded into the NMR instrument for analysis. An extended number of transients (nt), O-am-[A] = 1500+ and O-am-[B] = 4500, were required to obtain a suitable spectrum for each sample on the 400 MHz NMR.



Figure II-2. A suspension of O-am-[A] in CDCl₃ for NMR spectroscopy. It is aligned with a drawing provided by the TAMU NMR facility showing the location of the magnetic field with respect to the sample.

Synthesis of O-am[A]. In a fritted syringe, a 30 mg portion of TentaGel S-RAM[®] Resin-Beads (Loading = 0.4 mmol/g, 30 mg = 0.0069 mmol of –NH₂ sites) were swollen for about 15 minutes in dry DMF. Concurrently, a solution of 1.5 mg (0.0042 mmol) of (μ-pdt-COOH)(Fe(CO)₃)₂ ($\nu(\text{CO}) = 2077(\text{s}), 2034(\text{s}), 1992(\text{sh}) \text{ cm}^{-1}$ and $\nu(\text{C=O}) = 1730(\text{w}) \text{ cm}^{-1}$) was dissolved in 5 mL of THF. To this red solution was added roughly 2 μL of DIC (0.0129 mmol) and 5 μL of DIPEA (0.029 mmol). Any solid (μ-pdt-COOH)(Fe(CO)₃)₂ remaining quickly dissolved upon addition of the coupling agents indicating complete activation of the carboxylic acid. The activated (μ-pdt-COOH)(Fe(CO)₃)₂ was then combined with the swollen beads by drawing the solution into the syringe with a needle. The syringe was covered with foil to minimize exposure to light and the syringe was shaken via a mechanical shaker for 2 h. The beads were then washed 3 x each successively with DMF, MeOH, THF and finally Et₂O. The resulting ATR-FTIR of the bright-orange beads showed $\nu(\text{CO}) = 2074(\text{s}), 2034(\text{s}),$ and $1993(\text{sh}) \text{ cm}^{-1}$.

Synthesis of O-am[B]. In a fritted syringe, a 30 mg portion of TentaGel S-RAM[®] Resin-Beads (Loading = 0.23 mmol/g, 30 mg = 0.0069 mmol –NH₂ sites) were swollen for about 15 minutes in dry DMF. Concurrently, a solution of 2 mg (0.00329 mmol) of [B] ($\nu(\text{CO}) = 2041(\text{s}), 1981(\text{s}), 1962(\text{sh}), 1920(\text{w}) \text{ cm}^{-1}$, ³¹P: $\delta = 52.89(\text{s}) \text{ ppm}$) was dissolved in 5 mL of THF. To this red solution was added ca. 2 μL of DIC (0.0129 mmol) and 5 μL of DIPEA (0.029 mmol). Any remaining solid quickly dissolved indicating complete activation of the carboxylic acid. The activated [B] was then combined with the swollen beads by drawing the solution into the syringe with a needle.

The syringe was covered with foil to minimize exposure to light and allowed to shake mechanically for 2 h. The beads were then washed 3 x each successively with THF, DMF, MeOH, and finally Et₂O. The resulting ATR-FTIR of the bright-orange beads showed $\nu(\text{CO}) = 2038(\text{s}), 1976(\text{s}), 1950(\text{sh}), 1918(\text{w}) \text{ cm}^{-1}$. ³¹P NMR: $\delta = 52.89(\text{s}) \text{ ppm}$.

Synthesis of Resin-Bound O-[(μ -pdt)(Fe(CO)₃)(Fe(CO)₂PMe₃)]. In a 10 mL sample vial containing O-am-[A], approximately 15 μL of PMe₃ was added via an air-tight micro syringe and allowed to react for 4 h at room temperature. The beads were then washed 3 x each successively with THF, DMF, MeOH, and finally Et₂O. The resulting ATR-FTIR of the red-orange beads showed $\nu(\text{CO}) = 2036(\text{m}), 1981(\text{s}), 1960(\text{sh}), 1923(\text{w}) \text{ cm}^{-1}$. ³¹P NMR: $\delta = 26.1(\text{s}) \text{ ppm}$.

Synthesis of Resin-Bound O-[(μ -pdt)(Fe(CO)₃)(Fe(CO)₂PPh₃)]. In a sample vial with O-am-[A] a THF (~2mL) solution containing 2.5 mg of PPh₃ was added via cannula and allowed to react overnight at 55°C. The beads were then washed 3 x each successively with THF, DMF, MeOH and finally Et₂O. The resulting ATR-FTIR of the red-orange beads showed $\nu(\text{CO}) = 2045(\text{s}), 1985(\text{s}), 1960(\text{sh}), 1941(\text{w}) \text{ cm}^{-1}$.

Synthesis of Resin-Bound O-[(μ -pdt)(Fe(CO)₂PMe₃)₂]. Approximately, 15 μL (0.0146 mmol) of PMe₃ was added to a sample vial with O-am-[A] and allowed to react for 6 h at 50°C, manual shaking of vial every 30 min. The beads were then washed 3 x each successively with THF, DMF, MeOH and then Et₂O. The resulting ATR-FTIR of the red-orange beads showed $\nu(\text{CO}) = 1980(\text{m}), 1943(\text{s}), 1899(\text{s})$ and $1876(\text{w}) \text{ cm}^{-1}$. ³¹P NMR: $\delta = 27.4(\text{s}), 20.2(\text{s}) \text{ ppm}$.

Synthesis of Resin-Bound O-(μ -pdt)[Fe(CO)₂PMe₃][Fe(CO)₂P(C₂H₄COOH)₃].

A methanol solution ONMe₃ (2 mg, 0.026 mmol) was added to O-am-[B] followed by PMe₃ (15 μ L, 0.00146 mmol) and heated at 55°C overnight. The resulting red-orange beads were then washed with THF, DMF, MeOH and Et₂O. $\nu(\text{CO}) = 1981(\text{s}), 1943(\text{s}), 1909(\text{w}), \text{and } 1894(\text{sh}) \text{ cm}^{-1}$.

Synthesis of Resin-Bound O-(μ -pdt)[Fe(CO)₂CN][Fe(CO)₂P(C₂H₄COOH)₃].

A methanol solution of [Et₄N][CN] (3 mg, 0.0192 mmol) was added to O-am-[B]. The orange beads were then washed with THF, DMF, MeOH and Et₂O. The dried beads displayed an ATR-FTIR spectrum with $\nu(\text{CN}) = 2076, 2036 \text{ cm}^{-1}$ and $\nu(\text{CO}) = 1971(\text{m}), 1931(\text{s}), 1895(\text{w}), \text{and } 1880(\text{sh}) \text{ cm}^{-1}$.

Deprotonation of IMes. According to Arduengo and co-workers,⁶⁶ under argon the [IMes][Cl] carbene (6.8 mg, 0.0198 mmol) was loaded into a small round-bottom flask with KO^tBu (2.42 mg, 0.0216 mmol) and suspended in THF (~5 mL) under argon. After stirring for 45 minutes a yellow THF solution was obtained.

Synthesis of Resin-Bound O-(μ -pdt)(Fe(CO)₂IMes)(Fe(CO)₂P(C₂H₄COOH)₃). A methanol solution of ONMe₃ (2 mg, 0.026 mmol) was added to O-am-[B] followed by a THF solution of deprotonated IMes. After reaction for 24h at 50°C the beads were washed 3 x each successively with THF, DMF, MeOH, and then Et₂O. The resulting ATR-FTIR of the dried red-orange beads showed $\nu(\text{CO}) = 1980(\text{m}), 1943(\text{s}), 1911(\text{sh}), 1893(\text{m}) \text{ cm}^{-1}$.

Synthesis of Resin-Bound O-am-(μ -pdt)[Fe(CO)₃][Fe(CO)₂IMes]. The addition of deprotonated IMes solution to bright orange beads of O-am-[(μ -

pdt)(Fe(CO)₃(Fe(CO)₂PMe₃)] and reacting for 24 h at 55° resulted in red-orange beads. The resulting ATR-FTIR spectrum following washes with THF, DMF, MeOH, and Et₂O have $\nu(\text{CO}) = 1982(\text{m}), 1962(\text{s}), 1903(\text{m}), \text{ and } 1982(\text{sh}) \text{ cm}^{-1}$.

CHAPTER III

A NICKEL TRIPEPTIDE AS A METALLODITHIOLATE LIGAND ANCHOR

FOR RESIN-BOUND ORGANOMETALLICS*

The structures of numerous inorganic polymetallic compounds confirm the notion that NiN_2S_2 complexes may be considered as molecular construction units whose S-based aggregation properties can lead to unique, albeit largely unreactive, clusters.⁴⁴ This aggregative tendency can be controlled by use of interacting electrophiles with low affinity for sulfur or by steric blocks. The latter reaches a pinnacle in catalyst site isolation found in proteins, as demonstrated by the A-cluster in the active site of acetyl coA synthase, as described in Chapter I.

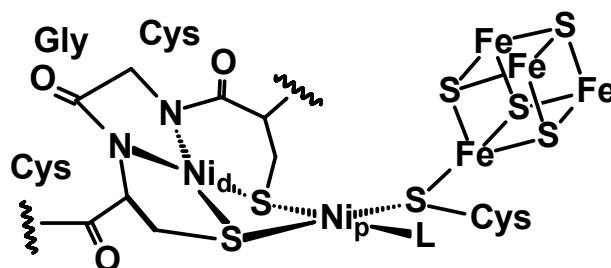


Figure III-1. Representation of the A-cluster active site of acetyl coA synthase.¹

* Reproduced with permission from Green, K. G.; Brothers, Jeffery, S. P.; Reibenspies, J. H.; Darensbourg, M. Y. *J. Am. Chem. Soc.* **2006**, *128*, 6493-6498. Copyright **2006** American Chemical Society.

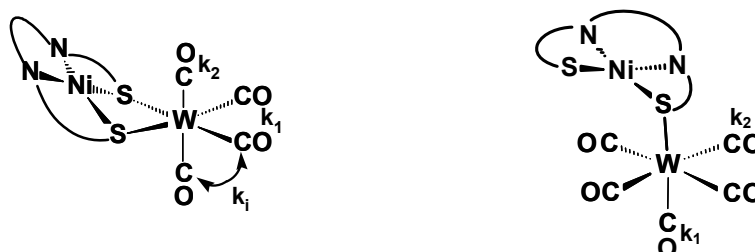
Small molecule models of metalloenzyme active sites are valuable as synthetic analogues of inorganic or organometallic natural products with potential for catalytic activity.⁴⁴ From an array of di- and tetra anionic tetradentate N_2S_2 ligands bound to nickel(II) we have established the following fundamental properties of NiN_2S_2 complexes as metalloligands: 1) They are good electron donors as established by the $\nu(CO)$ spectroscopy of $W(CO)_4$ derivatives⁵¹; 2) NiN_2S_2 complexes can bind as mono- or bidentate ligands, a property fundamental to hemilability^{4,51}; 3) the additional lone pair on each sulfur donor site impose an asymmetric feature to this ligand quite unlike other planar ligands. This steric feature is expressed in terms of a hinge angle defined by the NiN_2S_2 plane with respect to the binding site of the exogenous metal.⁵¹ Most important to our studies is the $\nu(CO)$ spectroscopy of tungsten carbonyl derivatives which can be used to identify NiN_2S_2 ligands. With this database, we can demonstrate that the naturally optimized $Ni(CGC)^{2-}$ ligand of acetyl coA synthase behaves as a typical NiN_2S_2 ligand to $W(CO)_x$ moieties ($x = 4, 5$) and it can also serve as an anchor for organometallics to polystyrene resin beads. Through Attenuated Total Reflectance Fourier Transform Infrared Spectroscopy, ATR-FTIR, the solid-supported $Ni(CGC)^{2-}$ is readily detectable as metal-carbonyl derivatives matching assignments of $\nu(CO)$ vibrational spectra to solution phase analogues. Such an Aufbau of characterization permits extensions to other resin-bound hybrid biological/organometallic moieties with potential as isolated single site catalysts, e.g., $\{Ni(CGC)Rh(CO)_2\}^-$.

Synthesis and Characterization of $[\text{Ni}(\text{CGC})][\text{W}(\text{CO})_4]^{2-}$ and $[\text{Ni}(\text{CGC})][\text{W}(\text{CO})_5]^{2-}$

According to Riordan's report,⁴⁹ we have prepared the CysGlyCys tripeptide derivative of nickel(II) and, through analogous syntheses which produced the series of NiN_2S_2 derivatives of $\text{W}(\text{CO})_4$ and $\text{W}(\text{CO})_5$, the $\text{K}_2[\text{Ni}(\text{CGC})\text{W}(\text{CO})_x]$ ($x = 4, 5$) compounds were prepared and isolated as yellow, air-sensitive non-crystalline solids.^{4,51} The potassium salt of $[\text{Ni}(\text{CGC})\text{W}(\text{CO})_5]^{2-}$ was also synthesized via the addition of a THF solution of $\text{W}(\text{CO})_5(\text{THF})$, prepared by photolysis of $\text{W}(\text{CO})_6$ in THF, to a MeOH solution of $\text{K}_2[\text{Ni}(\text{CGC})]$.⁴⁸ Similarly, the $[\text{Ni}(\text{CGC})\text{W}(\text{CO})_4]^{2-}$ complex anion was prepared in DMF solution by displacement of the labile piperidine ligands in $(\text{pip})_2\text{W}(\text{CO})_4$ by the thiolato donors from $\text{K}_2[\text{Ni}(\text{CGC})]$.

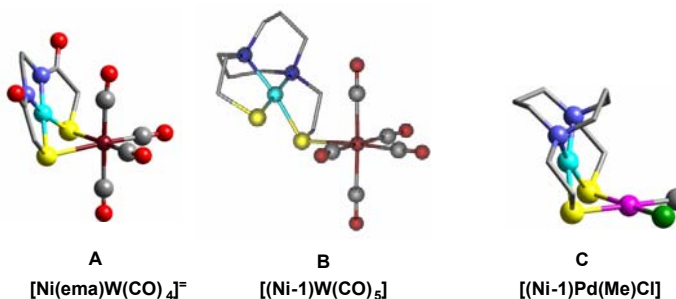
The $\nu(\text{CO})$ IR bands and associated CO force constants given in Table III-1 for $[\text{Ni}(\text{CGC})\text{W}(\text{CO})_4]^{2-}$ and $[\text{Ni}(\text{CGC})\text{W}(\text{CO})_5]^{2-}$ are similar to those reported for the analogous $[\text{Ni}(\text{ema})\text{W}(\text{CO})_{4,5}]^{2-}$ complexes (see Chart III-1 for abbreviations). Shown in Chart III-1 are the molecular structures derived from x-ray diffraction analysis of $[\text{Ni}(\text{ema})\text{W}(\text{CO})_4]^{2-}$ (A), and the $\text{W}(\text{CO})_5$ and $\text{Pd}(\text{Me})\text{Cl}$ derivatives of Ni-1, B and C, respectively.⁵¹ As the $[\text{Ni}(\text{ema})\text{W}(\text{CO})_5]^{2-}$ compound has not been crystallized, structure B serves as its neutral analogue.

Table III-1: CO stretching frequencies ($\text{NiN}_2\text{S}_2\text{W}(\text{CO})_4$ in dimethylformamide, DMF, and $\text{NiN}_2\text{S}_2\text{W}(\text{CO})_5$ in Tetrahydrofuran, THF, solvent) and calculated force constants (FC) for the $\text{W}(\text{CO})_x$ ($x = 4,5$) derivatives of the tripeptide $\text{Ni}(\text{CGC})^{2-}$ and the $\text{Ni}(\text{ema})^{2-}$ complex ions. The vibrational mode assignments and the calculation of force constants are according to ref. 67.



$\text{K}_2[\text{Ni}(\text{CGC})]$	1988w, 1863s, 1845sh, 1793ms cm^{-1}	2061w, 1974sh, 1917s, 1869m cm^{-1}
FC (mdyn/Å)	$k_1 = 13.43, k_2 = 14.92, k_i = 0.45$	$k_1 = 15.55, k_2 = 14.28, k_i = 0.36$
$[\text{NEt}_4]_2[\text{Ni}(\text{ema})]$	1986w, 1867s, 1837sh, 1791m cm^{-1}	2060w, 1967sh, 1918s, 1868m cm^{-1}
FC (mdyn/Å)	$k_1 = 13.41, k_2 = 14.77, k_i = 0.46$	$k_1 = 15.56, k_2 = 14.28, k_i = 0.35$

Chart III-1



Abbreviations: $\text{Ni}(\text{ema})^{2-}$ = (N,N'-ethylenebis-2-mercaptoacetamide) nickel(II); Ni-1 = (N-N'-bis-2-mercaptoethyl-N-N'-diazocyclooctane) nickel(II)

The comparison of the $\nu(\text{CO})$ stretching frequencies and calculation of the Cotton-Kraihanzel force constants ranks the donor ability of the $\text{Ni}(\text{CGC})^{2-}$ ligand with that of the dianionic NiN_2S_2 complex, $\text{Ni}(\text{ema})^{2-}$, and better than the neutral NiN_2S_2 as ligands; the latter are in turn better electron donors towards the $\text{W}(\text{CO})_x$ fragments than are classical diphosphine or diimine ligands, Figure III-2.⁵¹ This ranking has been extended to comparisons of $\nu(\text{CO})$ of *o*-phenanthroline and NiN_2S_2 ligand complexes of Pd^{II} in $[(\text{L}_2)\text{Pd}(\text{CO})(\text{C}=\text{O})\text{CH}_3]^+$.⁵¹ We conclude that $\text{Ni}(\text{ema})^{2-}$, with its carboxyamido nitrogens and its *cis* dithiolate donors which induce a hinge effect at the bridging sulfurs, is a good model for the distal nickel, Ni_d , of the acetyl coA synthase active site, Figure III-1. It is similar in electron donor properties to the nickel-containing CysGlyCys tripeptide motif which supports the organometallic chemistry at the Ni_p .

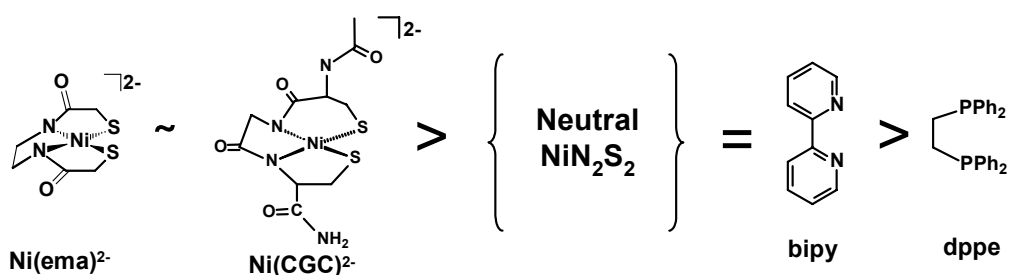


Figure III-2. Rank of electron donor ability as evidenced by $(\text{NiN}_2\text{S}_2)\text{W}(\text{CO})_4$ derivatives and their respective $\nu(\text{CO})$ IR bands and force constants.

Preparation of Resin-Bound O–Ni(CGC)W(CO)₅²⁻.

Synthesis of O–Ni(CGC)²⁻. Following the design of nature in the construction of the ACS active site, we strategized that the resin-bound CysGlyCys tripeptide should capture a nickel ion in N₂S₂ coordination and that this O–Ni(CGC)²⁻ might be detected by derivatization with W(CO)_x (x = 4,5). The TentaGel-S RAM solid support was chosen for this process as such resins are expected to contain microporous domains and they are capable of excellent swelling in a range of solvents. The latter feature is crucial to the synthesis of peptides as well as derivatives of resin-bound peptides. The Rink linker, which produces an amidated carboxy terminus up addition of a concentrated solution of trifluoroacetic acid, facilitates the CGC synthesis discussed below. However, the resin-bound complexes discussed herein decompose in the presence of acid and therefore cannot be cleaved from the resins intact. They will thus be identified by other means.

Thus according to the experiment depicted in Figure III-3, and discussed in detail in the Chapter II, 10 mL plastic fritted syringes were used as reaction vessels into which ca. 35 mg of TentaGel, polystyrene/polyethylene glycol beads were placed. The N-acylated CysGlyCys peptide was constructed on the resin using standard Fmoc techniques. Following removal of the cysteinyl Mmt protecting group, a basic solution of Ni(acac)₂ in CH₂Cl₂ was introduced to the resin bed. Concomitant with bleaching of the green nickel solution, the light yellow color of the beads developed into a bright orange. The orange beads were dried and stored in a vacuum desiccator, however limited exposure to air caused no discoloration or difference to the reactions described below.

Synthesis of O-Ni(CGC)W(CO)₅¹⁻. A portion of the dry O-Ni(CGC)²⁻ was swelled with CH₂Cl₂ and exposed to a THF solution of W(CO)₅ whereupon the beads changed from bright orange to a burnt yellow. Several washes with CH₂Cl₂ solvent preceded vacuum drying of the beads prior to infrared analysis. That the last wash was free of metal carbonyl was verified by its FTIR solution spectrum which showed the diatomic region (1800 - 2100 cm⁻¹) to be clear of absorptions. The dried beads were placed on the sample plate of the ATR-FTIR attachment. The resulting spectrum, Figure III-3, showed a pattern match with solution phase [Ni(CGC)W(CO)₅]⁻; the position of the intense E mode is identical. The 20 cm⁻¹ shift in position of the low frequency, medium intensity A₁² band, is attributed to ion-pairing effects, more operable for this band which is associated with the CO group trans to the S-donor. The high energy A₁¹ band of the solution complex was barely observable in the resin-bound analogue.

It should be noted that the addition of a green Ni^{II} solution to the peptide-free polystyrene resin-beads, with both Fmoc protected and deprotected N-termini, resulted in no change in the color of the beads. Additionally, when (pip)₂W(CO)₄ was added to both sets of beads, no color change was observed and there were no observable ν(CO) bands. Importantly, the addition of Ni^{II} to deprotected O-CysGly, a potentially tridentate ligand, produced deep red colored beads. Altogether these controls suggest a cysteine peptide is required for binding nickel to the resin. Furthermore, the CysGlyCys tripeptide creates an N₂S₂ ligand with similar ligating properties to that of solution Ni(CGC)W(CO)_x²⁻ (x = 4,5).

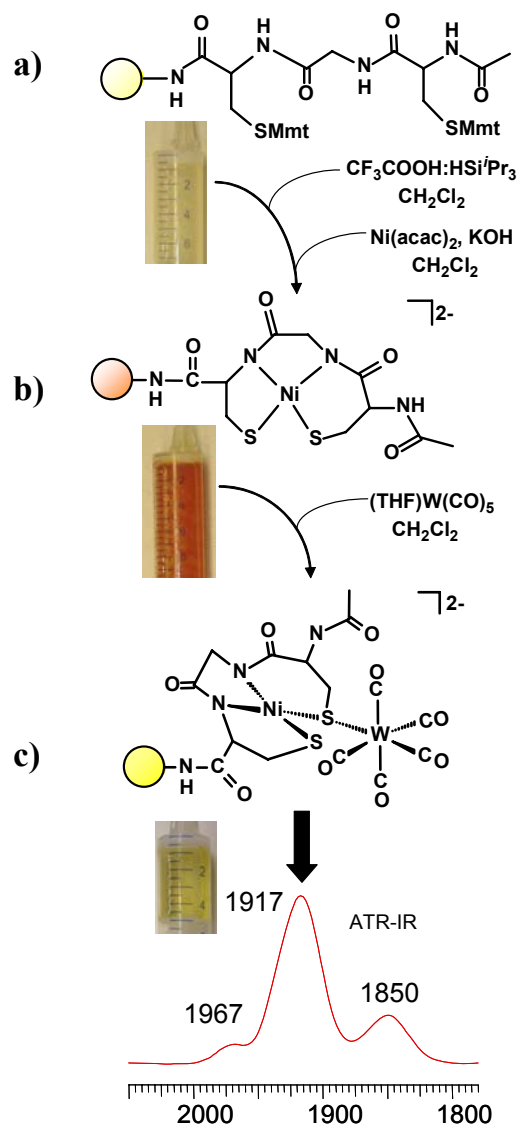


Figure III-3. (a) The O-CGC; (b) The bright orange beads consisting of O-Ni(CGC)²⁻ suspended in CH₂Cl₂; (c) The O-[Ni(CGC)]W(CO)₅²⁻ and its ATR-FTIR spectrum.

An interesting contrast to the reactivity of the unsupported $\text{Ni}(\text{CGC})^{2-}$ with $(\text{pip})_2\text{W}(\text{CO})_4$ (which produces $[\text{Ni}(\text{CGC})\text{W}(\text{CO})_4]^{2-}$) was noted as follows: When $(\text{pip})_2\text{W}(\text{CO})_4$ in CH_2Cl_2 was added to swelled $\text{O}-\text{Ni}(\text{CGC})^{2-}$, the ATR-FTIR spectrum acquired was identical to the one obtained when $\text{W}(\text{CO})_5(\text{THF})$ was used as the tungsten carbonyl source. This suggests that CO is released during the synthesis, possibly by both the $(\text{pip})_2\text{W}(\text{CO})_4$ precursor as well as the initial product,^{4,51} and the released CO is taken up by another $\text{O}-\text{Ni}(\text{CGC})\text{W}(\text{CO})_4^{2-}$. This CO-scavenging reaction occurred both within the confines of the closed syringe reaction vessel as well as when the derivatized beads were placed in a larger Schlenk flask kept at constant (1 atm) pressure or bubbled with CO. The capture of CO leads to the thermodynamically favored pentacarbonyl product, $\text{O}-\text{Ni}(\text{CGC})\text{W}(\text{CO})_5^{2-}$, expected to be structurally similar to B above. Notably for both resin-bound and resin-free forms of the Ni-W complexes, there is no evidence of further substitution of the $\text{Ni}(\text{CGC})^{2-}$ by CO to produce $\text{W}(\text{CO})_6$. As found for neutral $\text{NiN}_2\text{S}_2\text{W}(\text{CO})_5$ complexes, the $\text{Ni}(\text{CGC})^{2-}$ is tenacious as a mono-dentate, S-donor ligand to the 16-electron $\text{W}(\text{CO})_5$ species.^{4,51} The ATR-FTIR spectra of derivatized resin beads, stored as dried solids without exclusion of air, are identical to freshly prepared samples, indicating stability at a minimum of two weeks. Consistently, there is no discoloration of solvent used to swell the stored beads. This stabilization is attributed to the hydrophilic polyethylene glycol bead environment.

Preparation of Resin-Bound $\text{O-Ni(CGC)Rh(CO)}_2^{1-}$

Further derivatization of the resin-bound Ni tripeptide has been directed towards metal carbonyl moieties of potential catalytic ability. Analogous to diimine and diphosphine derivatives,⁶⁸ neutral NiN_2S_2 ligands form Ni-Pd binuclear complexes of $\text{Pd}^{\text{II}}(\text{CH}_3)_2$ or $\text{Pd}^{\text{II}}(\text{CH}_3)(\text{Cl})$, structure C, which exhibit organometallic reactivity of CO addition and insertion characteristic of the CO/olefin co-polymerization catalysis of polyketone.⁵¹ The rhodium(I) dicarbonyl unit, chelated by bidentate diimine or diphosphine ligands, is also known to catalyze a range of processes including intramolecular hydroamination,^{69, 70} decarbonylation,⁷¹ and carbonylation of methanol.⁷² As an analogue to the Pd complexes, $\text{Rh}^{\text{I}}(\text{CO})_2^+$ derivatives of Ni(CGC)^{2-} were pursued.

Addition of a CH_2Cl_2 solution of $[\text{Rh}(\text{CO})_2\text{Cl}]_2$ as the source of $\text{Rh}^{\text{I}}(\text{CO})_2^+$ to samples of the solvent-swelled O-Ni(CGC)^{2-} led to an immediate change in the orange color of the beads to a dark purple/brown hue. Upon washing with CH_2Cl_2 and drying as described before, the ATR-FTIR spectrum of the beads revealed two sharp bands of equal intensity at 2067 and 1990 cm^{-1} , indicative of the A_1 symmetric and B_1 asymmetric vibrational modes of the cis-CO groups at 90° angles ($I_a/I_s = \tan^2 \theta$) as would be expected for a square planar $\text{S}_2\text{Rh}(\text{CO})_2$ unit within the $\text{O-Ni(CGC)Rh(CO)}_2^{-1}$ bimetallic complex.⁷³

Synthesis of Solution Analogues, [(Ni-1)Rh(CO)₂][PF₆] and “[NEt₄][Ni(ema)Rh(CO)₂]”

The ability of NiN₂S₂ to bind to Rh(CO)₂⁺ was corroborated by synthesis of solution analogues that might be amenable to isolation and crystal structure analysis. On mixing of acetonitrile solutions of the red [Rh(CO)₂Cl]₂ dimer and the dark red [NEt₄]₂[Ni(ema)] compound, a purple/brown solution developed within an hour. The ν(CO) IR spectrum of this solution exhibited two sharp bands of equal intensity at 2063 and 1992 cm⁻¹, consistent with the expected [NEt₄][Ni(ema)Rh(CO)₂] product and similar in pattern and position to the solid state IR spectrum of O–Ni(CGC)Rh(CO)₂⁻. The negative mode of ESI-MS corroborated the presence of Ni(ema)Rh(CO)₂⁻ via the appropriate isotopic bundle at 421 m/z. The analogous cationic complex based on the neutral NiN₂S₂ complex, [(Ni-1)Rh(CO)₂][PF₆], was similarly prepared by addition of [Rh(CO)₂Cl]₂ to Ni-1 in CH₃CN. The symmetrical two-band ν(CO) IR absorbances for the red-orange [(Ni-1)Rh(CO)₂]⁺, are positioned at 2085 and 2017 cm⁻¹. The significant shift to higher frequencies as compared to [NEt₄]₂[Ni(ema)Rh(CO)₂]₂ and the O–Ni(CGC)Rh(CO)₂⁻ is consistent with the charge differences in the cationic vs. anionic derivatives.

Both the [Et₄N]₂[Ni(ema)Rh(CO)₂]₂ and [(Ni-1)Rh(CO)₂][PF₆] salts were crystallized and subjected to x-ray diffraction analysis. The solid state structures are given as thermal ellipsoid plots in Figures III-4 and III-5 along with ball and stick drawings of alternative views. In both structures the Rh^I is in S₂(CO)₂ square planar coordination with *cis* CO groups. The [(Ni-1)Rh(CO)₂]⁺ cation is a simple

heterobimetallic with a single NiN_2S_2 unit serving as a bidentate ligand to Rh^{I} in the same manner as the NiPd complex, structure C above.⁵¹ The $\text{Ni}(\text{ema})^{2-}$ derivative, however, crystallizes as a tetrametallic in which two $\text{Ni}(\text{ema})^{2-}$ units serve as bidentate bridges to two $\text{Rh}(\text{CO})_2^+$ components. The two $\text{S}_2\text{Rh}(\text{CO})_2$ planes in E are largely eclipsed with slight deviation resulting in SRhRhS torsion angles averaging to 16° , Figure A-1. The two $\text{S}_2\text{Rh}(\text{CO})_2$ planes are also, for the most part, parallel. The extrapolated intersection of these two planes is 3.7° .

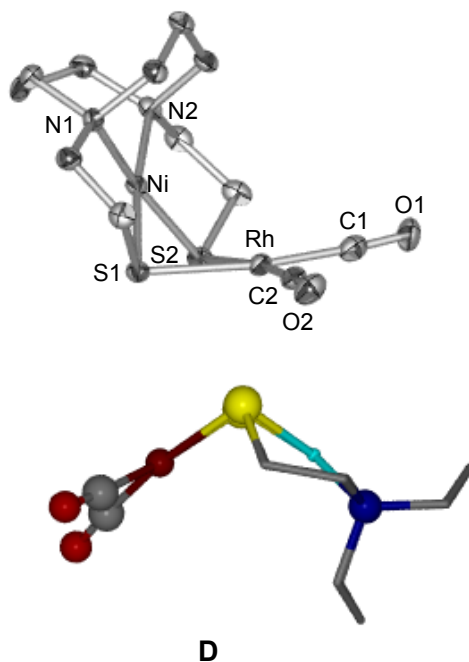


Figure III-4. Two views of $[(\text{Ni-1})\text{Rh}(\text{CO})_2]^+$, **D**, represented by a thermal ellipsoid plot as well as a ball and stick drawing; PF_6^- anion excluded.

The intersection of NiN_2S_2 and $\text{RhS}_2(\text{CO})_2$ square planes of cation **D** is 106° , which is slightly larger than the 101° angle found in the $(\text{Ni-1})\text{Pd}(\text{Me})\text{Cl}$ structure **C** above. An analogous hinge angle is defined for the tetrametallic structure **E** as the intersection of a NiN_2S_2 plane with the best plane defined by S_2Rh_2 . This turns out to be 107.4 and 98° ; as the two NiN_2S_2 units arrange to produce different angles with the dirhodium core.

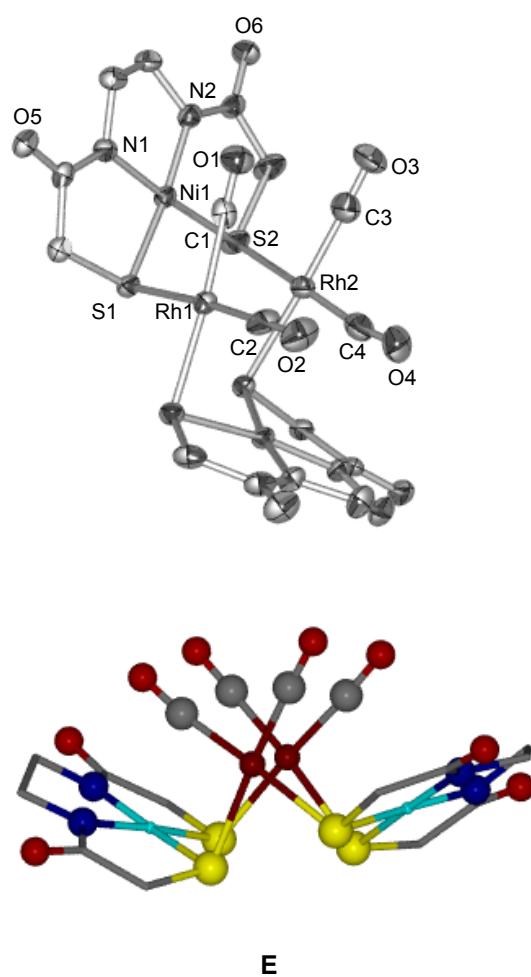


Figure III-5. Two views of $[(\text{Ni-ema})\text{Rh}(\text{CO})_2]_2^{2-}$, **E**, represented by a thermal ellipsoid plot and a ball and stick drawing, with Et_4N^+ cations excluded.

There are minor differences in the metric data between the free and bound NiN₂S₂ ligand. The $\angle_{\text{S-Ni-S}}$ of 84.65(3)° is slightly smaller in compound **D** than that of the free ligand, i.e., **Ni-1**, which is 89.4(1)°. The analogous angles in compound **E** and its free ligand (Ni(ema)²⁻) are 98.82(5) and 97.44(8).⁵⁰ The greater rigidity of Ni(ema)²⁻ coupled with its larger bite angle may account for the preference for binding in a bidentate bridging mode. It should be mentioned that the S₂Rh(CO)₂ units in **E** show less deviation from the 90° angles of regular square planarity as compared to structure **D**.

Conclusions for Chapter III

Altogether these results lead to the conclusion that the O–Ni(CGC)²⁻ binds to Rh(CO)₂ producing an S₂Rh(CO)₂ unit. While the precise morphology of the resin and relative positioning of the resin-bound metalloligands are unknown, other groups have shown that polystyrene/polyethylene glycol based resins form microdomains in which site isolation is prescribed.^{19,74} Based on this characteristic of the support utilized in our work, it is reasonable to assume that site isolation will limit aggregation and produce a complex similar to **D**. Although it is not clearly understood, the stabilization of resin-bound organometallic complexes has been noted.^{5,6,74} In our case, the prevention of deleterious reactions may be attributed to these microdomains formed by the polyethylene glycol tentacles of the TentaGel resins.^{16,19} Nevertheless in both the heterobimetallic and the heterotetrametallic [(NiN₂S₂)Rh(CO)₂]_x complexes (x = 1,2) the S donors produce a ligand field about Rh^I that reflects the donor ability of the respective NiN₂S₂ ligands. Interestingly, the sulfur donors from the dianionic NiN₂S₂, [Ni(ema)Rh(CO)₂]⁻ or O–

$\text{Ni}(\text{CGC})^{2-}$, create a $\text{Rh}(\text{CO})_2^+$ moiety that has electronic properties similar to $\text{Rh}(\text{CO})_2\text{I}_2^-$, ($\nu(\text{CO})$ values of 2059 and 1988 cm^{-1}),⁷² which is a catalyst precursor for the Monsanto Acetic Acid Process. Notably, the industrial catalysis invokes the same key steps of methyl oxidative addition, CO insertion, and ultimately reductive elimination, a process very similar to the mechanism of ACS.³ The catalytic potential of $\text{O}-\text{Ni}(\text{CGC})\text{Rh}(\text{CO})_2^-$ and solution analogues awaits exploration.

Altogether these results lead to the conclusion that the $\text{O}-\text{Ni}(\text{CGC})^{2-}$ binds to $\text{Rh}(\text{CO})_2$ producing an $\text{S}_2\text{Rh}(\text{CO})_2$ unit. While the precise morphology of the resin and relative positioning of the resin-bound metalloligands are unknown, other groups have shown that polystyrene/polyethylene glycol based resins form microdomains in which site isolation is prescribed.¹³ Based on this characteristic of the support utilized in our work, it is reasonable to assume that site isolation will limit aggregation and produce a complex similar to **D**. Although it is not clearly understood, the stabilization of resin-bound organometallic complexes has been noted.^{5,27,29,35} In our case, the prevention of deleterious reactions may be attributed to these microdomains formed by the polyethylene glycol tentacles of the TentaGel Resins.^{11,13} Nevertheless in both the heterobimetallic and the heterotetrametallic $[(\text{NiN}_2\text{S}_2)\text{Rh}(\text{CO})_2]_x$ complexes ($x = 1,2$) the S donors produce a ligand field about Rh that reflects the donor ability of the respective NiN_2S_2 ligands. Interestingly the sulfur donors from the dianionic NiN_2S_2 , $[(\text{Ni-ema})\text{Rh}(\text{CO})_2]^-$ or $\text{O}-\text{Ni}(\text{CGC})^{2-}$, create a $\text{Rh}(\text{CO})_2^+$ moiety that has electronic properties similar to $\text{Rh}(\text{CO})_2\text{I}_2^-$, ($\nu(\text{CO})$ values of 2059 and 1988 cm^{-1}),⁷² which is a catalyst precursor for the Monsanto Acetic Acid Process. Notably, the industrial catalysis invokes the same key steps of

methyl oxidative addition, CO insertion, and ultimately reductive elimination, a process very similar to the mechanism of ACS.⁴ The catalytic potential of $\text{O-Ni(CGC)Rh(CO)}_2^-$ and solution analogues awaits exploration.

CHAPTER IV
THE ACETYL CoA SYNTHASE PARADIGM FOR
HYBRID BIO-ORGANOMETALLICS:
QUANTITATIVE MEASURES FOR RESIN-BOUND Ni-Rh COMPLEXES[†]

In order to have a greater knowledge of the extent to which sites are available for incorporating the bioorganometallic hybrids into the resin beads, a quantitative approach to establishing resin-attached CGC, Ni and Rh concentrations has been developed. In the following report we describe the sequential approach to quantification of the loading of the CGC tripeptide, the incorporation of Ni into this tripeptide and the attachment of $\text{Rh}(\text{CO})_2^+$ to the $\text{O-Ni}(\text{CGC})^{2-}$ as well as the stability of the $\text{O-Ni}(\text{CGC})\text{Rh}(\text{CO})_2^{1-}$ adduct. Such studies are a reference point for future explorations of heterogeneous reaction chemistry based on the nickel tripeptide as an anchor for resin-bound bio-inspired organometallic complexes with catalytic potential.

[†] Reproduced with permission from Green, K. G.; James, W. D.; Cantillo, A. V.; Darensbourg, M.Y. *J. Organomet. Chem.* **2007**, *692*, 1392-1397. Copyright **2006** Elsevier.

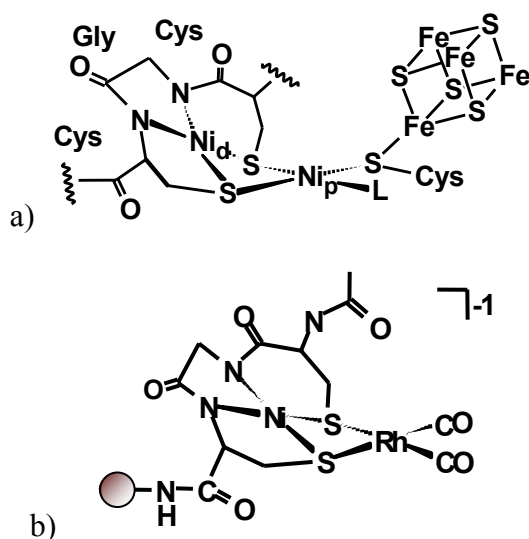


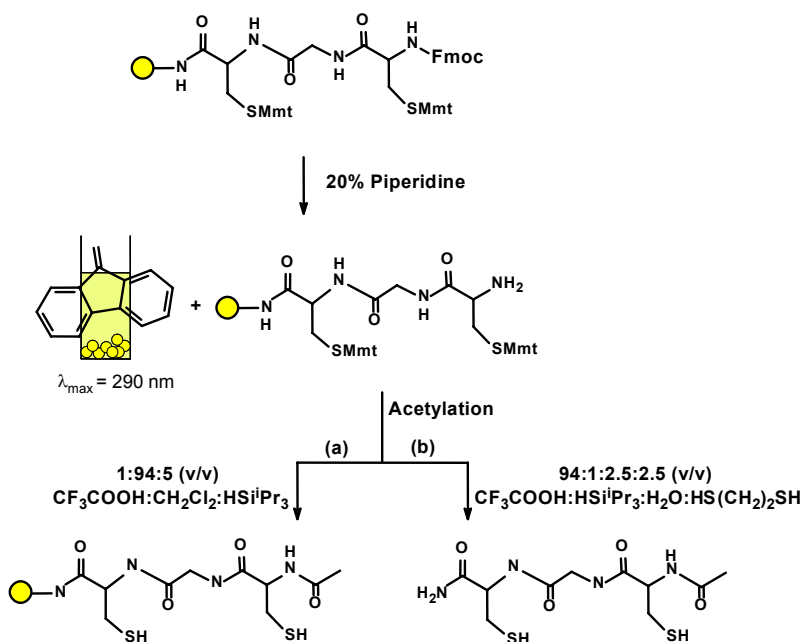
Figure IV-1. a) Representation of the A-Cluster active site of acetyl coA synthase¹ and b) presumed structure of ACS-inspired complex immobilized on TentaGel Resin.⁷⁵

Loading of Ni on $\text{O-Ni}(\text{CGC})^{2-}$

The extent to which the resin beads were derivatized with the Cys-Gly-Cys tripeptide, further loaded with nickel(II), and subsequently with rhodium(I) was evaluated according to the following protocol. As shown in Scheme IV-1, the solid phase synthesis of the tripeptide resulted in Mmt-protected cysteinyl sulfurs and an Fmoc-protected terminal amino group.⁷⁵ Deprotection by piperidine induces release of the Fmoc product, dibenzofulvene, which produced a pale yellow solution of characteristic $\lambda_{\text{max}} = 290 \text{ nm}$. Beer's law analysis of this solution yielded a CGC loading average of 0.143 mmol per gram of the resin beads.⁷⁶

As shown in Scheme IV-1, route (a), mild acid conditions selectively cleave the Mmt group and retain the amido-Rink linkage to the resin. Concentrated acid conditions, route (b), lead to Mmt loss as well as cleavage of the tripeptide as H_4CGC . That the H_4CGC was the main component on the beads was confirmed by analysis via ⁺ESI-MS.

Note that this is the same procedure used previously for preparing solution phase $\text{Ni}(\text{CGC})^{2-}$.⁴⁹ Addition of 1.4 mmol $\text{Ni}(\text{acac})_2$ and KOH to the resin-bound ligand, $\text{O-H}_4\text{CGC}$, produced bright orange beads within ten minutes. The reaction was allowed to proceed for a further 30 minutes to ensure completeness. (Extended times (days) gave identical results.) Following extensive washes and drying as described in the Chapter II, the nickel-loaded beads were analyzed by Neutron Activation Analysis. The average amount of nickel bound to the resin, i.e. the metal loading measured on four separately prepared samples, was determined to be 0.144 mmol of Ni atoms per gram of resin (mmol/g), as given in Table IV-1. The concurrence of CGC

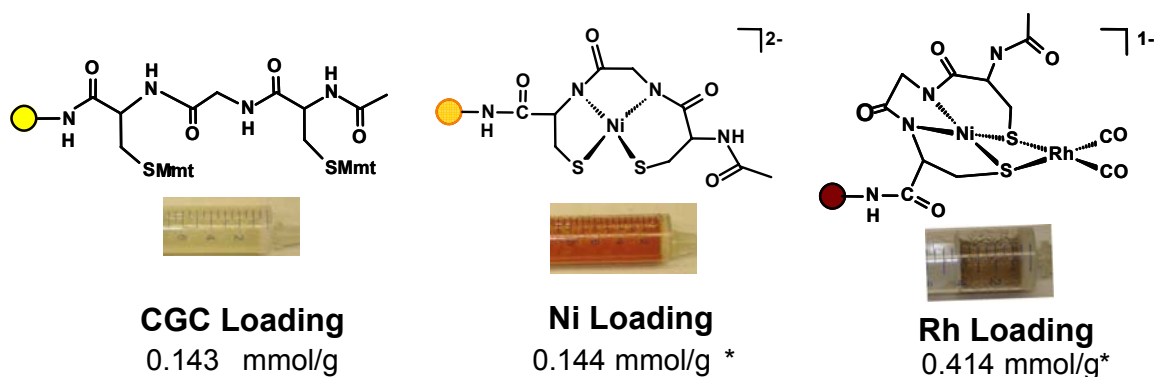


Scheme IV-1: Route for determining the CGC loading through Fmoc deprotection to produce dibenzofulvene as well as (a) deprotection of the thiolate sulfurs of $\text{O-Ni}(\text{CGC})^{2-}$ and (b) paralleled cleavage and deprotection of the H_4CGC tripeptide from the TentaGel Beads.

Table IV-1: Average loading of O-Ni(CGC)²⁻ (mmol Ni/g resin bead) determined via Neutron Activation Analysis on separately prepared samples.

Sample #	Loading (mmol/g)
1	0.152
2	0.143
3	0.152
4	0.129
Average	0.144

loading as reported in Figure IV-2 and the nickel loading is consistent with the uptake of a nickel(II) ion into each O-CGC site. This result is also consistent with earlier studies which demonstrated that O-Ni(CGC)²⁻ reaction with M(CO)_x reagents, (THF)W(CO)₅ and [Rh(CO)₂Cl]₂, display ν(CO) IR bands comparable to analogous resin-free complexes of [Ni(CGC)·W(CO)₅]²⁻ and [Ni(CGC)·Rh(CO)₂]¹⁻.⁷⁵ To verify this conclusion of selective Ni^{II} binding into the O-CGC site, a dichloromethane solution of Ni(acac)₂ and KOH was added to the underivatized (no peptide present) beads and showed no color change. Neutron Activation Analysis showed that the amount of nickel in this sample was less than 0.07 mmol/g, thus indicating that the tripeptide is required for binding of the Ni^{II} component.



* Loading may vary up to 0.01 mmol/g per batch.

Figure IV-2: Loading of Mmt-protected O-CGC; O-Ni(CGC)²⁻; and O-Ni(CGC)Rh(CO)₂⁻.

As a baseline study the number of resin sites accessible for tripeptide synthesis and metallation was also evaluated by UV-Vis analysis of dibenzofulvene produced upon Fmoc deprotection of the Rink amide termini of the peptide-free beads via a 20% piperidine/DMF solution. These studies showed that about 0.227 mmol/g resin of amide sites were available for construction of the tripeptide. As compared to the CGC loading described above, 0.143 mmol/g resin, only 63% of the Rink amide sites were utilized for tripeptide synthesis. This difference can be attributed to solvents used in the synthesis of the tripeptide. N,N-dimethylformamide (DMF) is avoided in peptide synthesis as it slows the rate of peptide bond-formation.⁷⁶ Hence, dichloromethane was used here. Although often considered a good swelling solvent for PS-PEG systems, dichloromethane is less optimal than DMF. It is likely, therefore, that a number of sites are not accessible during

peptide synthesis due to slightly restricted swelling in dichloromethane (as compared to DMF used in the Fmoc analysis above).

Loading of Rh on O-Ni(CGC)Rh(CO)₂¹⁻

As shown in Figure IV-3, the addition of a dichloromethane solution of [Rh(CO)₂Cl]₂ to the pre-swollen O-Ni(CGC)²⁻ beads transforms the orange into a purple/brown hue within 5 minutes. Again mixing time was extended to 30 minutes to ensure reagent access to all O-Ni(CGC)²⁻ sites. The beads were then washed with dichloromethane, methanol and diethyl ether. The signature $\nu(\text{CO})$ bands expressed for CH₃CN solution phase [Ni(CGC)·Rh^I(CO)₂]⁻ (2058 and 1986 cm⁻¹) were observed for these Ni/Rh loaded beads at 2067 and 1990 cm⁻¹ via ATR-FTIR spectroscopy.⁷⁵ Determination of the Ni and Rh loading on such derivatized beads showed that the Ni loading remained about constant, 0.132 mmol/g, and that the Rh loading was 0.414 mmol/g yielding a Rh:Ni ratio of ca. 3, Table IV-2.

The addition of [Rh(CO)₂Cl]₂ to the beads *sans* nickel-tripeptide induces an immediate color change from yellow to orange/brown. These beads showed $\nu(\text{CO})$ bands at 2076s and 1998s cm⁻¹ that dissipated after two hours, a marked difference from the stable O-Ni(CGC)Rh(CO)₂¹⁻. Metal analysis of these beads showed Rh loading to equal 0.221 mmol/g indicating that the PS-PEG polymers bind carbonyl-free rhodium species independent from those of the dithiolate-Rh contact in O-Ni(CGC)Rh(CO)₂¹⁻. As polyethylene glycol is well known for its ability to form complexes with metal ions, it is

assumed to be the site of interaction for the extraneous Rh ions.⁷⁷ It should be noted that attempts to add $[\text{Rh}(\text{CO})_2\text{Cl}]_2$ directly to O-CGC gave complicated, transient $\nu(\text{CO})$ spectra and substantial Rh uptake. We have seen no indication that rhodium displaces nickel in the O-Ni(CGC)²⁻ derivatives.

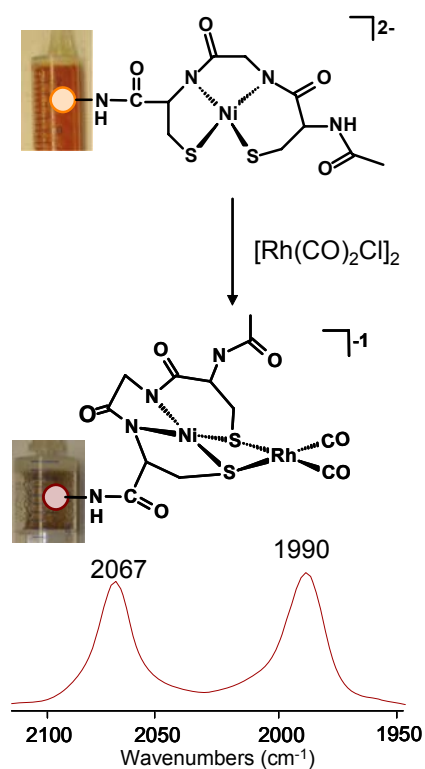


Figure IV-3: Synthetic Route to O-Ni(CGC)Rh(CO)₂ and its infrared spectrum obtained on vacuum dried polystyrene beads via ATR-FTIR.

Stability of O-Ni(CGC)Rh(CO)₂¹⁻

As complexes bound to solid supports, such as those used for heterogeneous catalysis, are often plagued by leaching, the robustness of the O-Ni(CGC)Rh(CO)₂¹⁻ complex was investigated under a variety of conditions. As shown in Table IV-2, and discussed in detail in the Experimental Section, several stresses on the environment of the O-Ni(CGC)Rh(CO)₂¹⁻ complex were attempted. Samples 2-4 showed no discoloration of the beads or the supernatant solutions used in the experiments or after being washed with ether and dried. Furthermore the amount of nickel and of rhodium remaining on the beads is substantially the same as in the control sample. The supernatant benzene showed no $\nu(\text{CO})$ bands and the ether washes were colorless. The FTIR $\nu(\text{CO})$ spectrum of the beads showed only a minor decline in intensity. We have taken this preliminary data as indication that the Ni/Rh derivatized beads are largely stable.

Table IV-2: Ni and Rh loadings for O-Ni(CGC)Rh(CO)₂¹⁻ resulting from induced stress conditions.

Sample	Ni Loading (mmol/g)	Rh Loading (mmol/g)	Loading Rh: Ni ratio	Conditions [‡]
1a	0.132	0.414	3.13	†
1b	0.134	0.375	2.80	-
2	0.123	0.415	3.36	Shake in Benzene
3	0.122	0.421	3.44	Bubbled w/Air
4	0.126	0.427	3.40	Swell/Dry

[‡] Conditions discussed in detail may be found in Experimental Section. Duration of stress in each case was 2 days.

† Standard = Complex made, washed with CH₂Cl₂, MeOH, and ether, then vacuum dried. Samples 2-4 were derived from batch 1a.

Conclusion for Chapter IV

Neutron Activation Analysis has been used to determine the metal loading of Ni and Rh on TentaGel S RAM® beads. The 1:1 Ni:CGC⁴⁻ ratio was confirmed via the use of the UV-vis spectrum of free Fmoc from deprotection of the terminal amine of the terminal cysteine whose concentration matched that of nickel analysis by Neutron Activation Analysis. Control experiments showed that the CGC ligand was necessary in order to produce the orange, resin-bound species O-Ni(CGC)²⁻ and that no PEG-Ni interaction was evident. In contrast rhodium uptake by the PEG-PS beads was observed, however this interaction was not responsible for the $\nu(\text{CO})$ bands attributed to O-Ni(CGC)Rh(CO)₂²⁻. The rhodium loading was determined to be about 3 Rh atoms per 1 Ni atom as determined by Neutron Activation Analysis. The ability for the O-Ni(CGC)²⁻ ligand to strongly secure the Rh moiety to the solid support implies potential for such metallodithiolato ligands to be utilized in catalysis and modeling of enzyme active-sites.

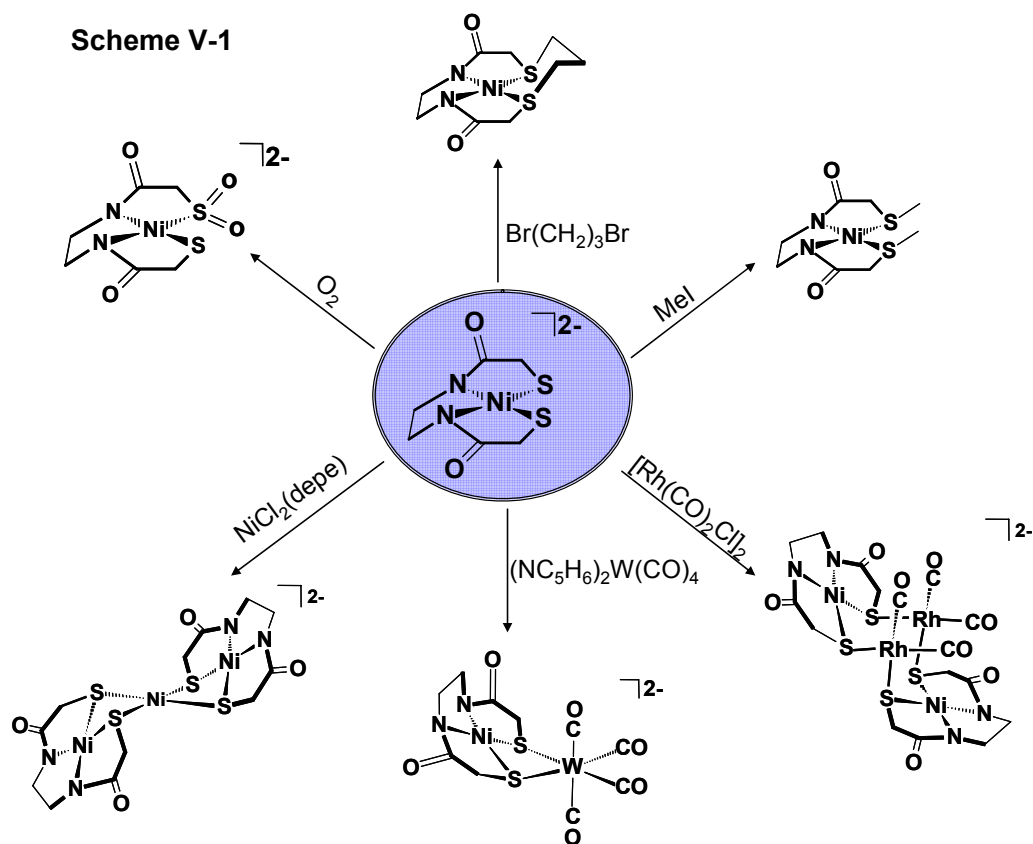
CHAPTER V
AN EXPERIMENTAL AND COMPUTATIONAL STUDY OF SULFUR-
MODIFIED NUCLEOPHILICITY IN A DIANIONIC NiN₂S₂ COMPLEX[‡]

The discovery of (N₂S₂)⁴⁻ donor sites in biology based on Cysteine-X-Cysteine tripeptide motifs has prompted examination of small molecule models that build on a well known literature that is based on (N₂S₂)²⁻ ligands which evolved over several decades.^{78,79} The chemistry of metalloproteins such as acetyl coA synthase (ACS) and nitrile hydratase (NHase) is particularly inviting in that post-translational modification is a controlling factor in enzyme activity, and such S-based reactivity can be reproduced in synthetic analogues.^{1,2,41,80,81}

Shown in Scheme V-1 are the results of prior reactivity studies of Holm's [Ni(N₂S₂)]²⁻ complex, [Ni(ema)]²⁻, Ni(II) (N,N'-ethylenebis-2-mercaptoacetamide), a minimal biomimetic of the Cys-Gly-Cys donor environment of the distal nickel site in ACS, containing as does ACS two cis-dithiolato S-donors and two carboxamido N-donors.^{1,50} The sulfurs are readily alkylated with MeI, and, when exposed to metal sources, unique polynuclear complexes in which exogenous metals are captured by the sulfurs are obtained.^{52,75,82} The tungsten carbonyl derivative at the 6 o'clock position in Scheme V-1 was used to establish that the donor ability of Ni(ema)²⁻ as a

[‡] Reproduced with permission from Green, K. G.; Brothers, S. M.; Jenkins, R. M.; Carson, C. E.; Grapperhaus, C. A.; Darensbourg, M. Y. *Inorg. Chem.* **2007**, *46*, 7536-7544. Copyright **2007** American Chemical Society.

metallodithiolate ligand is superior to that of neutral NiN_2S_2 complexes, Figure III-2.⁷⁵ Nevertheless, the reactivity of $\text{Ni}(\text{ema})^{2-}$ largely mirrors that of neutral NiN_2S_2 complexes, emphasizing the nucleophilicity of cis-dithiolates, regardless of the charge on the complex.^{83, 84, 85}



A recent addition to the N_2S_2 family of metalloproteins is Nickel superoxide dismutase (NiSOD) which contains an $\text{N}_2\text{SS}'$ trianionic site involving a His-Cys terminus dipeptide with a second cysteine three residues away.^{42,43} The interest in this active site from the view of S-based reactivity in NiN_2S_2 complexes is that it doesn't occur!⁸⁶ That

is, the SOD reaction produces oxygen and peroxide in the dismutation of O_2^- while avoiding S-oxygenation or S-oxidation.⁸⁴ Furthermore, a popular and reasonable mechanism proposes a Ni^{III} to account for the first oxidation in the ping-pong catalytic cycle.⁴² Current computational and biomimetic investigations into the mechanism have assumed inner sphere reactivity and have focused on the role of first coordination sphere effects in promoting Ni-based oxidative chemistry.^{86, 87} For example, the influence of anionic carboxyamido nitrogens as contrasted to neutral amine donors in N_2S_2 dithiolato complexes of Ni^{II} was explored by Grapperhaus, Kozlowski and Mullins by Density Functional Theory, concluding that as the amine donors are sequentially replaced by anionic carboxyamido nitrogens, electron density is delocalized onto both the nickel and the sulfur atoms.⁸⁸ Brunold, Maroney and coworkers have suggested that the presence of even one carboxyamido nitrogen will direct redox or oxidative activity to the nickel rather than sulfur.⁸⁶ Nevertheless, the potential for second coordination sphere effects is obvious from the protein crystal structure, and mechanisms for sulfur protection include hydrogen bonding as well as steric interactions.^{42,88} In view of the clear-cut connections between the synthetic and the Cys-X-Cys biological N_2S_2 ligand sets; of the likelihood that such ligand sets will be found in other biological settings; and of the great potential for S-based modification of such sites, we have endeavored to further develop the reactivity wheel of Scheme V-1 by studies of two additional S-based nucleophilic reactions of $Ni(ema)^{2-}$. While the reaction of $Ni(ema)^{2-}$ with O_2 had previously been reported by Hegg, et al.,⁵² the level of O_2 incorporation into nickel dithiolates can be complicated (yielding metallo sulfinato, sulfenato and sulfonato species) and an

unambiguous characterization of the product was needed.^{83,84} Chapter V reports the synthesis, characterization and molecular structures of the dianionic sulfinate $[\text{Et}_4\text{N}]_2[\text{Ni}(\text{ema})\cdot\text{O}_2]$ and the neutral macrocyclic $\text{Ni}(\text{ema})\cdot(\text{CH}_2)_3$, derivatives of $[\text{Et}_4\text{N}]_2[\text{Ni}(\text{ema})]$. The physical properties of these $\text{Ni}(\text{ema})^{2-}$ derivatives as well as Density Functional Theory (DFT) calculations, Natural Bond Order (NBO) and electrostatic potential (EP) analyses are contrasted within the series of $\text{Ni}(\text{ema})^{2-}$ derivatives and with certain neutral analogues.

Synthesis and Molecular Structures of $\text{Ni}(\text{ema})\cdot(\text{CH}_2)_3$ and $[\text{Et}_4\text{N}]_2[\text{Ni}(\text{ema})\cdot\text{O}_2]$

On addition of 1,3-dibromopropane to an acetonitrile solution of $[\text{Et}_4\text{N}]_2[\text{Ni}(\text{ema})]$, a red crystalline, air stable solid of $\text{Ni}(\text{ema})\cdot(\text{CH}_2)_3$ is obtained in good yield. The $\text{Ni}(\text{ema})\cdot(\text{CH}_2)_3$ is insoluble in hydrocarbons, acetonitrile, dichloromethane, and tetrahydrofuran but remains soluble in methanol, DMF, and water as is the $[\text{Et}_4\text{N}]_2[\text{Ni}(\text{ema})]$ precursor. The synthesis of $[\text{Et}_4\text{N}]_2[\text{Ni}(\text{ema})\cdot\text{O}_2]$ was accomplished via two routes. The higher yielding route results from placing dark red $\text{Ni}(\text{ema})^{2-}$ crystals under ether and exposing the heterogeneous mixture to small quantities of air. The crystals develop into a lighter, bright red color after 4-6 h as dioxygen diffuses into them. Alternatively, an acetonitrile solution of $[\text{Et}_4\text{N}]_2[\text{Ni}(\text{ema})]$ was slightly pressurized with $\text{O}_2(\text{g})$ and stirred for 30 min. The solution color perceptibly lightened and the reaction was monitored for completeness using UV-Vis and infrared spectroscopies.

Thermal ellipsoid plots of the square planar $\text{Ni}(\text{ema})\cdot(\text{CH}_2)_3$ and $\text{Ni}(\text{ema})\cdot\text{O}_2^{2-}$ as well as crystallographic data and full structural reports for $\text{Ni}(\text{ema})\cdot(\text{CH}_2)_3$ and

[Et₄N]₂[Ni(ema)•O₂] are given in Appendix A and B. The ball and stick drawings of Figure V-1 compare metric features of [Et₄N]₂[Ni(ema)],⁵⁰ [Et₄N]₂[Ni(ema)•O₂], Ni(ema)•(Me)₂,⁵² and Ni(ema)•(CH₂)₃. Parameters of interest include a slight restriction of the S-Ni-S angle in the Ni(ema)•(CH₂)₃ macrocycle complex relative to its open-chain analogue, Ni(ema)•(Me)₂, as well as Ni(ema)²⁻ and Ni(ema)•O₂²⁻. This restriction is compensated by increase of the N-Ni-N and the N-Ni-S angles.

Sulf-oxygenation in the [Et₄N]₂[Ni(ema)•O₂] results in a decreased Ni-S_{sulfinate} bond distance (2.152(2) Å) maintaining the Ni-S_{thiolate} (2.175(2) Å) statistically the same as in [Et₄N]₂[Ni(ema)].⁵⁰ The contracted Ni-S_{sulfinate} bond relative to the Ni-S_{thiolate} bond distances is observed in a number of sulfinate derivatives.⁸⁴ The S=O bond lengths, 1.444(6) and 1.436(6) Å, are slightly shorter than those observed for neutral S-oxygenates of NiN₂S₂, which average to 1.46 Å. Relative to Ni(ema)²⁻ the Ni-S_{thioether} distances are slightly elongated in the open chain dithioether Ni(ema)•(Me)₂, while in the macrocycle Ni(ema)•(CH₂)₃ the Ni-S distances are marginally shorter.⁵⁰

Solution Characterizations of Ni(ema)•(CH₂)₃ and [Et₄N]₂[Ni(ema)•O₂]

The NMR spectrum of Ni(ema)•(CH₂)₃ in MeOH at 22°C displays sharp signals including a pentet at 1.87 and a triplet at 2.72 ppm, assigned to the bridgehead methylene hydrogens and the two adjacent CH₂, respectively, of the propane dithioether moiety. A doublet of doublets AB pattern, at 3.645 and 3.488 ppm with J_{AB} = 56 Hz, is ascribed to the N to N -CH₂CH₂- linker while the CH₂ units between the carbonyl and the thiolate sulfur are poorly defined underneath the methanol signal. Much broader resonances are

seen in water as solvent. The infrared spectra of both $\text{Ni(ema)\cdot(CH}_2)_3$ and $\text{Ni(ema)\cdot(CH}_3)_2$ (in MeOH) display a band at 1582 cm^{-1} which is ascribed to the C=O stretch of the carboxamido group.

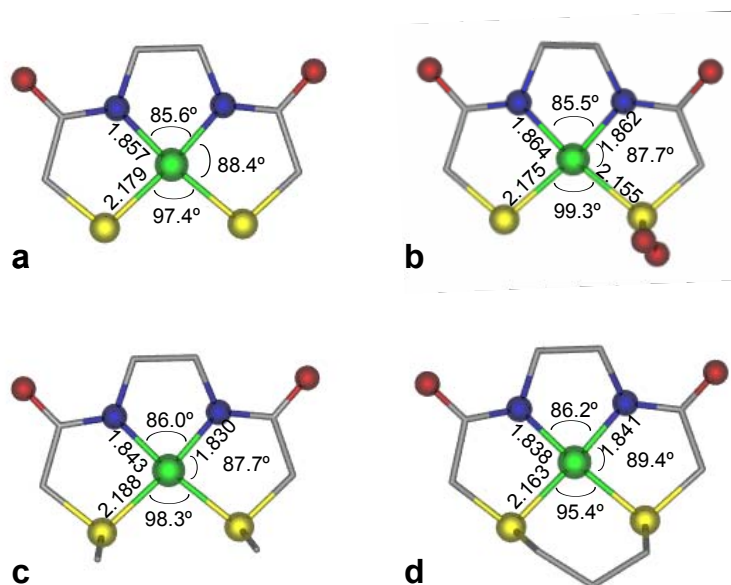
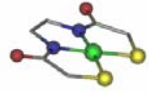
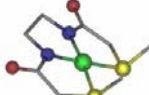

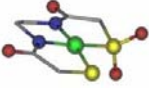


Figure V-1. Structures of (a) Ni(ema)^{2-} ⁽⁵⁰⁾, (b) $[\text{Et}_4\text{N}]_2[\text{Ni(ema)\cdot O}_2]$, (c) $\text{Ni(ema)\cdot(Me)}_2$ ⁽⁵²⁾ and (d) $\text{Ni(ema)\cdot(CH}_2)_3$ with selected bond distances (Å) and angles (°).

Electronic Absorption Spectroscopy. The UV-vis absorption spectrum of $\text{Ni(ema)\cdot(CH}_2)_3$ in methanol exhibits two d-d bands with λ_{max} at 396 and 476 nm as well as two intense ligand to metal charge transfer bands at 204 and 242 nm. As shown in Table V-1, the absorbances for both neutral alkylates are blue shifted from those of the anionic parent complex, $[\text{Et}_4\text{N}]_2[\text{Ni(ema)}]$, which is attributed to the overall stabilization

of the bond and lone pairs on reaction with the electrophiles. A lesser blue shift of absorbances relative to those of $[\text{Et}_4\text{N}]_2[\text{Ni}(\text{ema})]$ is seen for the $\text{Ni}(\text{ema})\cdot\text{O}_2^{2-}$ complex dissolved in methanol.

Table V-1. Summary of electronic absorption spectra for $\text{Ni}(\text{ema})^{2-}(\text{EtOH})^{50}$, $\text{Ni}(\text{ema})\cdot(\text{Me})_2(\text{CH}_3\text{CN})^{52}$, $\text{Ni}(\text{ema})\cdot(\text{CH}_2)_3(\text{MeOH})$, $\text{Ni}(\text{ema})\cdot\text{O}_2^{2-}(\text{MeOH})$.

	UV-vis λ_{max} (nm) (ϵ , $\text{M}^{-1} \text{cm}^{-1}$)			
	261 (22,500)		437 (405)	552 (79)
	241 (18,200)	300 (sh, 3370)	416 (360)	490 (130)
	204 (20,200)	242 (1547)	396 (70)	476 (30)
	250 (13,841)	297 (469)	413 (35)	

Infrared Analysis. Two $\nu(\text{S}=\text{O})$ bands with a symmetric stretch at 1151 cm^{-1} and the corresponding asymmetric stretch at 1030 cm^{-1} are observed in the CH_3CN solution IR spectrum of $\text{Ni}(\text{ema})\cdot\text{O}_2^{2-}$.⁵² A band at 1560 cm^{-1} (in MeOH) is assigned to the $\nu(\text{C}=\text{O})$ stretch and is the same as that of the parent $\text{Ni}(\text{ema})^{2-}$. The UV-vis and IR spectroscopic values correspond with those of the complex postulated by Hegg and co-

workers to be the same sulfinato product produced from Ni(ema)^{2-} in an oxygenated CH_3CN solution.⁵²

Mass Spectrometry. The parent ion of $\text{Ni(ema)•(CH}_2)_3$ is observed in the positive mode of the ESI-mass spectrum as the sodium adduct at 326.98 m/z with the expected isotopic envelope. Crystalline material from either synthetic route which produces $[\text{Ni(ema)•O}_2]^{2-}$ as described above has a parent isotopic bundle in the $^-$ ESI-MS clustered around 239.9 m/z which corresponds to $[\text{M}]^-$. Additional prominent isotopic bundles containing Ni correspond to the loss of O_2 and SO_2 presumed to be induced by ionization in the ESI-MS experiment. A similar phenomenon was observed in neutral NiN_2S_2 sulfinate species.⁸⁴

Electrochemical Studies. The cyclic voltammogram of $\text{Ni(ema)•(CH}_2)_3$ recorded in DMF solvent is given in Figure V-2 and is interpreted as follows. A reversible oxidation event at +1.05 V (vs. NHE) is assigned to the $\text{Ni}^{\text{III/II}}$ couple of the $\text{Ni(ema)•(CH}_2)_3$ complex, and an irreversible reduction at -1.53 V is assigned to the $\text{Ni}^{\text{II/I}}$ couple. The feature at -0.71 V is a consequence of the irreversible reduction at -1.53 V as it is absent in scans in the anodic direction initiated at points more positive than -1.2 V. The full scale CV of Ni(ema)•(Me)_2 , reported in Figure A-5, is similar to that of $\text{Ni(ema)•(CH}_2)_3$ with the exception that the reductive event becomes fully reversible in the complex with a more flexible open chain. The inset in Figure V-2 is an expansion of the $\text{Ni}^{\text{III/II}}$ couple of $\text{Ni(ema)•(CH}_2)_3$ with that of the Ni(ema)•(Me)_2 complex overlaid.

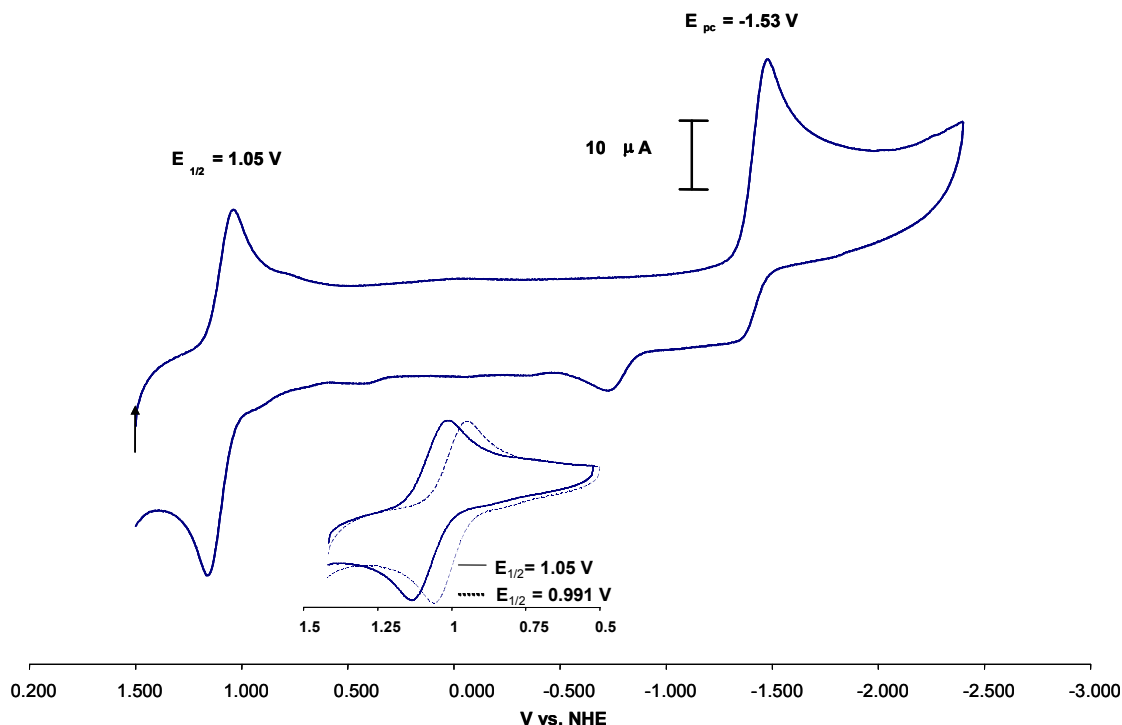


Figure V-2. Cyclic Voltammogram of a 3.7 mM DMF solution of Ni(ema)•(CH₂)₃ at a scan rate of 200 mV/s using a Ag/AgNO₃ reference electrode, 0.1 M [ⁿBu₄N][BF₄] electrolyte, a glassy carbon electrode and standardized to Fc/Fc⁺ and reported vs. NHE. The inset focuses on the reversible Ni^{II/III} couple of Ni(ema)•(CH₂)₃ (solid) and Ni(ema)•(Me)₂ (dashed).

The Ni^{II/III} couples of the dianionic Ni(ema)²⁻ and Ni(ema)•O₂²⁻ species appear as fully reversible waves at -0.160 and -0.114 V, respectively, while the Ni^{II/I} couple is shifted beyond the DMF solvent window. While the ca. 1 V difference between the Ni^{II/III} couples of the neutral and the dianionic complexes can readily be ascribed to charge, the small difference of ca. 50 mV between the Ni^{II/III} couples of Ni(ema)•O₂²⁻ and the Ni(ema)²⁻ precursor is more subtle. Despite S-oxygenation of the thiolate sulfur and the loss of π -donation, the sulfinato ligand remains a σ -donor, anionic ligand.^{89,90} Apparently, there is little change in the overall electron density of the Ni^{II} in the two

anions and the $\text{Ni}^{\text{II/III}}$ potential remains relatively constant. This result contrasts to electrochemical studies of analogous neutral NiN_2S_2 and $\text{NiN}_2\text{S}_2\cdot\text{O}_2$ complexes with regard to differences in the $\text{Ni}^{\text{II/I}}$ redox couple on oxygenation (the $\text{Ni}^{\text{II/III}}$ couple being beyond the solvent window).⁸⁴ In these cases the difference, +300 mV, is six times that observed for the difference in $\text{Ni}^{\text{II/III}}$ couples of $\text{Ni}(\text{ema})^{2-}$ vs. $\text{Ni}(\text{ema})\cdot\text{O}_2^{2-}$. As will be discussed below, the difference between $\text{Ni}(\text{ema})^{2-}$ and the neutral NiN_2S_2 complexes lies in the greater covalency in the Ni-S bonds of the former, and in the compensatory effect of both the unmodified thiolate and the carboxyamido nitrogens which is greater for the dianionic complexes.⁹⁰

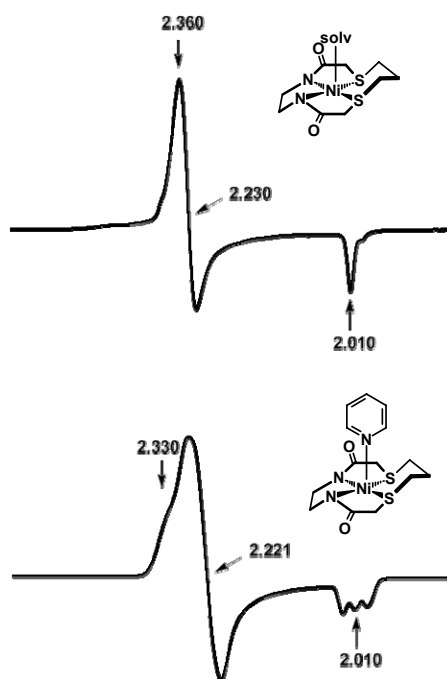


Figure V-3. X-band EPR spectra obtained from an oxidized solution of $\text{Ni}(\text{ema})\cdot(\text{CH}_2)_3$ in DMF at 10 K. Simulated g values listed.

EPR Studies of Ni(ema)•(CH₂)₃⁺. The good reversibility of the Ni^{II/III} couple in the CV indicated the likelihood of detection of Ni^{III} produced by bulk chemical oxidation. The EPR spectrum obtained by group member Roxanne Jenkins of the chemical oxidation product of Ni(ema)•(CH₂)₃, using CAN in DMF solvent (Figure V-3 (a)) displays a nearly axial EPR signal with $g_{\perp} > g_{\parallel}$; g values were simulated as $g_1 = 2.360$, $g_2 = 2.230$ and $g_3 = 2.010$. As g_{av} is significantly >2 , the assignment of the product to [Ni^{III}(ema)•(CH₂)₃]⁺ with $S = \frac{1}{2}$ and residence of the unpaired electron in a predominately Ni-d_{z²} orbital is reasonable. This spectrum is comparable to those reported by Holm, et al., for oxidized products derived from Ni(ema)²⁻ and other diamidodithiolato NiN₂S₂ analogues.⁵⁰ As in that work, the stabilization of the Ni^{III} oxidation state by interactions with donor molecules was probed by oxidation of Ni(ema)•(CH₂)₃ by CAN in the presence of pyridine (1 pyridine: 4 DMF, (v/v)). The color of the reaction mixture changed from red to clear brown, as observed in the oxidation product of the complex in the absence of pyridine. The overall EPR spectral envelope is similar to that in pure DMF, with the exception of the three ¹⁴N hyperfine lines imposed on the $g_3 = 2.01$ with $a_N = 18.5$ G. The EPR spectrum thus suggests a Ni^{III} species in a z-axis elongated square pyramid with one nitrogen ligand in the axial coordination site. The assumption that DMF is sufficiently coordinating to bind to Ni^{III} in the absence of pyridine, would account for the identical position of the g_3 signal.

Computational Details of Ni(ema)^{2-} , $[\text{Ni(ema)}\cdot\text{O}_2]^{2-}$, $\text{Ni(ema)}\cdot(\text{CH}_2)_3$, and $\text{Ni(ema)}\cdot(\text{Me})_2$.

Density functional theory calculations by group member Scott Brothers of Ni(ema)^{2-} , $[\text{Ni(ema)}\cdot\text{O}_2]^{2-}$, $\text{Ni(ema)}\cdot(\text{CH}_2)_3$, and $\text{Ni(ema)}\cdot(\text{Me})_2$ yielded optimized structures with bond distances and angles acceptably consistent with the crystallographic experimental data; these are listed in Table A-3, A-4. DFT calculations of the Ni(ema)^{2-} complex reproduce the energies, orbital populations, and bond distances previously reported by Grapperhaus, *et al.*⁸⁸ Figure V-4 presents the frontier molecular orbitals (FMO) of the four complexes under study. The HOMO of Ni(ema)^{2-} , Figure V-4 (a), displays a clear cut d_π - p_π antibonding orbital interaction with respect to the antisymmetric combination of the p_z orbitals of the two sulfurs (22% contribution per atom) and the d_{xz} orbital of the nickel (39% contribution). The HOMO-1, nearly degenerate with the HOMO, consists largely of the overlap of the Ni d_{yz} (44% contribution) and the symmetric combination of S p_z (14% contribution per atom). The non-degeneracy is due to the larger contributions of the amido nitrogen and carboxylate oxygen atoms, which cause slight energetic differences in the molecular orbitals. The LUMO is an antibonding σ orbital set comprised of 33% Ni d_{xy} character, 12% S $p_{x,y}$ character per sulfur atom, and 4% N $p_{x,y}$ character per nitrogen atom. The gap between the HOMO and LUMO is 4.12 eV.

As is shown in Figure V-4 (b), the electron density of the HOMO of the $[\text{Ni(ema)}\cdot\text{O}_2]^{2-}$ complex is localized as an antibonding orbital composed of 32% Ni d_{yz} , 45% $\text{S}_{\text{thiolate}}$ p_z character, 4% $\text{N}_{(1)}$ p_z character, and 3% $\text{O}_{(1)}$ p_z character, where $\text{N}_{(1)}$ and

O₍₁₎ are the amido atoms trans to S_{thiolate} and N₍₂₎ and O₍₂₎ are the amido atoms trans to S_{sulfinate}. Due to the singly modified sulfur in Ni(ema)•O₂²⁻, the near degeneracy of the HOMO and HOMO-1 orbitals of the Ni(ema)²⁻ parent complex is broken. Nevertheless, as in Ni(ema)²⁻, the HOMO-1 still appears to be a bonding orbital orthogonal to the HOMO with considerable electron density on the Ni d_{xz}, N₍₂₎ p_z, and O₍₂₎ p_z orbitals (36%, 20%, and 13% contributions, respectively). The LUMO has small percentage of electron density on the sulfenate oxygens but in other respects is largely the same as that of the Ni(ema)²⁻ parent complex. Interestingly, the HOMO-LUMO gap of this oxygenated complex is nearly identical to that in the parent complex, i.e., 4.15 eV.

In Ni(ema)•(Me)₂ and Ni(ema)•(CH₂)₃, the HOMO and the HOMO-1, shown in Figure V-4 (c) and (d), largely reflect the analysis described above for the cis-dithiolate. That is, the asymmetric combination of N p_z orbitals (16-18% contribution per atom) engage in antibonding overlap with the Ni d_{xz} orbital (21-22% contribution), producing the HOMO, and the symmetric combination of the N p_z orbitals (10-15% contribution per atom) with Ni d_{yz} (19-20% contribution) make up the HOMO-1. A more substantial contribution from the O p_z orbitals (5-10% contribution) relative to the parent Ni(ema)²⁻ complex is also observed. Again, the LUMO is in the σ framework of the square plane.

Natural Bond Orbital Analysis. Natural bond orbital (NBO) analysis is a technique derived from density functional theory as a powerful tool for clarification of the principal resonance structures of the molecule under study. Atomic charges from geometry optimization are used to determine the primary ground state structure. Delocalization of the electrons and resonance structures of the molecule is derived from

second-order effects. In the current study, this technique was employed to assign formal dative or coordinate-covalent bond character between the Ni-N and Ni-S bonds, which undergo significant change upon modification of the thiolate sulfurs. This consequently affects electron delocalization in the amido framework.

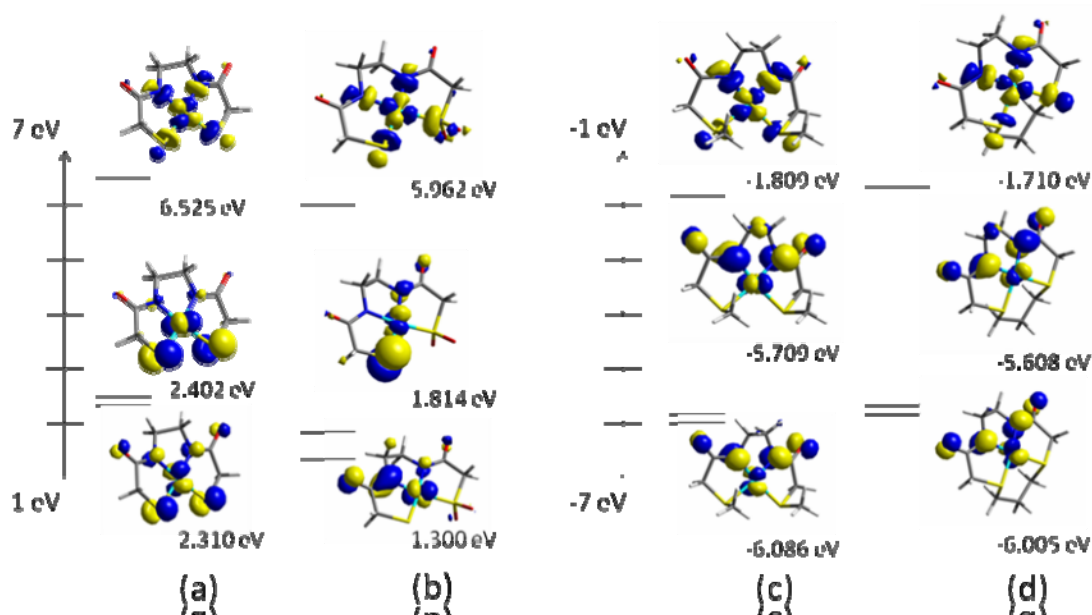


Figure V-4. Frontier molecular orbitals of (a) Ni(ema)^{2-} , (b) $[\text{Ni(ema)}\cdot\text{O}_2]^{2-}$, (c) $\text{Ni(ema)}\cdot(\text{CH}_3)_2$, and (d) $\text{Ni(ema)}\cdot(\text{CH}_2)_3$. In each column, the orbitals descend in the order LUMO, HOMO, and HOMO-1.

The NBO analysis of Ni(ema)^{2-} indicates an electronic population per covalent bond between the nickel and each sulfur atom of 1.95 electrons, with no covalency in the bond between nickel and nitrogen atoms. According to this analysis, 1.71 electrons were found on each nitrogen atom in an sp^2 hybridized orbital, with a strongly stabilized donor-

acceptor interaction between this quasi-lone pair and the corresponding trans Ni-S* antibond, which has 0.296 electrons in the most stable resonance structure. This stabilization is further indicative of a dative bond between the nickel and the nitrogen atoms with fully covalent bonds between the nickel and the sulfur atoms. At the 6-311G(d,p) level of theory, the second nitrogen lone pair on each nitrogen atom was not found; however, two bonds between nitrogen and the adjoining carbon atom were located with electronic populations of 1.99 and 1.78. The small electronic population of the second N-C_{amido} bond is a result of the missing lone pair on the nitrogen atom as part of the delocalized amido system. By using a hybrid basis set at a higher level of theory, the second nitrogen lone pair was resolved.

The NBO analysis of the S-alkylated complexes is also consistent with the DFT computations, for a reversal of major contributing atoms in the NiN₂S₂ core to the ground state electronic structure is also found in these results. In the case of Ni(ema)•(CH₂)₃, the nickel is covalently bonded to each nitrogen with an electronic bond population of 1.93 electrons, whereas each of the sulfurs has a lone pair of 1.72 electrons primarily in a p orbital with a slight amount of s mixing. This dative sulfur interaction has a large energetic stabilization through delocalization of these electrons into the Ni-N* antibond (0.318 electrons). This indicates that following the alkylation of the sulfurs of Ni(ema)²⁻, the formal dative bonds in the NiN₂S₂ core reverse positions. Also interesting to note is that, in contrast to the parent complex Ni(ema)²⁻, two fully covalent bonds exist between the carbon and oxygen on the amido backbone, indicating a significant decrease in delocalization. This result is graphically displayed in Figure V-5.

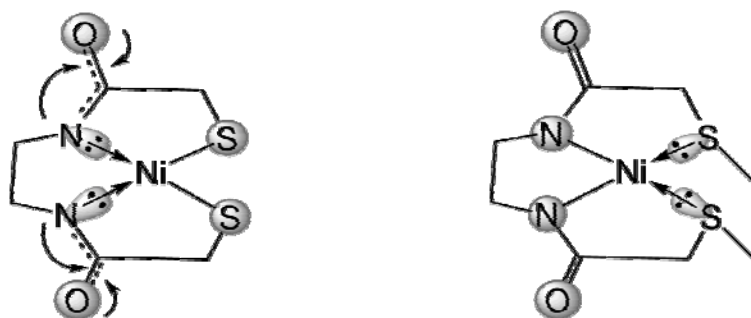


Figure V-5. The principal resonance structures of $\text{Ni}(\text{ema})^{2-}$ and $\text{Ni}(\text{ema})\cdot(\text{CH}_3)_2$ as identified by natural bond orbital (NBO) analysis. Dative bonds are a donation of the lone pair shown on the tail of the arrow into *the corresponding trans Ni-X antibond* ($X = \text{S}, \text{N}$).

Electrostatic Potentials. The electrostatic potential maps of $\text{Ni}(\text{ema})^{2-}$ and the related derivatives are displayed in Figure V-6. The color coding for positive potential (blue) and negative potential (red) of atoms in each compound readily mirrors the change in electronic distribution through the series and the sites of greatest potential reactivity. It should be noted that due to the difference in electrostatic parameters between neutral and dianionic complexes, only a qualitative comparison of the surfaces is possible. The sites of greatest negative potential in the NiN_2S_2 core of $\text{Ni}(\text{ema})^{2-}$ are the lone pairs on the thiolate sulfurs, indicating that reactions at these sites with electrophiles should be facile, as has been found. Furthermore, the negative character of the amido nitrogens is on the

lone pairs on the p_z orbitals; however, this negative character is a great deal less than the corresponding thiolate sulfur character. These results correlate with the dative bond-covalent bond argument presented by the NBO analysis.

Upon oxygenation of one of the thiolate sulfurs, pronounced changes occur as follows. The electron density localized on the thiolate sulfurs in the parent $\text{Ni}(\text{ema})^{2-}$ complex shifts onto the lone pairs of oxygens on the sulfenato group. In addition, upon the incorporation of oxygen into $\text{Ni}(\text{ema})^{2-}$, electron density is withdrawn from the thiolate sulfur cis to the sulfenato sulfur, which is expected to decrease the reactivity of the thiolate sulfur with additional dioxygen or electrophiles. The electron density of the amido nitrogens is also decreased following the S-oxygenation of $\text{Ni}(\text{ema})^{2-}$. This shift is consistent with computational studies by Maroney et al. on neutral NiN_2S_2 complexes.⁹¹ Interestingly, such a withdrawal of electron density from the overall NiN_2S_2 core via S-oxygenation is similar to that experienced from H-bonding to a single thiolate.^{88,89} Both effects serve to deactivate the remaining thiolate sulfur with significant implication for biological systems that use analogous peptidic MN_2S_2 active sites.^{88,90} Finally, the alkylation of the thiolates in $\text{Ni}(\text{ema})^{2-}$ with electrophiles such as CH_3^+ or $(\text{CH}_2)_3^{2+}$, produces pronounced changes in the EP maps as suggested by DFT and NBO calculations. In the thioether or the macrocycle, the negativity of the thiolate sulfurs of $\text{Ni}(\text{ema})^{2-}$ is almost completely quenched, leaving behind only a slight negative character on the lone pair oriented exo to the NiN_2S_2 core. As compared to the modified sulfur atoms in $\text{Ni}(\text{ema})\cdot(\text{Me})_2$ and $\text{Ni}(\text{ema})\cdot(\text{CH}_2)_3$, the amido nitrogen atoms are the sites

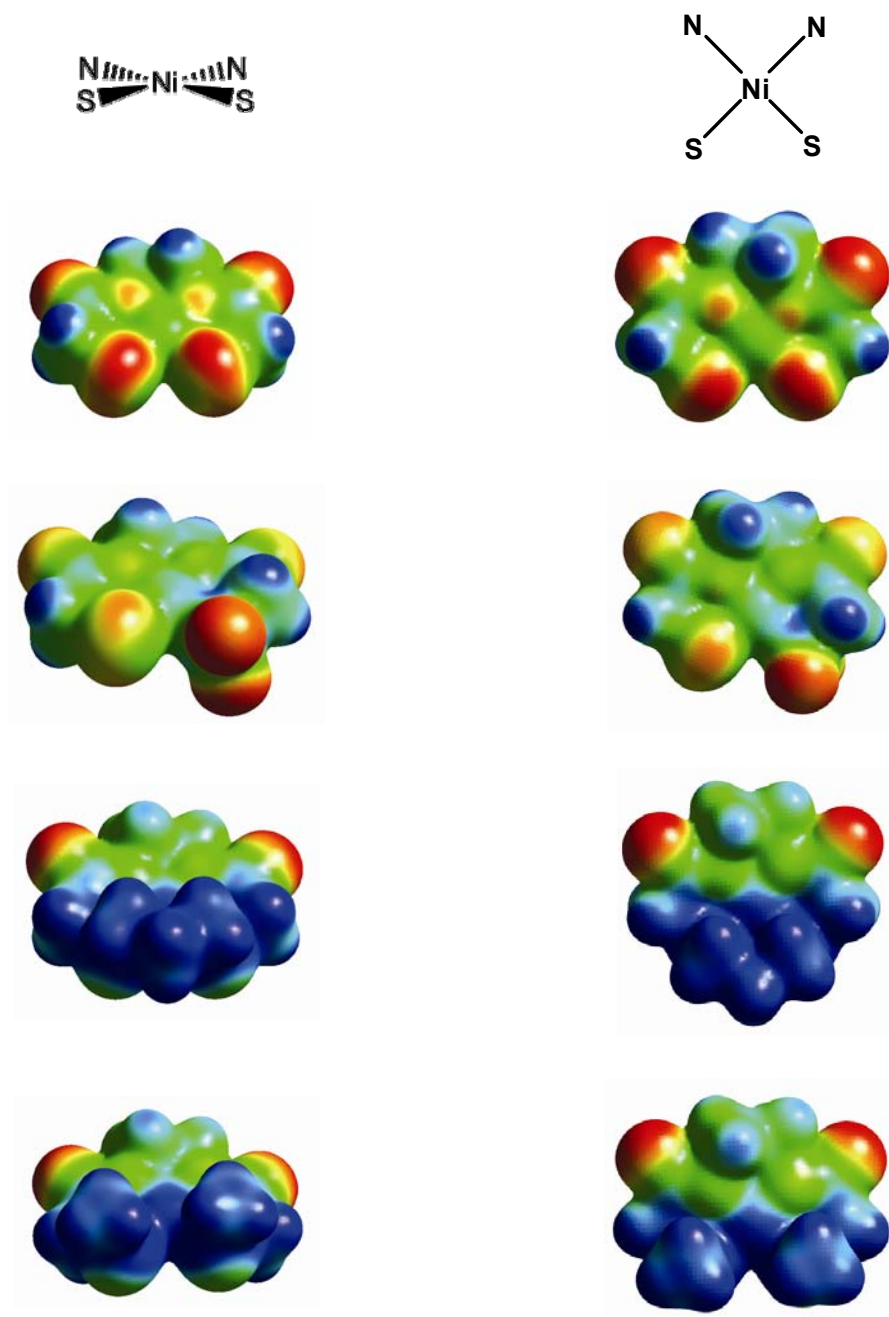


Figure V-6. In order of descent: Electrostatic potentials of $\text{Ni}(\text{ema})^{2-}$, $[\text{Ni}(\text{ema})\cdot\text{O}_2]^{2-}$, $\text{Ni}(\text{ema})\cdot(\text{CH}_2)_3$ and $\text{Ni}(\text{ema})\cdot(\text{Me})_2$. The range was taken from 1.00 (the most electropositive region, dark blue) to 0.33 (the most electronegative region, bright red). Views are along bisector of S-Ni-S angle and from top as noted.

of greater negativity, owing to the lone pair and formal negative charge on the nitrogen. It is important to note that in the parent complex $\text{Ni}(\text{ema})^{2-}$ and all of the derivatized complexes presented herein, use of the Mulliken charges or the atomic charges as the basis for the electrostatic potentials indicates little to no negative character on the nickel center.

Conclusions

The isolation of $[\text{Ni}(\text{ema})\cdot\text{O}_2]^{2-}$ and $\text{Ni}(\text{ema})\cdot(\text{CH}_2)_3$ demonstrates that thiolate S-based reactivity of the dianionic NiN_2S_2 complexes based on carboxamido nitrogen donor scaffolds is as extensive as that previously established for neutral analogues with primary and secondary amine frameworks. The $[\text{Ni}(\text{ema})\cdot\text{O}_2]^{2-}$ complex, reported earlier by Hegg, et al.,⁵² and isolated here for full characterization is the first dianionic $\text{NiN}_2\text{S}_{\text{thiolate}}\text{S}_{\text{sulfinato}}$ derived from controlled reactivity of $\text{NiN}_2\text{S}_2^{2-}$ with O_2 to form a sulfinato complex analogous to neutral NiN_2S_2 complexes. In this study we find a solid state reaction of crystalline $[\text{Et}_4\text{N}]_2[\text{Ni}(\text{ema})]$ is the most efficient mode of preparation. The unambiguous characterization of $[\text{Et}_4\text{N}]_2[\text{Ni}(\text{ema})\cdot\text{O}_2]$ via x-ray crystallography is significant in that the conventional expectation of outer sphere oxidation producing a Ni^{III} or ligand oxidation with degradation can be avoided under the correct synthetic approach.

It is of consequence that mild conditions involving dioxygen at ambient pressures lead to S-oxygenates of both neutral and dianionic NiN_2S_2 complexes. *Qualitatively the latter are significantly more reactive.* Maroney and co-workers have noted an increased reactivity with anionic NiNS_2 systems as well.⁹¹ As stated by Shearer et. al and

Grappnerhaus and et. al., a mixed amido/amine complex should show reactivity between the neutral NiN_2S_2 and the anionic $\text{NiN}_2\text{S}_2^{2-}$.^{92,88} This has been experimentally established by Shearer and coworkers who demonstrated that a mixed carboxamido/amine complex is more stable in the presence of O_2 as compared to an analogous dicarboxamido species.⁹² Nevertheless, rates of reaction with O_2 appear to be much slower, even in the dianionic complexes, than rates responsible for the turnover frequency of NiSOD (reported as $k_{\text{cat}} = 10^9 \text{M}^{-1}\text{s}^{-1}$ per Ni).⁹¹ This difference is a palpable answer to the lack of destruction of the enzyme active site as deleterious products, arise; however a definitive answer awaits further study.

The cyclic voltammogram of $[\text{Ni}(\text{ema})\cdot\text{O}_2]^{2-}$ shows that sulf-oxy modifications of dithiolates fine tune the $\text{Ni}^{\text{III/II}}$ redox couple of dianionic complexes. This result is of significance to enzymatic systems which use the Cys-Ser-Cys peptide backbone as an N_2S_2 binding site, post-translationally modified by sulf-oxygenation, as found in cobalt and iron nitrile hydratase. It has been proposed that the sulfoxxygenated groups of the N_2S_2 peptidic ligand are required to regulate the Lewis acidity of the metal for the conversion of metal-bound nitriles to amines.⁹⁰

DFT studies and derived parameters from NBO and electrostatic potential analysis report on the electron distribution in the dianionic NiN_2S_2 complexes and neutral derivatives derived from alkylation. Despite the formal negative charge on each N and S donor atom in $\text{Ni}(\text{ema})^{2-}$, reactivity with electrophiles is at sulfur. Once the active lone pairs of the thiolato sulfurs are quenched by covalent bond formation with carbon or oxygen, the negative charge in the carboxamido frame becomes localized on nitrogen,

creating, in the NBO analysis, covalent bond character in the N-Ni bond with the dative bond character shifting into the thioether S to Ni bond. The electrostatic potential maps show the polar character of the carboxyamido groups remains in the neutral derivatives as sites for H-bonding, explaining the solubility characteristics in H-bonding solvents. Nevertheless, further reactivity with electrophiles is lost, yielding a class of dianionic tetradentate N_2S_2 ligands and stable, tractable neutral NiN_2S_2 complexes for exploration of metal-based redox activity and reactivity.

CHAPTER VI

SYNTHESIS AND CHARACTERIZATION OF A SERIES OF $\text{CuN}_2\text{S}_2^{2-}$

COMPLEXES AND STABILIZATION THROUGH

A RESIN-BOUND Cu^{II} ANALOGUE

The biomimetic study of enzyme active sites and metalloproteins encompasses a vast range of synthetic analogues including synthetic organic ligands, peptides as ligands, and hybrid molecules composed of both. As an example of the latter, Burrows and co-workers recently produced a hybrid complex of peptides and the salen ligand, which was shown to readily bind to Ni^{II} , Figure VI-1.⁹³ Existing biomimetic libraries include small coordination complexes comprised of minimal donor sites to the biometal,^{83,84,85} larger ligands designed to include second coordination sphere effects, and peptides that more closely mirror the protein.^{49,92,94} When applied sequentially, such a buildup of complexity can help develop understanding of structural features that lead to spectroscopic matches to the native active sites.

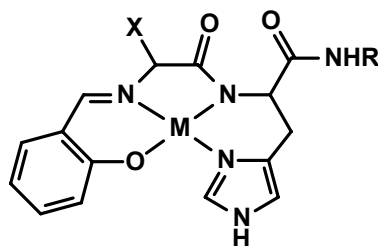


Figure VI-1: Salen-peptide complex by Burrows *et al.*⁹³

Our specific interests in this chapter are in biologically active copper that is bound to sulfur donors from cysteine residues. While most metal-sulfur interactions in biology result from strictly cysteinyl or methionine residues, there have been several discoveries of S-containing binding sites that also utilize the peptide backbone; i.e. the carboxyamido nitrogens, such as the Cys-Ser-Cys motif in nitrile hydratase which chelates Fe or Co in N_2S_2 binding pockets.⁴¹ Other prime examples are the Cys-Gly-Cys N_2S_2 which binds nickel in acetyl coA synthase, or the His-Cys-XXX-Cys arrangement in nickel-containing superoxide dismutase.^{1,42,443} While there are no known copper analogues, i.e. $Cu(Cys-X-Cys)^{2-}$, a number of CuN_2SS' coordination spheres have been reported to occur in nature. These include the redox active $Cu^{II}N_2SS'$ sites of plastocyanin⁹⁵ (Figure VI-2), cucumber basic blue⁹⁶, and nitrite reductase⁹⁷. These $His_2CysMet$ active sites, commonly referred to as Blue Copper Proteins or Type I Cu sites, can be found in electron-transfer proteins (cupredoxins) as well where the $Cu^{II/I}$ shuttle occurs rapidly at very positive redox potentials resulting in only minimal structural changes.⁹⁸

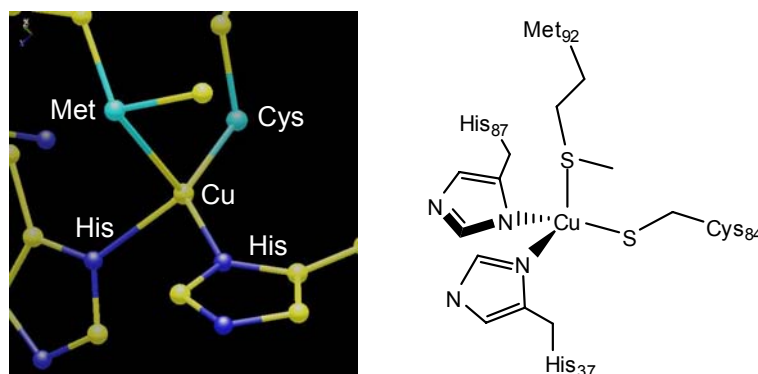


Figure VI-2. Active Site of plastocyanin.

These Blue Copper Proteins utilize the enzyme superstructure to fine tune the geometry of the active site to accommodate both oxidation states in the $\text{Cu}^{\text{II/I}}$ redox couple. Crystal field theory tells us that Cu^{I} complexes favor a tetrahedral geometry while Cu^{II} complexes prefer square planar. The geometry found in Type 1 copper sites is a hybrid of the two, thus allowing rapid redox processes to occur while maintaining activity. For synthetic complexes, such as CuN_2S_2 , developing thiolate containing ligands capable of supporting both copper redox states is difficult as autoreduction of $\text{Cu}^{\text{II}}\text{-S}$ is often observed. This process, $2\text{Cu}^{\text{II}} + 2\text{RS}^- \rightarrow 2\text{Cu}^{\text{I}} + \text{RSSR}$, followed by uptake of the Cu^{I} ion by other $\text{Cu}^{\text{II}}\text{N}_2\text{S}_2$ complexes results in multimetallic, aggregated species and has hindered isolation of many monomeric Cu^{II} -thiolate complexes. One example of the mutual attraction of Cu^{I} and thiolate sulfurs, is the adamantane structure, shown in Figure VI-3, resulting from the addition of $\text{Cu}(\text{acac})_2$ to the $\text{bme}^*\text{-daco}$ ligand to produce $\text{Cu}(\text{bme}^*\text{-daco})$ followed by the addition of CuCl . The complex shows that any Cu^{I} is scavenged by the $\text{Cu}(\text{bme}^*\text{-daco})$ complex resulting in a central Cu_4S_4 cage common for Cu^{I} .¹⁰¹ Several examples of these aggregate complexes have been reported as they are the thermodynamically favored product from the interaction of Cu^{I} with metal bound thiolate sulfurs.^{44,98, 99}

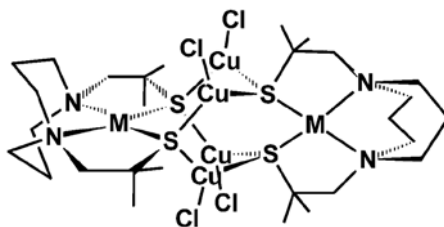


Figure VI-3. Representation of Cu_5S_4 adamantane.

The active sites of Type 1 copper containing enzymes are composed of ligand sets capable of minor changes in geometry. Solomon recently compared the distortions of the His₂CysMet ligand set found in plastocyanin, a nitrite reductase and cucumber blue protein.¹⁰⁰ In each of these enzymes the amino acids used as ligands to the Cu are separated in the polypeptide chain, resulting in a ligand set that can vary in geometry. As shown in Figure VI-4, the S_{Met}-Cu-S_{Cys} angles are different in the three metalloprotein sites. Although these enzymes all possess the same donor set, these geometric changes produce large differences in the electronic structure of Cu^{II} resulting in visible color differences between these enzymes.¹⁰⁰ Solomon's work is a prime example of how the physical and spectral properties of Cu complexes are affected by the geometric and coordination environment.

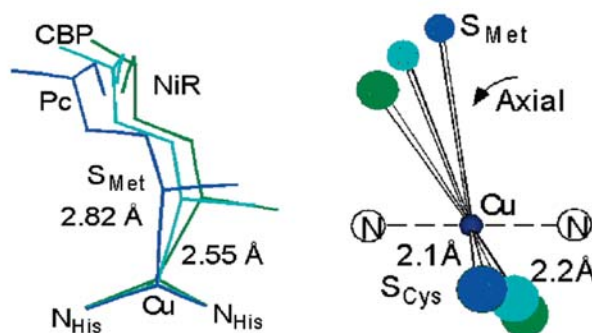


Figure VI-4. A comparison of tetragonal distortion in the Cu^{II}N₂SS' active sites of plastocyanin (Pc), cucumber blue protein (CBP) and nitrite reductase (NiR) showing positions of the S_{Cys} and S_{Met} compared to the N-Cu-N plane.¹⁰⁰

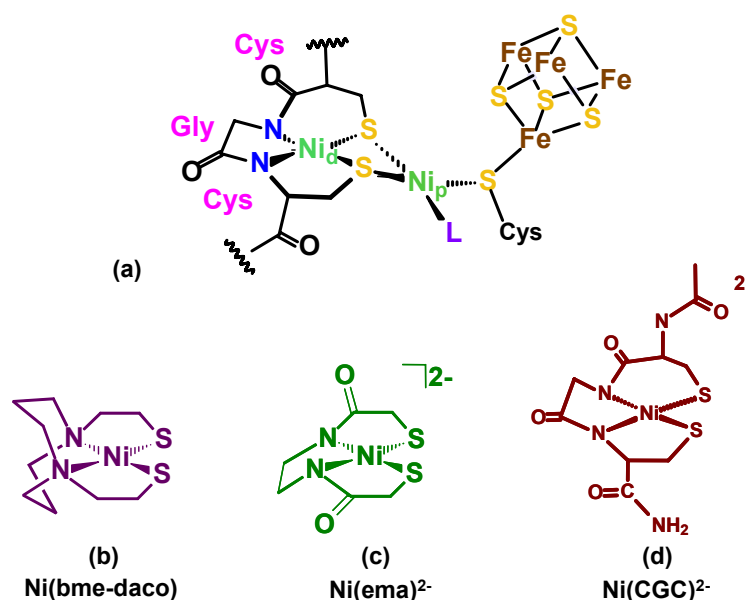


Figure VI-5. Representative drawing of (a) the active site of acetyl coA Synthase and (b-d) a few examples of small molecule models for the Ni_d site acetyl coA Synthase.^{1,49,50, 101}

Biomimetic studies of enzyme active sites such as acetyl coA synthase (ACS), nitrile hydratase, and Ni(SOD) have produced a large number of N₂S₂ ligands and their respective nickel complexes.^{84,85,92} A few examples of ACS active site models are shown in Figure VI-5. Inspired by enzyme active sites such as ACS, the potential for thiolate capture of exogenous metal ions was initially addressed through reactivity studies of the neutral NiN₂S₂ complexes.⁴⁴ More recently, dianionic NiN₂S₂ complexes based on amido nitrogen donors have been explored as closer models of Cys-X-Cys active site units.^{44c,50,52} The reactivity of these dianionic NiN₂S₂ complexes, largely parallels that of the neutral NiN₂S₂ complexes.^{52,75,82} Studies utilizing Ni(ema)²⁻ (ema = N, N'-ethylenebis(2-mercaptoacetamide), and Ni(CGCC)²⁻, have established that the two NiN₂S₂²⁻

complexes are equal in S-based donor ability as defined by position of the infrared $\nu(\text{CO})$ bands arising from the $\text{W}(\text{CO})_4$ derivatives of each.⁷⁵ Additionally, *in silico* studies of $\text{Ni}(\text{ema})^{2-}$ reported in Chapter V, have shown that thiolate alkylation redistributes electron density from the thiolate sulfurs to the amido backbone. Furthermore, thiolate modifications of $\text{Ni}(\text{ema})^{2-}$ have provided insight into the spectroscopic and electrochemical consequences of S-alkylation and oxygenation. As the synthesis, characterization, and reactivity of the $\text{NiN}_2\text{S}_2^{2-}$ complexes is well established, it was my goal, in collaboration with Dr. David Rockcliffe and assisted by his undergraduate student Boram Lee, to prepare the analogous Cu^{II} complexes. The affinity for Cu^{II} to ligate in a square planar arrangement was used to produce the complexes shown in Chart VI-1 as models of $\text{CuN}_2\text{SS}'$ metalloenzymes. While no biological CuN_2S_2 active sites utilizing the Cys-X-Cys motif are yet known, the fact that copper frequently substitutes for Ni has been shown in synthetic complexes as well as enzymes such as acetyl coA synthase.^{2,102} Therefore, transmetallation studies of Cu and Ni complexes bound to resin-beads are of interest.

Beginning in 1978, when the crystal structure of plastocyanin was first determined, a number of studies have been directed at modeling Type 1 copper sites.^{955a} Selected examples of small molecule models produced to mimic the $\text{CuN}_2\text{SS}'$ containing active sites are shown in Figure VI-6. Schugar *et al.* reported Complex **1** which was the first stable Cu^{II} complex to incorporate “biological” cysteine ligation.¹⁰³ The ligand backbone, composed of N,N' -ethylenebis(L-cysteine)₂, chelates the Cu^{II} in roughly square planar geometry. Complexes **2** and **3** are additional examples of neutral CuN_2S_2

complexes produced by chelation of a Cu^{II} ion by amine nitrogens and thiolate/thioether sulfur donors as models of $\text{CuN}_2\text{SS}'$ sites found in nature.^{99,104} Finally, Complex **4** reported by Krüger and co-workers is the first and only dianionic square-planar $\text{CuN}_2\text{S}_2^{2-}$ complex to our knowledge that incorporates amido nitrogen donors into the ligand set.¹⁰⁵ As a number of enzyme active sites utilize amido nitrogens from the amino acid backbone to chelate metal ion centers, the integration of carboxamido donors into the ligand set represents an additional step toward structurally mimicking enzyme active sites.^{1,41,42} A number of other CuN_2S_2 complexes have been reported as components of clusters bridged by Cu^{I} ions.^{99,99,106}

Each $\text{CuN}_2\text{S}_2^{x-}$ complex reported has provided insight into the unique spectroscopy of Cu^{II} systems and can give details about the ligand set's effects. For example, the respective electronic spectra of **1-4** display intense ($\epsilon_{\text{max}} \sim 5000 \text{ M}^{-1} \text{ cm}^{-1}$) absorptions around 400-600 nm attributed to a $\text{RS} \rightarrow \text{Cu}$ transition, consistent with Type I copper sites.^{98,99,100,105} Additionally, the A_{\parallel} hyperfine coupling values, serve as a reflection of the interaction of the unpaired copper electron with the copper nucleus. As less interaction occurs the A_{\parallel} value decreases, which can be shown in comparing **1** ($A_{\parallel} = 182 \times 10^{-4} \text{ cm}^{-1}$) with **4** ($A_{\parallel} = 195 \times 10^{-4} \text{ cm}^{-1}$) to type 1 Cu sites with $A_{\parallel} \sim 60 \times 10^{-4} \text{ cm}^{-1}$.^{98,103,105} The geometric differences derived from the ligand set of the synthetic analogues, largely square planar, compared to the native $\text{CuN}_2\text{SS}'$ enzymes, trigonal pyramidal to distorted tetrahedral, can play a large role in effecting these interactions.^{100,105}

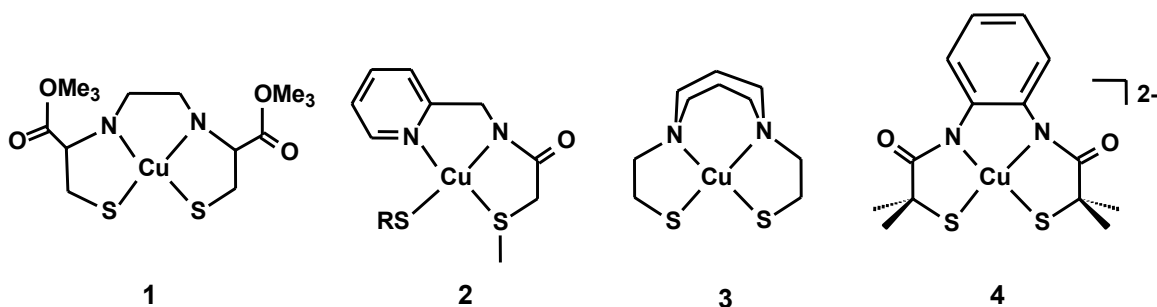
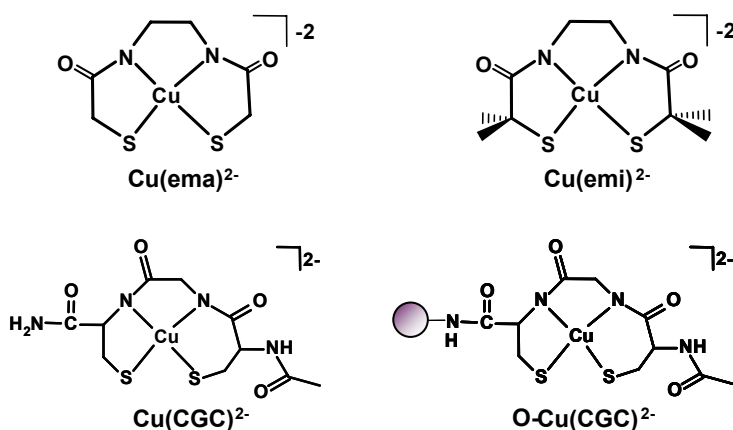


Figure VI-6. Examples of biomimetic $\text{CuN}_2\text{S}_2^{x-}$ complexes.^{99,103,104,105}

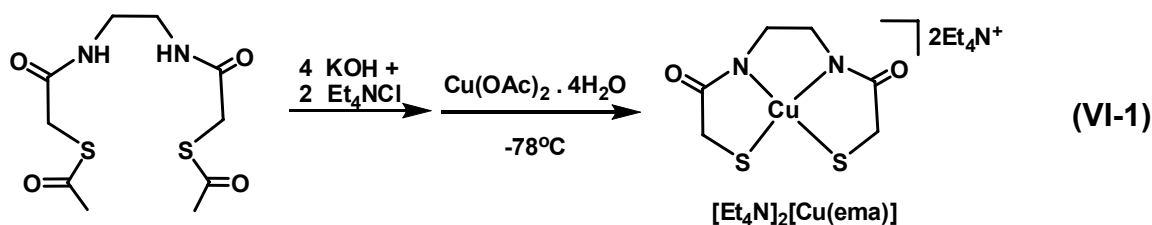
Herein the tetranionic ema and emi ligands (emi = N,N'-ethylenebis(2-(benzylthio)isobutyramide)), first reported by Holm and co-workers as the nickel derivatives, will be utilized to produce $\text{Cu}(\text{ema})^{2-}$ and $\text{Cu}(\text{emi})^{2-}$.⁵⁰ The characterization and properties of these Cu^{II} complexes will be compared to the previously reported complex 4.¹⁰⁵ Additionally, the spectroscopy, electrochemistry and reactivity of the series of $\text{CuN}_2\text{S}_2^{2-}$ complexes will be compared to the Ni analogues, $\text{Ni}(\text{ema})^{2-}$ and $\text{Ni}(\text{emi})^{2-}$.⁵⁰ Further studies have led to the use of peptides as ligands, both in solution and anchored to polystyrene-polyethylene glycol resin beads.

Chart VI-1



Synthesis and Characterization of $[\text{Et}_4\text{N}]_2[\text{Cu}(\text{ema})]$ and $[\text{Et}_4\text{N}]_2[\text{Cu}(\text{emi})]$

Synthesis of $[\text{Et}_4\text{N}]_2[\text{Cu}(\text{ema})]$. The deep purple solid, $[\text{Et}_4\text{N}]_2[\text{Cu}(\text{ema})]$, is obtained from the slow addition of a methanol solution of bright-blue $\text{Cu}^{\text{II}}(\text{OAc})_2 \cdot 4\text{H}_2\text{O}$ to a light-yellow deprotonated and thiolate deprotected ema ligand in a methanolic solution, as shown in Equation VI-1. The reaction is carried out at -78°C (dry-ice/acetone) and is complete within 15 minutes. Addition of Et_2O to the resulting purple solution produced a purple solid which was washed with Et_2O to give 83% yield. Low temperature and short reaction times are necessary to avoid complete conversion of the purple solution to an uncharacterized, insoluble red-brown precipitate presumed to be an aggregate species produced by autoreduction.¹⁰⁶ This reaction may be performed in the coordinating solvent DMF to avoid this insoluble product, however DMF results in lower yields (54% yield). The air-sensitive $\text{Cu}(\text{ema})^{2-}$ complex as its Et_4N^+ salt is soluble in DMF and soluble in CH_3CN upon heating to yield intensely, deep red solutions.



Because of the gem-dimethyl groups on the carbons neighboring the reactive thiolates, the emi ligand was employed to hinder aggregative decomposition as observed for $\text{Cu}(\text{ema})^{2-}$. Additionally, the gem-dimethyl groups will typically impart greater solubility to the complex. A red solution of $[\text{Et}_4\text{N}]_2[\text{Cu}(\text{emi})]$ was produced at room

temperature from drop wise addition of $\text{Cu}(\text{OAc})_2 \cdot 4\text{H}_2\text{O}$ in methanol to a basic methanol solution of the emi ligand. A mauve solid (74% yield) was obtained following precipitation with ether. The $[\text{Et}_4\text{N}]_2[\text{Cu}(\text{emi})]$ complex is soluble in DMF, CH_3CN , EtOH, and MeOH. It is most stable in coordinating solvents, such as DMF, and will degrade after 6h in MeOH to an uncharacterized brown, insoluble solid.

Molecular Structure of $[\text{Et}_4\text{N}]_2[\text{Cu}(\text{emi})]$. The thermal ellipsoid plot of $[\text{Et}_4\text{N}]_2[\text{Cu}(\text{emi})]$ is shown in Figure VI-7. Crystallographic data and full structural reports are given in Appendix B. An imposed mirror plane perpendicular to the CuN_2S_2 plane bisects the N-C-C-N linker backbone. Parameters of interest are the S-N-S angle, which is slightly wider than that reported for the $[\text{Et}_4\text{N}]_2[\text{Cu}(\text{phmi})]$ complex and nearly 5° wider than that of $[\text{Et}_4\text{N}]_2[\text{Ni}(\text{ema})]$.^{50,105} The wider S-Cu-S angle of $[\text{Et}_4\text{N}]_2[\text{Cu}(\text{emi})]$ results in compressed S(1)-Cu-N(1) angles, as shown in Table VI-1.

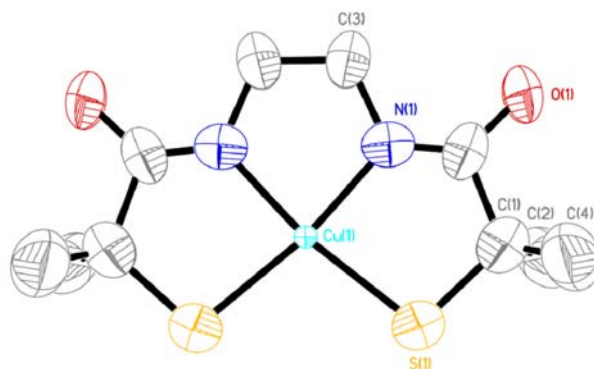


Figure VI-7. Thermal ellipsoid plot of $[\text{Et}_4\text{N}]_2[\text{Cu}(\text{emi})]$ showing 50% probability and the atom labeling scheme. The Et_4N^+ counterions are not shown.

Table VI-1. Selected bond distances (Å) and angles (°) for [Et₄N]₂[Cu(emi)] compared to [Et₄N]₂[Cu(phmi)] and [Et₄N]₂[Ni(ema)].^{50,105}

	[Et ₄ N] ₂ [Cu(emi)]	[Et ₄ N] ₂ [Cu(phmi)]	[Et ₄ N] ₂ [Ni(ema)]
Cu-S(1)	2.233 (3)	2.2381 (8)	2.170 (1)
Cu-N(1)	1.940 (8)	1.963 (2)	1.857 (3)
S(1)-Cu-S(2)	102.32 (15)	100.27 (3)	97.44 (8)
N(1)-Cu-N(2)	85.2 (5)	83.97 (9)	85.6 (2)
S(1)-Cu-N(1)	86.2 (3)	87.67(7)	88.4 (1)

Mass Spectrometry. The air-sensitive dianionic Cu(ema)²⁻ and Cu(emi)²⁻ complexes were characterized using ⁻ESI-MS, as shown in Figure VI-8. The ⁻ESI-MS spectrum revealed the parent molecular ions of Cu(ema)²⁻ and Cu(emi)²⁻ exist as the oxidized Cu^{III} species [Cu^{III}N₂S₂]⁻ at 266.9275 and 322.9899 m/z (Calculated: 266.9423 and 323.0490 m/z). Cooks and co-workers reported similar copper^{II/III} oxidation of copper (II) di-Bu dithiocarbamate induced by the MS experiment as well.¹⁰⁷ As first shown by Krüger with **4** and as evidenced by the CV data discussed below, the Cu^{III} state is easily accessible and stable for CuN₂S₂²⁻ complexes.¹⁰⁵ The experimental isotopic bundles of Cu(ema)²⁻ and Cu(emi)²⁻ clearly show the presence of Cu, which has two naturally occurring isotopes Cu-63 (69%) and Cu-65 (31%), and agree with calculated isotopic envelope. It is also important to note that a Tandem ESI-MS experiment with [Et₄N]₂[Cu(ema)] in CH₃CN:CH₃OH (50:50) showed MeOH coordination as [M+MeOH]⁻. Subsequent decomposition products were observed from deprotonation of the CuN₂S₂²⁻ complex and copper ion ejection, as evidenced by molecular ions

corresponding to ligand degradation products lacking the metal ion. However, no aggregative species were observed in the mass spectrometry experiment.

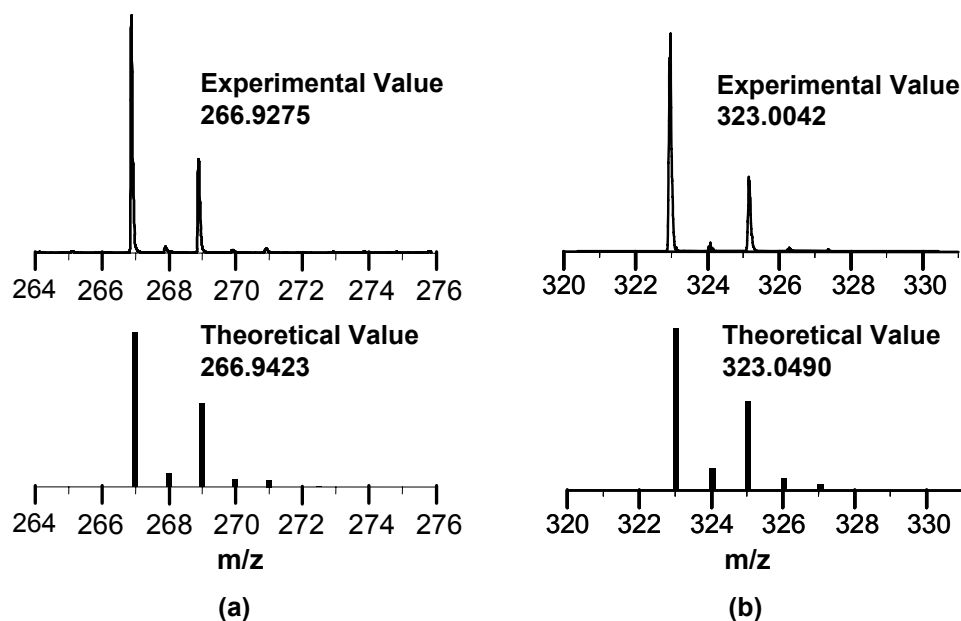


Figure VI-8. $^-$ ESI-MS spectra and theoretical isotopic bundles of (a) $\text{Cu}(\text{ema})^{2-}$ and (b) $\text{Cu}(\text{emi})^{2-}$.

Electronic Absorption Spectroscopy. The electronic absorbance spectrum of $\text{Cu}(\text{ema})^{2-}$ in CH_3CN , displays three intense bands attributed to ligand to metal charge transfer (LMCT) transitions observed at 233, 293, and a shoulder at 320 nm, Table VI-2.^{100,105} A $\text{S} \rightarrow \text{Cu}^{\text{II}}$ transition is observed at 407 nm as well.^{103,103} The absorbance spectrum of the $\text{Cu}(\text{emi})^{2-}$ complex is nearly identical with strong LMCT bands at 231, 294, and 322sh nm and a d-d transition at 367 nm. The intensity and position of these bands is indicative of a Cu^{II} ion in an N_2S_2 coordination sphere, such as those shown in

Figure VI-6.^{99,100,103,104,105} For example, the square planar **4** has LMCT bands at 230, 247, 255sh, 285sh, 294, and 310sh nm with ϵ in the range of 11,000 – 25,800 (M^{-1} , cm^{-1}).¹⁰⁵ A characteristic intense d-d transition is observed around 500 nm as well. The $CuN_2S_2^{2-}$ absorption spectra are slightly blue shifted compared to their nickel analogues, $Ni(ema)^{2-}$ and $Ni(emi)^{2-}$ ($\lambda_{max} = 261, 437, \text{ and } 552 \text{ nm}$ and $\lambda_{max} = 261, 430, \text{ and } 534 \text{ nm}$, respectively).⁵⁰ The intensities of the d-d transitions for these nickel analogues are also an order of magnitude lower than that of $Cu(ema)^{2-}$ and $Cu(emi)^{2-}$ which has been noted for other synthetic Cu^{II} complexes in an N_2S_2 coordination sphere.¹⁰⁰

Table VI-2: Summary of Electronic Absorption Spectra for $Cu(ema)^{2-}$, $Cu(emi)^{2-}$, $Cu(CGC)^{2-}$ in CH_3CN solvent.

	UV-vis λ_{max} (nm) (ϵ , M^{-1} , cm^{-1})			
$Cu(ema)^{2-}$	233 (24 880)	293 (28 700)	320sh(22 100)	407 (1740)
$Cu(emi)^{2-}$	231 (23 799)	294 (25 250)	319sh(22 340)	413 (2120)
$Cu(CGC)^{2-}$	232 (25 185)	294 (18 962)	322sh(13 450)	367 (930)

Electrochemical Measurements. The cyclic voltammogram of $Cu(ema)^{2-}$ recorded in DMF solvent has an irreversible oxidation at event at -1.202 V vs. Fc/Fc^+ and is presumed to be $Cu^{III/II}$. No evidence of the corresponding reduction event is observed when scanning in either the negative or positive direction at scan rates of 100 - 200 mV/s with varying starting points. In contrast, the CV of $Cu(emi)^{2-}$ in DMF reveals a fully reversible oxidation with $E_{1/2} = -1.40 \text{ V vs. } Fc/Fc^+$, Figure VI-9. Krüger and co-workers have reported that the CV of **4** displays a reversible $Cu^{III/II}$ oxidation event at -1.16 V vs.

Fc/Fc^+ in CH_3CN .¹⁰⁵ Although Cu^{III} is rare, access to the high valent cuprate state can be attributed to stabilization afforded by the highly polarizable carboxamido nitrogens from the ligand set.^{105,108} As such, this stability allowed for isolation and structural characterization of oxidized **4**.¹⁰⁵ No other redox events were observed in the solvent window for $\text{Cu}(\text{ema})^{2-}$ and $\text{Cu}(\text{emi})^{2-}$ consistent with the report for **4** as well. The shift of the $\text{Cu}^{\text{III/II}}$ couple to more negative potentials from the reversible $\text{Ni}^{\text{III/II}}$ couple for $\text{Ni}(\text{ema})^{2-}$ ($E_{1/2} = -0.836 \text{ V vs. Fc}/\text{Fc}^+$) is consistent with the greater effective nuclear charge of Cu^{II} over Ni^{II} .

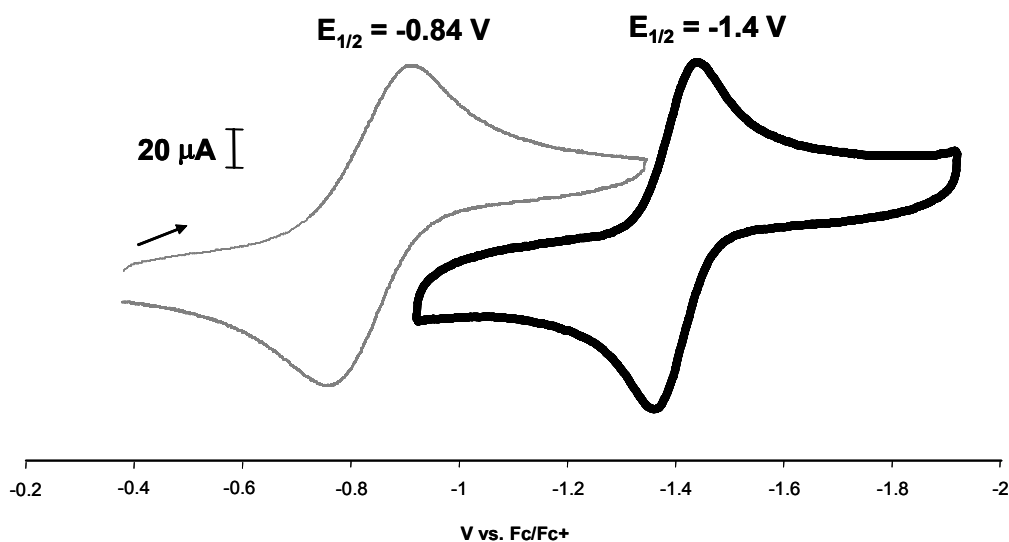


Figure VI-9: CV overlay of the $\text{Ni}^{\text{III/II}}$ couple of $[\text{Et}_4\text{N}]_2[\text{Ni}(\text{ema})]$ (3.7 mM) in grey and the $\text{Cu}^{\text{III/II}}$ couple of $[\text{Et}_4\text{N}]_2[\text{Cu}(\text{emi})]$ (2.3 mM) in black using DMF solvent at a scan rate of 100 mV/s using a Ag/AgNO_3 reference electrode, 0.1 M $[\text{nBu}_4\text{N}][\text{BF}_4]$ electrolyte, and a glassy-carbon electrode.

Electron Paramagnetic Resonance Spectroscopy. As the ground state of Cu^{II} has one unpaired electron producing a paramagnetic copper center, valuable data about the Cu^{II} coordination environment may be obtained through spectroscopic characterization using Electron Paramagnetic Resonance (EPR) spectroscopy. The X-Band EPR spectra of $\text{Cu}(\text{ema})^{2-}$ and $\text{Cu}(\text{emi})^{2-}$ in DMF at 9 K are shown in Figure VI-10. These spectra show an axial signal with $g_{\parallel} > g_{\perp}$, indicative of a paramagnetic Cu^{II} .^{100,109} The theoretical spectrum of a square planar copper(II) complex with an unpaired electron should exhibit 4 hyperfine splitting lines as the nuclear spin of Cu^{II} ($I=3/2$) couples with the electron spin ($2I+1 = 4$ lines). Simulations of $\text{Cu}(\text{ema})^{2-}$ and $\text{Cu}(\text{emi})^{2-}$ show this splitting, although there is some overlap of the g_{\parallel} signal with that of the g_{\perp} . The N_2S_2 coordination environment can be pinpointed by comparing the g_{\parallel} values to those of other CuN_2S_2 complexes.¹⁰⁹ In the presence of S-donation the g_{\parallel} EPR values are significantly shifted to lower g-values compared to those of nitrogen and/or oxygen-ligated systems.^{100,105,109} This is attributed to the increased electron donor ability of sulfur as a ligand to the Cu^{II} center. The g_{\parallel} values obtained for $\text{Cu}(\text{ema})^{2-}$ and $\text{Cu}(\text{emi})^{2-}$, 2.17 and 2.22 respectively, lie directly in range of other natural and synthetic $\text{Cu}^{\text{II}}\text{N}_2\text{S}_2$ complexes thus supporting the N_2S_2 coordination as was indicated by UV-Vis studies.^{109,110} Comparison of the g-values for $\text{Cu}(\text{emi})^{2-}$ and $\text{Cu}(\text{ema})^{2-}$ to those reported for complexes **1-3** shows that the dianions have g-values slightly higher than those of neutral complexes indicating that less Cu-S overlap occurs in the dianionic complexes.^{104,103,99} This is consistent with computations on $\text{NiN}_2\text{S}_2^{x-}$ complexes that have shown the ratio of electron density in the Ni-S bond is decreased when carboxamido nitrogens are part of the ligand

set.^{87,89,111} The electrostatic potential maps of neutral NiN_2S_2 complexes qualitatively show that electron density is primarily located on the thiolate sulfurs.^{88,111} However, the electrostatic potential maps of the dianionic NiN_2S_2 complexes show much greater delocalization, attributed to the polarizing amido donors. The same delocalization appears to hold in the dianionic $\text{CuN}_2\text{S}_2^{2-}$ complexes as well.^{88,111}

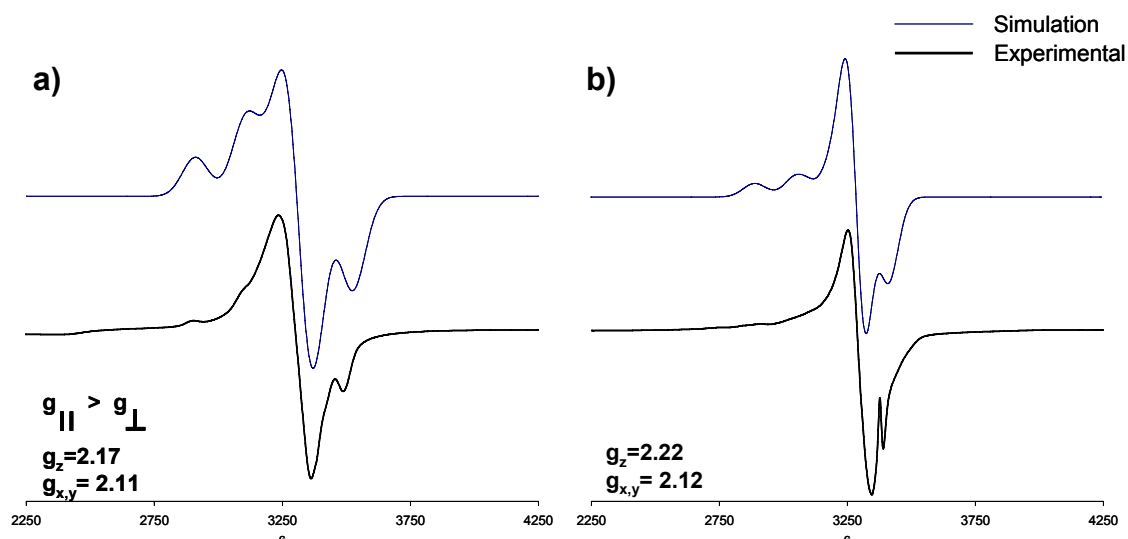
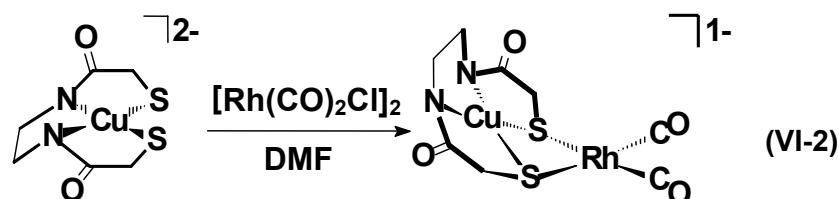


Figure VI-10. Experimental and simulated X-Band EPR spectra of (a) $[\text{Et}_4\text{N}]_2[\text{Cu}(\text{ema})]$ and (b) $[\text{Et}_4\text{N}]_2[\text{Cu}(\text{emi})]$ (2mM in DMF at 9 K, 9.75 GHz).

Thiolate Reactivity of $\text{Cu}(\text{ema})^{2-}$ and $\text{Cu}(\text{emi})^{2-}$ with $\text{Rh}(\text{CO})_2^+$

As the S-based reactivity towards $\text{M}(\text{CO})_x$ for the neutral and dianionic NiN_2S_2 complexes has been thoroughly explored, the reactivity of the CuN_2S_2 was pursued for comparison.^{44,84,111} In a preliminary investigation, adduct formation with a metal carbonyl was chosen as it would provide information as follows: (1) establish thiolate reactivity with $\text{Rh}(\text{CO})^+$ toward exogenous metal binding; and (2) probe the electron

donor ability of the Cu(ema)^{2-} and Cu(emi)^{2-} complexes for comparison to nickel analogues and classical ligands.^{50, 105} The Rh(CO)_2^+ was utilized for these reactions as adduct formation between Ni(ema)^{2-} and Ni(CGC)^{2-} and Rh(CO)_2^+ has been clearly established in solution and for the resin-bound Ni(CGC)^{2-} discussed below.⁷⁵



The $\text{Cu(ema)Rh(CO)}_2^{1-}$ and $\text{Cu(emi)Rh(CO)}_2^{1-}$ complexes were prepared in an analogous manner to their Ni^{II} analogues with the exception of the solvent, Equation VI-2.⁷⁵ These CuRh bimetallic products proved to be stable only in DMF, preventing synthesis and characterization in the better coordinating solvent CH_3CN . As shown in Equation VI-2, addition of a yellow solution of $[\text{Rh(CO)}_2\text{Cl}]_2$ ($\nu(\text{CO}) = 2081, 2005 \text{ cm}^{-1}$ in DMF) to the Cu(ema)^{2-} or Cu(emi)^{2-} resulted in deep red-brown solutions after 20 minutes. The DMF solution infrared spectra are shown in Figure VI-12. The symmetric and asymmetric $\nu(\text{CO})$ stretches of $\text{Cu(ema)Rh(CO)}_2^{1-}$ and $\text{Cu(emi)Rh(CO)}_2^{1-}$ are nearly identical to one another with $\nu(\text{CO}) = 2061$ and 1982 and $\nu(\text{CO}) = 2062$ and 1984 cm^{-1} , respectively. Thus the electron-donating gem-dimethyl groups on the carbons alpha to the thiolate donors in $\text{Cu(emi)Rh(CO)}_2^{1-}$ do not induce a shift to lower wavenumbers as compared to $\text{Cu(ema)Rh(CO)}_2^{1-}$. Nevertheless, the reactivity of the thiolates with $[\text{Rh(CO)}_2\text{Cl}]_2$ parallels that observed for the less electron-donating Ni^{II} analogues with

$\nu(\text{CO})$ values of 2061 and 1996 cm^{-1} for $\text{Ni}(\text{ema})\text{Rh}(\text{CO})_2^{1-}$ as well as 2067 and 1990 cm^{-1} for $\text{Ni}(\text{CGC})\text{Rh}(\text{CO})_2^{1-}$.⁷⁵ It should be noted that the molecular structure obtained for $\text{Ni}(\text{ema})\text{Rh}(\text{CO})_2^{1-}$ was not the expected bimetallic complex, such as that shown as the product in equation VI-2. It was, rather, a tetrametallic complex with two $\text{Ni}(\text{ema})^{2-}$ complexes bridging two $\text{Rh}(\text{CO})_2$ moieties, Figure VI-11. This pseudo-paddlewheel reflects a minimization of repulsive interactions between the highly negative electron density of $\text{Ni}(\text{ema})^{2-}$ and the electron rich xy-plane of the Rh^I acceptor which would exist in the later form if the complex were found as the bimetallic species.¹¹² The molecular structures of the CuRh complexes await crystallization.

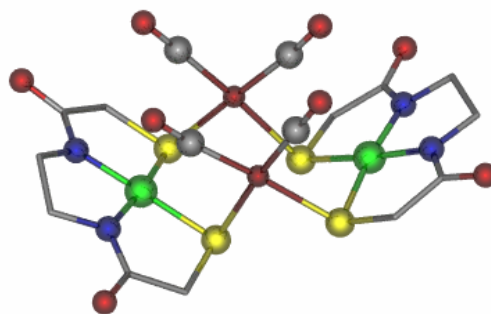


Figure VI-11. Molecular structure of $[\text{Et}_4\text{N}]_2[\text{Ni}(\text{ema})\text{Rh}(\text{CO})_2]_2$ with cations omitted.

The electronic absorption spectra of $\text{Cu}(\text{ema})\text{Rh}(\text{CO})_2^{1-}$ ($\lambda_{\text{max}}(\epsilon)$ (in DMF) = 270 (27,610) and 330 (18,610) nm) and $\text{Cu}(\text{emi})\text{Rh}(\text{CO})_2^{1-}$ ($\lambda_{\text{max}}(\epsilon)$ (DMF) = 289 (25,260) and 390 (18,540) nm) are blue shifted (~ 20 nm) compared to $\text{Cu}(\text{ema})^{2-}$ and $\text{Cu}(\text{emi})^{2-}$ in DMF, which is consistent with thiol-based derivatizations of NiN_2S_2 analogues.^{75, 112}

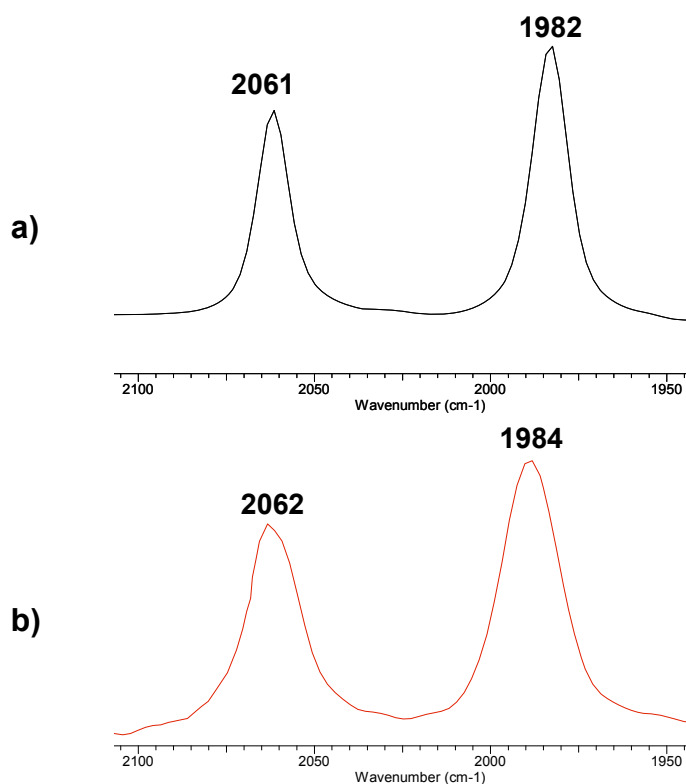


Figure VI-12: FTIR spectra (DMF) of (a) $[\text{Et}_4\text{N}][\text{Cu}(\text{ema})\text{Rh}(\text{CO})_2]$ and (b) $[\text{Et}_4\text{N}][\text{Cu}(\text{emi})\text{Rh}(\text{CO})_2]$.

Synthesis and Characterization of $[\text{K}]_2[\text{Cu}(\text{CGC})]$

The $\text{CuN}_2\text{S}_2^{2-}$ complexes discussed thus far serve as preliminary models of Cu metalloenzymes establishing the spectroscopy and reactivity of these dianionic paramagnetic square-planar systems. As the tripeptide CGC^{4-} has been thoroughly studied as a ligand to Ni^{II} , the reactivity with copper was investigated.

The $\text{Cu}(\text{CGC})^{2-}$ complex was produced in an identical manner to the $\text{Ni}(\text{CGC})^{2-}$ complex reported in Chapter III. The addition of $\text{Cu}(\text{OAc})_2 \cdot 4\text{H}_2\text{O}$ to a basic solution of

H₄CGC in DMF produced a purple solution. A lilac purple solid was obtained by Et₂O precipitation. The Cu(CGC)²⁻ product was characterized by ⁻ESI-MS which showed the molecular ion at 380.9721 m/z as the Cu^{III} product (Calculated = 380.9752 m/z). The EPR spectrum shows that in frozen DMF the complex contains a paramagnetic Cu^{II} with $g_{\parallel} = 2.185$ and $g_{\perp} = 2.105$, Figure VI-13. This highly air-sensitive Cu^{II} metalloprotein is soluble in DMF and slightly soluble in CH₃CN but, as observed with Cu(ema)²⁻, decomposes in MeOH. The absorption spectrum of Cu(CGC)²⁻ differs from Cu(ema)²⁻ and Cu(emi)²⁻ only by a slight blue shift in the intense d-d band at λ_{\max} (ϵ , M⁻¹, cm⁻¹) 367 (930) nm, Table VI-2. The ligand to metal charge transfer bands are observed at λ_{\max} (ϵ , M⁻¹, cm⁻¹) 232 (25,185), 294 (18,962), and 322 sh(13,450) nm. These electronic spectral features show little variation from other CuN₂S₂²⁻ complexes.^{99,103,104} This is consistent with the Ni^{II} analogues, where the electronic spectra of Ni(ema)²⁻ and Ni(CGC)²⁻ were nearly identical.^{49,50}

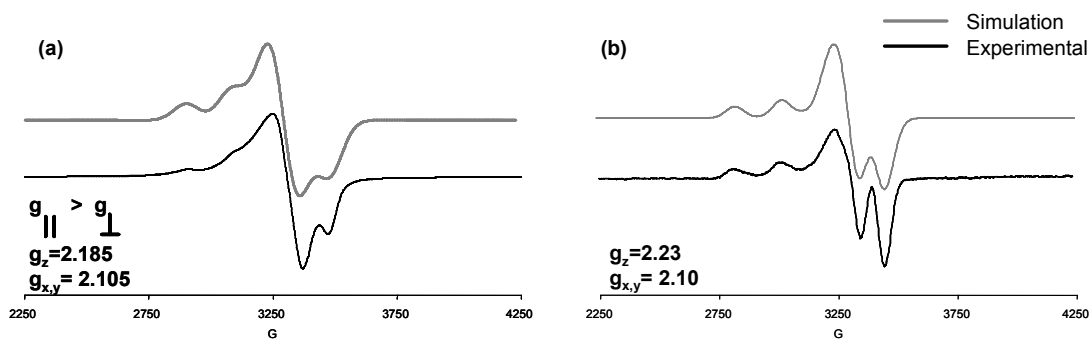


Figure VI-13: Experimental and simulated X-Band EPR spectra of (a) Cu(CGC)²⁻ and (b) O-Cu(CGC)²⁻ (2mM in DMF at 9 K, 9.75 GHz).

Synthesis and Characterization of O-Cu(CGC)²⁻

The following synthetic procedure was employed to produce the resin bound Cu(CGC)²⁻, referred to as O-Cu(CGC)²⁻ hereafter. In a fritted syringe, deep purple beads develop after 2 minutes following the addition of a bright blue solution of Cu(OAc)₂•4H₂O (1 equivalent based on the Rink-NH₂ loading) to thiolate deprotected O-CysGlyCys in basic methanol:CH₂Cl₂ (50:50). The reaction slurry was shaken for a total of 10 minutes, washed with MeOH, CH₂Cl₂, and Et₂O solvent and then dried *in vacuo*. The dried beads loaded with CGC and Cu^{II} can be left in air for +2 weeks with no apparent deleterious effects, supporting earlier observations that the resin-beads provide a protective environment for the air-sensitive resin-bound peptide complexes. The EPR spectrum obtained from a solid sample of the dry purple beads at 9 K is shown in Figure VI-13b. The axial signal with g-values of g_{||} = 2.23 and g_⊥ = 2.10 is very similar to those obtained for Cu(ema)²⁻, Cu(emi)²⁻, and Cu(CGC)²⁻ shown in Table VI-3 and confirm that the resin-bound CuCGC²⁻ complex, O-Cu(CGC)²⁻, has been produced.

Table VI-3. Comparison of g_{||}, g_⊥ and A_{||} values for CuN₂S₂²⁻ complexes.

	g	g _⊥	A (cm ⁻¹)
Cu(ema)²⁻	2.170	2.110	195
Cu(emi)²⁻	2.220	2.120	175
Cu(CGC)²⁻	2.185	2.105	186
O-Cu(CGC)²⁻	2.230	2.100	195

Metal Uptake Studies. The A-cluster active site of the bimetallic Ni enzyme, acetyl coA synthase, shown in Figure VI-5 utilizes the metallopeptide $\text{Ni}(\text{CGC})^{2-}$ as a ligand to the catalytically active nickel center, denoted as Ni_p (p = proximal), for the assembly of acetyl coA. Lindahl and co-workers have shown that the Ni_p site can be interchanged with Cu^{II} resulting in an inactivated form of the enzyme.¹¹³ In fact, the preliminary structural report of acetyl coA synthase showed a copper ion in the proximal site, which later proved to be the product of advantageous copper in the growth media.^{1,2} No transmetallation of the distal nickel, Ni_d , found in the $\text{Ni}(\text{CGC})^{2-}$ core has been reported.^{1,2,113} Similarly, small molecule model studies using the neutral NiN_2S_2 , $\text{Ni}(\text{bme-daco})$, showed the dithiolates had a great specificity for copper over nickel and zinc, but no Ni ejection from the N_2S_2 core.¹⁰² These studies showed that $\text{Ni}(\text{bme-daco})$ could serve as a reasonable structural model for the distal nickel of the acetyl CoA synthase active site.

As $\text{Ni}(\text{CGC})^{2-}$ found in acetyl coA synthase displays a high affinity for Cu^{II} and Ni^{II} and model studies of the synthetic, neutral NiN_2S_2 complexes gave similar results, uptake and possible transmetallation reactions of Cu^{II} with $\text{O-Ni}(\text{CGC})^{2-}$ and Ni^{II} with $\text{O-Cu}(\text{CGC})^{2-}$ were investigated. When 20 equivalents of $\text{Cu}(\text{OAc})_2 \cdot 4\text{H}_2\text{O}$ in MeOH: DMF (50:50) were added to bright orange beads of $\text{O-Ni}(\text{CGC})^{2-}$, no immediate color change was observed. After shaking for 6 h the beads were slightly darker in color. Following washes with DMF, MeOH, CH_2Cl_2 and Et_2O and vacuum drying, the EPR spectrum at 9 K showed an axial signal with g -values of $g_{\perp} = 2.110$ and $g_{\parallel} = 2.304$. The g_{\parallel} values, higher than the CuN_2S_2 complexes, indicate the presence of a paramagnetic Cu^{II} in an

oxygen rich donor environment.¹⁰⁹ To probe the assignment of this new EPR signal the TentaGel beads, sans peptide, were incubated with a $\text{Cu}(\text{OAc})_2 \cdot 4\text{H}_2\text{O}$ solution for 3 hrs. The EPR spectrum of the bright blue-green beads obtained from this experiment after washes and drying is shown in Figure VI-14a and largely matches that resulting from the addition of $\text{Cu}(\text{OAc})_2 \cdot 4\text{H}_2\text{O}$ to $\text{O-Ni}(\text{CGC})^{2-}$. More importantly, the lack of an EPR signal corresponding to a $\text{CuN}_2\text{S}_2^{2-}$ complex indicates that the nickel is not displaced from the CGC core. Likewise, the addition of 20 equivalents of $\text{Cu}(\text{OAc})_2 \cdot 4\text{H}_2\text{O}$ to $\text{O-Cu}(\text{CGC})^{2-}$ results in two overlapping signals, shown in Figure VI-14b. One species is attributed to the metalloprotein as evidenced by overlaying the simulated spectrum of $\text{O-Cu}(\text{CGC})^{2-}$. The other signal matches that of absorbed $\text{Cu}(\text{OAc})_2 \cdot 4\text{H}_2\text{O}$ discussed above. As 1 equivalent of $\text{Cu}(\text{OAc})_2 \cdot 4\text{H}_2\text{O}$ results in $\text{O-Cu}(\text{CGC})^{2-}$ alone we can conclude that uptake of Cu^{II} by the CGC moiety occurs first but excess Cu^{II} results in Cu-PEG absorption. A number of reports have shown that chelation by the PEG moiety to Rh or other transition metals can occur.^{77,114} As the majority of the TentaGel resin-beads are comprised of the polyethylene-glycol (PEG) spacer uptake of metals with an affinity for O-donors is not surprising, and is therefore not observed for Ni^{II} .^{75,114}

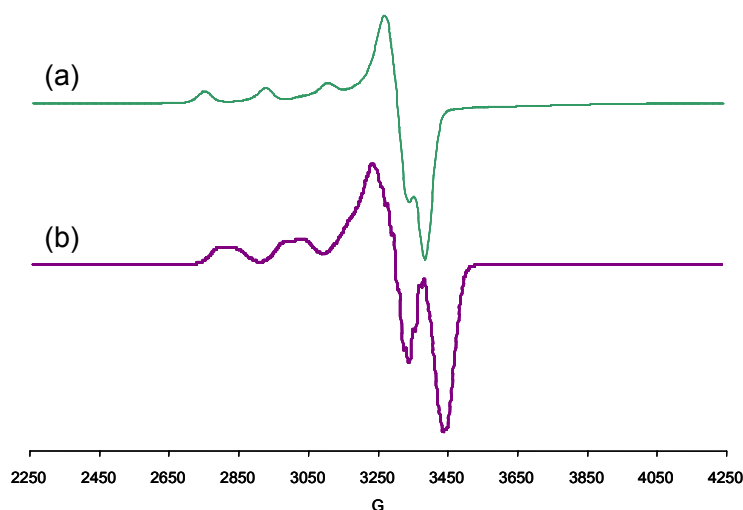


Figure VI-14. The resulting EPR spectra obtained from (a) TentaGel beads incubated with $\text{Cu}(\text{OAc})_2 \cdot 4\text{H}_2\text{O}$ and (b) 20 equivalents of $\text{Cu}(\text{OAc})_2 \cdot 4\text{H}_2\text{O}$ mixed with O-CysGlyCys.

Similarly, the addition of 20 equivalents of $\text{Ni}(\text{acac})_2$ to purple beads of O-Cu(CGC) $^{2-}$ result in no color change over the course of 6 h. Following washes and vacuum drying the resulting EPR spectrum displays the axial signal previously assigned to O-Cu(CGC) $^{2-}$ indicating that Ni^{II} is not exchanged for the Cu^{II} center. Furthermore, under the conditions described above the thiolates of the O-Ni(CGC) $^{2-}$ and O-Cu(CGC) $^{2-}$ do not produce stable paramagnetic, multimetallic species when exposed to exogenous Cu^{II} or Ni^{II} .

Thiolate Reactivity of $\text{Cu}(\text{CGC})^{2-}$ and $\text{O-Cu}(\text{CGC})^{2-}$ with $\text{Rh}(\text{CO})_2^+$

As the metal ion capture ability of $\text{Cu}(\text{emi})^{2-}$ and $\text{Cu}(\text{ema})^{2-}$ was established using the $\text{Rh}(\text{CO})_2$ unit, the same reactivity was explored with the $\text{Cu}(\text{CGC})^{2-}$. Additionally as discussed in Chapter III, previous studies of $\text{O-Ni}(\text{CGC})^{2-}$ utilized $\text{M}(\text{CO})_x$ derivatives and the resulting ATR-FTIR spectra to qualitatively identify the resin-bound NiN_2S_2 dithiolate ligand by comparison to solution $\text{NiN}_2\text{S}_2\text{M}(\text{CO})_x$ species.^{51,75} With $\text{Cu}(\text{ema})^{2-}$, $\text{Cu}(\text{emi})^{2-}$, and $\text{Cu}(\text{CGC})^{2-}$ as solution analogues for comparison, the synthesis of $\text{O-Cu}(\text{CGC})\text{Rh}(\text{CO})_2^{1-}$ can be used as secondary support for the immobilized $\text{O-Cu}(\text{CGC})^{2-}$ complex.

The brown solid of $\text{Cu}(\text{CGC})\text{Rh}(\text{CO})_2^{1-}$ was prepared in an analogous manner described for $\text{Cu}(\text{ema})^{2-}$ and $\text{Cu}(\text{emi})^{2-}$. The resulting infrared spectrum with $\nu(\text{CO}) = 2061$ and 1983 cm^{-1} is shown in Figure VI-15. These bands are nearly identical to the $\text{Rh}(\text{CO})_2$ derivatives of the other $\text{CuN}_2\text{S}_2^{2-}$ complexes. Based on the $\text{Rh}(\text{CO})_2^{2-}$ derivatives, $\text{Cu}(\text{ema})^{2-}$, $\text{Cu}(\text{emi})^{2-}$ and $\text{Cu}(\text{CGC})^{2-}$ may be designated as equal in donor ability to one another, but more electron donating than their Ni analogues, as shown in Table VI-3. The similarity in electron donor ability with varying ligand systems is observed for the analogous Ni complexes, $\text{Ni}(\text{ema})^{2-}$ and $\text{Ni}(\text{CGC})^{2-}$. Through synthesis of the $\text{NiN}_2\text{S}_2\text{W}(\text{CO})_4^{2-}$ derivatives and calculation of their respective Cotton-Kraihanzel force constants, $\text{Ni}(\text{ema})^{2-}$ and $\text{Ni}(\text{CGC})^{2-}$ were shown to be nearly equivalent in donor ability as ligands to $\text{M}(\text{CO})_x$ functionalities.⁷⁵

Addition of $[\text{Rh}(\text{CO})_2\text{Cl}]_2$ in CH_2Cl_2 to the deep purple CH_2Cl_2 suspension of $\text{O-Cu}(\text{CGC})^{2-}$ beads results in red beads after 10 min. Following washes with CH_2Cl_2 ,

MeOH, and Et₂O and drying *in vacuo* the resulting ATR-FTIR spectrum is indicative of cis-CO groups with two bands of almost equal intensity attributed to the symmetric and asymmetric stretches at 2066 and 1989 cm⁻¹ respectively, Figure VI-15. These bands provide secondary qualitative evidence for the synthesis of O-Cu(CGC)²⁻. The O-Cu(CGC)²⁻ species shows the same thiolate reactivity with Rh(CO)₂⁺ as the Ni analogue, O-Ni(CGC)Rh(CO)₂¹⁻, which has ν(CO) bands at 2061 and 1983 cm⁻¹ as shown in Table VI-4.

Table VI-4. Comparison of MN₂S₂Rh(CO)₂¹⁻ complexes (M=Cu, Ni).

MN ₂ S ₂ ²⁻	ν(CO) (cm ⁻¹)
†Cu(ema) ²⁻	2061, 1982
†Cu(emi) ²⁻	2062, 1984
†Cu(CGC) ²⁻	2061, 1983
*Ni(ema) ²⁻	2061, 1996
*Ni(CGC) ²⁻	2058, 1986

†DMF Solvent
* CH₃CN Solvent

To qualitatively test for the air-stability of the resin-bound species, samples of the dried O-Cu(CGC)²⁻ beads were exposed to air for up to two weeks and then swollen in THF and reacted with [Rh(CO)₂Cl]₂. The IR spectra consistently matched those obtained from a freshly prepared sample of O-Cu(CGC)²⁻. In contrast, exposure of a dried sample of Cu(CGC)²⁻ to air results in a green oil after 1 minute. The

reactivity shown with $\text{Rh}(\text{CO})_2^+$ parallels the reactivity observed of the original complexes in solution. Therefore, the anchoring to a solid-support does not affect the reactivity but does enhance the stability.

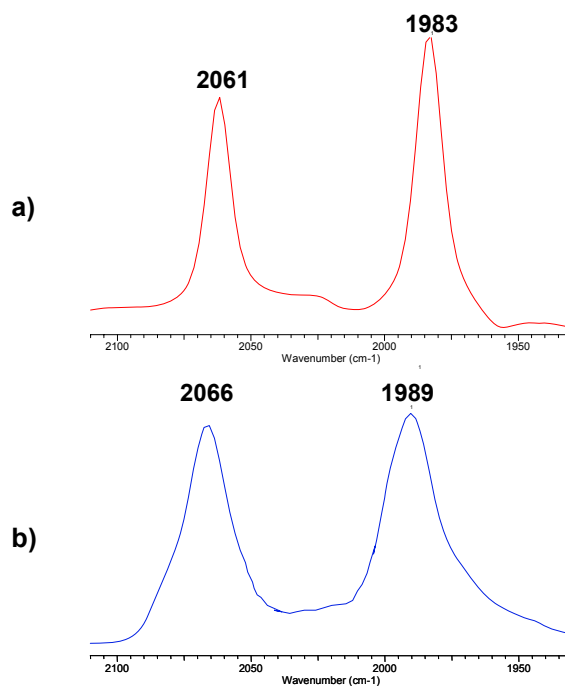


Figure VI-15: FTIR spectra of (a) $\text{O-Cu}(\text{CGC})\text{Rh}(\text{CO})_2^{1-}$ (ATR-FTIR) and (b) $\text{Cu}(\text{CGC})\text{Rh}(\text{CO})_2^{1-}$ (solution in DMF).

Conclusions

The synthesis of three new dianionic $\text{Cu}^{\text{II}}\text{N}_2\text{S}_2^{2-}$ complexes has been described along with characterization by ⁻ESI-MS, UV-Vis, and EPR which indicates a paramagnetic Cu^{II} coordinated by the two amido nitrogen and two thiolate sulfur donors provided by the ligands emi, ema, and CGC. The conclusions drawn from solution spectroscopy are corroborated by the solid state structure. The molecular structure of

Cu(emi)^{2-} shows Cu-S and Cu-N bond distances consistent with a Cu^{II} ion. Furthermore, the copper center is found in a symmetric square planar arrangement. The Rh(CO)_2^+ derivatives show that the thiolate reactivity with Rh(CO)_2^+ of these $\text{CuN}_2\text{S}_2^{2-}$ complexes parallels the well studied NiN_2S_2 analogues. The CuRh bimetallic series show that Cu(ema)^{2-} , Cu(emi)^{2-} , and Cu(CGC)^{2-} are equal in donor ability.

Synthesis of O-Cu(CGC)^{2-} using previously reported methodology for the O-Ni(CGC)^{2-} species produces dark purple beads that are stabilized against decomposition with oxygen.⁷⁵ The immobilized CuCGC^{2-} complex can be identified spectroscopically through EPR signals. Electron paramagnetic spectroscopy also showed that Cu^{II} binds to the underivatized TentaGel beads in the absence of the CGC unit, presumably to the ether oxygen donors of PEG. Nevertheless the capture of Cu^{II} by the CGC N_2S_2 units dominates the Cu-PEG interaction. Derivatization with the Rh(CO)_2^+ unit qualitatively shows that the Cu(CGC)^{2-} is immobilized and that the same reactivity may occur resin-bound as observed in solution.

Metal uptake studies showed that Cu^{II} and Ni^{II} are stable once in the N_2S_2 core, i.e. transmetallation or metal ion exchange in MN_2S_2 with Ni(acac)_2 and $\text{Cu(OAc)}_2 \cdot 4\text{H}_2\text{O}$, respectively, does not occur. Furthermore, multimetallic species formed by thiolates bridging to Ni^{II} or Cu^{II} were not observed using the acac or aceto sources for exogenous Ni or Cu. However, the reactivity with Rh(CO)_2^+ shows that stabilizing ligands on the exogenous metal ion can product bimetallic species such as $\text{O-Cu(CGC)Rh(CO)}_2^{1-}$.

Finally, no Cu^{II} active sites composed of the Cys-X-Cys ligand set have been reported to date. However, as examples of Ni, Fe, and Co have already been reported for enzymes with strikingly varying activities, and as our studies indicate a strong similarity between Ni^{II} and Cu^{II} in a N₂S₂²⁻ donor environments, an eventual siting of a Cys-X-Cys-Cu^{II} moiety will not be surprising.

CHAPTER VII

RESIN-BOUND MODELS OF THE [FeFe] HYDROGENASE ENZYME ACTIVE SITE AND REACTIVITY

The extraordinary facility in which the diiron subunit of the six-iron H-cluster of the [FeFe] Hydrogenase enzyme, [FeFe]H₂ase (Figure VII-1), combines protons and electrons to produce H₂ has focused attention on understanding the mechanistic features of the catalytic cycle.^{115,116,117} From such studies established principles might be applied to fuel cell technology, i.e. the replacement of platinum electrodes with more economical base metal electrocatalysts.¹¹⁸ Small molecule complexes which are derivatives of the classic organometallic complex (μ-pdt)[Fe^I(CO)₃]₂ (pdt = propanedithiol) have served to model the [FeFe]H₂ase enzyme active site.^{119, 120} It has been shown that this complex and its derivatives are competent in both electrochemical H₂ production and in H₂ uptake. Electrochemical studies have shown that the (μ-pdt)[Fe(CO)₃]₂ complex, as well as CO substituted derivatives, electrocatalytically produce H₂ upon acid addition under reductive conditions.^{121,122} Additional studies have shown that protonation of the disubstituted phosphine complex, (μ-pdt)[Fe^I(CO)₂PMe₃]₂ leads to the cationic (μ-H)(μ-pdt)[Fe^{II}CO)₂PMe₃]₂⁺ species.¹²³ An open site in this Fe^{II}Fe^{II} complex is generated by photolytic CO removal, allowing H₂ binding and activation to be studied according to H/D isotopic exchange reactions in D₂/H₂O mixtures.¹²³

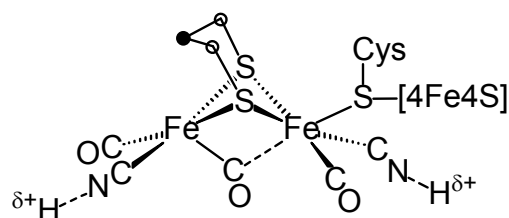


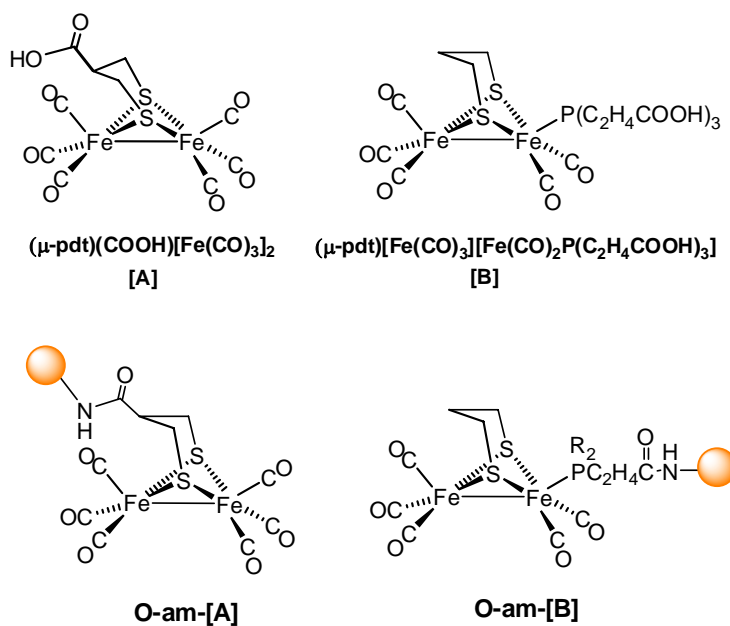
Figure VII-1: Representation of the dinuclear iron active site of [FeFe]H₂ase.^{123c}

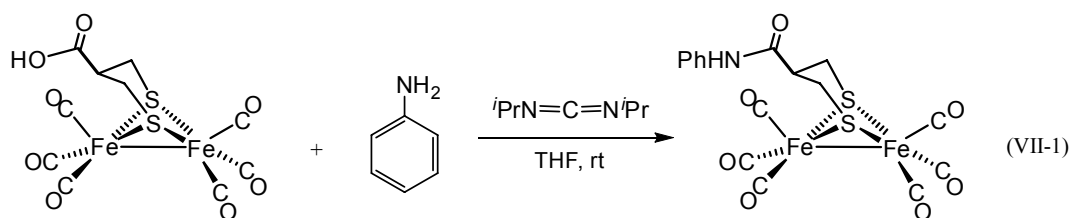
Attempts to harness the activity of the [FeFe]H₂ase biological catalyst has led to studies aimed at stabilizing the isolated enzyme through encapsulation in sol-gels.¹²⁴ Hydrogenase enzymes are typically oxygen sensitive and have a short shelf-life at room temperature. Through encapsulation of [FeFe] and [NiFe] Hydrogenase enzymes within sol-gel pellets, hydrogen evolution activity can be retained for more than a four week period, a great enhancement of stability.¹²⁴ Furthermore, immobilization of [FeFe]H₂ase models within electropolymer materials, through ester linkages, has produced electrode-bound films capable of hydrogen production.¹²⁵

Recently, additional [FeFe]H₂ase models have been synthesized as targets for immobilization on electrode surfaces with the purpose of making hydrogen producing electrocatalysts.^{65,126} This focus has yielded a new library of [FeFe]H₂ase model complexes functionalized for chemical attachment to surface-supported primary amines based on peptide like coupling techniques.^{65,126} One example shown in Chart 1 is the (μ-pdt-COOH)[Fe^I(CO)₃]₂ complex, hereafter denoted as [A], in which the propanedithiolate bridge to the [Fe(CO)₃]₂ units has been functionalized with a carboxylic acid.⁶⁵ A second example in Chart VII-1 is (μ-pdt)[Fe^I(CO)₃][Fe^I(CO)₂P(C₂H₄COOH)₃],

the monosubstituted tri(2-carboxyethyl)phosphine functionalized derivative of the $(\mu\text{-pdt})[\text{Fe}(\text{CO})_3]_2$ complex, which herein will be referred to as [B].⁶⁵ Upon activation of the carboxylic acid, these complexes have been shown to react with amines to produce stable amide derivatives.^{65,126} For example, to mimic the amido linkage of electrode immobilized models, reaction of [A] with aniline and the coupling agent diisopropylcarbodiimide produced the amide derivative shown in Equation VII-1.⁶⁵ These studies have also shown that reactivity of the (COOH)-functionalized $[\text{FeFe}]\text{H}_2\text{ase}$ model complexes with PMe_3 produced mono and disubstituted complexes, analogous to known substitution chemistry which yields $(\mu\text{-pdt})[\text{Fe}(\text{CO})_3][\text{Fe}(\text{CO})_2\text{PMe}_3]$ and $(\mu\text{-pdt})[\text{Fe}(\text{CO})_2\text{PMe}_3]_2$.¹²³ Overall, the carboxylic acid functionality at the bridgehead $\mu\text{-pdt}$ moiety has little effect on the structure, reactivity, and spectroscopy of the $[\text{Fe}(\text{CO})_3]_2$ core.

Chart VII-1





Immobilization of these complexes is not limited to electrode surfaces. In theory, these molecules could be linked to any surface or nanoparticle capable of supporting the amido linkages formed with the carboxylic acid functionalities of the [FeFe]H₂ase models. The growing number of biological applications for immobilized models suggests that resin-beads should be considered as one candidate for immobilization.^{37,39,38} A number of studies have recently provided examples of immobilization of biologically inspired complexes to polystyrene-polyethylene glycol based resin-beads. For example, the A-cluster of acetyl coA synthase utilizes the metallopeptide Ni(CGC)²⁻ as a dithiolate ligand to the Ni^{II} center responsible for the C-C coupling reaction that produces acetyl coA.¹ Earlier chapters detailed studies of the resin-bound Ni(CGC)²⁻ and its use as an anchor to attach M(CO)_x moieties which can be identified by ATR-FTIR of the dried beads.⁷⁵ Additionally P. Desrochers has shown that a resin-bound cysteine can chelate through the amido nitrogen and thiolate sulfur donors to (dppe)Ni and Tp^{*}Ni units. The resulting complexes, O-Cys[Ni(dppe)] and O-Cys[Ni(Tp^{*})] can be identified by the ³¹P NMR spectra obtained from CDCl₃ suspensions of the beads.¹²⁷ With isolation and characterization of resin-bound biomimetic complexes established, further studies directed toward the reactivity of immobilized model complexes can be pursued.

As the structure, spectroscopy and reactivity of the parent $(\mu\text{-pdt})[\text{Fe}^{\text{I}}(\text{CO})_3]_2$ complex has been well established to produce a range of $[\text{FeFe}]\text{H}_2\text{ase}$ models, the carboxylic acid derivatives serve as good candidates for (1) studying the effects endowed by the TentaGel S-RAM[®] environment on the properties (spectroscopy, reactivity and stability) of the resulting resin-bound model complexes; and (2) inferring from such differences the immediate environment or second-coordination sphere effects of the resin itself.^{122, 123, 128}

Isolation and characterization of the resin-bound organometallic $[\text{FeFe}]\text{H}_2\text{ase}$ model complexes shown in Chart VII-1, O-am-[A] and O-am-[B] (am = amide), through ATR-FTIR and ³¹P NMR spectroscopy will be reported herein. Specifically, the stability of the resulting complexes to air, light, and solvent will be evaluated. A range of substitution reactions with phosphines (PMe_3 and PPh_3), CN^- , and carbene ligands will be discussed and compared to the reactivity of analogous complexes in solution. The results from these investigations will be compared to solution analogues and evaluated for the effects and interactions of the resin-bead environment with the immobilized complexes.

Immobilization of $[\text{FeFe}]\text{H}_2\text{ase}$ Models

General Synthesis. Synthesis of the resin-bound (COOH) functionalized $[\text{FeFe}]\text{H}_2\text{ase}$ models, O-am-[A] and O-am-[B] was performed in plastic syringes with microporous frits. The TentaGel S-RAM[®] beads were swollen in DMF prior to attachment of the model complexes. For coupling to the amine of the beads, the carboxylic acid functionality of [A] and [B] was activated with a 1,3-

diisopropylcarbodiimide (DIC), *N,N*-diisopropylethylamine (DIPEA), and 1-hydroxy-7-azabenzotriazole (HOBt) “coupling cocktail”. Following the coupling of [A] and [B] to the resin-beads, the beads were washed with three times each with THF, DMF, MeOH, and Et₂O and then dried *in vacuo*.

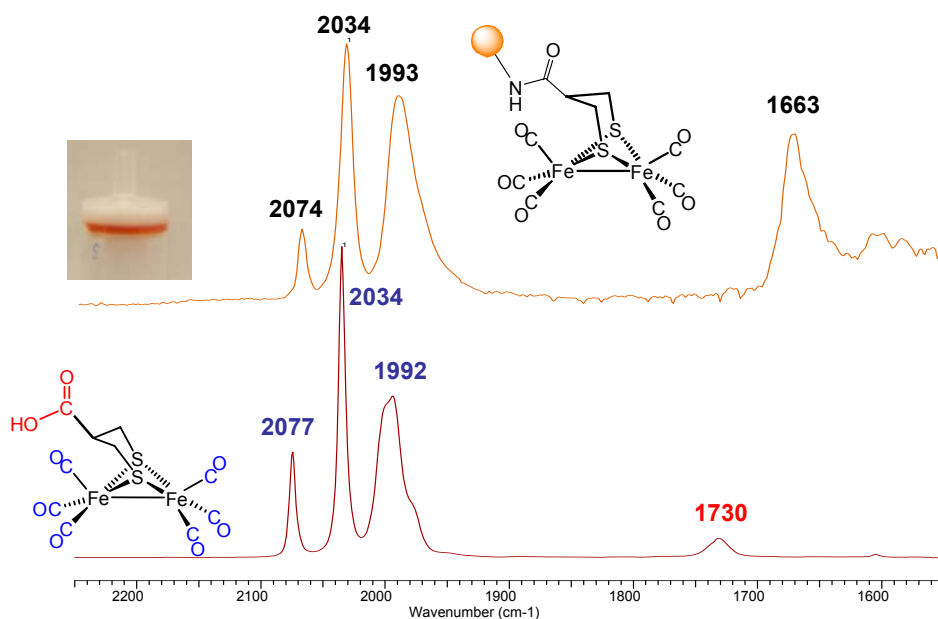


Figure VII-2. Comparison of infrared spectra for O-am-[A] (ATR-FTIR) (top) and [A] (THF) (Bottom).

Synthesis and Characterization of Resin-Bound (COOH)[Fe(CO)₃]₂ complexes, O-am-[A] and O-am-[B]. The bright-orange resin-bound complex, O-am-[A] was produced via the addition of an activated red-orange solution of [A] in THF to light yellow TentaGel S-RAM[®] Beads and shaking for 2 h. Following standard washes with THF, DMF, MeOH, and Et₂O (3 x each), and drying *in vacuo*; the solid state ATR-

FTIR spectrum of the beads showed $\nu(\text{CO})$ bands at 2074, 2034, and 1993 cm^{-1} , which is shown in Figure VII-2. Apart from the absence of the carboxylic acid stretching frequency, the band pattern and positions are nearly identical to those observed for the [A] in a THF solution, $\nu(\text{CO}) = 2077, 2034, 1992$ and $\nu(\text{C=O})\text{OH} = 1730 \text{ cm}^{-1}$.⁶⁵ A comparison of these bands to other [FeFe] H_2 ase models is shown in Table VII-1.

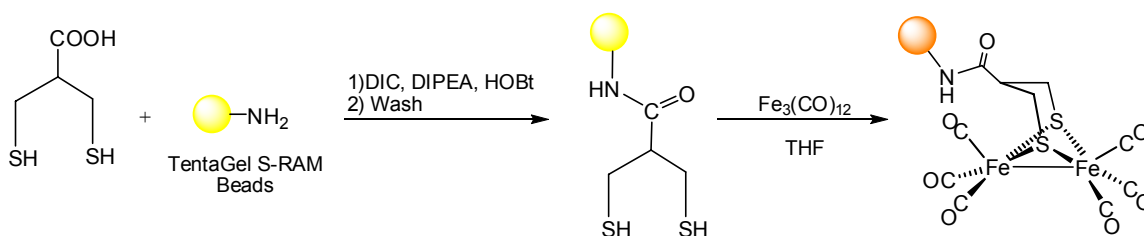
The loss of the $\nu(\text{C=O})\text{OH} = 1730 \text{ cm}^{-1}$ stretch for the O-am-[A] complex is indicative of the expected peptide bond formation. Unfortunately, the resulting amide stretching frequency is not distinguishable from similar bands arising from the Rink Linker ($\nu(\text{am})=1663 \text{ cm}^{-1}$) of the TentaGel S-RAM[®] beads, which contains an amide bond as well. To establish the covalent attachment via the amide bond and rule out physisorption of the complex, pre-swollen TentaGel S-RAM Beads were incubated with a THF solution of $(\mu\text{-pdt})[\text{Fe}(\text{CO})_3]_2$. Following the standard washes, no color change and no $\nu(\text{CO})$ bands were observed on the beads. This indicates that adsorption of the carboxy-derivatized [FeFe] H_2 ase model is not the mode of attachment and that the COOH moiety is required and results in covalent linkage. Additionally, group member Jen Hess has shown that coupling of 2-carboxy-1,3-propanedithiol to the TentaGel resin-beads followed by the addition of a green THF solution of $[\text{Fe}_3(\text{CO})_{12}]$ results in bright orange beads with identical $\nu(\text{CO})$ IR band pattern and position to O-am-[A]. This alternate synthesis to O-am-[A], Scheme VII-1, shows that coupling of 2-carboxy-1,3-propanedithiol to the amide resin produces a resin-bound dithiolate ligand that parallels solution reactivity.¹²⁹ The results serves as confirmatory evidence of an amide bond formation when [A] is coupled to the resin-bead.

Table VII-1. Comparison of Resin-Bound [FeFe]H₂ase model complexes with solution analogues.

Complex	$\nu(\text{CO})$ (cm ⁻¹)
O-am-[A]	2074(w), 2034(s), and 1993(m)
(μ -pdt)[Fe(CO) ₃] ₂ ¹²⁸	2074(m), 2036(s), 1995(m) [†]
[A] ⁶⁵	2077(w), 2034(s), 1992(m) $\nu(\text{C}=\text{O})\text{OH} = 1730$ [†]
Monosubstituted Complexes	
O-am-[B]	2038(s), 1976(s), 1950(sh), 1918(w)
[B] ⁶⁵	2041(s), 1981(s), 1962(sh), 1920(w) [†]
O-am-(μ -pdt)[Fe(CO) ₃][Fe(CO) ₂ PMe ₃]	2036(m), 1981(s), 1960 (sh), 1923(w)
O-am-(μ -pdt)[Fe(CO) ₃][Fe(CO) ₂ PPh ₃]	2045(s), 1985(s), 1960(sh), 1941(w)
(μ -pdt)[Fe(CO) ₃][Fe(CO) ₂ PMe ₃] ¹²⁸	2037(s), 1980(s), 1919(w) [‡]
Disubstituted Complexes	
O-am-(μ -pdt)[Fe(CO) ₂ PMe ₃] ₂	1980(m), 1943(s), 1899(s)
(μ -pdt-COOH)[Fe(CO) ₂ PMe ₃] ₂ ⁶⁵	1984(m), 1948(s), 1903(s) [†]
(μ -pdt)[Fe(CO) ₂ PMe ₃][Fe(CO) ₂ P(C ₂ H ₄ COOH) ₃] ⁶⁵	1980(m), 1942(s), 1899(w), 1876(sh) [†]
O-am-[Fe(CO) ₂ PMe ₃][Fe(CO) ₂ P(C ₂ H ₄ COOH) ₃](μ -pdt)	1981(m), 1943(s), 1909(w), 1894(sh)
Cyanide Derivatives	
O-am-[Fe(CO) ₂ CN][Fe(CO) ₂ P(C ₂ H ₄ COOH) ₃](μ -pdt)	1977(m), 1939(s), 1904(w), 1875(sh) $\nu(\text{CN})=2072, 2037$
(μ -pdt)[Fe(CO) ₂ CN][Fe(CO) ₂ PMe ₃] ¹²³	1971(m), 1931(s), 1895(w), 1880(sh) $\nu(\text{CN})=2078, 2036$ [†]
IMes Derivatives	
O-am-[Fe(CO) ₂ IMes][Fe(CO) ₂ P(C ₂ H ₄ COOH) ₃](μ -pdt)	1980(m), 1943(s), 1911(m), 1893(sh)
(μ -pdt)[Fe(CO) ₂ IMes][Fe(CO) ₂ PMe ₃] ¹³¹	1972(m), 1933(s), 1897(m), 1882(sh) [§]
O-am-[(μ -pdt)(Fe(CO) ₂ IMes)(Fe(CO) ₂ PMe ₃)]	1982(m), 1962(s), 1903(m), 1892(sh)

Solvent: [†]THF [‡]CH₃CN [§]CH₂Cl₂

As final proof for the resin-amine site reactivity, a ninhydrin test was carried out. This assay tests for the presence of active amines on the TentaGel beads via reaction with ninhydrin to give blue-purple colored beads.¹² The addition of the ninhydrin solution to the unmodified yellow TentaGel S-RAM beads followed by heating produced a deep blue hue due to reaction of ninhydrin to the Rink Linker amine sites. When ninhydrin was added to the iron-carbonyl loaded, bright-orange O-am-[A] beads, no color change was observed indicating that quantitative conversion of the amine sites to amides had occurred. Moreover, analogous solution coupling studies of the carboxy-functionalized [FeFe]H₂ase models to amines such as aniline utilizing DIC as a coupling agent results in rapid formation of the amide bond in high yield.⁶⁵



Scheme VII-1. Alternative Synthesis to O-am-[A].

The $(\mu\text{-pdt})[\text{Fe}(\text{CO})_3]_2$ complex is an air stable red solid.¹²⁸ The CO ligands may be substituted by better donors, such as PMe_3 .^{123,128,130,133} This reaction is facilitated by addition of Me_3NO resulting in oxidative elimination of CO_2 or UV photolysis.¹²³ However, loss of CO from $(\mu\text{-pdt})[\text{Fe}(\text{CO})_3]_2$ by exposure to ambient lab light has not been reported. Nevertheless, exposure of O-am-[A] to ambient lab light results in no

color change but complete loss of $\nu(\text{CO})$ bands after 4 h. The lack of color change indicates that some version of the FeFe-dithiolate unit is still attached to the beads, however. The IR spectrum of the supernatant solution shows no CO bands. Similar decomposition was also observed when the resin-bound complex was prepared and stored in CH_2Cl_2 . When stored in the dark as a suspension in dry THF, the $\nu(\text{CO})$ bands remained over 3 weeks. Exposure to air does not result in degradation of the complexes; however, they were stored under a N_2 environment to avoid excessive H_2O uptake. All subsequent substitution reactions discussed herein were therefore carried out in sample vials fitted with rubber septa and covered in foil to prevent light exposure.

Synthesis of the second resin-bound [FeFe] H_2ase model complex, O-am-[B] was accomplished in an identical manner to that of O-am-[A]. Following thorough washes of the resulting bright-orange beads and vacuum drying, the ATR-FTIR spectrum showed $\nu(\text{CO})$ bands at 2038(s), 1976(s), 1950(sh), 1918(w). A ^{31}P NMR spectrum of a CDCl_3 suspension of the beads showed a single resonance at 52.37 ppm. These solid phase or mixed phase spectra parallel those of the parent compound, [B] in solution as shown in Figure VII-3.⁶⁵ The stability of O-am-[B] mimics that of O-am-[A].

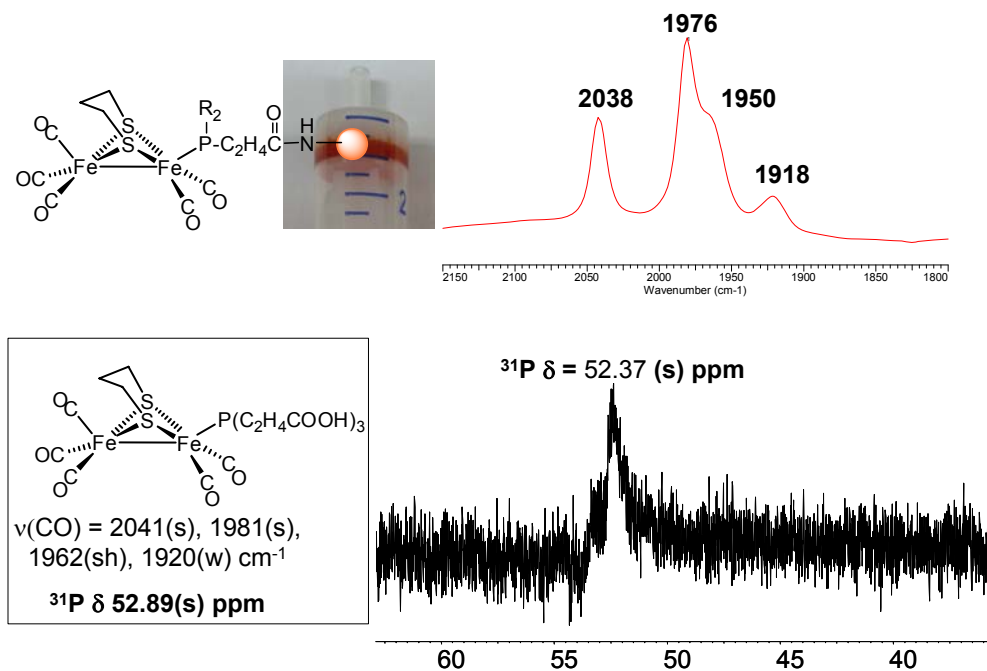


Figure VII-3. The ATR-FTIR and ³¹P spectra of O-am-[B] (inset: corresponding spectroscopy of [B] (IR spectrum in solution: THF, ³¹P NMR spectrum: CDCl₃).

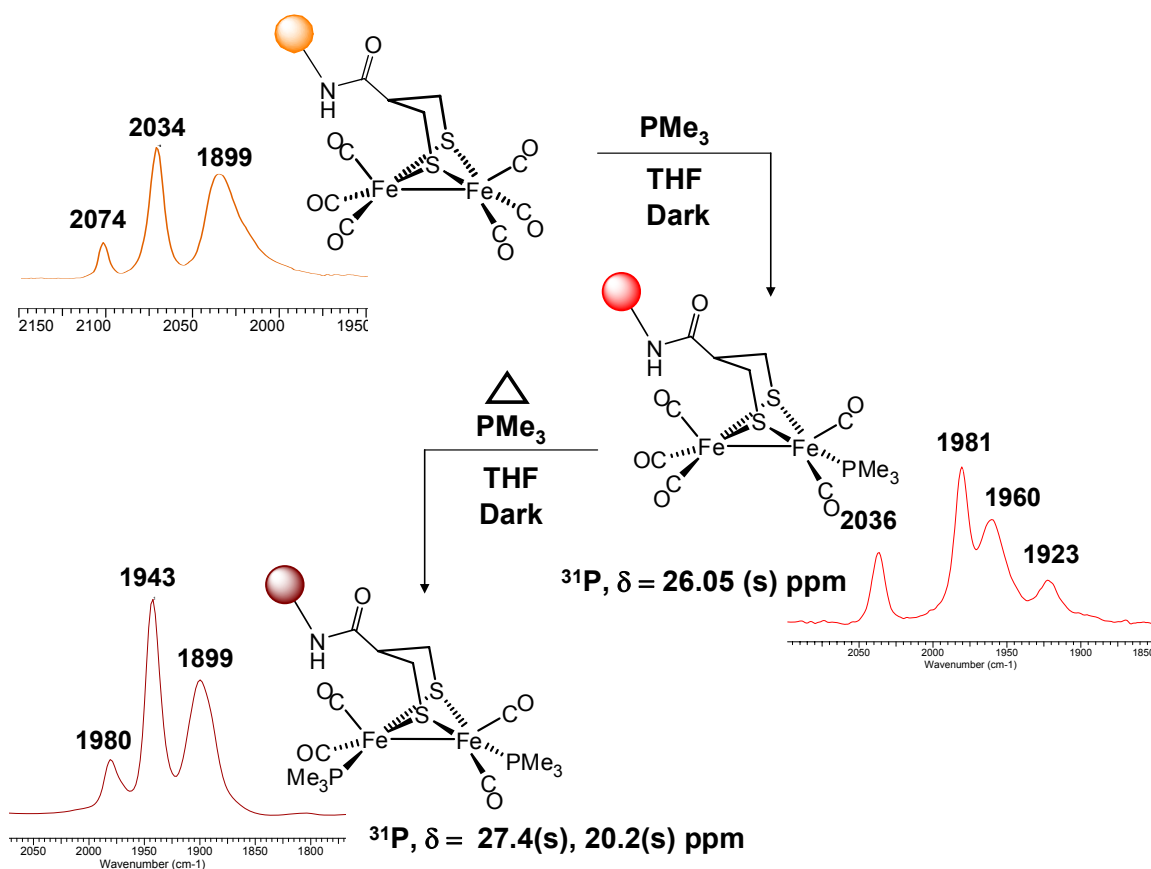
The synthesis of resin-bound O-am-[A] and O-am-[B] have shown that common coupling techniques can be used to produce resin-bound organometallic complexes. By establishing that all amine sites have been converted to amides, the ninhydrin test confirms that the (COOH)-functionalized [FeFe]H₂ase models are imbedded *within* the resin-beads.^{39a,40b} As these complexes have shown stability in the absence of light, substitution of the CO ligands can now be explored.

Synthesis of Monosubstituted Derivatives via Ligand Substitution on Immobilized FeFe Carbonyls

The isolation and IR spectroscopy of $(\mu\text{-pdt})[\text{Fe}(\text{CO})_3][\text{Fe}(\text{CO})_2\text{L}]$ ($\text{L} = \text{PMe}_3$, PMe_2Ph , $\text{P}(\text{OEt}_3)$, PPh_3) were recently compared.¹³⁰ These complexes were obtained through stoichiometrically controlled CO substitution. Careful addition of PMe_3 to $(\mu\text{-pdt})[\text{Fe}(\text{CO})_3]_2$ was particularly key to the synthesis of $(\mu\text{-pdt})[\text{Fe}(\text{CO})_3][\text{Fe}(\text{CO})_2\text{PMe}_3]$ complex in order to avoid the disubstituted species which readily forms.¹³⁰ Substitution of one CO group with a more electron-donating phosphine results in a new band pattern with an overall shift to lower wavenumbers. For example, the $(\mu\text{-pdt})[\text{Fe}(\text{CO})_3][\text{Fe}(\text{CO})_2\text{PMe}_3]$ complex has $\nu(\text{CO}) = 2037(\text{m})$, $1980(\text{s})$, and $1919(\text{w}) \text{ cm}^{-1}$ compared to $(\mu\text{-pdt})[\text{Fe}(\text{CO})_3]_2$ with $\nu(\text{CO}) = 2074(\text{m})$, $2036(\text{s})$, and $1995(\text{m}) \text{ cm}^{-1}$.¹²⁸ For the solution spectra of a series of $(\mu\text{-pdt})[\text{Fe}(\text{CO})_3][\text{Fe}(\text{CO})_2\text{L}]$, the most intense band is shifted on average 50 wavenumbers lower than that of $(\mu\text{-pdt})[\text{Fe}(\text{CO})_3]_2$.¹³⁰

Similar reactivity for resin-bound complexes may be achieved. Scheme VII-2 shows that addition of PMe_3 to an N_2 -flushed THF suspension of O-am-[A], followed by washes yielded red-orange beads after 4 h. The ATR-FTIR spectrum showed $\nu(\text{CO})$ bands at $2036(\text{m})$, $1981(\text{s})$, $1960(\text{sh})$, $1923(\text{w}) \text{ cm}^{-1}$. As shown in Table VII-1 and discussed above, these values are consistent with other monosubstituted solution species.¹³⁰ The intensity of the $\nu(\text{CO})$ bands arising from the Rink Linker can be used as an internal standard to monitor the stability of the CO-containing products. Compared to the $\nu(\text{C}=\text{O})\text{OH}$ bands from the beads, the intensity of the $\nu(\text{CO})$ bands arising from [A] remain unchanged upon CO-substitution with PMe_3 . Furthermore, the supernatant

solution remained colorless and free of $\nu(\text{CO})$ bands following reaction with PMe_3 . The ^{31}P NMR spectrum obtained from a CDCl_3 suspension of $\text{O-am-}[(\mu\text{-pdt})(\text{Fe}(\text{CO})_3)(\text{Fe}(\text{CO})_2\text{PMe}_3)]$ shows a singlet at 26.1 ppm, indicating that only one type of phosphorus-containing moiety is present.



Scheme VII-2. Synthesis and characterization of mono and disubstituted resin-bound derivatives of O-am-[A] .

Similarly, the addition of the more bulky phosphine PPh_3 in THF to a suspension of O-am-[A] results in an ATR-FTIR spectrum comprised solely of $\nu(\text{CO})$ bands at

2045(s), 1985(s), 1960(sh), 1941(w) cm^{-1} . These bands indicate that monosubstitution has occurred to form O-am-[(μ -pdt)(Fe(CO)₃)(Fe(CO)₂PPh₃)]; they are ~10 wavenumbers higher than those observed for the PMe₃ analogue, see Table VII-1. This shift is consistent with the poorer donor ability of PPh₃ as compared to PMe₃.¹³⁰ The full conversion of O-am-[A] to the monosubstituted PPh₃ species indicates that the bulkier phosphine can access all of the O-am-[A] sites within the bead. Likely due to its steric bulk, preparation of the di-substituted PPh₃ derivatives has not been reported for solution [FeFe]H₂ase models. This same substitution reactivity is found in the resin-bound species.

Disubstituted Derivatives and Their Reactivity

As shown in Figure VIII-1, the active site of [FeFe]H₂ase utilizes two cyanide donors which presumably facilitate the catalytic activity through structural and electronic effects.^{123a} Therefore, investigations of small molecule models of [FeFe]H₂ase have focused on substituting two of the CO groups of (μ -pdt)[Fe(CO)₃]₂ with cyanides as well as PMe₃, said to be a CN⁻ mimic in donor ability.^{123,128} An increase in electron density by better σ donors at Fe is important as oxidation of Fe^I and stabilization of Fe^{II} is required for generation of hydrogenic iron species, Fe^{II}-H or Fe(η^2 -H₂).^{123b} Furthermore, a second role for CN⁻ is its potential for H-bonding to the protein, thus locking in the rotated structure shown in Figure VII-1, even when reduction to an Fe^IFe^I redox level would

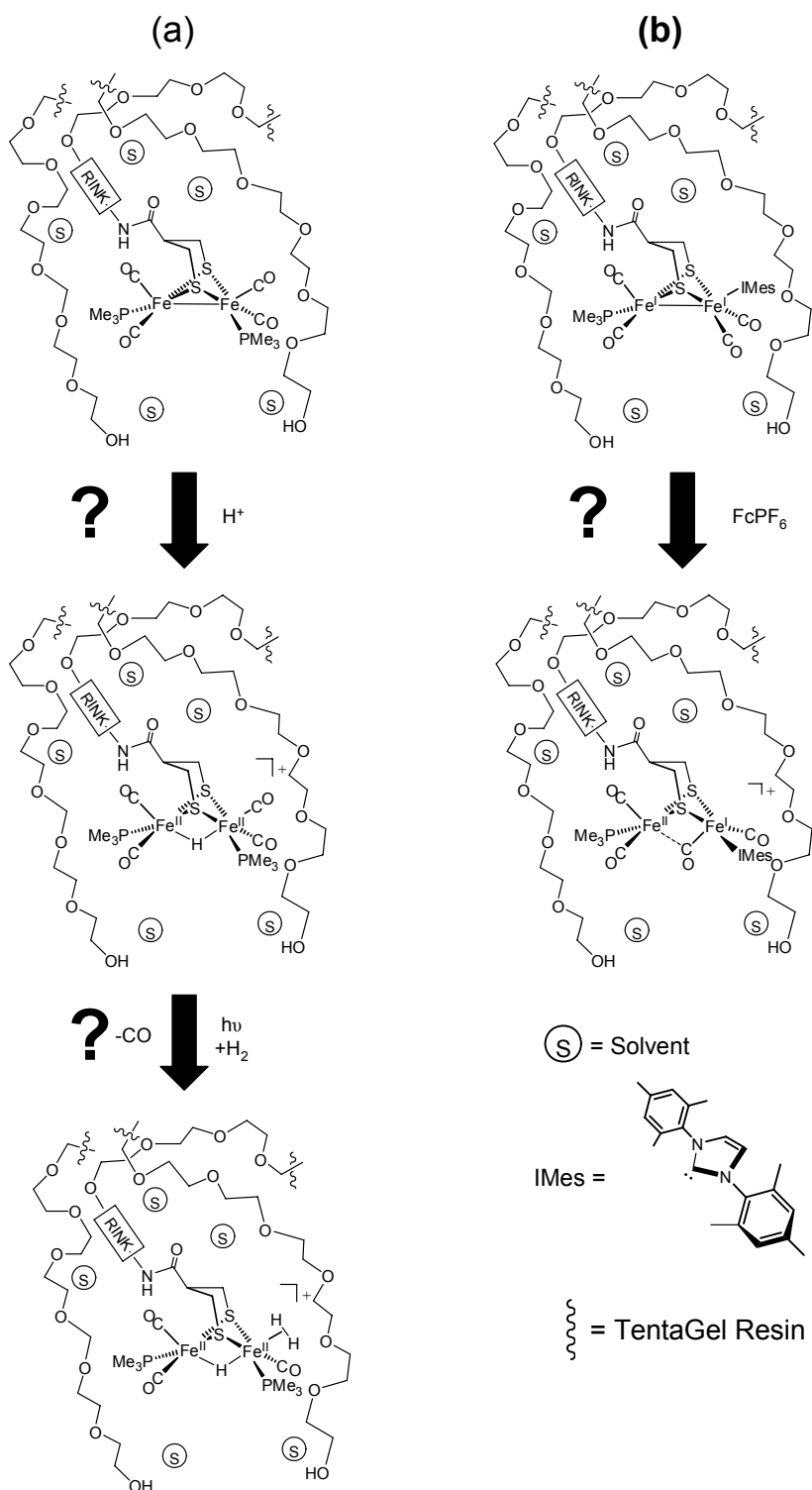
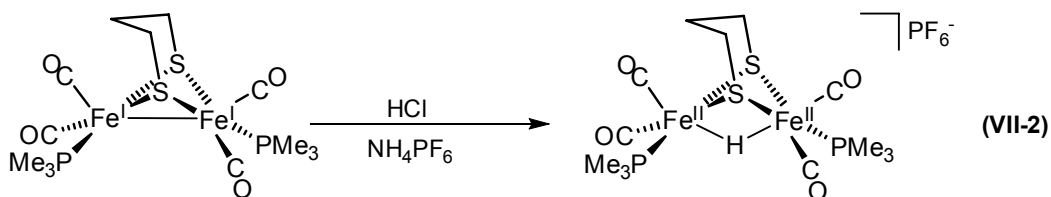


Figure VII-4. Targets for reactivity studies of resin-bound [FeFe]H₂ase models.

push the structure towards the symmetrical form typically seen in model complexes.^{123a} Hence my goal for resin-bound [FeFe]H₂ase model complexes was two-fold, with targets as shown in Figure VII-4. The first objective was (1) to produce the resin-bound bridging hydride, Fe^{II}(μ-H)Fe^{II}, species by acid addition to O-[Fe(CO)₂PMe₃]₂; (2) to create an open site by photochemically removing CO; and (3) to study H₂ uptake through isotopic exchange studies. The second target was to create a bridging CO group by oxidation of the resin-bound [Fe(CO)₂PMe₃][Fe(CO)₂(IMes)] ((IMes = 1,3-bis(2,4,6-trimethylphenyl)imidazol-2-ylidene)). As shown by co-worker T. Liu, the bulky IMes carbene assists in a unique rotation of the Fe(CO)₂IMes side, producing the bridging CO group and concomitantly yielding a open site.¹³¹

The addition of excess PMe₃ to a THF suspension of O-am-[A] and followed by heating at 50°C for 6 h yields ν(CO) bands at 1980(m), 1943(s), 1899(s) cm⁻¹. These values agree with assignment of the disubstituted species, O-am-[(μ-pdt)(Fe(CO)₂PMe₃)₂], shown in Scheme VII-2.¹²³ The same complex is obtained via the addition of PMe₃ to O-am-[(μ-pdt)(Fe(CO)₃)(Fe(CO)₂PMe₃)] upon heating. Phosphorus NMR spectra show two singlets with δ = 27.4 and 20.2 ppm which match the δ = 27.6(s), 21.5(s) ppm observed in solution for (μ-pdt-COOH)[Fe(CO)PMe₃]₂.⁶⁵ Comparison of the ν(CO) bands, shown in Table VII-1, and ³¹P NMR spectra of the resin-bound product to solution analogues has indicated that disubstitution of O-am-[A] proceeds to completion with little degradation. The O-am-[(μ-pdt)(Fe(CO)₂PMe₃)₂] complex is light sensitive, as are its resin-bound precursors, but it is stable as a THF suspension under an N₂ blanket.



As suggested by the goal expressed in Figure VII-4, Route (a), the reactivity of the stable resin-bound disubstituted complex toward protonation and ligand exchange was explored. As mentioned above, further investigations have produced a bridging hydride, $\text{Fe}^{\text{II}}(\mu\text{-H})\text{Fe}^{\text{II}}$, obtained upon addition of HCl to $(\mu\text{-pdt})[\text{Fe}(\text{CO})_2\text{PMe}_3]_2$ and shown in Equation VII-2.¹²³ On photolysis, the complex loses a CO group yielding an open site capable of reversibly binding H_2 .¹²³ In an attempt to access the resin-bound ($\mu\text{-H}$) species, reaction of the O-am- $[(\mu\text{-pdt})(\text{Fe}(\text{CO})_2\text{PMe}_3)_2]$ complex with dilute (1%) solutions of acids such as HCl, CH_3COOH , and CF_3COOH were investigated. However, as evidenced by the bleaching of color from the beads upon addition of HCl and CH_3COOH , cleavage of the carboxamido linkage and decomposition of O-am- $[(\mu\text{-pdt})(\text{Fe}(\text{CO})_2\text{PMe}_3)_2]$ occurs. While, the resulting supernatant THF solution became orange in color, it did not display detectable $\nu(\text{CO})$ bands. Addition of NH_4PF_6 as a stabilizing counterion gave identical results. When a 1% THF solution of CF_3COOH , was added to O-am- $[(\mu\text{-pdt})(\text{Fe}(\text{CO})_2\text{PMe}_3)_2]$, decomposition again occurred. However, very low intensity bands at 2017 and 1963 cm^{-1} were observed. These bands, although similar in pattern, do not match the position of those observed for $[(\mu\text{-pdt-COOH})(\mu\text{-$

H)(Fe(CO)₂PMe₃)₂]PF₆ ($\nu(\text{CO}) = 2034(\text{s}), 1994(\text{s}) \text{ cm}^{-1}$).⁶⁵ The amide derivative of [A], shown as the product in Equation VII-1, has also been studied for its stability with acids. The amide bond in solution proved to be robust when exposed to 10 equivalents of CH₃COOH and HCl. However, when exposed to concentrated solutions of HCl, the solution bleached resulting in uncharacterized brown solids over the course of one hour.¹²³ The resin-bound species is presumably undergoing similar decomposition, even in the presence of dilute solutions of acid.

The O-am-[B] complex was much less reactive toward ligand exchange than its parent complex, [B], in solution. Addition of PMe₃ to [B] in toluene results in infrared spectral changes of $\nu(\text{CO}) = 1980, 1942, 1899, \text{ and } 1876 \text{ cm}^{-1}$, consistent with a diphosphine complex with one P-donor on each iron.¹³² More rigorous conditions are required to obtain the resin-bound analogue. The reaction consisted of the addition of Me₃NO to a THF suspension of O-am-[B] followed by PMe₃ and heating at 55°C overnight. These beads were then washed with DMF, THF, MeOH and Et₂O and dried *in vacuo*. The ATR-FTIR spectrum of the red-orange beads showed complete conversion to $\nu(\text{CO}) = 1981(\text{m}), 1943(\text{s}), 1909(\text{w}), 1894(\text{sh}) \text{ cm}^{-1}$. These bands correspond to the IR spectrum of $(\mu\text{-pdt})[\text{Fe}(\text{CO})_2\text{PMe}_3][\text{Fe}(\text{CO})_2\text{P}(\text{C}_2\text{H}_4\text{COOH})_3]$ complex produced in solution and show that CO substitution of O-am-[B] occurs, albeit slowly.

Reactivity with Cyanide. The [FeFe]H₂ase active site utilizes CN⁻ as ligands that are believed to participate in H-bonding with surrounding amino acid side chains, thereby preventing rotation from the bridging CO state and loss of the structure that provides an open site for H₂ bonding or proton addition.^{123a} Small molecule models with

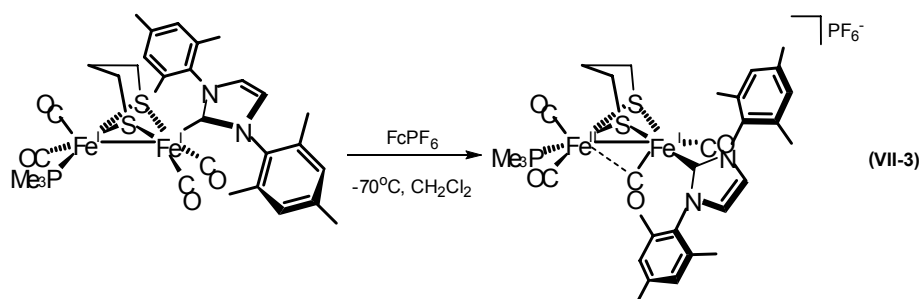
CN⁻ ligands have been produced as more faithful models to the active site. Substitution of two CO groups with CN⁻ results in a cyanide group on each Fe subunit, similar to that observed with the phosphine derivatives of (μ-pdt)[Fe(CO)₃]₂.¹²³ Unfortunately, reported attempts to obtain a bridging hydride species through reaction with acids, resulted in the production of HCN and degradation, rather than a μ-H species.¹²³

Resin-bound cyanide substituted species can be produced as well. The addition of a methanolic solution of [Et₄N][CN] to a THF suspension of O-am-[B] at room temperature for 12 h results in CO-substitution to yield an IR spectrum with ν(CN) = 2072, 2037 cm⁻¹ and ν(CO) = 1977(m), 1939(s), 1904(w), 1875(sh) cm⁻¹. The two CN bands are consistent with the presence of isomers which have been observed for solution complexes of (μ-pdt)[Fe(CO)₂CN][Fe(CO)₂PMe₃] (ν(CN) = 2076, 2036 cm⁻¹ and ν(CO) = 1971(m), 1931(s), 1895(w), 1880(sh) cm⁻¹).¹³²

With two good donors capable of stabilizing higher Fe oxidation states, the (μ-H) and rotated structure or (μ-CO) species were pursued, the former by protonation and the latter by 1 e⁻ oxidation. Regrettably, the addition of the oxidant FcPF₆ (2 equivalents) to THF suspensions of O-am-[Fe(CO)₂CN][Fe(CO)₂P(C₂H₄COOH)₃](μ-pdt) resulted in no change in ν(CO) bands. Addition of a 1% solution of HCl resulted in degradation of the resin-bound complexes as was observed for the phosphine derivatives.

Reactivity with the N-Heterocyclic Carbenes, IMes. Recently, the addition of the N-heterocyclic carbene, IMes, to (μ-pdt)[Fe(CO)₃]₂, followed by PMe₃ substitution, was shown to result in the Fe^IFe^I complex (μ-pdt)[Fe(CO)₂PMe₃][Fe(CO)₂IMes].¹³¹ As shown in Equation VII-3, the addition of FcPF₆ at low temperature to a CH₂Cl₂ solution

of this complex yielded an $\text{Fe}^{\text{I}}\text{Fe}^{\text{II}}$ species. This species is of importance for a number of reasons. The EPR spectrum of this mixed valent complex shows an $S = 1/2$ system, which is also observed in the H_{ox} state of the $[\text{FeFe}]$ Hydrogenase enzyme.¹³³ Also, the IR spectrum has a weak band at 1861 cm^{-1} , which suggests the presence of a bridging CO.¹³⁴ This feature, critical to a structural and spectroscopic model of the as-isolated $[\text{FeFe}]\text{H}_2\text{ase}$ active site, was confirmed by the molecular structure.¹³¹ The bridging CO species is an excellent structural model of the $[\text{FeFe}]\text{H}_2\text{ase}$ active site, both structurally and spectroscopically.¹³¹ However, further studies of this mixed valent species have been impeded by its thermal and air sensitive nature.



As immobilization has been reported to impart stabilization to resin-bound complexes, substitution of O-am-[A] and O-am-[B] with the IMes carbene followed by PMe_3 addition has been pursued.^{5,6} Sequential addition of Me_3NO and IMes to a suspension of O-am-[B] in THF and heating at $50\text{ }^\circ\text{C}$ for 24 h produced an IR spectrum with $\nu(\text{CO}) = 1980(\text{m}), 1943(\text{s}), 1911(\text{w}), 1893(\text{sh})\text{ cm}^{-1}$. These bands parallel those observed for $(\mu\text{-pdt})[\text{Fe}(\text{CO})_2\text{PMe}_3][\text{Fe}(\text{CO})_2\text{IMes}]$, $\nu(\text{CO}) = 1972(\text{s}), 1933(\text{vs}), 1897(\text{s}),$ and $1882(\text{sh})\text{ cm}^{-1}$.¹³¹ Unfortunately, attempts to oxidize the O-am-

$[\text{Fe}(\text{CO})_2\text{IMes}][\text{Fe}(\text{CO})_2\text{P}(\text{C}_2\text{H}_4\text{COOH})_3](\mu\text{-pdt})$ with FcPF_6 at room temperature result in loss of the IMes ligand, as evidenced by the resulting IR spectrum $\nu(\text{CO})$ bands at 2038(s), 1976(s), 1950(sh), 1918(w) which corresponds to O-am-[B], Table VII-1. The CO needed to regenerate O-am-[B] is likely obtained through a scavenging mechanism similar to that reported to produce O-Ni(CGC)W(CO)₅²⁻ from O-Ni(CGC)W(CO)₄²⁻.⁷⁵

When Me_3NO and IMes were added sequentially to O-am-[($\mu\text{-pdt}$)(Fe(CO)₃)(Fe(CO)₂PMe₃)] and heated at 55°C for 24 h, the resulting $\nu(\text{CO})$ bands (1982(m), 1962(s), 1903(m), 1892(sh) cm⁻¹) show that IMes substitution was successful. Again, attempts to oxidize with FcPF_6 resulted in loss of the IMes ligand and regeneration of the mono-substituted resin-bound complex, O-am-[($\mu\text{-pdt}$)(Fe(CO)₃)(Fe(CO)₂PMe₃)] ($\nu(\text{CO}) = 2036(\text{m}), 1981(\text{s}), 1960(\text{sh}), 1923(\text{w}) \text{ cm}^{-1}$). The addition CO needed to regenerate O-am-[($\mu\text{-pdt}$)(Fe(CO)₃)(Fe(CO)₂PMe₃)] is assumed to result from a scavenging mechanism. Currently, studies are being directed at other oxidizing agents and conditions to obtain the mixed valent species.

Interactions of TentaGel S-RAM[®] Beads with O-am-[A]

Understanding the environment and interactions surrounding resin-bound complexes would assist in elucidating the reactivity at that site. By comparing the effects of solvent polarity on the $\nu(\text{CO})$ bands of O-am-[A], the interactions of the TentaGel S-RAM[®] beads with the immobilized compound may be better understood. As assigned through computational studies by Dr. Christine Thomas and shown in Figure VII-5, the pseudo C_{2v} molecule has 5 IR active CO stretches. The deconvoluted spectrum for these

bands have been overlaid with the experimental ATR-FTIR spectrum of O-am-[A], showing that the three bands at lower wavenumbers have coalesced into one broad band.¹³⁶ That this line broadening is independent of any solvent “trapped” inside the beads was confirmed by NMR spectroscopy. Following synthesis of O-am-[A], the beads undergo extensive washes with DMF, THF, MeOH and Et₂O and then drying *in vacuo*. The wash with Et₂O is especially important as it is key to removing coordinating solvents that cannot escape easily from the beads upon drying. These beads may then be suspended in CDCl₃, a good solvent for swelling.⁹ The resulting ¹H NMR shows that a suspension of the beads washed and dried according to the protocol will display the resonance for CDCl₃ alone. However, when the protocol is not followed, the swelling in CDCl₃ allows for trapped solvents to leave the beads and for identification in the ¹H NMR spectrum of the wash.¹³⁵

As shown in Figure VII-6, the polarity of the solvent for (μ-pdt)[Fe(CO)₃]₂ affects the lowest frequency bands with respect to their overlap. When (μ-pdt)[Fe(CO)₃]₂ is dissolved in polar solvents such as MeOH, similar broadening occurs as observed for O-am-[A]. As solvent polarity decreases, however, these 3 lower frequency CO bands are resolved and are clearly distinguishable in benzene, the least polar of the solvents studied.

To mimic and compare the polyethylene glycol rich environment, expected for the TentaGel S-RAM[®] resin-bound complexes, the (μ-pdt)[Fe(CO)₃]₂ complex was dissolved in the polyether, tetraglyme (CH₃(OCH₂CH₂)₄OCH₃). The resulting infrared spectrum of this polyether oil shows the same broadening of the lower frequency bands observed in polar solvents and is consistent with the IR spectrum of the O-am-[A] model complex.

These results indicate that the line broadening of resin-bound complexes is a result of the resin-environment and that the TentaGel S-RAM[®] superstructure is not an inert, static environment. Rather, it interacts through dipole-dipole interactions with complexes imbedded within reminiscent of enzyme secondary coordination sphere contacts.

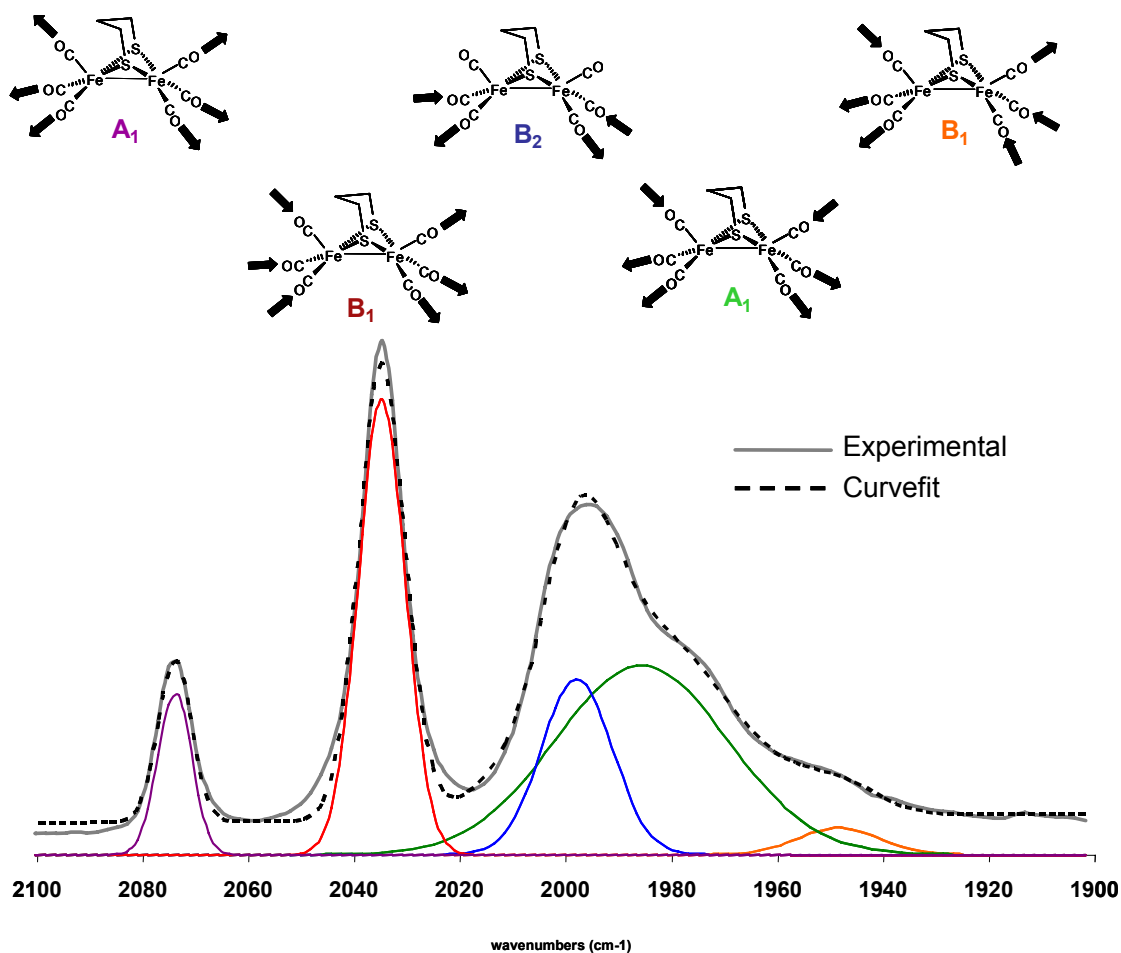


Figure VII-5. (Top) Assignment of vibrational modes for the $(\mu\text{-pdt})[\text{Fe}(\text{CO})_3]_2$ molecule and (Bottom) deconvoluted IR spectrum of O-am-[A] with the resulting fitted spectrum (---) and the experimental ATR-FTIR spectrum (—) overlaid.¹³⁶

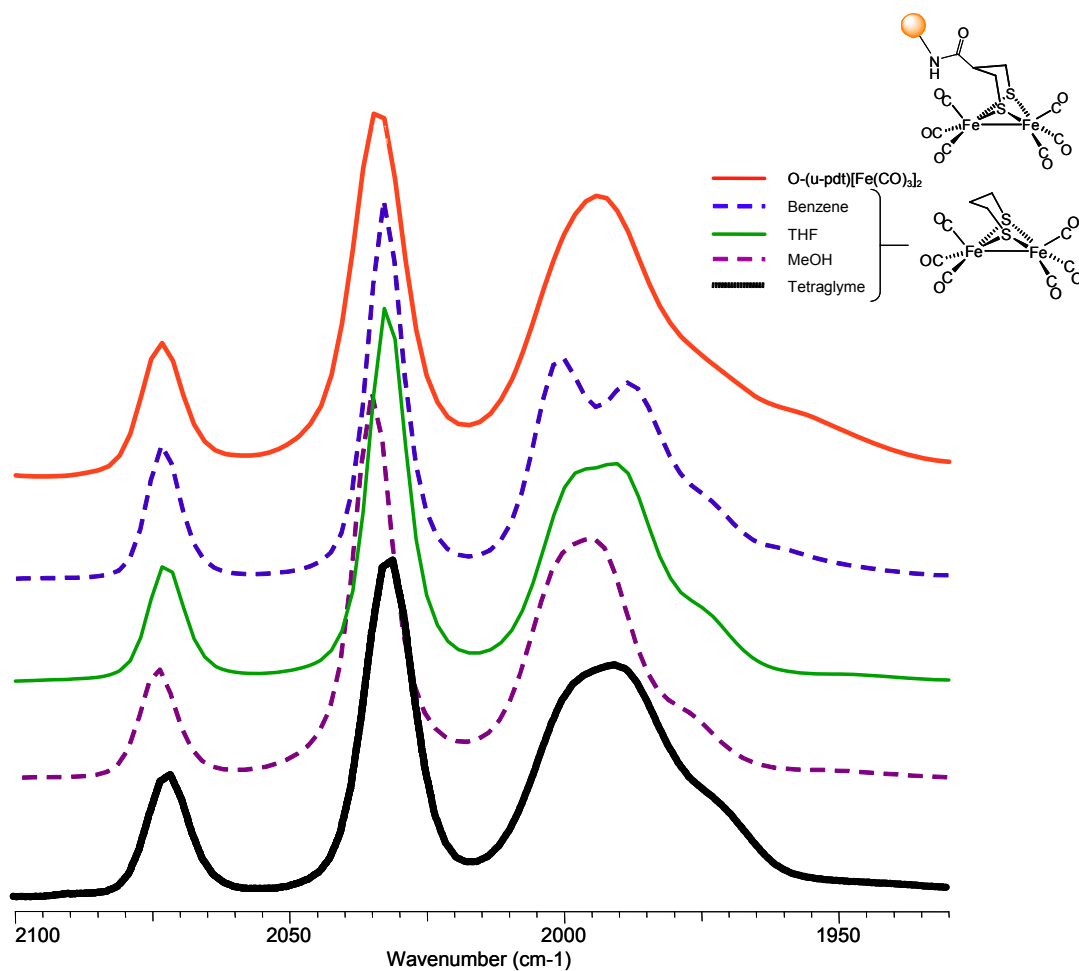


Figure VII-6. Overlay of Infrared Spectra of **O-am-[A]** and $(\mu-pdt)[Fe(CO)_3]_2$ dissolved in polar to non-polar solvents.

Comments and Conclusions

Immobilization of carboxy functionalized FeFe[H₂ase] model complexes using the TentaGel S-RAM[®] solid support was confirmed by comparison of the $\nu(\text{CO})$ bands obtained via ATR-FTIR to solution analogues. The substitution of CO ligands with phosphines was clearly established through the $\nu(\text{CO})$ bands and ³¹P NMR spectra, indicating that resin-bound reactivity parallels that on the resin-bead. Substitution with cyanide and N-heterocyclic carbene ligands is also possible as evidenced by the resulting band pattern and shift of CO bands to lower wavenumbers when compared to the parent resin-bound complex and the complexes in solution. The ability for these resin-bound complexes to exhibit the same substitution reactions shows that the resin-bead is an immobilized support that provides an environment capable of supporting solution type chemistry. That the solvation properties in the microenvironment are hydrophobic as expected from the formulation of the TentaGel Beads was also demonstrated in this work. Future work will focus on obtaining and stabilizing bridging functionalities such as $\mu\text{-CO}$ and $\mu\text{-H}$.

The work reported here established by the ninhydrin test that quantitative conversion of all the amine sites to amides occurs upon addition of the (COOH)[FeFe]H₂ase model complexes. Furthermore, reactivity with larger substituting ligands proved successful. Therefore, the use of the TentaGel S-RAM[®] bead as a mimic of the protein for model studies of biological systems is possible. However, the use of the Rink Linker is not necessary for attachment and other, acid stable linkers could and should be used.

To experimentally define the environment of the resin-bound complex, analysis of the “solvation” environment and its effect on the shape of the CO bands revealed that interactions with the resin-bound models and the PEG superstructure are similar to that observed for polar solvents, such as MeOH. As further evidence, the broadening of the lower frequency bands of the resin-bound model, O-am-[A], are directly mimicked by the polyether tetraglyme. These results indicate that (1) PEG is the environment surrounding the model and (2) environments reminiscent of secondary coordination spheres within enzyme active sites exist. To date, the literature has assumed that the microenvironment of a resin-bound complex is rich in PEG.¹¹ The work reported here experimentally establishes that PEG is the microenvironment surrounding the immobilized complexes. By defining the immobilization, reactivity and microenvironment of the resin-bound FeFe[H₂ase] models, further investigations into heterogenizing bioorganometallic catalytic systems will surely ensue.

CHAPTER VIII

CONCLUSIONS

The immobilization of catalysts onto polymeric supports has yet to achieve widespread use in industry although it has been shown to stabilize catalysts and provide a wide range of active catalysts.^{27,28} Despite these advantages slow turnover rates, metal leaching, and low catalyst loading have hindered extensive use.²⁸ Detailed studies aimed at carefully characterizing the catalyst resin-bound are only now becoming widespread.¹³⁷ These investigations will develop a better understanding of the effects of the support on the resin-bound catalyst and assuredly improve these immobilized systems, “catalyzing” their widespread use.

An additional approach at designing new catalysts as well as the polymeric supports for them takes lessons from nature. Nature has elegantly designed enzymes utilizing amino acids to construct peptide chains that fold into conformations suitable for carrying out chemical processes at rates higher than any man-made catalyst. Metalloenzymes, for example have rates of reaction that are typically several orders of magnitude higher than their synthetic counterparts.¹³⁸ Enzymes are capable of achieving this high level of performance using several optimizations. The redox potential of the metal is tuned by the surrounding proteins so that a normally irreversible redox reaction becomes reversible. The tuning can be done using specific ligands, held in precise geometries. Through this, proteins can stabilize a transition state by forcing the metal site into a geometry which has the appearance of a transition state intermediate. Furthermore,

proteins provide a substrate pocket for binding in specific geometries thereby facilitating a situation in which very few collisions are needed for a reaction to occur. By housing the metal center in a superstructure composed of this biological polymer, the catalytic site is primed for activity.

Understanding the mechanisms of metalloenzyme catalytic cycles has been advanced in myriad studies of small molecule models which focused on the primary coordination sphere surrounding the catalytic metal center. These models have utilized mainly synthetic organic ligands, but as shown in this work and that of others, more ligands composed of peptide or peptide like chelates are under investigation. Inspired by nature's use of a polymeric support for isolating enzymatic catalysts, the immobilization of biomimetic complexes of active sites in acetyl coA synthase, Type I copper sites, and [FeFe]H₂ase have been explored and the results discussed in this dissertation.

Inspired by the immobilized biological ligand found in acetyl coA synthase the resin-bound metallopeptide Ni(CGC)²⁻, O-Ni(CGC)²⁻, was constructed on TentaGel beads using Merrifield Peptide Synthesis and then metallated using standard synthetic inorganic techniques. Through ATR-FTIR spectroscopy of metal-carbonyl derivatives, resin-bound and in solution, the qualitative identification of the O-Ni(CGC)²⁻ complex was possible. To our knowledge this is the first time that M(CO)_x derivatives have been used in such a way. Additionally, quantitative identification of O-Ni(CGC)²⁻ and O-Ni(CGC)Rh(CO)₂⁻ was made using Neutron Activation Analysis (NAA), UV-Vis studies and IR spectroscopy. The accidental discovery of an Rh-PEG interaction provided a foundation for the expectation of other M-PEG contacts to follow. This resin-bound work was

largely paralleled in solution through the use of $\text{K}_2\text{Ni}(\text{CGC})$ and $[\text{Et}_4\text{N}]_2[\text{Ni}(\text{ema})]$. The $\text{O-Ni}(\text{CGC})\text{M}(\text{CO})_x$ derivatives were compared to solution complexes $\text{Ni}(\text{CGC})\text{W}(\text{CO})_4^{2-}$, $\text{Ni}(\text{ema})\text{W}(\text{CO})_4^{2-}$, and $\text{Ni}(\text{ema})\text{Rh}(\text{CO})_2^{1-}$. The former two complexes were used to establish that $\text{Ni}(\text{ema})^{2-}$ is a good model of the electron donor ability of $\text{Ni}(\text{CGC})^{2-}$. Therefore, as examples of thiolate reactivity and modification are found in several enzyme active sites, ACS and nitrile hydratase for example, the thiolate reactivity of $\text{Ni}(\text{ema})^{2-}$ was expanded upon and compared to the reactivity of neutral NiN_2S_2 complexes. The sulfinato species, $\text{Ni}(\text{ema})\cdot\text{O}_2^{2-}$, produced by exposure of crystalline $\text{Ni}(\text{ema})^{2-}$ to oxygen is the first dianionic $\text{NiN}_2\text{S}_{\text{thiolate}}\text{S}_{\text{sulfinato}}$ species reported while the synthesis of the macrocyclic complex, $\text{Ni}(\text{ema})\cdot(\text{CH}_2)_3$, parallels that established for the neutral complexes. The electrostatic potential maps generated by Scott Brothers for the macrocycle shows the molecule is now polarized, with $\text{S}-(\text{CH}_2)_3\text{-S}$ linker being electropositive and the electronegative region located abaft. By studying thiolate modification of the dianionic $\text{NiN}_2\text{S}_2^{2-}$ complex insights into the spectroscopic, structural and electrochemical implications of biological thiolate modification may be better understood.

Having firmly established the thiolate reactivity of the dianionic $\text{NiN}_2\text{S}_2^{2-}$ complexes the study of the copper(II) analogues of these complexes in collaboration with Dr. David Rockcliffe and his undergraduate student Boram Lee, to produce models of $\text{CuN}_2\text{SS}'$ active sites was carried out. Given the great tendency for $\text{Cu}^{\text{II}}/\text{RS}^-$ to participate in intramolecular redox processes and subsequent generation of Cu^{I} bridging CuN_2S_2 complexes, we were pleasantly surprised by the actual ease with which the $\text{Cu}(\text{ema})^{2-}$,

Cu(emi)^{2-} , and Cu(CGC)^{2-} were prepared and isolated. As indicated by spectroscopic solution studies, the molecular structure obtained for Cu(emi)^{2-} confirms that the Cu^{II} is found in a square planar N_2S_2 coordination sphere. As a number of the Cu^{II} complexes showed instability in solution, immobilization of Cu(CGC)^{2-} to TentaGel resin-beads to provide stabilization as observed for the O-Ni(CGC)^{2-} complex was carried out. The thiolate reactivity of these complexes, solution and resin-bound, was studied using Rh(CO)_2^+ . The cis-CO bands observed in the respective IR spectra showed that the Cu complexes serve as bidentate ligands to the Rh^+ center that the $\text{CuN}_2\text{S}_2^{2-}$ complexes are slightly better donors than the Ni^{II} analogues. Furthermore, the reactivity of the resin-bound complex, O-Cu(CGC)^{2-} , parallels that observed in solution and is almost identical to that of O-Ni(CGC)^{2-} . Moreover, with the stability of the resin-bound and solution $\text{CuN}_2\text{S}_2^{2-}$ complexes, a fundamental comparison of the spectroscopic, electrochemical and structural properties to the Ni^{II} analogues was made.

Finally, (COOH)-functionalized $[\text{FeFe}]\text{H}_2\text{ase}$ models were covalently anchored to TentaGel resin beads. The CO-substitution reactions of these light sensitive immobilized models with phosphines parallel the chemistry observed in solution resulting in mono- and disubstituted derivatives. Attempts to produce derivatives capable of binding H_2 proved unsuccessful; utilizing an acid tolerable linker would likely remedy this issue. Nevertheless, the CO-bands of the resin-bound complexes were used as a “handle” for understanding the immediate environment of the $[\text{FeFe}]\text{H}_2\text{ase}$ models. This study showed that the PEG-rich environment produced CO band broadening similar to that observed in spectra obtained from $(\mu\text{-pdt})[\text{Fe(CO)}_3]_2$ when dissolved in polar solvents such as

tetraglyme. We can therefore conclude, that these sites are surrounded by the polyether PEG.

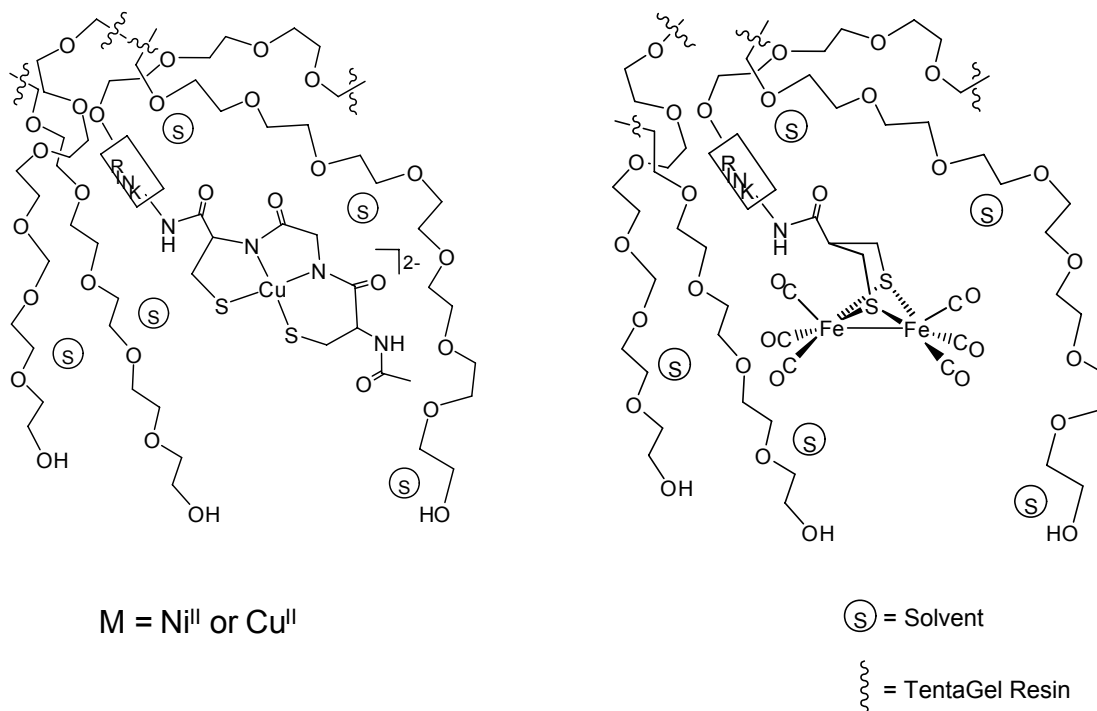


Figure VIII-1. Representation of O-M(CGC)²⁻ where M = Ni or Cu (left) and O-[A] (Right)

As a whole, the reactivity of solution bio-inspired model complexes is mirrored by the resin-bead immobilized analogues shown in Figure VIII-1. This indicated that the PEG microenvironment is highly mobile showing little steric hindrance to reactive substrates offered to the immobilized active sites. Characterization of the resin-bound complex, a problem in many heterogeneous catalysis systems, is possible using EPR for paramagnetic (EPR active) species but may also be accomplished by utilizing derivatives with CO or phosphine ligands through ATR-FTIR and ³¹P NMR spectroscopy. The

stability imparted by the resin-bead can be used to slow or prevent decomposition products that result from exposure to air. This work has been a fundamental study to show that resin-bound polymers as mimics of peptide superstructures can be utilized to isolate and characterize complexes while still retaining the reactivity.

Altogether the work presented in this dissertation has served to shed light on previously poorly-defined resin-bound complexes. Using the combined studies in Chapter III and VII, establishing the linkage of the resin-bound complexes served as a platform to understanding the immobilized complexes, Step 1 in Figure VIII-II. Based on the IR, EPR, and ^{31}P NMR spectroscopy, the structure of the resin bound complexes can be predicted by comparison to solution analogues. Additionally, through the use of solvent interactions with $(\mu\text{-pdt})[\text{Fe}(\text{CO})_3]_2$ and comparison to O-am-[A] a PEG rich environment could be firmly established. By the stepwise removal of the “black-box” a much more defined picture of the resin-bound complex can be composed.

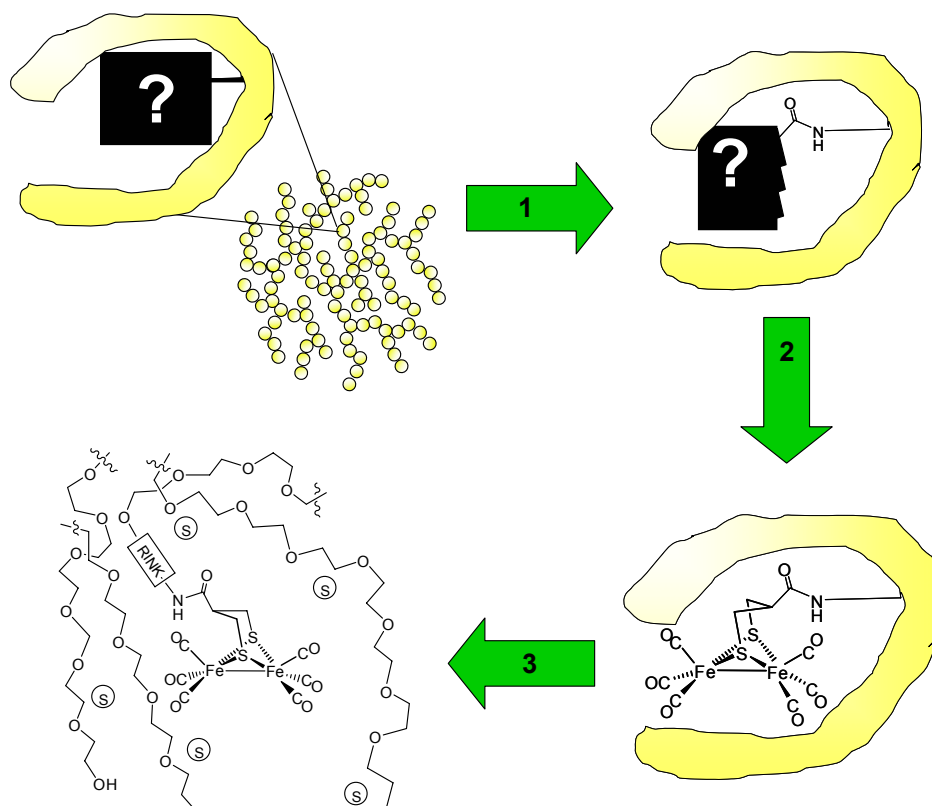


Figure VIII-2. The stepwise understanding of resin-bound complexes reported in this dissertation using O-am-[A] as an example.

Sir Isaac Newton once said, “If I have seen further than others, it is by standing on the shoulders of giants” and this sentiment is repeated often in our labs. As a scientist, we build our research on the platforms laid by others who have come before us. The basic principles of coordination chemistry, first established by Werner, apply to metalloenzymes as well. By applying the principles of inorganic chemistry to peptides produced by Merrifield type peptide synthesis a new type of heterogeneous system has been produced. Specifically, my work has also “stood on the shoulders” of another giant (and Nobel prize winner), Bob Grubbs, whose work in the immobilization of Wilkinson’s catalyst on polystyrene inspired me and led the way to my own work. Closer to home, group members Missy Golden, Steve Jeffery, and Marilyn Rampersad paved the way for the characteristic structural and solution chemistry that allowed me to “see” my immobilized derivatives. Thus the work discussed in this dissertation is novel in that it provides information about the fundamental properties of resin-bound complexes as well as their characterization. This work adds to the foundation for use of resin-bound complexes as functional catalysts, biological or industrial, by utilizing the protective resin-environment.

REFERENCES

-
1. Darnault, C.; Volbeda, A.; Kim, E.J.; Legrand, P.; Vernede, X.; Lindahl, P.A.; Fontecilla-Camps, J.C. *Nat. Struct. Biol.* **2003**, *10*, 271-279.
 2. (a) Dokov, I.T.; Iverson, T.M.; Seravalli, J.; Ragsdale, S.W.; Drennan, C.L. *Science* **2002**, *298*, 567-572. (b) Amara, P.; Fonticella-Camps, J.C.; Field, M. *J. Am. Chem. Soc.* **2005**, *127*, 2776-2784.
 3. Webster, C. E., Darensbourg, M. Y., Lindahl, P. A. & Hall, M. B. *J. Am. Chem. Soc.* **2004**, *126*, 3410-3411.
 4. Phelps, A. L.; Rampersad, M. V.; Fitch, S. B.; Darensbourg, M. Y.; Darensbourg, D. J. *Inorg. Chem.* **2006**, *45*, 119-126.
 5. Grubbs, R.H.; Kroll, L.C. *J. Am. Chem. Soc.*, **1971**, *93*, 3062 -3063.
 6. For an excellent review of polymer-supported catalysts see Ford, W. T.; Bergbreiter, D. E.; Waller, F. J.; Ekerdt, J. G.; Garrou, P. E.; Neckers, D. C.; Taylor, R. T.; Wulff, G.; Patchornick, A.; Nov, E.; Jacobson, K. A.; Shai, Y. (1986) In *Polymer Reagents and Catalysts* (ACS Symposium Series 308; American Chemical Society).
 7. (a) Kunquan, Y.; McKittrick, M. W.; Jones, C. W. *Organometallics* **23**, 4089-4096. (b) Annis, D. A.; Jacobsen, E. N. *J. Am. Chem. Soc.* **1999**, *121*, 4147-4154. (c) Leadbeater, N. *J. Org. Chem.* **2001**, *66*, 2168-2170.

-
8. (a) Helfferich, F. “*Ion Exchange*”, McGraw-Hill, New-York, 1962. Ch. 11. (b) Gait, M. J. Int6 “*Polymer-supported Reactions in Organic Synthesis*”; Hodge, P.; Sherrington, D. C.; Eds.; Wiley-Interscience, New York, 1980, Ch 3.
9. Novabiochem 2006-2007 Catalog, Merck Biosciences AG, 2006, 195-204, 219-336, 359-408.
10. Shapiro, B. L (1984) In *Heterogeneous Catalysis (Proceeding of the Second Symposium of the Industry-University Cooperative Chemistry Program of the Department of Chemistry, Texas A&M University)*.
11. Hodge, P. *Chem. Soc. Rev.* **1997**, 26, 417-424.
12. Chan, W. G.; White, P. D. *Fmoc solid phase peptide synthesis, A Practical Approach*; Oxford University Press, New York, 2000, pp. 1-5.
13. Sheppard, R. C. *Ann. Rep.* **1963**, 60, 448-466.
14. Merrifield, R. B. *J. Am. Chem. Soc.* **1963**, 85, 2149-2154.
15. Merrifield, R.B. *J. Am. Chem. Soc.* **1964**, 86, 304 – 305.
16. Bayer, E. *Angew. Chem. Int. Ed. Engl.* **1991**, 30, 113-129.
17. Chan, W. G.; White, P. D. *Fmoc solid phase peptide synthesis, A Practical Approach*; Oxford University Press, New York, 2000, pp. 15-20.
18. Chan, W. G.; White, P. D. *Fmoc solid phase peptide synthesis, A Practical Approach*; Oxford University Press, New York, 2000, pp. 13-15.
19. Sherrington, D.C. *Chem. Comm.* **1998**, 2275-2286.
20. Novabiochem 2006-2007 Catalog, Merck Biosciences AG, 2006, Section 2.1.1.

-
21. Chan, W. G.; White, P. D. *Fmoc solid phase peptide synthesis, A Practical Approach*; Oxford University Press, New York, 2000, pp. 15.
22. Novabiochem 2006-2007 Catalog, Merck Biosciences AG, 2006, Section 2.2.1.
23. Novabiochem 2006-2007 Catalog, Merck Biosciences AG, 2006, Section 2.3.1.
24. Novabiochem 2006-2007 Catalog, Merck Biosciences AG, 2006, pp. 223.
25. Chan, W. G.; White, P. D. *Fmoc solid phase peptide synthesis, A Practical Approach*; Oxford University Press, New York, 2000, pp. 65-66.
26. For reviews on supported catalysts, see: (a) McNamara, C. A.; Dixon M. J.; Bradley, M. *Chem. Rev.* **2002**, *102*, 3275 – 3300. (b) Dickerson, T. J.; Reed, N. N.; Janda, K. D. *Chem. Rev.* **2002**, *102*, 3325 – 3344. (c) Bergbreiter, D. E. *Chem. Rev.* **2002**, *102*, 3345 – 3384. (d) Fan, Q.-H.; Li, Y.-M.; Chan, A. S. C. *Chem. Rev.* **2002**, *102*, 3385 – 3466. (e) Benaglia, M.; Puglisi, A.; Cozzi, F. *Chem. Rev.* **2003**, *103*, 3401 – 3430.
27. Clavier, H.; Grela, K.; Kirschning, A.; Mauduit, M.; Nolan, S. P. *Angew. Chem.* **2007**, *46*, 6786-6801.
28. Heitbaum, M.; Glorius, F.; Escher, I. *Angew. Chem. Int. Ed.* **2006**, *45*, 4732-4762.
29. Nguyen, S. T.; Grubbs, R. H. *J. Organomet. Chem.* **1995**, *487*, 195-200.
30. Mennecke, K.; Grela, K.; Kunz, U.; Kirschning, A. *Synlett.* **2005**, 2948-2952.
31. Cannon, S. J.; Blechert, S. *Biorg. Med. Chem. Lett.* **2002**, *12*, 1873-1876.
32. Grela, K.; Tryznowski, M.; Bieniek, M. *Tetrahedron Lett.* **2002**, *43*, 9055-9059.

-
33. (a) Yao, Q *Angew. Chem.* **2000**, *112*, 4060-4062. (b) Yao, G. *Tetrahedron Lett.* **2004**, *45*, 2447-2451. (c) Varray, S.; Lazaro, R.; Martinez, J.; Lamaty, F. *Organometallics* **2003**, *22*, 2426-2435.
34. Annis, D. A.; Jacobsen, E. N. *J. Am. Chem. Soc.* **1999**, *121*, 4147-4154.
35. Ford, W. T.; Bergbreiter, D. E.; Waller, F. J.; Ekerdt, J. G.; Garrou, P. E.; Neckers, D. C.; Taylor, R. T.; Wulff, G.; Patchornick, A.; Nov, E.; Jacobson, K. A.; Shai, Y. (1986) In *Polymer Reagents and Catalysts* (ACS Symposium Series 308; American Chemical Society). pp. 13, 84-106.
36. Gladysz, J.A. *Pure Appl. Chem.* **2001**, *73*, 1319-1324.
37. Skander, M.; Hubert, N.; Collot, J.; Graninaru, J.; Klein, A.; Sauser, J.; Zocchi, A.; Gilardoni, F., Ward, T. *J. Am. Chem. Soc.*, **2004**, *126*, 14411-14418.
38. Carey, J.; Ma, S.; Pfister, T.; Garner, D.; Kim, H.; Abramite, J.; Wang, Z.; Lu, Y. *J. Am. Chem. Soc.* **2004**, *126*, 10812-10813.
39. (a) Grether, U.; Waldmann, H. *Chem. Eur. J.* **2001**, *7*, 959-970. (b) Sauerbrei, B.; Jungmann, V.; Waldmann, H. *Angew. Chem. Int. Ed.* **1998**, *37*, 1143-1146.
40. (a) Vágner, J.; Barany, G.; Lam, K. S.; Krchňák, V.; Sepetov, N. F.; Ostrem, J. A.; Strop, P.; Lebl, M. *Proc. Natl. Acad. Sci USA* **1996**, *93*, 8194-8199. (b) Kress, J.; Analetti, R.; Amour, A.; Ladlow, M.; Frey, J. G.; Bradley, M. *Chem. Eur. J.* **2002**, *8*, 3769-3772.
41. Nagashima, S.; Nakasako, M.; Dohmae, N.; Tsujimura, M.; Takio, K.; Odaka, M.; Yohda, M.; Kamiya, N.; Endo, I. *Nat. Struct. Biol.* **1998**, *5*, 347 – 351.

-
42. Barondeau, D. P.; Kassmann, C. J.; Bruns, C.K.; Tainer, J.A.; Getzoff, E.D. *Biochemistry* **2004**, *43*, 8038-8047. (c) Wuerges, J.; Lee, J.-W.; Yim, Y.-I.; Yim, H.-S.; Kang, S.-O.; Carugo, K. D. *Proc. Natl. Acad. Sci. USA* **2004**, *101*, 8569-8574.
43. (a) Choudhury, S. B.; Davidson, G.; Yim, Y.-I.; Bose, K.; Sharma, M. L.; Kang, S.-O.; Cabelli, D. E.; Maroney, M. J. *Biochemistry*, **1999**, *38*, 3744-3752. (b) Wuerges, J.; Lee, J.-W.; Yim, Y.-I.; Yim, H.-S.; Kang, S.-O.; Carugo, K. D. *Proc. Natl. Acad. Sci. USA* **2004**, *101*, 8569-8574.
44. (a) Golden, M. L.; Rampersad, M. V.; Reibenspies, J. H.; Darensbourg, M. Y. *Chem. Comm.* **2003**, 1824-1825. (b) Jeffery, S. P.; Lee, J.; Darensbourg, M. Y. *Chem. Comm.* **2005**, 1122-1124. (c) Rao, P. V.; Bhaduri, S.; Jiang, J.; Holm, R. H. *Inorg. Chem.* **2004**, *43*, 5833-5849.
45. Gordon, A. J.; Ford, R. A. *The Chemist's Companion*; Wiley and Sons: New York. 1972; 429-436.
46. Connelly, N.G.; Geiger, W.E. *J. Am. Chem. Soc.* **1996**, *96*, 877-910.
47. *WINEPR SIMFONIA version 1.25*, Bruker Analytische Messtechnik GmbH, 1996.
48. Darensbourg, D. J.; Kump, R. L. *Inorg. Chem.* **1978**, *17*, 2680-2682.
49. Krishnan, R.; Riordan, C. G. *J. Am. Chem. Soc.* **2004**, *126*, 4484-4485.
50. Krüger, H.-J.; Peng, G.; Holm, R. H. *Inorg. Chem.* **1991**, *30*, 734-742.
51. Rampersad, M. V.; Jeffery, S. P.; Golden, M. L.; Lee, J.; Reibenspies, J. H.; Darensbourg, D. J.; Darensbourg, M. Y. *J. Am. Chem. Soc.* **2005**, *127*, 17323-17334.

-
52. Hatlevik, Ø; Blanksma, M. C.; Mathrubootham, V.; Arif, A. M.; Hegg, E. L. *J. Biol. Inorg. Chem.* **2004**, *9*, 238-246.
53. SAINT V6.63 "Program for Reduction of Area Detector Data" BRUKER AXS Inc., 5465 East Cheryl Parkway, Madison, WI 53711-5373 USA
54. SADABS, Sheldrick, G. M. "Program for Absorption Correction of Area Detector Frames," BRUKER AXS Inc., 5465 East Cheryl Parkway, Madison, WI 53711-5373 USA.
55. L. J. Barbour, "X-Seed - A software tool for supramolecular crystallography" *J. Supramol. Chem.* **2001**, *1*, 189-191.
56. Becke, A. D. *J. Chem. Phys.* **1993**, *98*, 5648.
57. Lee, C.; Yang, W.; Parr, R. G. *Phys. Rev.* **1988**, *37*, 785.
58. Frisch, M. J.; Trucks, G. W.; Schlegel, H. B.; Scuseria, G. E.; Robb, M. A.; Cheeseman, J. R.; Montgomery, Jr., J. A.; Vreven, T.; Kudin, K. N.; Burant, J. C.; Millam, J. M.; Iyengar, S. S.; Tomasi, J.; Barone, V.; Mennucci, B.; Cossi, M.; Scalmani, G.; Rega, N.; Petersson, G. A.; Nakatsuji, H.; Hada, M.; Ehara, M.; Toyota, K.; Fukuda, R.; Hasegawa, J.; Ishida, M.; Nakajima, T.; Honda, Y.; Kitao, O.; Nakai, H.; Klene, M.; Li, X.; Knox, J. E.; Hratchian, H. P.; Cross, J. B.; Bakken, V.; Adamo, C.; Jaramillo, J.; Gomperts, R.; Stratmann, R. E.; Yazyev, O.; Austin, A. J.; Cammi, R.; Pomelli, C.; Ochterski, J. W.; Ayala, P. Y.; Morokuma, K.; Voth, G. A.; Salvador, P.; Dannenberg, J. J.; Zakrzewski, V. G.; Dapprich, S.; Daniels, A. D.; Strain, M. C.; Farkas, O.; Malick, D. K.; Rabuck, A. D.; Raghavachari, K.; Foresman, J. B.; Ortiz, J. V.; Cui, Q.; Baboul, A. G.; Clifford, S.;

Cioslowski, J.; Stefanov, B. B.; Liu, G.; Liashenko, A.; Piskorz, P.; Komaromi, I.; Martin, R. L.; Fox, D. J.; Keith, T.; Al-Laham, M. A.; Peng, C. Y.; Nanayakkara, A.; Challacombe, M.; Gill, P. M. W.; Johnson, B.; Chen, W.; Wong, M. W.; Gonzalez, C.; and Pople, J. A.; Gaussian 03, Revision C.02, Gaussian, Inc., Wallingford CT, 2004.

59. Dunning, T.H. *J. Chem. Phys.* **1989**, *98*, 1007.
60. Dunning, T.H. *J. Chem. Phys.* **1970**, *53*, 2823.
61. Dunning, T.H.; Hay, P.J. *In Methods of Electronic Structure Theory Vol. 2*, H.F. Schaefer III, Ed., Plenum Press, New York 1977.
62. Cerius 2 3.0, MSI Cambridge, UK.
63. Manson, J. M. B.; Webster, C. E.; Hall, M. B. Jimp 2 Version 0.91, 1/8/07, Microsoft Windows XP; Department of Chemistry, Texas A&M University, College Station, TX 77842, (<http://www.chem.tamu.edu/jimp2/>).
64. Dennington II, Roy; Keith, Todd; Millam, John; Eppinnett, Ken; Hovell, W. Lee; and Gilliland, Ray; GaussView, Version 3.09, Semichem, Inc., Shawnee Mission, KS, 2003.
65. Thomas, C. M.; Rudiger, O.; Liu, T.; Carson, C. E.; Hall, M. B.; Darensbourg, M. Y. *Organometallics* **2007**, *26*, 3976-3984.
66. Arduengo III, A. J.; Dias, H. V. R.; Harlow, R. L.; Kline, M. *J. Am. Chem. Soc.* **1992**, *114*, 5530.
67. Cotton, F. A.; Kraihanzel, C. S. *J. Am. Chem. Soc.* **1962**, *84*, 4432-4438.

-
68. van Leeuwen, P. W. N. M.; Kamer, P. C. J.; Reek, J. N. H.; Dierkes, P. *Chem. Rev.* **2000**, *100*, 2741-2769.
69. Burling, S.; Field, L. D.; Messerle, B. A.; Turner, P. *Organometallics* **2004**, *23*, 1714-1721.
70. Burling, S.; Field, L. D.; Li, H. L.; Messerle, B. A.; Turner, P. *Eur. J. Inorg. Chem.* **2003**, 3179-3184.
71. Del Zotto, A.; Costella, L.; Mezzetti, A.; Rigo, P. *J. Organomet. Chem.* **1991**, *414*, 109-118.
72. (a) Rankin, J.; Poole, A. D.; Benyei, A. C.; Cole-Hamilton, D. J. *Chem. Commun.* **1997**, 1835-1836. (b) Dilworth, J. R.; Miller, J. R.; Wheatley, N.; Baker, M. J.; Sunley, J. G. *Chem. Commun.* **1995**, 1579-1581. (c) Baker, M. J.; Giles, M. F.; Orpen, A. G.; Taylor, M. J.; Watt, R. J. *Chem. Commun.* **1995**, 197-198.
73. Manning, A.R. *J. Chem. Soc. (A)* **1967**, 1982- 1987.
74. Annis, D. A.; Jacobsen E. N. *J. Am. Chem. Soc.* **1995**, *121*, 4147-4154.
75. K.N. Green, S.P. Jeffery, J.H. Reibenspies, M.Y. Darensbourg, *J. Am. Chem. Soc.* **2006**, *128*, 6493-6498.
76. W.C. Chan, and P.C. White, *Fmoc solid phase peptide synthesis: A Practical Approach*, Oxford University Press, New York, New York, 2000, pp. 62-64.
77. J. Milton Harris, *Polyethylene Glycol Chemistry: Biotechnical & Biomedical applications*, Plenum Press, New York, 1992, 10, pp. 13-15.
78. Bouwman, E.; Reedijk, J. *Coord. Chem. Rev.* **2005**, *249*, 1555-1581 and references therein.

-
79. Jicha, D. C.; Busch, D. H. *Inorg. Chem.* **1962**, *1*, 872-877.
80. Kitagawa, T.; Dey, A.; Lugo-Mas, P.; Benedict, J. B.; Kaminsky, W.; Solomon, E. ; Kovacs, J.A. *J. Am. Chem. Soc.* **2006**, *128*, 14448-14449.
81. Harrop, T. C.; Mascharak, P. K. *Coord. Chem. Rev.* **2005**, *249*, 3007-3024.
82. (a) Duff, S. E.; Barclay J. E.; Davies S. C.; Evans, D. J. *Inorg. Chem. Commun.* **2005**, *8*, 170-173. (b) Duff, S. E.; Barclay, J. E.; Davies, S. C.; Hitchcock, P. B.; Evans, D. J. *Eur. J. Inorg. Chem.* **2005**, 4527-4532
83. (a) Osterloh, F.; Saak, W.; Pohl, S. *J. Am. Chem. Soc.* **1997**, *119*, 5648-5656. (b) Perra, A.; Davies, E. S.; Hyde, J. R.; Wang, Q.; McMaster, J.; Schröder, M. *Chem. Comm.* **2006**, 1103-1105. (c) Linck, R. C.; Spahn, C. W.; Rauchfuss, T. B.; Wilson, S. R. *J. Am. Chem. Soc.* **2003**, *125*, 8700-8701.
84. (a) Farmer, P. J.; Verpeaux, J. N.; Amatore, C. J. Darenbourg, M. Y.; Musie, G. *J. Am. Chem. Soc.* **1994**, *116*, 9355-9356. (b) Kaasjager, V. E.; Bouwman, E.; Gorter, S.; Reedjik, J.; Grapperhaus, C.A.; Reibenspies, J. H.; Smee, J. J.; Darenbourg, M. Y.; Derecskei-Kovacs, A.; Thomson, L. M. *Inorg. Chem.* **2002**, *41*, 1837-1844 and references therein. (c) Buonomo, R. M.; Font, I.; Maguire, M. J.; Reibenspies, J. H.; Tuntulani, T.; Darenbourg, M. Y. *J. Am. Chem. Soc.* **1995**, *117*, 963-973. (d) Mirza, S. A.; Pressler, M. A.; Kumar, M.; Day, R. O.; Maroney, M. J. *Inorg. Chem.*, **1993**, *32*, 977-987. (e) Schrauzer, G. N.; Zhang, C.; Chadha, R. *Inorg. Chem.* **1990**, *29*, 4104-4107.
85. a) Musie, G.; Reibenspies, J. H.; Darenbourg, M. Y. *Inorg. Chem.* **1998**, *37*, 302-310. (b) Smee, J. J.; Miller, M. L.; Grapperhaus, C. A.; Reibenspies, J. H.;

-
- Darensbourg, M. *Inorg. Chem.* **2001**, *40*, 3601-3605. (c) Smee, J. J.; Goodman, D. C.; Reibenspies, J. H.; Darensbourg, M. Y. *Eur. J. Inorg. Chem.* **1999**, 539-546. (d) Hsaio, Y.-M.; Chojnacki, S.S.; Hinton, P.; Reibenspies, J. H.; Darensbourg, M. Y. *Organometallics* **1993**, *12*, 870-875.
86. Fiedler, A. T.; Bryngelson, P. A.; Maroney, M. J.; Brunold, T. C. *J. Am. Chem. Soc.* **2005**, *127*, 5449-5462.
87. Fiedler, A. T.; Brunold, T. C. *Inorg. Chem.* **2007**; *ASAP Article*.
88. Mullins, C. S.; Grapperhaus, C. A.; Kozlowski, P. M. *J. Biol Inorg. Chem.* **2006**, *11*, 617-625.
89. Farmer, P. J.; Reibenspies, J.H.; Lindahl, P. A.; Darensbourg, M.Y. *J. Am. Chem. Soc.* **1993**, *115*, 4665-4674.
90. Lugo-Mas, P.; Dey, A.; Xu, L.; Davin, S. D; Benedict, J.; Kaminsky, W.; Hodgson, K. O.; Hedman, B.; Solomon, E. I.; Kovacs, J.A. *J. Am. Chem. Soc.* **2006**, *128*, 11211-11221.
91. Maroney, M. J.; Choudhury, S. B.; Bryngelson, P. A.; Mirza, S. A.; Sherrod, M. J. *Inorg. Chem.* **1996**, 1073-1076.
92. a) Shearer, J.; Zhao, N. *Inorg. Chem.* **2006**, *45*, 9637-9639. (b) Shearer, J.; Long, L. M. *Inorg. Chem.* **2006**, 2358-2360.
93. Korniyushyna, O; Stemmler, A.; Graybosch, D.; Bergenthal, I.; Burrows, C. *Bioconjugate Chem.* **2005**, *16*, 178-183.
94. Rockcliffe, D. A.; Cammers, A.; Murali, A.; Russell, W. K.; Derose, V. J. *Inorg. Chem.* **2006**, *45*, 472-474.

-
95. (a) Colman, P. M.; Freeman, H. C.; Guss, J. M.; Murata, M.; Norris, V. A.; Ramshaw, J. A. M.; Venkatappa, M. P. *Nature* **1978**, *272*, 319. (b) Guss, J. M.; Bartunik, H. D.; Freeman, H. C. *Acta Crystallogr, Sect.B* **1992**, *48*, 790-811.
96. Guss, J. M.; Merritt, E. A.; Phizackerley, R. P.; Freeman, H. C. *J. Mol. Biol.* **1996**, *262*, 686-705.
97. Adman, E. T.; Godden, J. W.; Turley, S. *J. Biol. Chem.* **1995**, *270*, 27,458-27,474.
98. Kraatz, H. -B.; Metzler-Nolte, N. (2006) in *Concepts and Models in Bioinorganic Chemistry*, Wiley, Weinheim, Germany, pp. 364-395.
99. Houser, R. P.; Tolman, W. B. *Inorg. Chem.* **1995**, *34*, 1632-1633.
100. Solomon, E. I. *Inorg. Chem.* **2006**, *45*, 8012-8025.
101. Mills, D. K.; Reibenspies, J. H.; Darensbourg, M. Y. *Inorg. Chem.* **1990**, *29*, 4364-4366.
102. Golden, M. L.; Whaley, C. M.; Rampersad, M. V.; Reibenspies, J. H.; Hancock, R. D.; Darensbourg, M. Y. *Inorg. Chem.* **2005**, *44*, 875-883.
103. Bharadwaj, P. K.; Potenza, J. A.; Schugar, H. J. *J. Am. Chem. Soc.* **1986**, *108*, 1351-1352.
104. Klein, E. L.; Khan, M. A.; Houser, R. P. *Inorg. Chem.* **2004**, *43*, 7272-7274.
105. Hanss, J.; Krüger, H. J. *Angew. Chem. Int. Ed. Engl.* **1996**, *23*, 2827-2830.
106. Miller, M. L.; Ibrahim, S. A.; Golden, M. L.; Darensbourg, M. Y. *Inorg. Chem.* **2003**, *42*, 2999-3007.

-
107. Nefliu, M.; Cooks, G. R.; Moore, C. *J. Am. Soc. Mass Spectrom.* **2006**, *17*, 1091-1095.
108. Cotton, F.A.; Wilkinson, G. *Advanced Inorganic Chemistry*, 3rd Ed. John Wiley & Sons, New York, 1972.
109. Peisach, J.; Blumberg, W.E. *Arch. Biochem. Biophys.* **1974**, *165*, 691-708.
110. Bereman, R. D.; Sheilds, G. D.; Bordner, J.; Dorfman, J. R. *Inorg. Chem.* **1981**, *20*, 2165-2169.
111. Green, K. N.; Brothers, S. M.; Jenkins, R. M.; Carson, C. E.; Grapperhaus, C. A.; Darensbourg, M. Y. *Inorg. Chem.* **2007**, *46*, 7536-7544.
112. Jeffery, S. P.; Green, K. N.; Rampersad, M. V.; Reibenspies, J. H.; Darensbourg, M. Y. *Dalton Trans.* **2006**, 4244-4252.
113. Bramlett, M. R.; Tan, X.; Lindahl, P. A. *J. Am. Chem. Soc.* **2003**, *125*, 9316-9317.
114. Green, K. N.; James, W. D.; Cantillo, A. V.; Darensbourg, M. Y. *J. Organomet. Chem.* **2007**, *692*, 1392-1397.
115. Nicolet, Y.; de Lacey, A. L.; Vernéde, X.; Fernandez, V. M.; Hatchikian, E. C.; Fontecilla-Camps, J. C. *J. Am. Chem. Soc.* **2001**, *123*, 1596-1601.
116. Chen, Z.; Lemon, B. J.; Huang, S.; Swartz, D. J.; Peters, J. W.; Bagley, K. A. *Biochemistry* **2002**, *41*, 2036-2043.
117. Nicolet, Y.; Lemon, B. J.; Fontecilla-Camps, J. C.; Peters, J. W. *Trends Biochem. Sci.* **2000**, *25*, 138-143.

-
118. (a) Adams, M. W. W.; Stiefel, E. I. *Science* **1998**, *282*, 1842-1843. (b) Cammack, R.; Frey, M.; Robson, R. *Hydrogen as a Fuel: Learning from Nature*; Taylor and Francis: London, 2001.
119. (a) Reihlen, H.; Gruhl, A.; Hessling, G. *Liebigs Ann. Chem.* **1929**, *472*, 268. (b) Seyferth, D.; Womack, G. B.; Archer, C. M.; Dewan, J. C. *Organometallics* **1989**, *8*, 430-442. (c) Bor, G. J. *J. Organomet. Chem.* **1968**, *11*, 195-197.
120. Darensbourg, M. Y.; Lyon, E. J.; Smee, J. J. *Coord. Chem. Rev.* **2000**, *206-207*, 533-561 and references therein.
121. Evans, D. J.; Pickett, C. J. *Chem. Soc. Rev.* **2003**, *32*, 268-275.
122. (a) Chong, D.; Georgakaki, I. P.; Mejia-Rodriguez, R.; Sanabria-Chinchilla, J.; Soriaga, M. P.; Darensbourg, M. Y. *Dalton Trans.* **2003**, 4158-4163. (b) Mejia-Rodriguez, R.; Chong, D.; Reibenspies, J. H.; Soriaga, M. P.; Darensbourg, M. Y. *J. Am. Chem. Soc.* **2004**, *126*, 12004-12014.
123. (a) Darensbourg, M. Y.; Lyon, E. J.; Zhao, X.; Georgakaki, I. P. *Proc. Natl. Acad. Sci.* **2003**, *100*, 3683-3688. (b) Tye, J. W.; Hall, M. B.; Georgakaki, I. P.; Darensbourg, M. Y. *Adv. Inorg. Chem.* **2004**, *56*, 1-26. (c) Zhao, X.; Georgakaki, I. P.; Miller, M. L.; Yarbrough, J. C.; Darensbourg, M. Y. *J. Am. Chem. Soc.* **2001**, *123*, 9710-9711. (d) Zhao, X.; Chiang, C.-Y.; Miller, M. L.; Rampersad, M. V.; Darensbourg, M. Y. *J. Am. Chem. Soc.* **2003**, *125*, 518-524. (e) Georgakaki, I. P.; Miller, M. L.; Darensbourg, M. Y. *Inorg. Chem.* **2003**, *42*, 2489-2494.
124. Elgren, T. E.; Zadvorny, O. A.; Brecht, E.; Douglas, T.; Zorin, N. A.; Maroney, M. J.; Peters, J. W. *Nano Letters* **2005**, *5*, 2085-2087.

-
125. Ibrahim, S. K.; Liu, X.; Tard, C.; Pickett, C. *Chem. Commun.* **2007**, 1535-1537.
126. (a) Vijaikanth, V.; Capon, J. F.; Gloaguen, F.; Petilon, F. Y.; Schollhammer, P.; Talarmin, J. *J. Organomet. Chem.* **2007**, 692, 4177-4181. (b) Volkers, P. I.; Rauchfuss, Wilson, S. R. *Eur. J. Inorg. Chem.* **2006**, 4793-4799.
127. Desrochers, P. J.; Duong, D. S.; Marshall, A. S.; Lelievre, S. A.; Hong, B.; Brown, J. R.; Tarkka, R. M.; Manion, J. M.; Holman, G.; Merkert, J. W.; Vicic, D. A. *Inorg. Chem.* **2007**, ASAP Article.
128. Lyon, E. J.; Georgakaki, I. P.; Reibenspies, J. H.; Darensbourg, M. Y. *Angew. Chem. Int. Ed.* **1999**, 38, 3178-3180.
129. Seyferth, D.; Henderson, R. S.; Song, L. C. *J. Organomet. Chem.* **1980**, 192, C1-C5.
130. Li, P.; Wang, M.; He, C.; Li, G.; Liu, X.; Chen, C.; Akermark, B.; Sun, L. *Eur. J. Inorg. Chem.* **2005**, 2506-2513.
131. Liu, T.; Darensbourg, M. Y. *J. Am. Chem. Soc.* **2007**, 129, 7008-7009.
132. Gloaguen, F.; Lawrence, J. D.; Schmidt, M.; Wilson, S. R.; Rauchfuss, T. B. *J. Am. Chem. Soc.* **2001**, 123, 12518-12527.
133. Bennett, B.; Lemon, B. J.; Peters, J. W. *Biochemistry* **2000**, 39, 7455-7460.
134. Rosenboom, W.; de Lacey, A. L.; Vernede, X.; Fernandez, V.M.; Hatchikian, E. C.; Fontecilla-Camp, J. C. *J. Biol. Inorg. Chem.* **2006**, 11, 102-118.
135. Gottlieb, H. E.; Kotlyar, V.; Nudelman, A. *J. Org. Chem.* **1997**, 62, 7512-7515.
136. PeakFit 2.1
137. Zheng, X.; Jones, C.; Weck, M. *Chem. Eur. J.* **2006**, 12, 576-583.

-
138. Voet, D.; Voet, J. G.; Pratt, C. W. *Fundamentals of Biochemistry*; Wiley & Sons: New York, 2002; pp 282-284.

APPENDIX A

SUPPLEMENTAL MATERIAL FOR CHAPTERS III-VII

Contents

Figure A-1. Ball and Stick representation of the $[S_2Rh(CO)_2]_2$ unit of **E**, showing the deviation from eclipsed conformation. (Rh(2A) is located directly behind Rh(1A)).

Figure A-2. Packing diagram of $[Et_4N]_2[Ni(ema)Rh(CO)_2]_2$.

Table A-1. Infrared $\nu(CO)$ stretching frequencies for selected complexes.

Figure A-3. Packing diagram of $Ni(ema)\bullet(CH_2)_3$.

Figure A-4. Packing diagram of $[Et_4N]_2[Ni(ema)\bullet O_2]$.

Figure A-5. The ^-ESI -mass spectrum of $[Et_4N]_2[Ni(ema)\bullet O_2]$ showing the fragmentation by loss of O_2 and SO_2 .

Figure A-6. X-band EPR spectra (top) obtained from an oxidized solution of $Ni(ema)\bullet(CH_2)_3$ using CAN in DMF (a) and its pyridine adduct (b) in a DMF/pyridine solution (4:1 v/v) at 10 K and the corresponding simulations (c,d respectively).

Figure A-7. Representation of the NiN_2S_2 plane for $Ni(ema)\bullet(CH_2)_3$ and $Ni(ema)\bullet O_2^{2-}$ and deviations of each atom from the best plane.

Figure A-8. Cyclic Voltammogram of a 3.4 mM solution of $Ni(ema)[Me]_2$ in DMF at a scan rate of 200 mV/s using a Ag/AgNO₃ reference electrode, 0.1 M $[nBu_4N][BF_4]$ electrolyte, a glassy carbon electrode standardized to Fc/Fc⁺. Values are reported vs. NHE.

Figure A-9. Cyclic Voltammogram of a 1.8 mM solution of $[Et_4N]_2[Ni(ema)\bullet O_2]$ in DMF at a scan rate of 200 mV/s using a Ag/AgNO₃ reference electrode, 0.1 M $[nBu_4N][BF_4]$ electrolyte, a glassy carbon electrode standardized to Fc/Fc⁺. Values are reported vs. NHE.

Figure A-10: Cyclic Voltammograms of $Ni(ema)^{2-}$ and $Ni(ema)\bullet O_2^{2-}$ obtained in DMF at a scan rate of 200 mV/s using a Ag/AgNO₃ reference electrode, 0.1 M $[nBu_4N][BF_4]$ electrolyte, a glassy carbon electrode standardized to Fc/Fc⁺. Values are reported vs. NHE.

Figure A-11. a) Thermal ellipsoid plots of (a) $\text{Ni}(\text{ema})\cdot(\text{CH}_2)_3$ and (b) $[\text{Et}_4\text{N}]_2[\text{Ni}(\text{ema})\cdot\text{O}_2]$ showing 50% probability and the atom labeling scheme. The Et_4N^+ counterions of $[\text{Et}_4\text{N}]_2[\text{Ni}(\text{ema})\cdot\text{O}_2]$ are not shown.

Table A-2: Selected bond distances and angles for $\text{Ni}(\text{ema})\cdot(\text{CH}_2)_3$ and $[\text{Et}_4\text{N}]_2[\text{Ni}(\text{ema})\cdot\text{O}_2]$.

Table A-3. Selected Experimental and Optimized Parameters for $\text{Ni}(\text{ema})\cdot(\text{CH}_2)_3$.

Table A-4. Selected Experimental and Optimized Parameters for $\text{Ni}(\text{ema})\cdot\text{O}_2^{2-}$.

Details of Higher order NBO Analysis

Figure A-12. Packing diagram of $[\text{Et}_4\text{N}]_2[\text{Cu}(\text{emi})]$.

Figure A-13. ^{31}P NMR spectrum of O-am-[B] as a suspension in CDCl_3 (400 MHz NMR, referenced to phosphoric acid).

Figure A-14. ^{31}P NMR spectrum of O-am-(μ -pdt) $[\text{Fe}(\text{CO})_3][\text{Fe}(\text{CO})_2\text{PMe}_3]$ as a suspension in CDCl_3 (400 MHz NMR, referenced to phosphoric acid).

Figure A-15. ^{31}P NMR spectrum of O-am-(μ -pdt) $[\text{Fe}(\text{CO})_2\text{PMe}_3]_2$ as a suspension in CDCl_3 (400 MHz NMR, referenced to phosphoric acid).

Figure A-16. Synthesis of resin-bound $[\text{Ni}(\text{CGC})][\text{dppeNi}]$.

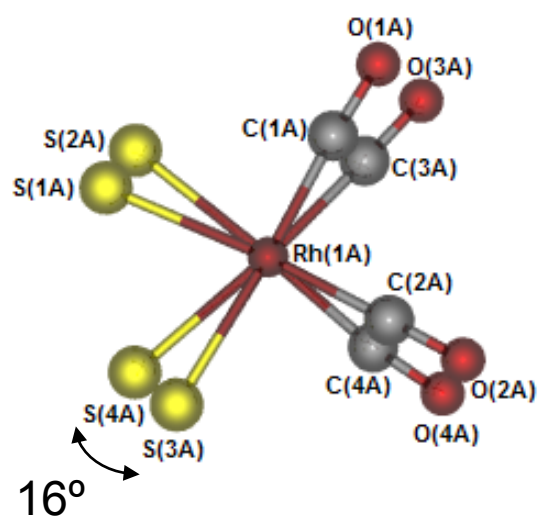


Figure A-1. Ball and Stick representation of the $[S_2Rh(CO)_2]_2$ unit of $[Et_4N]_2[Ni(ema)Rh(CO)_2]_2$, showing the deviation from eclipsed conformation. (Rh(2A) is located directly behind Rh(1A)).

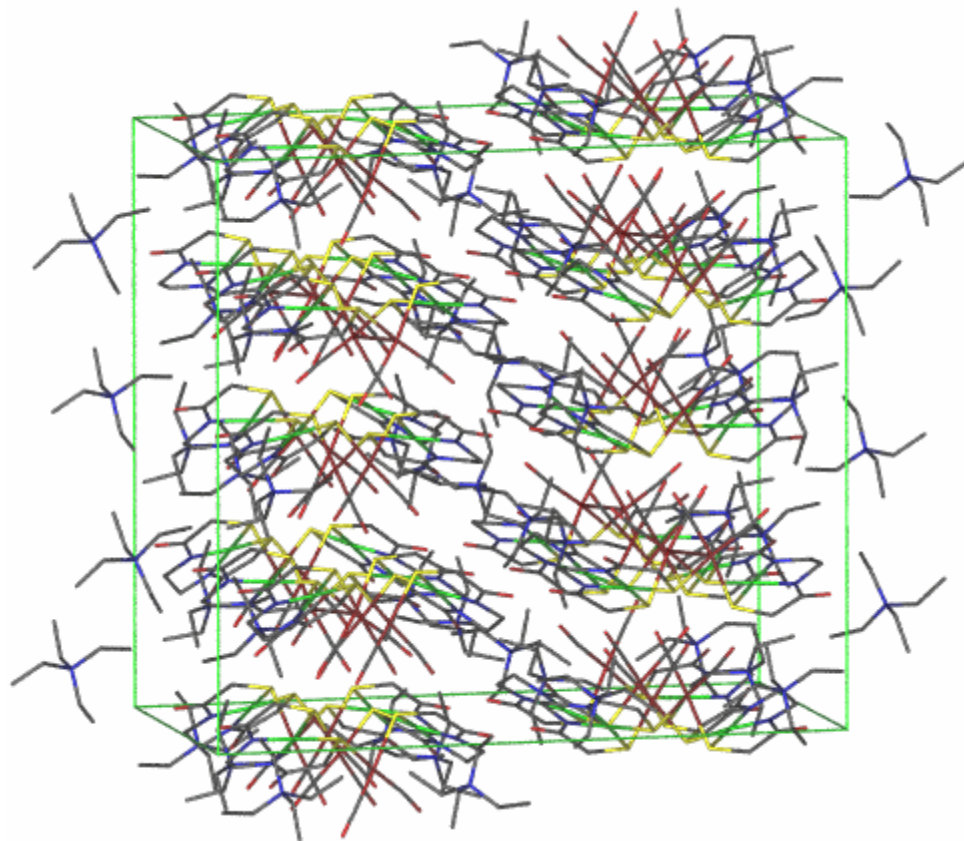
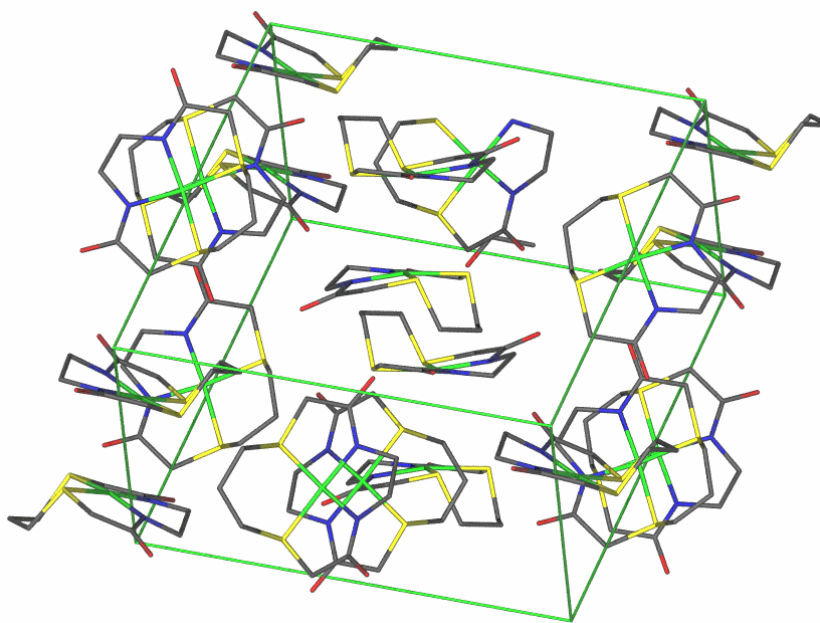


Figure A-2. Packing diagram of $[\text{Et}_4\text{N}]_2[\text{Ni}(\text{ema})\text{Rh}(\text{CO})_2]_2$.

Table A-1. Infrared $\nu(\text{CO})$ stretching frequencies for selected complexes.

Complex	$\nu(\text{CO})$ (cm^{-1})	Sample Form
$\text{K}_2[\text{Ni}(\text{CGC})]\text{W}(\text{CO})_4$	1988w, 1863s, 1845sh, 1793ms	DMF Solution
$[\text{NEt}_4]_2[\text{Ni}(\text{ema})]\text{W}(\text{CO})_4$	1986w, 1867s, 1837sh, 1791m	ref. 15
$\text{K}_2[\text{Ni}(\text{CGC})]\text{W}(\text{CO})_5$	2044w, 1959sh, 1925s, 1870m	DMF Solution
$\text{O}-\text{Ni}(\text{CGC})\text{W}(\text{CO})_5^{2-}$	1967w, 1915s, 1845w	ATR on beads
$[\text{NEt}_4]_2[\text{Ni}(\text{ema})]\text{Rh}(\text{CO})_2$	2061s, 1996s	CH_3CN Solution
$\text{O}-\text{Ni}(\text{CGC})\text{Rh}(\text{CO})_2^-$	2067s, 1990s	ATR on beads
$[(\text{Ni-1})\text{Rh}(\text{CO})_2]^+$	2077s, 2017s	CH_3CN Solution
$\text{Rh}(\text{CO})_2\text{I}_2^-$	2059s, 1988s	ref. 25

**Figure A-3.** Packing diagram of $\text{Ni}(\text{ema})\cdot(\text{CH}_2)_3$.

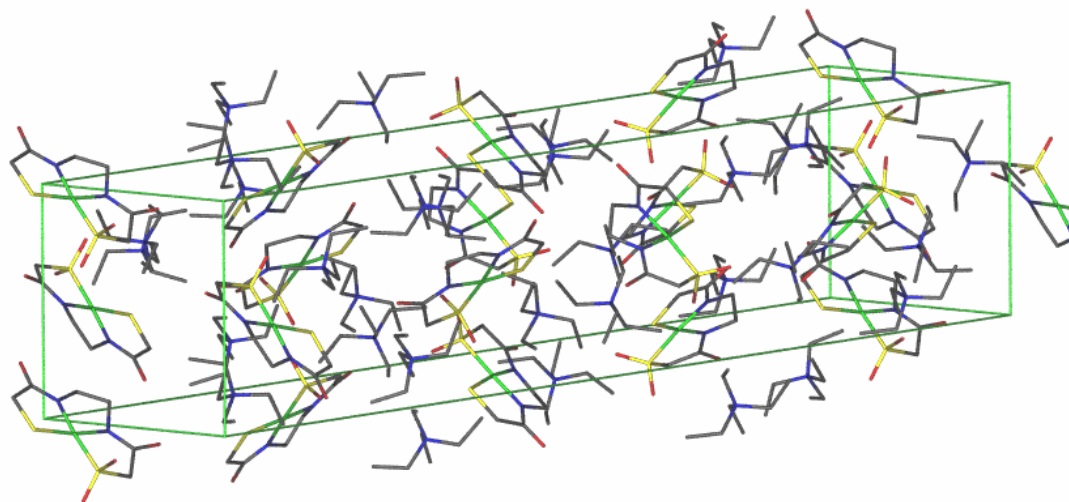


Figure A-4. Packing diagram of $[\text{Et}_4\text{N}]_2[\text{Ni}(\text{ema})\cdot\text{O}_2]$.

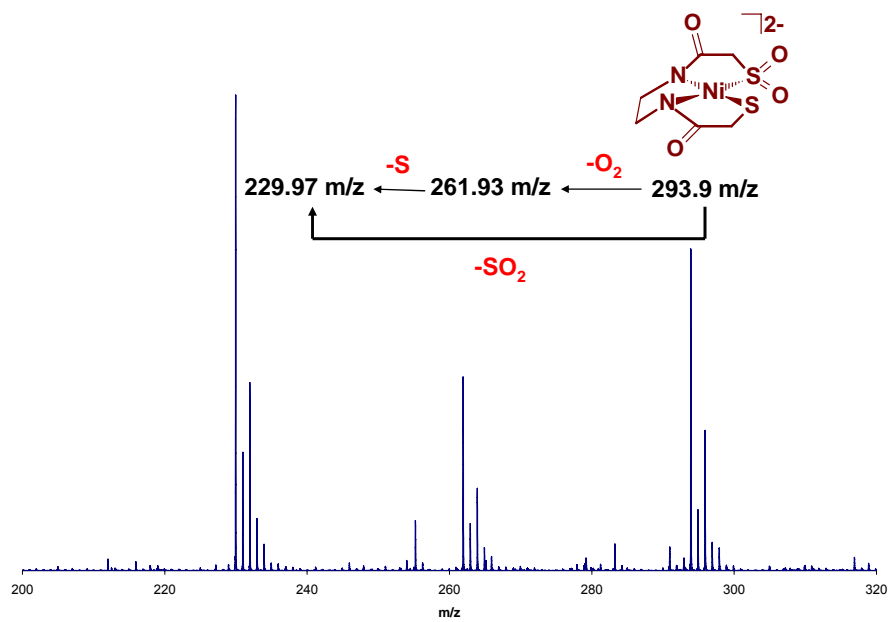


Figure A-5. The $^-$ ESI-mass spectrum of $[\text{Et}_4\text{N}]_2[\text{Ni}(\text{ema})\cdot\text{O}_2]$ showing the fragmentation by loss of O_2 and SO_2 .

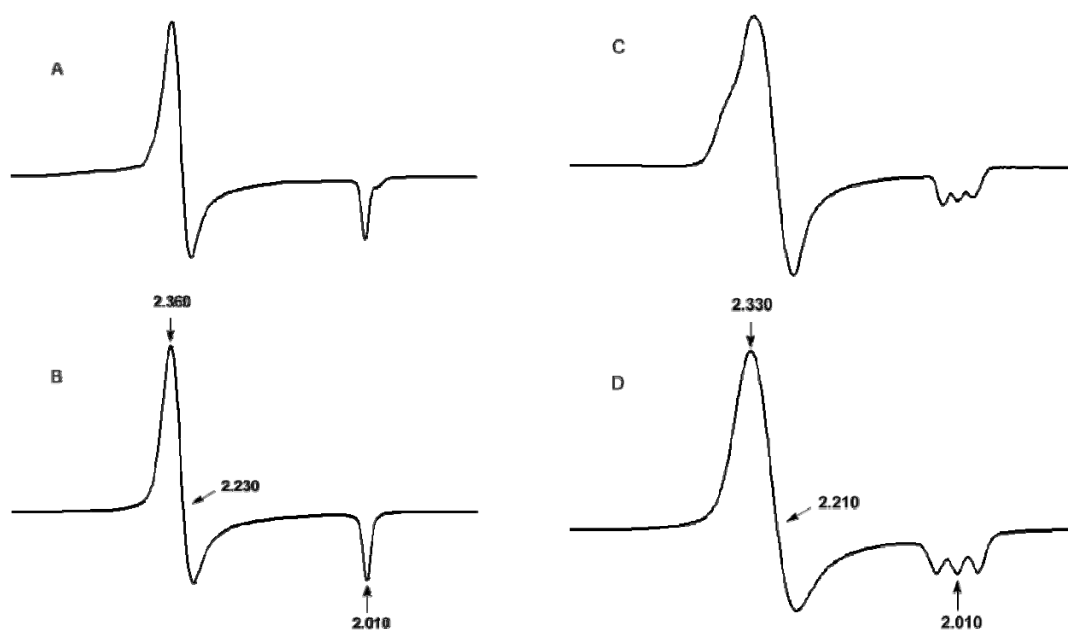


Figure A-6. X-band EPR spectra (top) obtained from an oxidized solution of $\text{Ni(ema)•(CH}_2\text{)}_3$ using CAN in DMF (a) and its pyridine adduct (b) in a DMF/pyridine solution (4:1 v/v) at 10 K and the corresponding simulations (c,d respectively).

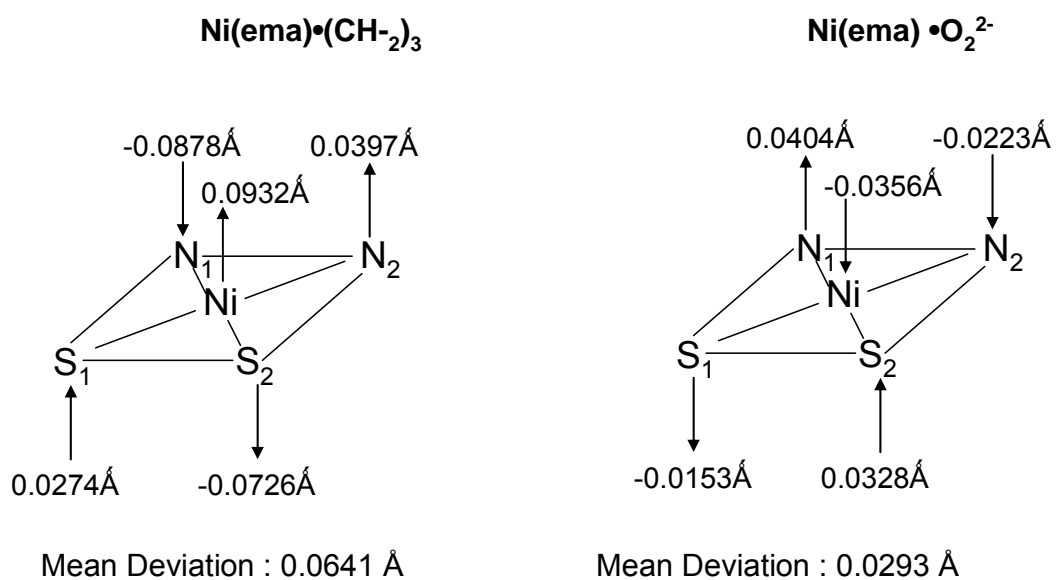


Figure A-7. Representation of the NiN₂S₂ plane for Ni(ema)•(CH₂)₃ and Ni(ema)•O₂²⁻ and deviations of each atom from the best plane.

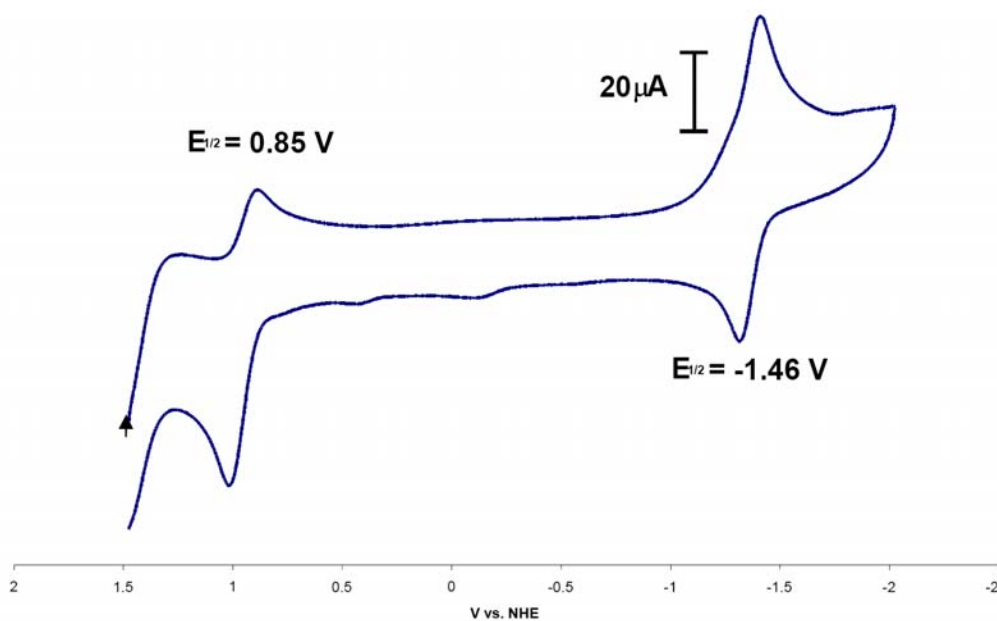


Figure A-8. Cyclic Voltammogram of a 3.4 mM solution of Ni(ema)[Me]₂ in DMF at a scan rate of 200 mV/s using a Ag/AgNO₃ reference electrode, 0.1 M [nBu₄N][BF₄] electrolyte, a glassy carbon electrode standardized to Fc/Fc⁺. Values are reported vs. NHE.

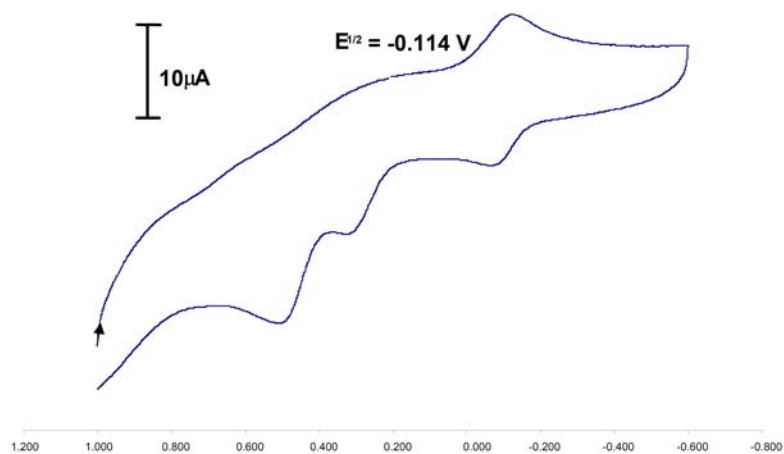


Figure A-9. Cyclic Voltammogram of a 1.8 mM solution of $[\text{Et}_4\text{N}]_2[\text{Ni}(\text{ema})\cdot\text{O}_2]$ in DMF at a scan rate of 200 mV/s using a Ag/AgNO₃ reference electrode, 0.1 M $[\text{nBu}_4\text{N}][\text{BF}_4]$ electrolyte, a glassy carbon electrode standardized to Fc/Fc⁺. Values are reported vs. NHE.

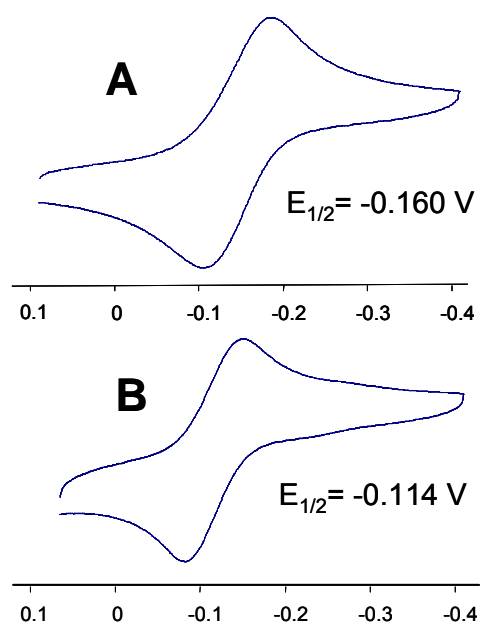


Figure A-10: Cyclic Voltammograms of $\text{Ni}(\text{ema})^{2-}$ and $\text{Ni}(\text{ema})\cdot\text{O}_2^{2-}$ obtained in DMF at a scan rate of 200 mV/s using a Ag/AgNO₃ reference electrode, 0.1 M $[\text{nBu}_4\text{N}][\text{BF}_4]$ electrolyte, a glassy carbon electrode standardized to Fc/Fc⁺. Values are reported vs. NHE.

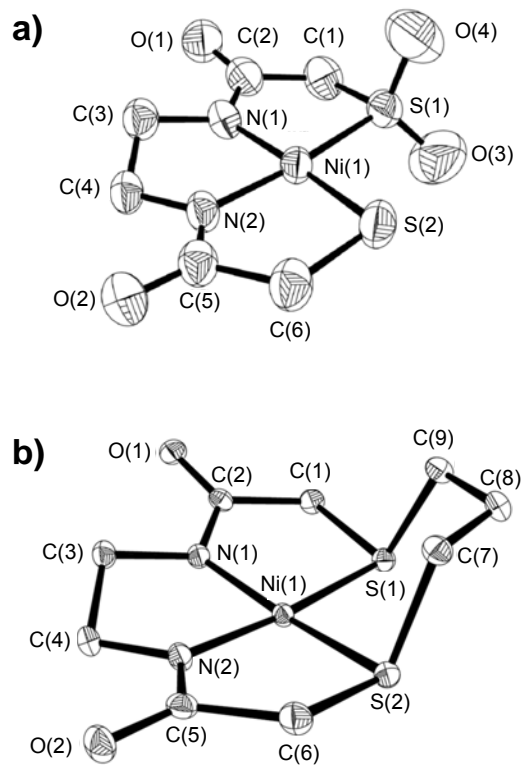


Figure A-11. a) Thermal ellipsoid plots of (a) $\text{Ni(ema)} \cdot (\text{CH}_2)_3$ and (b) $[\text{Et}_4\text{N}]_2[\text{Ni(ema)} \cdot \text{O}_2]$ showing 50% probability and the atom labeling scheme. The Et_4N^+ counterions of $[\text{Et}_4\text{N}]_2[\text{Ni(ema)} \cdot \text{O}_2]$ are not shown.

Table A-2: Selected bond distances and angles for $\text{Ni(ema)\bullet(CH}_2)_3$ and $[\text{Et}_4\text{N}]_2[\text{Ni(ema)\bullet O}_2]$.

	$\text{Ni(ema)\bullet(CH}_2)_3$	$\text{Ni(ema)\bullet O}_2$
Ni-S(1)	2.1635(6) Å	2.1519(15) Å
Ni-S(2)	2.1628(7)	2.1752(15)
Ni-N(1)	1.8431(15)	1.861(4)
Ni-N(2)	1.8301(14)	1.861(4)
S(1)-O(3)	-	1.444(6)
S(1)-O(4)	-	1.436(6)
S(1)-Ni(1)-S(2)	95.36(5) °	99.22(6) °
N(1)-Ni(1)-N(2)	86.23(6)	85.39(19)
N(1)-Ni(1)-S(1)	89.36(5)	87.71(14)
N(2)-Ni(1)-S(2)	88.60(5)	87.60(13)
O(3)-S(1)-O(4)	-	116.7(4)

Table A-3. Selected Experimental and Optimized Parameters for $\text{Ni(ema)\bullet(CH}_2)_3$

	Experimental	Calculated
Ni-S(1)	2.1635(6) Å	2.231
Ni-S(2)	2.1628(7)	2.227
Ni-N(1)	1.8431(15)	1.843
Ni-N(2)	1.8301(14)	1.838
S(1)-Ni(1)-S(2)	95.36(5) °	95.144
N(1)-Ni(1)-N(2)	86.23(6)	87.014

Table A-4. Selected Experimental and Optimized Parameters for $\text{Ni(ema)\bullet O}_2^{2-}$

	Experimental	Calculated
Ni-S(1)	2.155(1)	2.189
Ni-S(2)	2.175(1)	2.234
Ni-N(1)	1.863(4)	1.887
Ni-N(2)	1.859(4)	1.876
S(1)-O(1)	1.427(6)	1.50589
S(1)-O(2)	1.445(6)	1.50648
S(1)-Ni(1)-S(2)	99.27(7)	100.823
N(1)-Ni(1)-N(2)	85.45(17)	85.777
O(1)-S(1)-S(1)	116.9(5)	114.659

Details of Higher order NBO Analysis

In order to ascertain the existence of the second nitrogen lone pair, additional calculations at a higher level of theory using a hybrid basis set (see experimental section for details) were performed. In this analysis, the lone pair was resolved with an electronic population of 1.56 and resides in a p_z orbital, which is highly delocalized into the amido system and correlates well with the original 6-311G(d,p) calculations. Additional lone pair delocalizations in **Ni(ema)**²⁻ occur between the O p_z lone pair and the C-N* and C-C* antibonds in the amido system. A schematic of these effects is given in Figure 8. The NBO analysis relates to the DFT frontier molecular orbitals in that the HOMO of **Ni(ema)**²⁻ is largely S-based with minor contributions from the amido nitrogens.

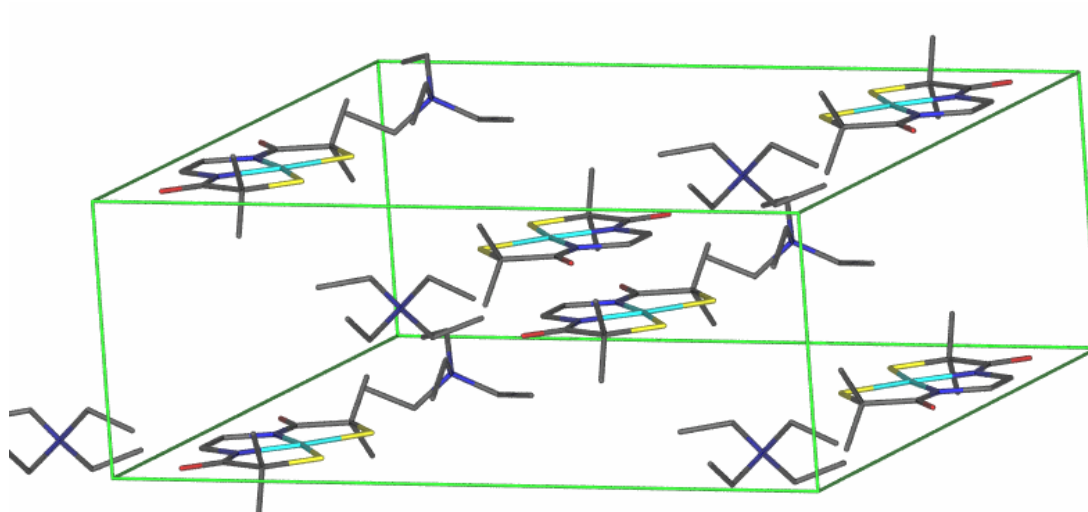


Figure A-12. Packing diagram of $[\text{Et}_4\text{N}]_2[\text{Cu}(\text{emi})]$.

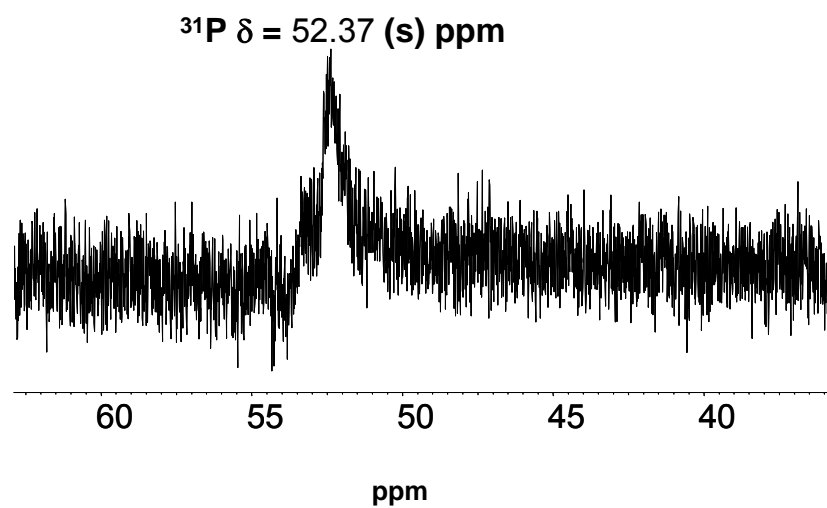


Figure A-13. ^{31}P NMR spectrum of O-am-[B] as a suspension in CDCl_3 (400 MHz NMR, referenced to phosphoric acid).

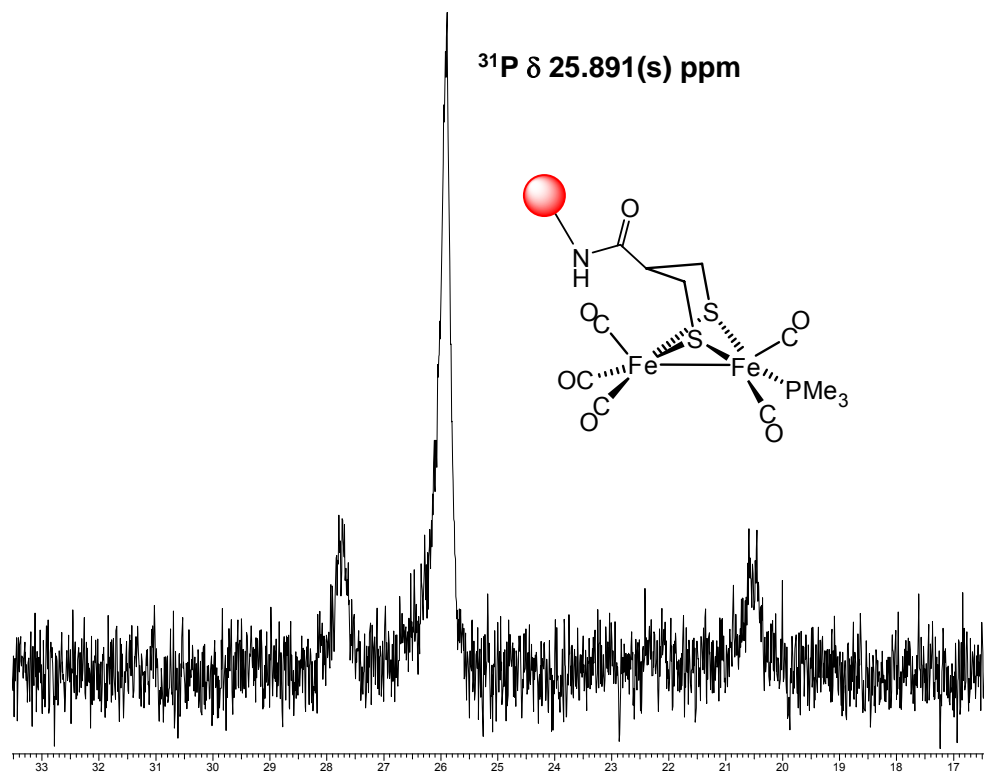


Figure A-14. ^{31}P NMR spectrum of $\text{O-am-(}\mu\text{-pdt)[Fe(CO)}_3\text{][Fe(CO)}_2\text{PMe}_3\text{]}$ as a suspension in CDCl_3 (400 MHz NMR, referenced to phosphoric acid).

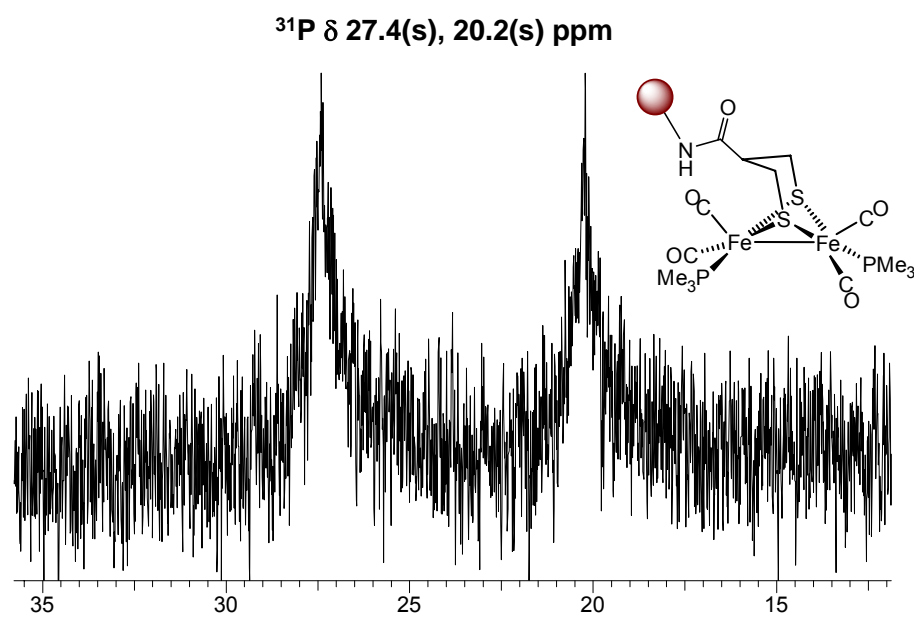


Figure A-15. ^{31}P NMR spectrum of $\text{O-am-(}\mu\text{-pdt)[Fe(CO)}_2\text{PMe}_3\text{]}_2$ as a suspension in CDCl_3 (400 MHz NMR, referenced to phosphoric acid).

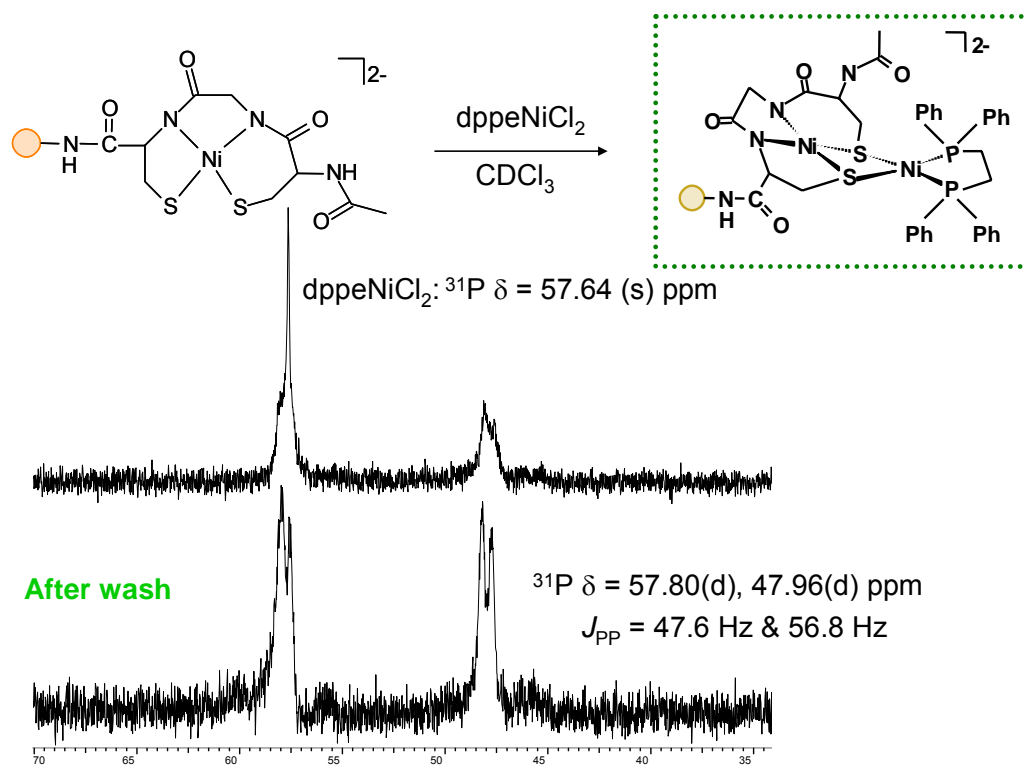


Figure A-16. Synthesis of resin-bound [Ni(CGC)][dpeNi].

APPENDIX B

CRYSTALLOGRAPHIC DATA FOR STRUCTURES

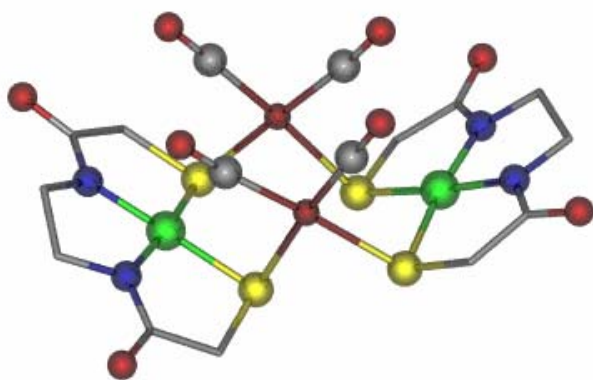
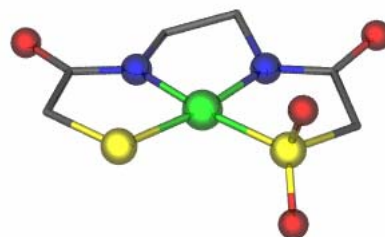
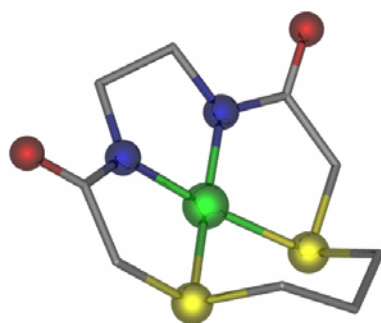
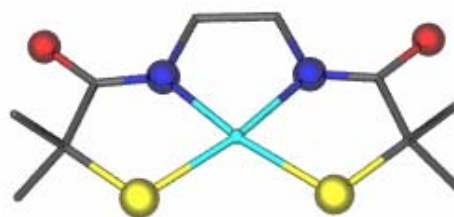
 $[\text{Et}_4\text{N}]_2[\text{Ni}(\text{ema})\text{Rh}(\text{CO})_2]_2$  $[\text{Et}_4\text{N}]_2[\text{Ni}(\text{ema})\cdot\text{O}_2]$  $\text{Ni}(\text{ema})\cdot(\text{CH}_2)_3$  $[\text{Et}_4\text{N}]_2[\text{Cu}(\text{emi})]$

Table B-1. Crystal data and structure refinement for [Et₄N]₂[Ni(ema)Rh(CO)₂]₂.

Empirical formula	C ₁₆ H ₂₈ N ₃ Ni O ₄ Rh S ₂
Formula weight	552.15
Temperature	110(2) K
Wavelength	0.71073 Å
Unit cell dimensions	a = 27.950(5) Å alpha = 90 deg. b = 23.526(4) Å beta = 112.113(3) deg. c = 28.457(5) Å gamma = 90 deg.
Volume	17336(5) Å ³
Z, Calculated density	32, 1.692 Mg/m ³
Absorption coefficient	1.849 mm ⁻¹
F(000)	9024
Crystal size	0.50 x 0.10 x 0.10 mm
Theta range for data collection	1.74 to 25.00 deg.
Limiting indices	-28<=h<=33, -19<=k<=27, -33<=l<=29
Reflections collected / unique	44130 / 15117 [R(int) = 0.0254]
Completeness to theta = 25.00	99.0 %
Max. and min. transmission	0.8367 and 0.4584
Refinement method	Full-matrix least-squares on F ²
Data / restraints / parameters	15117 / 0 / 975
Goodness-of-fit on F ²	1.091
Final R indices [I>2sigma(I)]	R1 = 0.0551, wR2 = 0.1273
R indices (all data)	R1 = 0.0722, wR2 = 0.1435
Largest diff. peak and hole	3.993 and -1.019 e. Å ⁻³

Table B-2. Bond lengths [Å] and angles [°] for [Et₄N]₂[Ni(ema)Rh(CO)₂]₂.

Rh(1A)-C(2A)	1.873(6)
Rh(1A)-C(1A)	1.872(6)
Rh(1A)-S(3A)	2.3779(13)
Rh(1A)-S(1A)	2.4060(12)
Rh(2A)-C(3A)	1.876(6)
Rh(2A)-C(4A)	1.888(7)
Rh(2A)-S(2A)	2.3493(15)
Rh(2A)-S(4A)	2.4269(13)
S(1A)-C(5A)	1.826(5)
S(1A)-Ni(1A)	2.2009(14)
S(2A)-C(10A)	1.840(6)
S(2A)-Ni(1A)	2.2065(15)
S(3A)-C(11A)	1.845(5)
S(3A)-Ni(2A)	2.1938(14)
S(4A)-C(16A)	1.814(5)
S(4A)-Ni(2A)	2.1790(13)
Ni(1A)-N(2A)	1.865(4)
Ni(1A)-N(1A)	1.867(4)
Ni(2A)-N(3A)	1.846(4)
Ni(2A)-N(4A)	1.861(4)
O(1A)-C(1A)	1.143(6)
O(2A)-C(2A)	1.141(6)
O(3A)-C(3A)	1.139(7)
O(4A)-C(4A)	1.130(7)
O(5A)-C(6A)	1.260(6)
O(6A)-C(9A)	1.251(6)
O(7A)-C(12A)	1.251(6)
O(8A)-C(15A)	1.259(6)
N(1A)-C(6A)	1.310(6)
N(1A)-C(7A)	1.473(6)
N(2A)-C(9A)	1.327(6)
N(2A)-C(8A)	1.463(6)
N(3A)-C(12A)	1.331(7)
N(3A)-C(13A)	1.466(7)
N(4A)-C(15A)	1.316(7)
N(4A)-C(14A)	1.481(6)
C(5A)-C(6A)	1.521(7)
C(7A)-C(8A)	1.536(7)
C(9A)-C(10A)	1.530(7)
C(11A)-C(12A)	1.535(8)
C(13A)-C(14A)	1.528(8)
C(15A)-C(16A)	1.542(7)
Rh(1B)-C(2B)	1.870(6)
Rh(1B)-C(1B)	1.877(5)
Rh(1B)-S(2B)	2.3780(13)
Rh(1B)-S(1B)	2.4183(13)
Ni(1B)-N(2B)	1.854(4)
Ni(1B)-N(1B)	1.871(4)
Ni(1B)-S(1B)	2.1925(13)
Ni(1B)-S(2B)#1	2.1996(14)
S(1B)-C(3B)	1.832(5)
S(2B)-C(8B)#1	1.836(5)
S(2B)-Ni(1B)#1	2.1995(14)

(Table B-2 continued)

O(1B)-C(1B)	1.140(6)
O(2B)-C(2B)	1.143(7)
O(3B)-C(4B)	1.267(6)
O(4B)-C(7B)	1.262(6)
N(1B)-C(4B)	1.308(6)
N(1B)-C(5B)	1.483(6)
N(2B)-C(7B)	1.325(7)
N(2B)-C(6B)	1.474(6)
C(3B)-C(4B)	1.520(7)
C(5B)-C(6B)	1.516(7)
C(7B)-C(8B)	1.513(7)
C(8B)-S(2B)#1	1.836(5)
Rh(1C)-C(2C)	1.874(6)
Rh(1C)-C(1C)	1.899(6)
Rh(1C)-S(2C)	2.3538(13)
Rh(1C)-S(1C)	2.4091(13)
Rh(1C)-Rh(1C)#1	3.1503(9)
Ni(1C)-N(2C)	1.856(4)
Ni(1C)-N(1C)	1.867(4)
Ni(1C)-S(1C)	2.1889(14)
Ni(1C)-S(2C)#1	2.1913(14)
S(1C)-C(3C)	1.824(5)
S(2C)-C(8C)#1	1.845(5)
S(2C)-Ni(1C)#1	2.1912(14)
O(1C)-C(1C)	1.139(7)
O(2C)-C(2C)	1.145(6)
O(3C)-C(4C)	1.258(6)
O(4C)-C(7C)	1.251(6)
N(1C)-C(4C)	1.310(6)
N(1C)-C(5C)	1.481(6)
N(2C)-C(7C)	1.327(6)
N(2C)-C(6C)	1.472(6)
C(3C)-C(4C)	1.534(7)
C(5C)-C(6C)	1.524(7)
C(7C)-C(8C)	1.527(7)
C(8C)-S(2C)#1	1.845(5)
N(1D)-C(7D)	1.506(6)
N(1D)-C(1D)	1.518(6)
N(1D)-C(3D)	1.526(6)
N(1D)-C(5D)	1.527(6)
C(1D)-C(2D)	1.533(8)
C(3D)-C(4D)	1.524(7)
C(5D)-C(6D)	1.509(7)
C(7D)-C(8D)	1.507(8)
N(1E)-C(5E)	1.510(6)
N(1E)-C(7E)	1.516(6)
N(1E)-C(1E)	1.521(6)
N(1E)-C(3E)	1.526(6)
C(1E)-C(2E)	1.518(7)
C(3E)-C(4E)	1.515(7)
C(5E)-C(6E)	1.518(7)
C(7E)-C(8E)	1.514(7)
N(1F)-C(5F)	1.500(7)
N(1F)-C(3F)	1.499(7)

(Table B-2 continued)

N(1F)-C(7F)	1.501(8)
N(1F)-C(1F)	1.525(7)
C(1F)-C(2F)	1.506(9)
C(3F)-C(4F)	1.478(13)
C(5F)-C(6F)	1.497(15)
C(7F)-C(8F)	1.489(9)
N(1G)-C(3G)	1.512(6)
N(1G)-C(1G)	1.518(7)
N(1G)-C(5G)	1.525(7)
N(1G)-C(7G)	1.527(6)
C(1G)-C(2G)	1.511(8)
C(3G)-C(4G)	1.510(8)
C(5G)-C(6G)	1.536(8)
C(7G)-C(8G)	1.486(8)
C(2A)-Rh(1A)-C(1A)	91.3(2)
C(2A)-Rh(1A)-S(3A)	91.45(17)
C(1A)-Rh(1A)-S(3A)	175.54(16)
C(2A)-Rh(1A)-S(1A)	175.70(18)
C(1A)-Rh(1A)-S(1A)	92.98(16)
S(3A)-Rh(1A)-S(1A)	84.26(4)
C(3A)-Rh(2A)-C(4A)	88.7(3)
C(3A)-Rh(2A)-S(2A)	93.0(2)
C(4A)-Rh(2A)-S(2A)	176.60(18)
C(3A)-Rh(2A)-S(4A)	175.5(2)
C(4A)-Rh(2A)-S(4A)	95.64(17)
S(2A)-Rh(2A)-S(4A)	82.62(5)
C(5A)-S(1A)-Ni(1A)	98.04(16)
C(5A)-S(1A)-Rh(1A)	101.15(16)
Ni(1A)-S(1A)-Rh(1A)	102.82(5)
C(10A)-S(2A)-Ni(1A)	98.47(18)
C(10A)-S(2A)-Rh(2A)	112.4(2)
Ni(1A)-S(2A)-Rh(2A)	95.53(6)
C(11A)-S(3A)-Ni(2A)	97.81(18)
C(11A)-S(3A)-Rh(1A)	109.91(18)
Ni(2A)-S(3A)-Rh(1A)	90.29(5)
C(16A)-S(4A)-Ni(2A)	97.95(16)
C(16A)-S(4A)-Rh(2A)	102.76(16)
Ni(2A)-S(4A)-Rh(2A)	96.57(5)
N(2A)-Ni(1A)-N(1A)	85.72(18)
N(2A)-Ni(1A)-S(1A)	173.33(13)
N(1A)-Ni(1A)-S(1A)	87.62(13)
N(2A)-Ni(1A)-S(2A)	87.84(13)
N(1A)-Ni(1A)-S(2A)	172.77(13)
S(1A)-Ni(1A)-S(2A)	98.82(5)
N(3A)-Ni(2A)-N(4A)	85.76(18)
N(3A)-Ni(2A)-S(4A)	171.92(14)
N(4A)-Ni(2A)-S(4A)	87.59(13)
N(3A)-Ni(2A)-S(3A)	88.71(14)
N(4A)-Ni(2A)-S(3A)	171.88(13)
S(4A)-Ni(2A)-S(3A)	98.36(5)
C(6A)-N(1A)-C(7A)	118.7(4)
C(6A)-N(1A)-Ni(1A)	125.6(3)
C(7A)-N(1A)-Ni(1A)	115.1(3)
C(9A)-N(2A)-C(8A)	117.3(4)

(Table B-2 continued)

C(9A)-N(2A)-Ni(1A)	126.0(3)
C(8A)-N(2A)-Ni(1A)	115.6(3)
C(12A)-N(3A)-C(13A)	117.6(4)
C(12A)-N(3A)-Ni(2A)	126.4(4)
C(13A)-N(3A)-Ni(2A)	115.6(3)
C(15A)-N(4A)-C(14A)	117.4(4)
C(15A)-N(4A)-Ni(2A)	125.5(3)
C(14A)-N(4A)-Ni(2A)	116.5(3)
O(1A)-C(1A)-Rh(1A)	174.8(5)
O(2A)-C(2A)-Rh(1A)	178.0(5)
O(3A)-C(3A)-Rh(2A)	178.0(6)
O(4A)-C(4A)-Rh(2A)	172.0(5)
C(6A)-C(5A)-S(1A)	112.0(3)
O(5A)-C(6A)-N(1A)	125.6(5)
O(5A)-C(6A)-C(5A)	119.3(4)
N(1A)-C(6A)-C(5A)	115.1(4)
N(1A)-C(7A)-C(8A)	107.7(4)
N(2A)-C(8A)-C(7A)	108.1(4)
O(6A)-C(9A)-N(2A)	126.2(5)
O(6A)-C(9A)-C(10A)	118.9(5)
N(2A)-C(9A)-C(10A)	114.9(4)
C(9A)-C(10A)-S(2A)	112.1(4)
C(12A)-C(11A)-S(3A)	112.7(4)
O(7A)-C(12A)-N(3A)	126.6(5)
O(7A)-C(12A)-C(11A)	119.5(5)
N(3A)-C(12A)-C(11A)	113.9(4)
N(3A)-C(13A)-C(14A)	109.1(4)
N(4A)-C(14A)-C(13A)	107.6(4)
O(8A)-C(15A)-N(4A)	126.5(5)
O(8A)-C(15A)-C(16A)	119.6(5)
N(4A)-C(15A)-C(16A)	113.8(4)
C(15A)-C(16A)-S(4A)	111.8(3)
C(2B)-Rh(1B)-C(1B)	89.9(2)
C(2B)-Rh(1B)-S(2B)	91.79(17)
C(1B)-Rh(1B)-S(2B)	178.18(15)
C(2B)-Rh(1B)-S(1B)	173.89(17)
C(1B)-Rh(1B)-S(1B)	94.76(15)
S(2B)-Rh(1B)-S(1B)	83.52(4)
N(2B)-Ni(1B)-N(1B)	85.84(18)
N(2B)-Ni(1B)-S(1B)	172.24(14)
N(1B)-Ni(1B)-S(1B)	87.42(13)
N(2B)-Ni(1B)-S(2B)#1	88.11(13)
N(1B)-Ni(1B)-S(2B)#1	171.63(13)
S(1B)-Ni(1B)-S(2B)#1	98.97(5)
C(3B)-S(1B)-Ni(1B)	97.71(15)
C(3B)-S(1B)-Rh(1B)	100.92(16)
Ni(1B)-S(1B)-Rh(1B)	100.46(5)
C(8B)#1-S(2B)-Ni(1B)#1	97.73(17)
C(8B)#1-S(2B)-Rh(1B)	110.05(18)
Ni(1B)#1-S(2B)-Rh(1B)	87.16(5)
C(4B)-N(1B)-C(5B)	118.3(4)
C(4B)-N(1B)-Ni(1B)	124.9(3)
C(5B)-N(1B)-Ni(1B)	115.5(3)

(Table B-2 continued)

C(7B)-N(2B)-C(6B)	118.7(4)
C(7B)-N(2B)-Ni(1B)	126.2(4)
C(6B)-N(2B)-Ni(1B)	114.8(3)
O(1B)-C(1B)-Rh(1B)	173.8(5)
O(2B)-C(2B)-Rh(1B)	178.1(5)
C(4B)-C(3B)-S(1B)	111.9(3)
O(3B)-C(4B)-N(1B)	125.4(5)
O(3B)-C(4B)-C(3B)	119.1(4)
N(1B)-C(4B)-C(3B)	115.4(4)
N(1B)-C(5B)-C(6B)	107.9(4)
N(2B)-C(6B)-C(5B)	108.8(4)
O(4B)-C(7B)-N(2B)	125.8(5)
O(4B)-C(7B)-C(8B)	119.7(5)
N(2B)-C(7B)-C(8B)	114.5(4)
C(7B)-C(8B)-S(2B)#1	113.1(3)
C(2C)-Rh(1C)-C(1C)	90.9(2)
C(2C)-Rh(1C)-S(2C)	91.33(16)
C(1C)-Rh(1C)-S(2C)	171.28(16)
C(2C)-Rh(1C)-S(1C)	172.35(16)
C(1C)-Rh(1C)-S(1C)	94.41(16)
S(2C)-Rh(1C)-S(1C)	84.27(5)
C(2C)-Rh(1C)-Rh(1C)#1	90.47(16)
C(1C)-Rh(1C)-Rh(1C)#1	92.77(16)
S(2C)-Rh(1C)-Rh(1C)#1	95.65(3)
S(1C)-Rh(1C)-Rh(1C)#1	83.76(3)
N(2C)-Ni(1C)-N(1C)	85.94(18)
N(2C)-Ni(1C)-S(1C)	173.65(14)
N(1C)-Ni(1C)-S(1C)	88.01(13)
N(2C)-Ni(1C)-S(2C)#1	88.11(13)
N(1C)-Ni(1C)-S(2C)#1	172.69(13)
S(1C)-Ni(1C)-S(2C)#1	98.06(5)
C(3C)-S(1C)-Ni(1C)	98.01(17)
C(3C)-S(1C)-Rh(1C)	105.38(17)
Ni(1C)-S(1C)-Rh(1C)	95.01(5)
C(8C)#1-S(2C)-Ni(1C)#1	98.32(17)
C(8C)#1-S(2C)-Rh(1C)	111.22(19)
Ni(1C)#1-S(2C)-Rh(1C)	103.27(5)
C(4C)-N(1C)-C(5C)	118.5(4)
C(4C)-N(1C)-Ni(1C)	125.6(4)
C(5C)-N(1C)-Ni(1C)	114.7(3)
C(7C)-N(2C)-C(6C)	117.2(4)
C(7C)-N(2C)-Ni(1C)	126.0(4)
C(6C)-N(2C)-Ni(1C)	115.8(3)
O(1C)-C(1C)-Rh(1C)	172.1(5)
O(2C)-C(2C)-Rh(1C)	174.3(5)
C(4C)-C(3C)-S(1C)	112.1(3)
O(3C)-C(4C)-N(1C)	126.7(5)
O(3C)-C(4C)-C(3C)	119.0(4)
N(1C)-C(4C)-C(3C)	114.2(4)
N(1C)-C(5C)-C(6C)	108.1(4)
N(2C)-C(6C)-C(5C)	108.2(4)
O(4C)-C(7C)-N(2C)	126.7(5)
O(4C)-C(7C)-C(8C)	118.8(4)

(Table B-2 continued)

N(2C)-C(7C)-C(8C)	114.6(4)
C(7C)-C(8C)-S(2C)#1	111.8(3)
C(7D)-N(1D)-C(1D)	110.7(4)
C(7D)-N(1D)-C(3D)	108.8(4)
C(1D)-N(1D)-C(3D)	110.6(4)
C(7D)-N(1D)-C(5D)	111.3(4)
C(1D)-N(1D)-C(5D)	107.7(4)
C(3D)-N(1D)-C(5D)	107.8(4)
N(1D)-C(1D)-C(2D)	114.0(4)
C(4D)-C(3D)-N(1D)	115.7(4)
C(6D)-C(5D)-N(1D)	114.5(4)
N(1D)-C(7D)-C(8D)	115.8(4)
C(5E)-N(1E)-C(7E)	112.0(4)
C(5E)-N(1E)-C(1E)	109.2(4)
C(7E)-N(1E)-C(1E)	108.3(4)
C(5E)-N(1E)-C(3E)	108.5(4)
C(7E)-N(1E)-C(3E)	108.5(4)
C(1E)-N(1E)-C(3E)	110.2(4)
C(2E)-C(1E)-N(1E)	115.7(4)
C(4E)-C(3E)-N(1E)	115.8(4)
N(1E)-C(5E)-C(6E)	115.1(4)
N(1E)-C(7E)-C(8E)	115.2(4)
C(5F)-N(1F)-C(3F)	106.3(6)
C(5F)-N(1F)-C(7F)	110.3(6)
C(3F)-N(1F)-C(7F)	111.7(5)
C(5F)-N(1F)-C(1F)	110.9(5)
C(3F)-N(1F)-C(1F)	111.2(5)
C(7F)-N(1F)-C(1F)	106.5(4)
C(2F)-C(1F)-N(1F)	116.1(5)
C(4F)-C(3F)-N(1F)	113.3(8)
N(1F)-C(5F)-C(6F)	114.4(9)
C(8F)-C(7F)-N(1F)	116.8(5)
C(3G)-N(1G)-C(1G)	111.9(4)
C(3G)-N(1G)-C(5G)	111.5(4)
C(1G)-N(1G)-C(5G)	105.3(4)
C(3G)-N(1G)-C(7G)	106.7(4)
C(1G)-N(1G)-C(7G)	110.6(4)
C(5G)-N(1G)-C(7G)	110.9(4)
C(2G)-C(1G)-N(1G)	113.8(5)
C(4G)-C(3G)-N(1G)	115.5(5)
N(1G)-C(5G)-C(6G)	114.3(5)
C(8G)-C(7G)-N(1G)	116.5(5)

Symmetry transformations used to generate equivalent atoms: #1 $-x+1, y, -z+1/2$

Table B-3. Crystal data and structure refinement for Ni(ema)•(CH₂)₃.

Empirical formula	C7 H14 N2 Ni O2 S2
Formula weight	281.03
Temperature	273(2) K
Wavelength	0.71073 Å
Crystal system, space group	Orthorhombic, Pbcn
Unit cell dimensions	a = 16.098(3) Å alpha = 90 deg. b = 8.9666(10) Å beta = 90 deg. c = 15.299(2) Å gamma = 90 deg.
Volume	2208.4(5) Å ³
Z, Calculated density	8, 1.691 Mg/m ³
Absorption coefficient	2.111 mm ⁻¹
F(000)	1168
Theta range for data collection	2.53 to 28.64 deg.
Limiting indices	-21<=h<=11, -11<=k<=11, -17<=l<=10
Reflections collected / unique	5952 / 2420 [R(int) = 0.0551]
Completeness to theta = 28.64	85.3 %
Absorption correction	None
Refinement method	Full-matrix least-squares on F ²
Data / restraints / parameters	2420 / 0 / 65
Goodness-of-fit on F ²	1.065
Final R indices [I>2sigma(I)]	R1 = 0.0534, wR2 = 0.1709
R indices (all data)	R1 = 0.0625, wR2 = 0.1779
Largest diff. peak and hole	1.094 and -1.441 e. Å ⁻³

Table B-4. Bond lengths [Å] and angles [°] for Ni(ema)•(CH₂)₃.

Ni(1)-N(2)	1.833(4)
Ni(1)-N(1)	1.848(4)
Ni(1)-S(2)	2.1640(13)
Ni(1)-S(3)	2.1669(12)
S(2)-C(7)	1.822(5)
S(2)-C(3)	1.837(4)
S(3)-C(9)	1.828(5)
S(3)-C(1)	1.846(5)
C(1)-C(2)	1.515(6)
C(2)-C(3)	1.543(6)
N(2)-C(6)	1.344(6)
N(2)-C(5)	1.455(6)
N(1)-C(8)	1.345(5)
N(1)-C(4)	1.479(6)
C(9)-C(8)	1.527(6)
C(8)-O(1)	1.235(5)
C(6)-O(2)	1.243(6)
C(6)-C(7)	1.528(6)
C(5)-C(4)	1.539(6)
N(2)-Ni(1)-N(1)	86.13(17)
N(2)-Ni(1)-S(2)	88.81(13)
N(1)-Ni(1)-S(2)	169.08(11)
N(2)-Ni(1)-S(3)	174.55(12)
N(1)-Ni(1)-S(3)	89.17(12)
S(2)-Ni(1)-S(3)	95.36(5)
C(7)-S(2)-C(3)	102.4(2)
C(7)-S(2)-Ni(1)	99.06(16)
C(3)-S(2)-Ni(1)	96.70(15)
C(9)-S(3)-C(1)	102.7(2)
C(9)-S(3)-Ni(1)	98.90(15)
C(1)-S(3)-Ni(1)	101.08(14)
C(2)-C(1)-S(3)	111.5(3)
C(1)-C(2)-C(3)	116.8(4)
C(2)-C(3)-S(2)	110.1(3)
C(6)-N(2)-C(5)	119.9(4)
C(6)-N(2)-Ni(1)	125.1(3)
C(5)-N(2)-Ni(1)	114.9(3)
C(8)-N(1)-C(4)	118.2(4)
C(8)-N(1)-Ni(1)	123.3(3)
C(4)-N(1)-Ni(1)	114.3(3)
C(8)-C(9)-S(3)	111.4(3)
O(1)-C(8)-N(1)	125.4(4)
O(1)-C(8)-C(9)	119.6(4)
N(1)-C(8)-C(9)	115.0(4)
O(2)-C(6)-N(2)	125.3(4)
O(2)-C(6)-C(7)	119.9(4)
N(2)-C(6)-C(7)	114.7(4)
N(2)-C(5)-C(4)	106.4(4)
C(6)-C(7)-S(2)	111.6(3)
N(1)-C(4)-C(5)	105.9(4)

Symmetry transformations used to generate equivalent atoms:

Table B-5. Crystal data and structure refinement for [Et₄N]₂Ni(ema)•O₂.

Empirical formula	C ₂₂ H ₄₈ N ₄ Ni O ₄ S ₂
Formula weight	555.47
Temperature	110(2) K
Wavelength	0.71073 Å
Crystal system, space group	Tetragonal, P43212
Unit cell dimensions	a = 10.1135(6) Å alpha = 90 deg. b = 10.1135(6) Å beta = 90 deg. c = 52.752(5) Å gamma = 90 deg.
Volume	5395.7(7) Å ³
Z, Calculated density	8, 1.368 Mg/m ³
Absorption coefficient	0.908 mm ⁻¹
F(000)	2400
Crystal size	0.30 x 0.10 x 0.10 mm
Theta range for data collection	1.54 to 25.00 deg.
Limiting indices	-11 ≤ h ≤ 12, -12 ≤ k ≤ 11, -62 ≤ l ≤ 62
Reflections collected / unique	41593 / 4626 [R(int) = 0.0414]
Completeness to theta = 25.00	97.0 %
Absorption correction	Semi-empirical from equivalents
Max. and min. transmission	0.9147 and 0.7723
Refinement method	Full-matrix least-squares on F ²
Data / restraints / parameters	4626 / 252 / 381
Goodness-of-fit on F ²	1.040
Final R indices [I > 2σ(I)]	R1 = 0.0597, wR2 = 0.1571
R indices (all data)	R1 = 0.0642, wR2 = 0.1619
Absolute structure parameter	0.00(9)
Largest diff. peak and hole	0.763 and -0.491 e.Å ⁻³

Table B-6. Bond lengths [Å] and angles [°] for [Et₄N]₂Ni(ema)•O₂.

Ni(1)-N(2)	1.861(4)
Ni(1)-N(1)	1.861(4)
Ni(1)-S(1)	2.1519(15)
Ni(1)-S(2)	2.1752(15)
S(1)-O(2)	1.436(6)
S(1)-O(1)	1.444(6)
S(1)-C(1)	1.826(7)
N(1)-C(2)	1.338(7)
N(1)-C(3)	1.491(7)
C(1)-C(2)	1.489(8)
C(1)-H(1A)	0.9900
C(1)-H(1B)	0.9900
S(2)-C(6)	1.836(6)
N(2)-C(5)	1.308(7)
N(2)-C(4)	1.478(6)
C(2)-O(3)	1.259(7)
C(3)-C(4)	1.484(8)
C(3)-H(3A)	0.9900
C(3)-H(3B)	0.9900
O(4)-C(5)	1.258(6)
C(4)-H(4J)	0.9900
C(4)-H(4K)	0.9900
C(5)-C(6)	1.530(7)
C(6)-H(6J)	0.9900
C(6)-H(6K)	0.9900
N11-C71	1.474(7)
N11-C11	1.507(7)
N11-C31	1.517(7)
N11-C51	1.526(7)
C11-C21	1.530(8)
C11-H1C1	0.9900
C11-H1D1	0.9900
C21-H2A1	0.9800
C21-H2B1	0.9800
C21-H2C1	0.9800
C31-C41	1.487(9)
C31-H3C1	0.9900
C31-H3D1	0.9900
C41-H4A1	0.9800
C41-H4B1	0.9800
C41-H4C1	0.9800
C51-C61	1.529(8)
C51-H5A1	0.9900
C51-H5B1	0.9900
C61-H6A1	0.9800
C61-H6B1	0.9800
C61-H6C1	0.9800
C71-C81	1.512(8)
C71-H7A1	0.9900
C71-H7B1	0.9900

Table B-6 (continued)

C81-H8A1	0.9800
C81-H8B1	0.9800
C81-H8C1	0.9800
N12-C72	1.476(7)
N12-C12	1.507(7)
N12-C52	1.524(7)
N12-C32	1.519(7)
C12-C22	1.532(9)
C12-H1E2	0.9900
C12-H1F2	0.9900
C22-H2D2	0.9800
C22-H2E2	0.9800
C22-H2F2	0.9800
C32-C42	1.487(9)
C32-H3E2	0.9900
C32-H3F2	0.9900
C42-H4D2	0.9800
C42-H4E2	0.9800
C42-H4F2	0.9800
C52-C62	1.531(8)
C52-H5C2	0.9900
C52-H5D2	0.9900
C62-H6D2	0.9800
C62-H6E2	0.9800
C62-H6F2	0.9800
C72-C82	1.514(8)
C72-H7C2	0.9900
C72-H7D2	0.9900
C82-H8D2	0.9800
C82-H8E2	0.9800
C82-H8F2	0.9800
N13-C73	1.472(6)
N13-C13	1.507(6)
N13-C53	1.524(6)
N13-C33	1.525(6)
C13-C23	1.531(7)
C13-H1G3	0.9900
C13-H1H3	0.9900
C23-H2G3	0.9800
C23-H2H3	0.9800
C23-H2I3	0.9800
C33-C43	1.490(8)
C33-H3G3	0.9900
C33-H3H3	0.9900
C43-H4G3	0.9800
C43-H4H3	0.9800
C43-H4I3	0.9800
C53-C63	1.530(7)
C53-H5E3	0.9900
C53-H5F3	0.9900
C63-H6G3	0.9800
C63-H6H3	0.9800
C63-H6I3	0.9800
C73-C83	1.515(7)

Table B-6 (continued)

C73-H7E3	0.9900
C73-H7F3	0.9900
C83-H8G3	0.9800
C83-H8H3	0.9800
C83-H8I3	0.9800
N(2)-Ni(1)-N(1)	85.39(19)
N(2)-Ni(1)-S(1)	173.03(14)
N(1)-Ni(1)-S(1)	87.71(14)
N(2)-Ni(1)-S(2)	87.60(13)
N(1)-Ni(1)-S(2)	171.98(15)
S(1)-Ni(1)-S(2)	99.22(6)
O(2)-S(1)-O(1)	116.7(4)
O(2)-S(1)-C(1)	102.4(4)
O(1)-S(1)-C(1)	104.9(4)
O(2)-S(1)-Ni(1)	112.6(3)
O(1)-S(1)-Ni(1)	117.9(3)
C(1)-S(1)-Ni(1)	98.81(19)
C(2)-N(1)-C(3)	118.7(4)
C(2)-N(1)-Ni(1)	124.4(4)
C(3)-N(1)-Ni(1)	114.4(4)
C(2)-C(1)-S(1)	111.0(4)
C(2)-C(1)-H(1A)	109.4
S(1)-C(1)-H(1A)	109.4
C(2)-C(1)-H(1B)	109.4
S(1)-C(1)-H(1B)	109.4
H(1A)-C(1)-H(1B)	108.0
C(6)-S(2)-Ni(1)	98.94(17)
C(5)-N(2)-C(4)	118.5(4)
C(5)-N(2)-Ni(1)	127.2(3)
C(4)-N(2)-Ni(1)	114.3(3)
O(3)-C(2)-N(1)	125.3(5)
O(3)-C(2)-C(1)	120.5(5)
N(1)-C(2)-C(1)	114.2(5)
C(4)-C(3)-N(1)	106.2(4)
C(4)-C(3)-H(3A)	110.5
N(1)-C(3)-H(3A)	110.5
C(4)-C(3)-H(3B)	110.5
N(1)-C(3)-H(3B)	110.5
H(3A)-C(3)-H(3B)	108.7
N(2)-C(4)-C(3)	109.4(4)
N(2)-C(4)-H(4J)	109.8
C(3)-C(4)-H(4J)	109.8
N(2)-C(4)-H(4K)	109.8
C(3)-C(4)-H(4K)	109.8
H(4J)-C(4)-H(4K)	108.2
O(4)-C(5)-N(2)	125.9(5)
O(4)-C(5)-C(6)	120.0(5)
N(2)-C(5)-C(6)	114.0(5)
C(5)-C(6)-S(2)	112.2(4)
C(5)-C(6)-H(6J)	109.2

Table B-6 (continued)

S(2)-C(6)-H(6J)	109.2
C(5)-C(6)-H(6K)	109.2
S(2)-C(6)-H(6K)	109.2
H(6J)-C(6)-H(6K)	107.9
C71-N11-C11	111.9(5)
C71-N11-C31	107.8(5)
C11-N11-C31	111.3(5)
C71-N11-C51	111.2(5)
C11-N11-C51	105.0(5)
C31-N11-C51	109.7(5)
N11-C11-C21	114.4(6)
N11-C11-H1C1	108.7
C21-C11-H1C1	108.7
N11-C11-H1D1	108.7
C21-C11-H1D1	108.7
H1C1-C11-H1D1	107.6
C11-C21-H2A1	109.5
C11-C21-H2B1	109.5
H2A1-C21-H2B1	109.5
C11-C21-H2C1	109.5
H2A1-C21-H2C1	109.5
H2B1-C21-H2C1	109.5
C41-C31-N11	117.4(7)
C41-C31-H3C1	108.0
N11-C31-H3C1	108.0
C41-C31-H3D1	107.9
N11-C31-H3D1	108.0
H3C1-C31-H3D1	107.2
C31-C41-H4A1	109.5
C31-C41-H4B1	109.4
H4A1-C41-H4B1	109.5
C31-C41-H4C1	109.5
H4A1-C41-H4C1	109.5
H4B1-C41-H4C1	109.5
N11-C51-C61	114.5(5)
N11-C51-H5A1	108.6
C61-C51-H5A1	108.6
N11-C51-H5B1	108.6
C61-C51-H5B1	108.6
H5A1-C51-H5B1	107.6
C51-C61-H6A1	109.5
C51-C61-H6B1	109.5
H6A1-C61-H6B1	109.5
C51-C61-H6C1	109.5
H6A1-C61-H6C1	109.5
H6B1-C61-H6C1	109.5
N11-C71-C81	117.0(6)
N11-C71-H7A1	108.0
C81-C71-H7A1	108.0
N11-C71-H7B1	108.0
C81-C71-H7B1	108.0
H7A1-C71-H7B1	107.3
C71-C81-H8A1	109.5

Table B-6 (continued)

C71-C81-H8B1	109.5
H8A1-C81-H8B1	109.5
C71-C81-H8C1	109.5
H8A1-C81-H8C1	109.5
H8B1-C81-H8C1	109.5
C72-N12-C12	111.6(6)
C72-N12-C52	111.2(6)
C12-N12-C52	105.9(6)
C72-N12-C32	107.5(7)
C12-N12-C32	111.5(6)
C52-N12-C32	109.2(6)
N12-C12-C22	113.7(7)
N12-C12-H1E2	108.8
C22-C12-H1E2	108.8
N12-C12-H1F2	108.8
C22-C12-H1F2	108.8
H1E2-C12-H1F2	107.7
C12-C22-H2D2	109.4
C12-C22-H2E2	109.5
H2D2-C22-H2E2	109.5
C12-C22-H2F2	109.5
H2D2-C22-H2F2	109.5
H2E2-C22-H2F2	109.5
C42-C32-N12	117.3(8)
C42-C32-H3E2	108.0
N12-C32-H3E2	108.0
C42-C32-H3F2	107.9
N12-C32-H3F2	108.0
H3E2-C32-H3F2	107.2
C32-C42-H4D2	109.5
C32-C42-H4E2	109.4
H4D2-C42-H4E2	109.5
C32-C42-H4F2	109.5
H4D2-C42-H4F2	109.5
H4E2-C42-H4F2	109.5
N12-C52-C62	114.0(7)
N12-C52-H5C2	108.8
C62-C52-H5C2	108.7
N12-C52-H5D2	108.7
C62-C52-H5D2	108.7
H5C2-C52-H5D2	107.6
C52-C62-H6D2	109.5
C52-C62-H6E2	109.5
H6D2-C62-H6E2	109.5
C52-C62-H6F2	109.5
H6D2-C62-H6F2	109.5
H6E2-C62-H6F2	109.5
N12-C72-C82	116.1(7)
N12-C72-H7C2	108.3
C82-C72-H7C2	108.3
N12-C72-H7D2	108.3
C82-C72-H7D2	108.3
H7C2-C72-H7D2	107.4

Table B-6 (continued)

C72-C82-H8D2	109.5
C72-C82-H8E2	109.5
H8D2-C82-H8E2	109.5
C72-C82-H8F2	109.5
H8D2-C82-H8F2	109.5
H8E2-C82-H8F2	109.5
C73-N13-C13	112.4(4)
C73-N13-C53	111.9(4)
C13-N13-C53	105.7(4)
C73-N13-C33	107.4(4)
C13-N13-C33	110.9(4)
C53-N13-C33	108.6(4)
N13-C13-C23	113.8(4)
N13-C13-H1G3	108.8
C23-C13-H1G3	108.8
N13-C13-H1H3	108.8
C23-C13-H1H3	108.8
H1G3-C13-H1H3	107.7
C13-C23-H2G3	109.5
C13-C23-H2H3	109.5
H2G3-C23-H2H3	109.5
C13-C23-H2I3	109.5
H2G3-C23-H2I3	109.5
H2H3-C23-H2I3	109.5
C43-C33-N13	116.6(5)
C43-C33-H3G3	108.1
N13-C33-H3G3	108.1
C43-C33-H3H3	108.2
N13-C33-H3H3	108.1
H3G3-C33-H3H3	107.3
C33-C43-H4G3	109.5
C33-C43-H4H3	109.5
H4G3-C43-H4H3	109.5
C33-C43-H4I3	109.5
H4G3-C43-H4I3	109.5
H4H3-C43-H4I3	109.5
N13-C53-C63	114.1(5)
N13-C53-H5E3	108.7
C63-C53-H5E3	108.7
N13-C53-H5F3	108.7
C63-C53-H5F3	108.8
H5E3-C53-H5F3	107.6
C53-C63-H6G3	109.5
C53-C63-H6H3	109.4
H6G3-C63-H6H3	109.5
C53-C63-H6I3	109.5
H6G3-C63-H6I3	109.5
H6H3-C63-H6I3	109.5
N13-C73-C83	116.5(5)
N13-C73-H7E3	108.2
C83-C73-H7E3	108.2
N13-C73-H7F3	108.2
C83-C73-H7F3	108.2
H7E3-C73-H7F3	107.3

Table B-6 (continued)

C73-C83-H8G3	109.5
C73-C83-H8H3	109.5
H8G3-C83-H8H3	109.5
C73-C83-H8I3	109.5
H8G3-C83-H8I3	109.5
H8H3-C83-H8I3	109.5

Table B-7. Crystal data and structure refinement for [Et₄N]₂[Cu(emi)].

Empirical formula	C ₁₈ H ₃₈ Cu _{0.50} N ₃ O ₄ S ₂
Formula weight	456.40
Temperature	60(2) K
Wavelength	0.71073 Å
Crystal system, space group	Orthorhombic, C ₂ cm
Unit cell dimensions	a = 8.021(2) Å alpha = 90 deg. b = 21.893(6) Å beta = 90 deg. c = 19.809(6) Å gamma = 90 deg.
Volume	3478.8(17) Å ³
Z, Calculated density	4, 0.871 Mg/m ³
Absorption coefficient	0.468 mm ⁻¹
F(000)	982
Crystal size	0.30 x 0.10 x 0.10 mm
Theta range for data collection	3.72 to 24.98 deg.
Limiting indices	-9 ≤ h ≤ 9, -25 ≤ k ≤ 26, -23 ≤ l ≤ 23
Reflections collected / unique	8136 / 1306 [R(int) = 0.0785]
Completeness to theta = 24.98	76.7 %
Absorption correction	Semi-empirical from equivalents
Max. and min. transmission	0.9547 and 0.8723
Refinement method	Full-matrix least-squares on F ²
Data / restraints / parameters	1306 / 169 / 118
Goodness-of-fit on F ²	1.089
Final R indices [I > 2σ(I)]	R ₁ = 0.0906, wR ₂ = 0.2154
R indices (all data)	R ₁ = 0.1463, wR ₂ = 0.2681
Largest diff. peak and hole	0.413 and -0.355 e.Å ⁻³

Table B-8. Bond lengths [\AA] and angles [$^\circ$] for $[\text{Et}_4\text{N}]_2[\text{Cu}(\text{emi})]$.

Cu(1)-N(1)#1	1.940(8)
Cu(1)-N(1)	1.940(8)
Cu(1)-S(1)#1	2.233(3)
Cu(1)-S(1)	2.233(3)
S(1)-C(1)	1.825(13)
O(1)-C(2)	1.272(13)
N(1)-C(2)	1.214(12)
N(1)-C(3)	1.482(16)
C(1)-C(4)	1.441(12)
C(1)-C(4)#2	1.442(12)
C(1)-C(2)	1.571(14)
C(3)-C(3)#1	1.41(2)
C(3)-H(3A)	0.9600
C(4)-H(4A)	0.9600
C(4)-H(4B)	0.9598
C(4)-H(4C)	0.9600
O(1W)-H(1)	0.8800
O(1W)-H(2)	0.8799
N11-C11	1.495(4)
N11-C71	1.494(4)
N11-C51	1.496(4)
N11-C31	1.497(4)
C11-C21	1.501(5)
C11-H1A1	0.9900
C11-H1B1	0.9900
C21-H2A1	0.9800
C21-H2B1	0.9800
C21-H2C1	0.9800
C31-C41	1.500(5)
C31-H3B1	0.9900
C31-H3C1	0.9900
C41-H4D1	0.9800
C41-H4E1	0.9800
C41-H4F1	0.9800
C51-C61	1.499(5)
C51-H5A1	0.9900
C51-H5B1	0.9900
C61-H6A1	0.9800
C61-H6B1	0.9800
C61-H6C1	0.9800
C71-C81	1.500(5)
C71-H7A1	0.9900
C71-H7B1	0.9900
C81-H8A1	0.9800
C81-H8B1	0.9800
C81-H8C1	0.9800
N12-C72	1.494(4)
N12-C52	1.496(4)
N12-C32	1.497(4)
N12-C12	1.494(4)
C12-C22	1.499(5)
C12-H1C2	0.9900

Table B-8 (continued)

C12-H1D2	0.9900
C22-H2D2	0.9800
C22-H2E2	0.9800
C22-H2F2	0.9800
C32-C42	1.499(5)
C32-H3D2	0.9900
C32-H3E2	0.9900
C42-H4G2	0.9800
C42-H4H2	0.9800
C42-H4I2	0.9800
C52-C62	1.500(5)
C52-H5C2	0.9900
C52-H5D2	0.9900
C62-H6D2	0.9800
C62-H6E2	0.9800
C62-H6F2	0.9800
C72-C82	1.498(5)
C72-H7C2	0.9900
C72-H7D2	0.9900
C82-H8D2	0.9800
C82-H8E2	0.9800
C82-H8F2	0.9800
N(1)#1-Cu(1)-N(1)	85.2(5)
N(1)#1-Cu(1)-S(1)#1	86.2(3)
N(1)-Cu(1)-S(1)#1	171.4(3)
N(1)#1-Cu(1)-S(1)	171.4(3)
N(1)-Cu(1)-S(1)	86.2(3)
S(1)#1-Cu(1)-S(1)	102.32(15)
C(1)-S(1)-Cu(1)	98.4(4)
C(2)-N(1)-C(3)	119.8(9)
C(2)-N(1)-Cu(1)	126.9(7)
C(3)-N(1)-Cu(1)	113.3(7)
C(4)-C(1)-C(4)#2	105.5(12)
C(4)-C(1)-C(2)	109.9(7)
C(4)#2-C(1)-C(2)	109.9(7)
C(4)-C(1)-S(1)	109.7(6)
C(4)#2-C(1)-S(1)	109.7(6)
C(2)-C(1)-S(1)	112.0(8)
N(1)-C(2)-O(1)	130.4(10)
N(1)-C(2)-C(1)	116.5(10)
O(1)-C(2)-C(1)	113.2(9)
C(3)#1-C(3)-N(1)	114.1(6)
C(3)#1-C(3)-H(3A)	109.0
N(1)-C(3)-H(3A)	108.3
C(1)-C(4)-H(4A)	108.0
C(1)-C(4)-H(4B)	112.0
H(4A)-C(4)-H(4B)	109.5
C(1)-C(4)-H(4C)	108.4
H(4A)-C(4)-H(4C)	109.5
H(4B)-C(4)-H(4C)	109.5
H(1)-O(1W)-H(2)	96.7
C11-N11-C71	109.7(4)
C11-N11-C51	109.5(4)
C71-N11-C51	109.6(4)

Table B-8 (continued)

C11-N11-C31	109.3(4)
C71-N11-C31	109.4(4)
C51-N11-C31	109.3(4)
N11-C11-C21	116.6(5)
N11-C11-H1A1	108.1
C21-C11-H1A1	108.1
N11-C11-H1B1	108.2
C21-C11-H1B1	108.2
H1A1-C11-H1B1	107.3
C11-C21-H2A1	109.5
C11-C21-H2B1	109.4
H2A1-C21-H2B1	109.5
C11-C21-H2C1	109.5
H2A1-C21-H2C1	109.5
H2B1-C21-H2C1	109.5
N11-C31-C41	116.5(5)
N11-C31-H3B1	108.2
C41-C31-H3B1	108.1
N11-C31-H3C1	108.2
C41-C31-H3C1	108.1
H3B1-C31-H3C1	107.3
C31-C41-H4D1	109.5
C31-C41-H4E1	109.4
H4D1-C41-H4E1	109.5
C31-C41-H4F1	109.5
H4D1-C41-H4F1	109.5
H4E1-C41-H4F1	109.5
N11-C51-C61	116.7(5)
N11-C51-H5A1	108.1
C61-C51-H5A1	108.2
N11-C51-H5B1	108.1
C61-C51-H5B1	108.1
H5A1-C51-H5B1	107.3
C51-C61-H6A1	109.4
C51-C61-H6B1	109.5
H6A1-C61-H6B1	109.5
C51-C61-H6C1	109.5
H6A1-C61-H6C1	109.5
H6B1-C61-H6C1	109.5
N11-C71-C81	116.8(5)
N11-C71-H7A1	108.1
C81-C71-H7A1	108.2
N11-C71-H7B1	108.1
C81-C71-H7B1	108.0
H7A1-C71-H7B1	107.3
C71-C81-H8A1	109.5
C71-C81-H8B1	109.6
H8A1-C81-H8B1	109.5
C71-C81-H8C1	109.4
H8A1-C81-H8C1	109.5
H8B1-C81-H8C1	109.5
C72-N12-C52	109.5(4)
C72-N12-C32	109.4(4)
C52-N12-C32	109.3(4)

Table B-8 (continued)

C72-N12-C12	109.7(4)
C52-N12-C12	109.4(4)
C32-N12-C12	109.4(4)
N12-C12-C22	117.0(5)
N12-C12-H1C2	108.0
C22-C12-H1C2	108.2
N12-C12-H1D2	108.1
C22-C12-H1D2	107.9
H1C2-C12-H1D2	107.3
C12-C22-H2D2	109.5
C12-C22-H2E2	109.7
H2D2-C22-H2E2	109.5
C12-C22-H2F2	109.3
H2D2-C22-H2F2	109.5
H2E2-C22-H2F2	109.5
N12-C32-C42	116.7(5)
N12-C32-H3D2	107.9
C42-C32-H3D2	108.1
N12-C32-H3E2	108.3
C42-C32-H3E2	108.2
H3D2-C32-H3E2	107.3
C32-C42-H4G2	109.4
C32-C42-H4H2	109.4
H4G2-C42-H4H2	109.5
C32-C42-H4I2	109.6
H4G2-C42-H4I2	109.5
H4H2-C42-H4I2	109.5
N12-C52-C62	116.8(5)
N12-C52-H5C2	108.3
C62-C52-H5C2	107.6
N12-C52-H5D2	108.1
C62-C52-H5D2	108.5
H5C2-C52-H5D2	107.3
C52-C62-H6D2	109.6
C52-C62-H6E2	109.0
H6D2-C62-H6E2	109.5
C52-C62-H6F2	109.9
H6D2-C62-H6F2	109.5
H6E2-C62-H6F2	109.5
N12-C72-C82	117.0(5)
N12-C72-H7C2	107.8
C82-C72-H7C2	107.3
N12-C72-H7D2	108.0
C82-C72-H7D2	109.0
H7C2-C72-H7D2	107.3
C72-C82-H8D2	109.2
C72-C82-H8E2	108.8
H8D2-C82-H8E2	109.5
C72-C82-H8F2	110.4
H8D2-C82-H8F2	109.5
H8E2-C82-H8F2	109.5

Symmetry transformations used to generate equivalent atoms: #1 -x,y,-z+1/2 #2 -x,y,z

VITA

Kayla Nance Green was born 1981 in Austin, TX and adopted by Howard and Kathy Nance. She grew up in the small town of Tolar, TX . She received her Bachelor of Science degree in chemistry from Tarleton State University in 2003 and began her graduate studies at Texas A&M University in August of 2003 under the direction of Marcetta Y. Darenbourg. Kayla can be contacted through her parents, Howard and Kathy Nance, at P.O. Box 457, Tolar, TX 76476, 254-835-4888.